THE UNIVERSITY OF QUEENSLAND

AUSTRALIA

Nonequilibrium dynamics of a one-dimensional Bose gas via the coordinate Bethe ansatz

Jan Christoph Zill

Dipl. Phys.

A thesis submitted for the degree of Doctor of Philosophy at

The University of Queensland in 2016

School of Mathematics and Physics

Abstract

This thesis is concerned with non-equilibrium phenomena in interacting quantum many-body systems. Specifically, we investigate the time-evolution and relaxation dynamics of Bose gases in a highly restricted geometry, which constrains the dynamics to one spatial dimension. This leads to a description of the system in terms of a simple model Hamiltonian which permits exact many-body quantum mechanical solutions due to its integrability.

In the first part of this thesis, a computational method is developed to obtain experimentally relevant correlation functions in the framework of the coordinate Bethe ansatz. We employ this method to compute exact ground-state correlation functions of the Lieb–Liniger gas for up to seven particles covering the whole regime of repulsive interactions. We also investigate the dynamics of the system after an instantaneous change of the interaction strength. This quantum quench deposits large amounts of energy that cannot be dissipated due to the system being closed, and so the dynamics far from equilibrium are probed. We prepare the system in two different initial states, and quench to the same final interaction strength. The latter is determined in such a way that the added energy due to the quench is the same for both scenarios. Conventional statistical mechanics predicts the same relaxed state, but due to the integrability of the system all considered correlation functions of the relaxed states differ from each other and also from the thermal ones.

We then investigate the dynamics and relaxed state for a quench from zero to repulsive interactions in more detail, focussing on the mechanism of relaxation and the involved time-scales. We find that local correlation functions relax on time-scales determined by the interaction strength, in contrast to non-local correlation functions, whose relaxation time-scale is proportional to the system size.

Next, we employ the same methodology to study the one-dimensional Bose gas with attractive interactions. In this case many-body bound states are permissible solutions of the Lieb–Liniger model. We compare exact ground-state correlation functions of up to seven particles to their corresponding mean-field solution. The latter displays a quantum phase transition at a critical interaction strength, marking the transition from a uniform-density state to a localized bright soliton. Our exact results agree remarkably well with the corresponding mean-field solution past the critical point. We also investigate the dynamics

following an interaction strength quench, starting again from the non-interacting ground state. Bound states strongly influence correlation functions for all post-quench interaction strengths, and local correlation functions are largely increased compared to their initial value.

In the last part of this thesis, we investigate the behavior of the one-dimensional Bose gas under periodic driving of the interaction strength. To this end, we extend the coordinate Bethe-ansatz formalism by employing Floquet theory to obtain solutions for the full time-dependent Hamiltonian. This realizes an extension to non-integrable systems in a way that allows controlled breaking of integrability. We compare the dynamics of the system following an interaction quench to a fixed final interaction strength to that of a system with periodically modulated post-quench interaction strength. For fast driving, the system evolves according to the time-averaged Hamiltonian and correlation functions are nearly identical to those of the undriven system. The response of the system qualitatively changes at resonances of the time-averaged Hamiltonian, where we observe energy absorption and a marked change in correlation functions. However, the system does not absorb energy indefinitely.

Declaration by author

This thesis is composed of my original work, and contains no material previously published or written by another person except where due reference has been made in the text. I have clearly stated the contribution by others to jointly-authored works that I have included in my thesis.

I have clearly stated the contribution of others to my thesis as a whole, including statistical assistance, survey design, data analysis, significant technical procedures, professional editorial advice, and any other original research work used or reported in my thesis. The content of my thesis is the result of work I have carried out since the commencement of my research higher degree candidature and does not include a substantial part of work that has been submitted to qualify for the award of any other degree or diploma in any university or other tertiary institution. I have clearly stated which parts of my thesis, if any, have been submitted to qualify for another award.

I acknowledge that an electronic copy of my thesis must be lodged with the University Library and, subject to the policy and procedures of The University of Queensland, the thesis be made available for research and study in accordance with the Copyright Act 1968 unless a period of embargo has been approved by the Dean of the Graduate School.

I acknowledge that copyright of all material contained in my thesis resides with the copyright holder(s) of that material. Where appropriate I have obtained copyright permission from the copyright holder to reproduce material in this thesis.

Publications during candidature

Peer-reviewed papers

1. Jan C. Zill, Tod M. Wright, Karén V. Kheruntsyan, Thomas Gasenzer, and Matthew J. Davis, *Relaxation dynamics of the Lieb–Liniger gas following an interaction quench: A coordinate Bethe-ansatz analysis*, Physical Review A **91**, 023611 (2015).

2. Jan C. Zill, Tod M. Wright, Karén V. Kheruntsyan, Thomas Gasenzer, and Matthew J. Davis, *An exact computational method for the one-dimensional Bose gas via the coordinate Bethe ansatz*, invited special issue "Focus on Strongly Interacting Quantum Gases in One Dimension" in New Journal of Physics **18** 045010 (2016).

Publications included in this thesis

The following publications arose during candidature and are reproduced verbatim in the indicated chapters.

- Jan C. Zill, Tod M. Wright, Karén V. Kheruntsyan, Thomas Gasenzer, and Matthew J. Davis, *Relaxation dynamics of the Lieb–Liniger gas following an interaction quench: A coordinate Bethe-ansatz analysis*, Physical Review A **91**, 023611 (2015) — incorporated as Chapter 4.

Author	Contribution
Jan C. Zill	→ Performed numerical calculations (100%) → Interpreted results (35%) → Wrote manuscript (35%)
Tod M. Wright	→ Interpreted results (35%) → Wrote and edited manuscript (35%)
Karén V. Kheruntsyan	→ Interpreted results (5%) → Edited manuscript (5%)
Thomas Gasenzer	→ Interpreted results (5%) → Edited manuscript (5%)
Matthew J. Davis	→ Interpreted results (20%) → Edited manuscript (20%)

- Jan C. Zill, Tod M. Wright, Karén V. Kheruntsyan, Thomas Gasenzer, and Matthew J. Davis, *An exact computational method for the one-dimensional Bose gas via the coordinate Bethe ansatz*, invited special issue "Focus on Strongly Interacting Quantum Gases in One Dimension" in New Journal of Physics **18** 045010 (2016) — incorporated as Chapter 3.

Author	Contribution
Jan C. Zill	→ Performed numerical calculations (100%) → Interpreted results (35%) → Wrote manuscript (35%)
Tod M. Wright	→ Interpreted results (35%) → Wrote and edited manuscript (35%)
Karén V. Kheruntsyan	→ Interpreted results (5%) → Edited manuscript (5%)
Thomas Gasenzer	→ Interpreted results (5%) → Edited manuscript (5%)
Matthew J. Davis	→ Interpreted results (20%) → Wrote and edited manuscript (20%)

Contributions by others to the thesis

Concerning the first part of the thesis (i.e. quench-related physics in Chapters 3, 4, and 5), Matt and Thomas helped frame the initial broad research questions. Matt, Tod and Karén contributed to the interpretation of results and the direction of research. Tod spent a considerable amount of time turning the draft of my first paper (included as Chapter 4) into a much better work, teaching me a great deal about how to write a paper in the process.
In Chapter 6, Matt framed the initial question of periodic driving and had the idea to utilize the 'simple' square-wave driving protocol.
Simon Haine and Matt proofread the introduction and background section.

Statement of parts of the thesis submitted to qualify for the award of another degree

None.

Acknowledgement

First off, I want to thank Matt for the opportunity to come to Brisbane and work on interesting topics. Thank you for throwing out ideas for me to explore without insisting, I enjoyed a lot of freedom while still getting guidance and feedback. A big thank you to Tod for his patience and taking time for explaining things to me, and for putting considerable effort into improving my work even after he wasn't around anymore. Thanks also go to Karén, whom I could talk to directly when Matt and Tod where gone.

I also want to thank Joachim Brand and Victor Gurarie for examining this thesis.

I'm grateful to Thomas for initiating the work and getting me interested in this field, and therefore indirectly opening up the opportunity for me to move to Brisbane, and his thoughtful and thorough feedback on the manuscripts.

I spent a considerable amount of time in and around the office and I want to thank Rob, Jim, Simon (special thanks for proofreading the first two chapters), Behnam, Nick, Stuart, Yasar, and all the other people that made these times fun. Outside the office, a couple of people, commonly referred to as 'the crazy guys', made me feel home in Brisbane from the beginning (special shout-out to Tim for the balcony sessions and for listening to my ramblings when I was writing up this thesis). The french connection I met later on should not go unmentioned. To my friends in Europe: Thank you for showing up to the wedding (this list includes Jan and Falko, you wanted to come and I appreciate it), and especially Nico for being my best man (your speech wasn't bad either...).

Last but not least, I want to thank my families: The one in Germany, especially my parents, who always supported me in every which way. The new one in France, especially Maryse and Patrick, who welcomed me with open arms and made the time there very enjoyable.

The wedding was absolutely amazing and this is due to both families putting in a lot of effort!

And this naturally leads to to the last person to thank: Marie, my family in Australia! Thank you for countless things, among them keeping me sane and happy during busy times, for putting up with me during my lazy/annoying times, and for convincing me to get a dog.

Keywords

Bethe ansatz, Lieb–Liniger model, one-dimensional quantum systems, nonequilibrium quantum systems, strongly correlated systems, ultracold atoms, Floquet theory.

Australian and New Zealand Standard Research Classifications (ANZSRC)

ANZSRC code: 020601, Degenerate Quantum Gases and Atom Optics, 100%.

Fields of Research (FoR) Classification

FoR code: 0206, Quantum Physics, 100%.

Contents

List of Figures

List of Tables

1

Introduction

Equilibrium statistical mechanics is one of the cornerstones of modern physics [11–13]. However, understanding how systems far from equilibrium evolve towards states where they can be described within its framework is surprisingly elusive. An important goal is to connect the evolution of the microscopic equations of motion with the well-established fact that systems out of equilibrium relax to generic time-independent states. The mathematical formulation of *classical* statistical mechanics is performed in phase space, where the generalized coordinates and momenta identify the microstate. The key concept is ergodicity, which arises because generic classical systems evolve according to non-linear equations of motions, which lead to the chaotic behavior of trajectories in phase space. This justifies the fundamental assumption of statistical mechanics, which states that every microstate of a given system compatible with its macroscopic state is equiprobable. For macroscopic systems, this also

justifies the use of the Gibbs ensemble, which assigns a temperature to systems.[1]

The above situation is quite generic, but it is well known that there are also classical systems that do not relax. In their seminal numerical experiment, Fermi, Pasta, Ulam and Tsingou[2] studied the dynamics of a chain of weakly non-linear interacting harmonic oscillators [15]. A system of up to 64 masses was initialized with all energy in the first few Fourier modes, and the authors expected to observe equipartition of energy amongst all modes after some time due to the non-linear coupling. However, to their great surprise, they instead observed a complicated temporal behavior with quasi-recurrences and no equipartition of energy, and hence no thermalization. It was later found that different initial conditions lead to thermalization [16]. The theoretical framework to explain this is the famous Kolmogorov–Arnol'd–Moser (KAM) theorem [16], based on integrable systems and slight perturbations to these, and the fact that the continuous analog of the Fermi–Pasta–Ulam–Tsingou system is described by the integrable Korteweg–deVries equation [17]. A classical system is said to be integrable if it has as many constants of motion as degrees of freedom. This leads to a foliation of the $2N$–dimensional phase space into N–dimensional periodic tori, where N is the number of constants of motions. As a consequence, ergodicity is violated and the system will never thermalize. The essence of the KAM theorem is that small non-linear perturbations to an integrable system lead to a deformation of some of the invariant tori but keep them periodic, while others are destroyed. This results in a part of phase space supporting quasi-periodic motion (and the measure of that phase space volume is positive). For initial conditions in this part, the system will not thermalize due to non-ergodicity, while for different initial conditions it can.

Quantum thermalization

Our currently accepted fundamental microscopic theory is quantum mechanics, so some natural questions at hand are [13, 18–21]: Can relaxation towards equilibrium be explained

[1] Ergodicity means that time–averaging and ensemble averaging are equivalent. This implies that measurements of macroscopic observables involve time–averaging over the system's phase–space trajectories. Some authors reject this assumption, referring to statistical independence instead (which is based on subsystem considerations, justified by the fact that the measurement of observables usually only concern these).

[2] Mary Tsingou Menzel implemented the computer code but wasn't cited as an author due to the conventions at Los Alamos at the time, see e.g. Ref. [14].

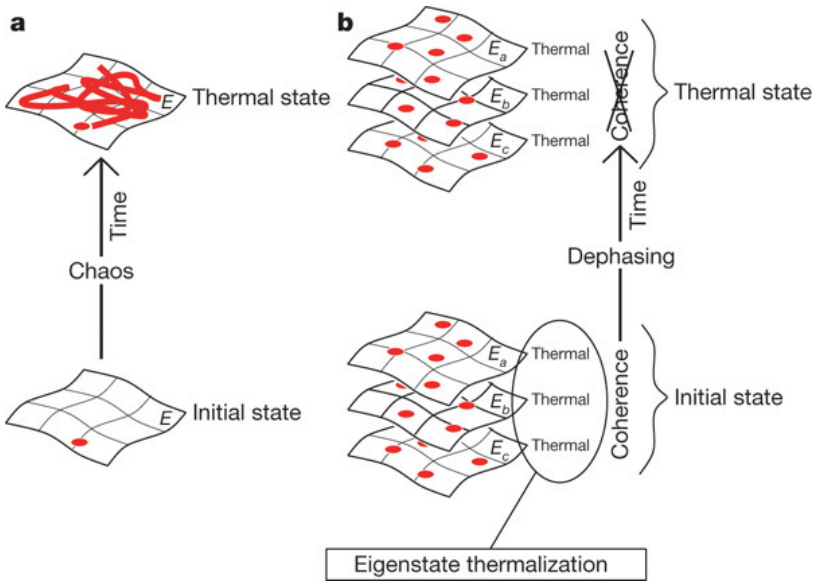

FIGURE 1.1: Thermalization mechanism in classical and quantum systems. **a**: Classical system. For a generic system prepared in an initial state with energy E, the non-linear equations of motion lead to chaotic dynamics in phase-space, covering the entire volume compatible with the energy of the system ergodically, and the system thermalizes. **b**: Quantum system. The expectation value of a physical operator in any energy eigenstate equals the microcanonical thermal average. Initially, the system is in a coherent superposition of eigenstates. During the time evolution these coherences dephase, and for operators whose expectation value depend smoothly on the energy, the relaxed value is described by a microcanonical ensemble.

with quantum mechanics? Is there a quantum analog of integrability, i.e. a separation of dynamical systems into distinct classes of completely different physical behavior? If so, does breaking quantum integrability lead to an analog of the classical KAM theorem?

In isolated systems, the time-evolution is unitary, and for non-relativistic systems is governed by Schrödinger's equation. The question thus is if interactions between particles are sufficient to make the system ergodic. Some care has to be taken to define quantum ergodicity: Since the notion of coordinates in phase space becomes meaningless in quantum mechanics due to the fundamental canonical commutation relations, the correspondence to the classical case is not one to one. Additionally, a system prepared in a pure state will remain pure for all times, making a description of the entire system in terms of a mixed thermal density matrix impossible. For macroscopic systems under very general conditions, von Neumann [22] constructed commuting macroscopic observables, coarse-grained over microcanonical shells, which do satisfy what he called the quantum ergodic theorem. Another result, referred to as canonical typicality, is that for a macroscopic system initially prepared

in a typical eigenstate of the Hamiltonian, the density matrix of a small subsystem is described by the canonical ensemble [23]. But what happens if the system is not in a typical eigenstate? Is there a mechanism that leads to thermalization for systems in a superposition of many energy eigenstates?

One proposed mechanism is the so-called Eigenstate Thermalization Hypothesis [1, 24, 25]. It states that the expectation value of macroscopic observables are smooth functions of energy in the energy eigenbasis. If this is the case, then thermalization follows for any initial condition sufficiently narrow in energy (where the expectation value of observables over all these eigenstates is practically constant and hence the microcanonical postulate is valid). Initially, coherences between eigenstates mask this thermal state and time evolution reveals it via the dephasing of energy eigenstates, as depicted in Fig. 1.1. While this hypothesis was recently examined in numerical experiments [1] and found to be the mechanism of relaxation, the question of whether this scenario is universal is still not clear [19–21, 26–31].

One drawback of the Eigenstate Thermalization Hypothesis is that it does not provide answers to questions with respect to thermalization times, or how equilibrium is established in a system. The former is important since equilibration on very long time-scales would mean we can never actually observe it. General bounds on thermalization times, based on very few generic assumptions, are available [32–37], but they are far off from those observed in numerical calculations and actual experiments, see Ref. [28] and references therein. Concerning the approach to equilibrium, it was conjectured that equilibrium is established locally for short-range interacting models, and then spreads through the system by means of quasi-particle propagation [38]. This was experimentally verified in Ref. [39]. However, the experiment probed the low-lying energy excitations (in this case phonons with linear dispersion), and it is not clear what would happen for larger energies, where excitations are free particles with quadratic dispersion. Ref. [40] formulated the local relaxation picture on a lattice, based on a Lieb-Robinson bound. A Lieb-Robinson bound is a model-dependent bound on the speed with which correlations spread in short-range interacting non-relativistic quantum systems. It was originally introduced in Ref. [41] for a one-dimensional spin model and "The physical content of the statement is that information can propagate in the system only with a finite group velocity" [41]. Outside the 'light cone' defined by this

velocity, correlations are exponentially suppressed [42]. The first experimental observation with ultracold atoms was reported in Ref. [43]. Recently, long-range interacting systems in certain parameter regimes were found to obey Lieb-Robinson bounds as well [44–49].

Non-thermalizing quantum systems

Thermalization is a very generic property and ubiquitous in nature, however, there are quantum systems that do not thermalize. Since the ground breaking work of Anderson [50], it is well known that disorder can lead to localization of particles and prevent thermalization. The original work was at the single-particle level, but recently, many-body localization of quantum systems has been an intense area of research, both experimentally [51–53] and theoretically, see Refs. [28, 29, 54] and references therein. In this thesis, we will not deal with disorder. But even in this case, there are systems that do no thermalize. In the seminal experiment of Kinoshita *et al.* [2], an array of tubes of strongly interacting atomic bosons was created with an optical lattice. The energy of the atoms was much lower than the trapping potential so that tunneling between different tubes was negligible and each tube realized an isolated one-dimensional system. Subjecting the system to two appropriately timed Bragg laser pulses put the atoms in an initial superposition of two different momentum states $\pm 2p_0$, where p_0 is the photon momentum. Since the kinetic energy of the atoms after the pulse was small compared to the next transverse excited state of the trap, the dynamics remained one-dimensional. Due to an additional weak harmonic trap in this dynamical direction, the atoms oscillated back and forth, colliding with each other. It was found that even after thousands of collisions, the momentum distribution of the gas did not thermalize, see Fig. 1.2(a). Repeating the experiment in three spatial dimensions, the authors found thermalization after as few as three collisions on average. The suggested explanation was that the one-dimensional system is very close to the quantum integrable Lieb–Liniger model [55, 56]. Sutherland [55] in his book defines quantum integrability as a feature of systems that are solvable by Bethe ansatz, i.e. systems in which the scattering between particles is non-diffractive.[3] This leads to an algebraic set of equations, known as Yang–Baxter equations [58, 59]. A fundamental question that has attracted a lot of recent

[3] Let us remark, however, that this is only a good definition for continuous systems such as the Lieb–Liniger gas we will be concerned with in this thesis. Care has to be taken for generalizations to lattice systems, for a discussion see Ref. [57].

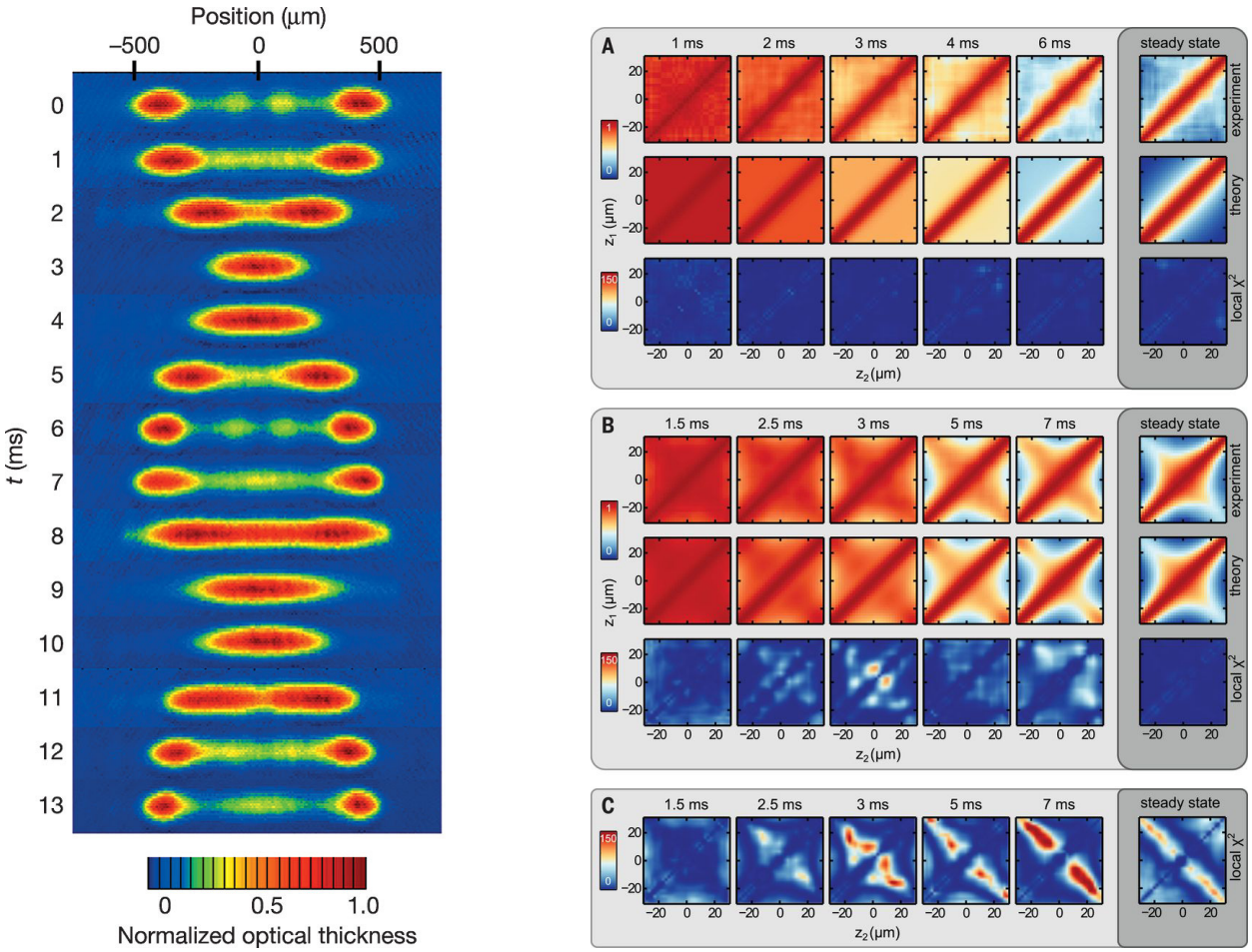

(a) (b)

FIGURE 1.2: Experimental realizations of non-equilibrium states in one-dimensional bosonic systems that do not thermalize. (a) The quantum Newton's cradle experiment, realized in a tight optical trap so that the particles are strongly interacting and the dynamics takes place in one spatial dimension. The image shows the density of the gas after expansion (corresponding to the momentum distribution) for different evolution times in the trap. (b) Generalized Gibbs Ensemble on an atom-chip for weakly interacting systems. A one-dimensional Bose gas is split into two identical copies, and the subsequent time-evolution is monitored by absorption images after trap-release. The interference fringes are used to calculate the displayed two-point phase correlation function. Subfigures A and B correspond to different splitting protocols. For the former, a single effective temperature describes the relaxed state well. The latter needs at least two different temperatures, as illustrated in Subfigure C, where a comparison of the experimental data with a model based on the usual Gibbs ensemble with a single temperature has large χ^2 values.

(a) Reprinted by permission from Macmillan Publishers Ltd: Nat. Phys. **440**, 900, copyright 2006 (Ref. [2]).

(b) From Science **348**, 207 (2015) (Ref. [3]). Reprinted with permission from AAAS.

interest is: do quantum integrable systems that are initially out of equilibrium relax towards a steady state? If so, can that steady state be described with statistical mechanics?

Contrary to systems for which the only conserved quantity is the energy, integrable systems have many constants of motion, and the information of the initial state encoded in these will survive in the subsequent dynamics for all times. Turning to Jaynes' maximum entropy principle [60, 61], a generalization of the conventional Gibbs ensemble (hence the name generalized Gibbs ensemble (GGE)) can be derived by explicitly fixing all constants of motion, leading to Lagrange multipliers (effective 'temperatures') for the expectation values of the conserved quantities [62]. Recently, a GGE was observed in the experiment of Ref. [3]. A system of one-dimensional ultracold bosons was initially prepared on an atom-chip, before being coherently split into two identical halves. The time-resolved observation of phase-fluctuations was achieved by taking absorption images of the interfering (quasi-)condensates after trap release for different in-trap evolution times. From this, the two-point phase correlation function was extracted, see Fig. 1.2(b). Interestingly, for the first splitting protocol in the experiment [Fig. 1.2(b)A], the steady state of the two-point correlation function was well described by a (quasi-)thermal ensemble with a single (effective) temperature. For a different splitting protocol [Fig. 1.2(b)B], this was not the case and two different temperatures had to be used. Performing a more detailed analysis, the authors fitted a model of non-interacting phonons to the data,[4] finding that only the first ten modes contribute significantly. This is in contrast to the number of atoms involved, which was on the order of 5000.

This raises several questions [18, 19, 28, 63, 64]: Which conserved quantities are important, and how can they be classified? Which correlation functions are actually described by the GGE? Does the GGE work in systems that are not mappable to free (quasi-)particles?[5] What happens if the initial state breaks the symmetry of the final Hamiltonian? What role does locality play?

A lot of progress has been made recently, without answering all questions. For example, the authors that coined the term GGE studied hard-core bosons [62], which are mappable

[4] The experiment was performed in the weakly interacting regime, and can thus be modeled with a Bogoliubov-method for quasi-condensates.

[5] A quadratic Hamiltonian can arise as the effective low-energy description of a system or via some (possibly non-local) mapping [65], not necessarily implying non-interacting systems.

to free fermions via a Jordan–Wigner mapping [66]. The fermionic quasi-momentum distribution is fixed, and the number of conserved quantities is thus equal to the number of lattice sites, highlighting the concept of locality. There is a large body of work for systems mappable to a quadratic Hamiltonian, each showing that the GGE correctly captures the relaxed state (either in terms of sub-system considerations [67, 68], or in terms of local correlation functions [69–79]). For non-local quantities, on the other hand, this is only true in general if there are no correlations between the eigenmodes of the post-quench Hamiltonian in the initial state [67, 80–82].

Recent works have found disagreement for fully interacting theories[6] between the relaxed state in spin-chains and the GGE constructed from all (known) local charges [83, 84]. In subsequent work, it was suggested that the GGE still applies, but only if one takes into account charges that are slightly non-local [85, 86]. Refs. [85, 86] showed that this leads to a correct description of the relaxed state in interacting Heisenberg spin-chains. The authors also hinted at a truncated construction of the GGE by only keeping the most local conserved charges along the lines of Ref. [69], and reported rapid convergence. Another approach concerning the efficient construction of the GGE by stochastically sampling the relevant Hilbert space with appropriate measure was presented in Ref. [87].

The previous discussion applied to integrable models. But as discussed in connection with the experiments of Refs. [2, 3], an additional weak potential in the dynamical direction breaks integrability. Nevertheless, both systems did not thermalize on experimental observable time-scales, so a natural question at hand is if there is some kind of quantum analogue of the classical KAM theorem. Theoretical studies have found that for sufficiently weak integrability breaking,[7] a state compatible with a GGE (possibly built out of approximate conserved quantities) survived for intermediate times, while in the long-time limit the system tends to true thermal equilibrium [88–93]. The intermediate state is often referred to as being pre-thermalized, a term coined in Ref. [94] and experimentally observed in Refs. [95–98]. The time-scales for which this pre-thermalized state survives, as well as how it comes about, are important open questions. A physically intuitive picture was given in Ref. [38],

[6] In the sense of not mappable to a quadratic Hamiltonian.

[7] One could think of a Hamiltonian of the form $\hat{H} = \hat{H}_0 + \epsilon\hat{V}$, where $\hat{H}_0$ is integrable and ϵV is much smaller than any other energy scale.

where the authors described the dynamics of a system following a quench[8] by means of quasi-particle excitations above the equilibrium state. The quasi-particles propagate through the system, determining the time-scale of relaxation, while integrability-breaking interactions between them lead to thermalization [92].

Non-equilibrium protocols

Due to the unprecedented control over ultracold quantum gases [99], there are many different ways to bring a quantum system out of equilibrium. Two possible scenarios, considered in this thesis, are the following. A so-called *quench* refers to preparing a system in a stationary state of some Hamiltonian and then suddenly changing a parameter of this Hamiltonian. Sudden in an experimental context refers to a change on a time-scale much shorter than any other in the system. This can for example be achieved by employing a Feshbach resonance to change the strength of interactions, as explained in Chapter 2. The quench puts the system into a superposition of highly excited eigenstates. For closed systems, the added energy can not be dissipated, and the dynamics far from equilibrium are probed. For example, in Chapters 3, 4, 5 of this thesis we will investigate the influence of instantaneously changing the interaction strength of a system of one-dimensional bosons, starting from either the non-interacting ground state, or a correlated ground state with strong interactions. This sudden interaction quench scenario is conceivably the simplest way of putting a system out of equilibrium. Another possible way of studying non-equilibrium effects is given by the *periodic driving scenario*. In this case, the Hamiltonian is modulated periodically in time, invalidating a direct description in terms of the powerful methods of time-independent quantum mechanics. But due to the periodicity of the Hamiltonian, it is possible to incorporate the time-dependence into the basis states leading to a description in terms of time-periodic Floquet modes and their quasi-energies [100–103]. This is in complete analogy with the better-known space-periodic case, where Bloch waves and their quasi-momenta give valuable insight into condensed matter systems [104]. For stroboscopic times, i.e. integer multiples of the driving period, the time evolution can be described in terms of a hermitian operator, the so-called Floquet Hamiltonian. This quasi-Hamiltonian depends on the specific system and driving parameters, making it possible to engineer systems with properties very different to

[8] For a definition of 'quench' see below.

those of the instantaneous Hamiltonian. This has lead to the experimental realization of prototypical condensed-matter Hamiltonians, like the Harper–Hofstadter model [105–107] and the Haldane model [108], and there exist numerous theoretical proposals [103, 109–124] and experimental realizations of a wide range of systems [125–147].

Intuitively, generic interacting driven systems absorb energy continuously and heat up to an infinite-temperature thermal state. This was indeed theoretically found to be the case for systems that obey an extension of the eigenstate thermalization hypothesis with regards to the Floquet states [148–152]. However, several recent works found that for certain parameter regimes, heating can be suppressed on experimental time-scales [148, 152–157], and the system can reach a non-thermal steady state, in analogy with the prethermalization scenario discussed earlier [153, 158–160]. For systems for which the instantaneous Hamiltonian is integrable, observables can synchronize with the driving [161] and in Ref. [162] a periodic version of the GGE was constructed for a driven hard-core boson system. The effective Hamiltonian for this system can be mapped to a quadratic Hamiltonian, in analogy to the non-driven case described earlier [62], and the constants of motions are again given by the occupation numbers of the non-interacting Jordan–Wigner fermions on each lattice site. Focusing on the properties of the Floquet (effective) Hamiltonian, Ref. [163] showed that even if the instantaneous Hamiltonian is integrable, a system might thermalize, depending on the instantaneous constants of motions. Ref. [164] also came to the conclusion that the integrability of the instantaneous Hamiltonian does not allow to predict the behavior of the corresponding driven system. In Chapter 6, we will study a specific global driving scenario with the instantaneous Hamiltonian given by the Lieb–Liniger model, which allows us to access a wide range of interparticle interaction strengths in a continuum model.

Outline of thesis

In **Chapter 2**, we develop the background and introduce the theoretical tools we will be using throughout this thesis. We show how in our three-dimensional world, certain systems can have one-dimensional dynamics and how we can describe the interactions between atoms in dilute, ultracold Bose gases with a simple model potential. We give a short overview of some theoretical tools for the one-dimensional Bose gas out of equilibrium, before focusing on the technique used throughout this thesis: the coordinate Bethe ansatz. We also briefly

introduce the (zero temperature) thermodynamic Bethe ansatz.

Chapter 3 is a reproduction of Ref. [165] and introduces a computational method for calculating matrix elements in the Lieb–Liniger model via the coordinate Bethe ansatz. We compute several ground-state correlation functions for system sizes of up to seven particles and characterize the finite-size scaling of the system, before turning to a non-equilibrium scenario. We prepare the system in two distinct initial states, one the non-interacting ground state, the other a correlated ground state at strong interactions. We then perform a sudden quench to a common final interaction strength, determined in such a way that the post-quench energy is the same for both initial states. We compute dynamical correlation functions for five particles and also compare the distinct relaxed states to the predictions of conventional statistical mechanics.

Chapter 4 deals with the quench to repulsive interaction strengths from the initially non-interacting ground state in more detail and was published as Ref. [166]. We characterize several dynamical correlation functions, as well as the instantaneous fidelity for several representative post-quench interaction strengths. We also investigate the relaxed state of the system in terms of correlation functions and compare these to their corresponding thermal counterparts.

In **Chapter 5**, we take the same non-interacting initial state, but this time quench to attractive interactions. The behavior of correlation functions is influenced by bound states in this case, and they contribute to dynamical as well as relaxed correlation functions. We also calculate ground state correlation functions for up to seven particles and compare these to mean-field results.

Chapter 6 is concerned with periodically driving the interaction strength of the Lieb–Liniger gas. Our aim is to compare the post-quench dynamics of the integrable, time-independent Hamiltonian following a quench (as studied in the previous chapters) to that of the periodically driven system with the same initial (post-quench) state. The driving amplitude and frequency are adjustable in our calculations, and we present results for several parameters and characterize their influence on correlation functions.

We conclude with the final **Chapter 7**, where we summarize our findings and also outline some open questions.

2

Background

In this chapter, we describe the theoretical background of this thesis. We start by considering the relevant length scales governing the physical properties of ultracold (bosonic) atomic gases. Next, we derive an effective interatomic potential for particles. At the very low temperatures realized in experiments, it turns out that the full scattering problem can be replaced by a simple pseudo-potential, whatever the microscopic details of the exact interatomic potential are. Equipped with this result, we derive an effective low-energy Hamiltonian for scattering of particles that are tightly trapped and therefore confined to one spatial dimension. We then give an overview of different theoretical approaches to non-equilibrium dynamics in this one-dimensional system, before focussing on the techniques used in this thesis. We introduce the coordinate Bethe ansatz by solving the two-particle problem for attractive and repulsive interactions, which already turns out to have a rich structure. Next, we generalize this approach to N particles, paying special attention to the emerging Yang–Baxter integrability. We also shortly introduce the thermodynamic Bethe

ansatz at zero temperature and discuss its excitation spectrum.

2.1 Interactions in ultra-cold gases

The first experimental realizations of Bose-Einstein condensates in 1995 where performed with alkali gases that were cooled to temperatures below $1\mu K$ [167–169]. The interatomic potential between two alkali atoms can be approximated by a Lennard-Jones potential

$$V(r) = \frac{C_{12}}{r^{12}} - \frac{C_6}{r^6} \,, \tag{2.1}$$

where $r = |\vec{r}_2 - \vec{r}_1|$ is the distance between atom 1 and 2 and the coefficients C_{12} and C_6 are given by the atomic properties [170]. At short interparticle separations, the electronic orbitals overlap and the Pauli principle leads to strong repulsion. At distances further away, the interaction is dominated by the induced dipole-dipole interactions between the electrons, resulting in the attractive r^{-6} van der Waals potential. The *relevant length scales* of physical quantities in the system are the following. The atoms are trapped in magneto-optical potentials, which usually provides by far the longest length scale of the system. This means that the system can be treated in the local density approximation.[1] At the very low temperatures we are considering, the deBroglie (or thermal) wavelength $\lambda_{\mathrm{dB}} = (\frac{2\pi\hbar^2}{mk_BT})^{1/2}$ is large. The interparticle distance l_n is determined by the density of the system, and for the system to be in the quantum degenerate regime, we require the wavelength of the particles to be on the same order, $l_n/\lambda_{\mathrm{dB}} \approx 1$. The length scale associated with interactions can be deduced from Eq. (2.1) by equating the kinetic energy with the interaction potential, yielding $l_{\mathrm{vdW}} = (\frac{mC_6}{\hbar^2})^{1/4}$. For typical values of C_6, the van der Waals length is much smaller than the interparticle distance. Thus, the atoms never resolve physics on shorter ranges, corresponding to high energies. This already hints at something we will discover in the next section: the physics of ultracold gases can be described by an effective low-energy Hamiltonian.

[1] The local density approximation states that the trapped system locally behaves like a uniform system. In a grand-canonical description, the chemical potential of the trapped system can be approximated by the chemical potential of the uniform system, depending on the density of atoms at a space point, plus the contribution of the trapping potential at the same point. This leads to an implicit equation for the density of atoms in the trapped system, the well-known Thomas-Fermi equation [170].

2.1.1 Scattering theory

For the derivation of the afore-mentioned effective low energy Hamiltonian, we first review some basic properties of scattering between two atoms in the same internal state without transitions to other states (elastic scattering) and in vacuum. Later, we will briefly comment on inelastic properties since they determine the rate of loss of atoms out of traps in experiments. We will generally favor physical intuition over mathematical rigor. The interatomic potential is taken to be arbitrary, but decaying faster than r^{-1}. The center-of-mass motion decouples and we are left to solve the relative problem, defined by the Hamiltonian

$$\hat{H} = \frac{\vec{p}^2}{2\mu} + V(\vec{r}) \ , \tag{2.2}$$

where $\mu = m/2$ is the relative mass and $\vec{p} = (\vec{p}_1 - \vec{p}_2)/2$ the relative momentum of the particles. If we can find the stationary states of this Hamiltonian, the time-evolution of an arbitrary initial state can be constructed in a straight-forward manner.We will refer to the solutions of Eq. (2.2) with positive energy as scattering states. Note that this equation looks like that of a single particle scattering from a fixed target, hence the theory we develop here is quite general. One important difference is that the particle and the target are distinguishable and therefore the wavefunction does not have to be symmetrized. We neglect this issue for now and take our two particles to be distinguishable as well, before including symmetrization effects later on. The (rearranged) time-independent Schrödinger equation in position space reads

$$[\Delta_r + k^2]\Psi_{\vec{k}}(\vec{r}) = U(\vec{r})\Psi_{\vec{k}}(\vec{r}) \ , \tag{2.3}$$

where we defined $E = \frac{\hbar^2 k^2}{2\mu}$, $V(\vec{r}) = \frac{\hbar^2}{2\mu}U(\vec{r})$ and Δ_r is the Laplacian of the relative coordinate. This differential equation can be solved by finding the homogeneous solution of the differential operator $\Delta_r + k^2$ and one particular solution to the full problem. The latter can be constructed for arbitrary potentials by the method of Green's functions, which is defined by

$$[\Delta_r + k^2]G(\vec{r}) = \delta(\vec{r}). \tag{2.4}$$

This particular Green's function is well known (see e.g. App. A3 of Ref. [171])[2]

$$G(\vec{r}) = -\frac{1}{4\pi}\frac{\mathrm{e}^{ikr}}{r} \tag{2.5}$$

and so the full solution of Eq. (2.3) reads[3]

$$\Psi_{\vec{k}}(\vec{r}) = \mathrm{e}^{i\vec{k}\cdot\vec{r}} - \frac{1}{4\pi}\int \mathrm{d}^3r' \frac{\mathrm{e}^{ik|\vec{r}-\vec{r'}|}}{|\vec{r}-\vec{r'}|} U(\vec{r'})\Psi_{\vec{k}}(\vec{r'}) \ . \tag{2.6}$$

Here, the integration is over the influence-region $\vec{r'}$ of the potential.[4] This type of equation is known as a Lippmann-Schwinger equation. For our physical situation, we are interested in the *far-field solution*, i.e. far away from the scattering event, defined by $|\vec{r}| \gg |\vec{r'}|$. We can expand the difference $|\vec{r}-\vec{r'}|$ to first order, obtaining

$$G(\vec{r}-\vec{r'}) \simeq -\frac{1}{4\pi}\frac{\mathrm{e}^{ikr}}{r}\mathrm{e}^{-ik\vec{e}_r\cdot\vec{r'}} \ , \tag{2.7}$$

where $\vec{e}_r$ is the unit vector in the scattering direction $\vec{r}$. In the following, we will denote far-field results with the symbol $\simeq$. With this, Eq. (2.6) becomes

$$\Psi_{\vec{k}}(\vec{r}) \simeq \mathrm{e}^{i\vec{k}\cdot\vec{x}} - \frac{1}{4\pi}\frac{\mathrm{e}^{ikr}}{r} f_{\vec{k}}(\vec{r'}) \ , \tag{2.8}$$

where we defined the scattering amplitudes

$$f_{\vec{k}}(\vec{r'}) \simeq \frac{1}{4\pi}\int \mathrm{d}^3r' \mathrm{e}^{-ik\vec{e}_r\cdot\vec{r'}} U(\vec{r'})\Psi_{\vec{k}}(\vec{r'}) \ . \tag{2.9}$$

One could try and solve Eq. (2.9) iteratively in $\Psi_{\vec{k}}(\vec{r'})$, starting with the incoming wave, which leads to the well known Born series. However, this series doesn't always converge, and we take a different (common) approach here. Based on the spherical symmetry of

[2] The plus-sign in the exponent is chosen to represent an outgoing scattered wave, i.e. we choose the retarded Green's function of the operator in order to satisfy the Sommerfeld radiation condition.

[3] We specify the homogeneous solution by a plane wave, but do not take normalization into account. One could take into account a finite momentum spread of an initial wavepacket, which would lead to normalizable (and non-stationary) solutions, see e.g. Ref. [171].

[4] This implies that the influence region of the potential is restricted, and so the far-field solution discussed in the following exists. This is evidently the case for finite-ranged potentials, but can be extended to potentials $\propto r^{-(1+\epsilon)}$, i.e. faster decaying than the Coulomb potential.

the interaction potential, we can look for simultaneous eigenfunctions of the Hamiltonian [Eq. (2.2)] and the angular momentum operators $\hat{L}^2$ and $\hat{L}_z$. This is the so-called method of *partial waves*. The solution of the time-independent Schrödinger equation in spherical coordinates (r, θ, ϕ) with a spherically symmetric potential can generally be written as

$$\Psi_{k,l,m}(\vec{r}) = R_{k,l}(r) Y_l^m(\theta, \phi) = \frac{u_{k,l}(r)}{r} Y_l^m(\theta, \phi) \ , \tag{2.10}$$

where $Y_l^m(\theta, \phi)$ are the spherical harmonics and the radial wavefunction $R_{k,l}(r)$ depends on the specific potential (which we do not specify as yet). In the last equality we defined $u_{k,l}(r)$ such that the resulting radial part of the Schrödinger equation looks like a one-dimensional Schrödinger equation with an effective potential containing a centrifugal term

$$\Big[-\frac{\mathrm{d}^2}{\mathrm{d}r^2} + \frac{l(l+1)}{r^2} + U(r) \Big] u_{k,l}(r) = k^2 u_{k,l}(r) \tag{2.11}$$

and we require $u_{k,l}(r = 0) = 0$ as a boundary condition ($R_{k,l}(r)$ should be regular at $r = 0$). This already hints at a result we shall derive more rigorously in the following: For low relative momenta between the two particles, which is the case in ultracold gases, only the $l = 0$ partial wave will contribute, because the centrifugal barrier cannot be overcome (provided that we do not have a large attractive r^{-2} interaction potential) and so the particles do not experience the full interaction potential. For spherically symmetric problems, we can choose the homogenous solution of Eq. (2.3) without restriction to be propagating along the z-axis, $\vec{k} \cdot \vec{r} = kr \cos\theta \equiv kz$. This allows us to write

$$\mathrm{e}^{ikz} = \sum_{l=0}^{\infty} \sum_{m=-l}^{l} i^l \sqrt{4\pi(2l+1)} j_l(kr) Y_l^m(\theta) \equiv \sum_{l=0}^{\infty} i^l (2l+1) j_l(kr) P_l(\cos\theta) \ , \tag{2.12}$$

where the ϕ-dependence drops out and therefore only the $m = 0$ term of the spherical harmonics contributes. Here, $j_l(kr)$ are the spherical Bessel functions and $P_l(\cos\theta)$ the Legendre polynomials. Let us also formally expand the scattering amplitudes and the stationary scattering states and make use of ϕ-independence,

$$f_{\vec{k}}(\theta) = \sum_{l=0}^{\infty} (2l+1) f_l P_l(\cos\theta) \ , \tag{2.13}$$

$$\Psi_{\vec{k}}(r,\theta) = \sum_{l=0}^{\infty} i^l (2l+1) R_l(r) P_l(\cos\theta) \ , \tag{2.14}$$

where we included factors of $(2l+1)$ for later convenience and f_l are the so-called partial wave scattering amplitudes (which are unknown expansion coefficients at this point). To be able to relate Eqs. (2.14) and (2.8), we first inspect the far-field solution of Eq. (2.14) for each partial wave l, i.e. we require r large enough to be outside the influence of the potential. If we additionally take r to be large,[5] then Eq. (2.11) simplifies to

$$\Big[-\frac{\mathrm{d}^2}{\mathrm{d}r^2} + k^2 \Big] u_{k,l}(r) \simeq 0 \ , \tag{2.15}$$

whose general solution is

$$u_k(r) \simeq A\mathrm{e}^{ikr} + B\mathrm{e}^{-ikr} \ . \tag{2.16}$$

A and B can't be independent due to the $r = 0$ boundary condition. Importantly, the scattering we consider here is elastic, so $|A| = |B|$ due to probability current conservation, which leads to

$$u_k(r) \simeq |A| \Big(\mathrm{e}^{ikr}\mathrm{e}^{i\phi_1} + \mathrm{e}^{-ikr}\mathrm{e}^{i\phi_2} \Big) \tag{2.17}$$

with relative phases $\phi_{1,2}$. Put differently

$$u_{k,l}(r) \simeq C \sin(kr - l\pi/2 + \delta_l) \ , \tag{2.18}$$

where we introduced the phase-shift δ_l and an arbitrary shift $l\pi/2$.[6] The reason for the latter becomes apparent when comparing this expression with the far-field solution of the un-scattered wave,[7] Eq. (2.12)

$$j_l(kr) \simeq \frac{1}{r} \sin(kr - l\pi/2) \ . \tag{2.19}$$

Thus, δ_l describes the phase shift of each partial wave l due to the influence of the potential compared to the non-scattered solution. The phase-shifts are completely determined by

[5] This condition simplifies the following discussion. We could have kept the centrifugal term in Eq. (2.15) and used the general solution in terms of spherical Bessel and Neumann functions, but it is not necessary at this point.

[6] Which would have arisen naturally for the general solution mentioned in the previous footnote.

[7] Recall that we defined the full radial solution $R_{k,l}(r) = u_{k,l}(r)/r$

matching the far-field solution to the full solution of the radial equation (2.11), i.e. by continuity of the solution inside and outside of the potential region. However, the latter depends on the specific form of the involved potential which we still haven't specified. Rewriting Eq. (2.18) by introducing a global phase and fixing the normalization constant[8] leads to

$$u_{k,l}(r) \simeq \frac{\mathrm{e}^{i\delta_l}}{2ik}\Big(\mathrm{e}^{i(kr-l\pi/2+\delta_l)} - \mathrm{e}^{-i(kr-l\pi/2+\delta_l)}\Big). \tag{2.20}$$

Combining this with Eqs. (2.13), (2.14) we can write the scattering states in the far-field region

$$\Psi_{\vec{k}}(\vec{r}) \simeq \sum_{l=0}^{\infty} \frac{2l+1}{kr} P_l(\cos\theta)\Big[\frac{i^l}{2i}\Big(\mathrm{e}^{i(kr-l\pi/2)} - \mathrm{e}^{-i(kr-l\pi/2)}\Big) + k f_l \mathrm{e}^{ikr}\Big]\,. \tag{2.21}$$

Comparing this to Eq. (2.8) and using the far-field expansion of Eq. (2.12), we finally obtain

$$f_l = \frac{\mathrm{e}^{i\delta_l}\sin\delta_l}{k} \equiv \frac{\mathrm{e}^{2i\delta_l}-1}{2ik} \tag{2.22}$$

for the partial scattering amplitudes, which leads to

$$f_k(\theta) = \frac{1}{k}\sum_{l=0}^{\infty}(2l+1)\mathrm{e}^{i\delta_l}\sin\delta_l P_l(\cos\theta) \tag{2.23}$$

for the scattering amplitudes.

So far, we haven't really simplified the original problem. In order to obtain the phase shifts δ_l, we have to solve the radial equation (2.11) for each l for a specified potential. But let's have a look at a general finite range potential, i.e. $V(r) = 0$ for $r > a$. For these, only partial waves with $l \lesssim ka$ contribute, where k is the momentum of the relative motion of the two particles. This is due to the fact that for $r > a$, only the centrifugal term of the potential in Eq. (2.11) contributes. For a particle with kinetic energy $\propto k^2$, the (classical) turning radius r_t is determined by equating the centrifugal barrier with this kinetic energy, leading to $r_t = \frac{\sqrt{l(l+1)}}{k}$. This means there can only be scattering for $r_t \leq a \iff \sqrt{l(l+1)} \approx l \leq ka$, otherwise the centrifugal barrier is too high. For ultracold bosonic gases, this leads to scattering with only the $l = 0$ partial wave contributing as we will see in the next section.

[8] For a discussion of different normalization conventions, see e.g. Ref. [172].

It can be shown that the contributions of the partial waves to the total cross section are additive

$$\sigma = \sum_{l=0}^{\infty} \sigma_l = \sum_{l=0}^{\infty} \frac{4\pi}{k^2}(2l+1)\sin^2\delta_l \ . \tag{2.24}$$

2.1.2 Low-energy scattering

For $k \to 0$, i.e. vanishingly small kinetic energy, the far-field solution $u(r)$ of the radial equation (2.11) reduces to

$$u(r) \propto r - a \tag{2.25}$$

where a is an integration constant. It can be shown that $\delta_l \propto k^{2l+1}$ for low k and sufficiently short-ranged potentials, see e.g. p.338 in Ref. [171], and therefore $\delta_0 \propto k$ (modulo π). Therefore, Eq. (2.20) becomes

$$u(r) \simeq \frac{\mathrm{e}^{i\delta_0}}{k}\sin(kr+\delta_0) \overset{k\to 0}{=} r + \frac{\delta_0}{k} \ . \tag{2.26}$$

Comparing to Eq. (2.25) leads us to introduce the *s-wave scattering length*

$$a = -\lim_{k\to 0}\frac{\delta_0}{k} \ . \tag{2.27}$$

With this, the partial wave scattering amplitude [Eq. (2.23)] becomes

$$f_0(k) = \frac{\mathrm{e}^{i\delta_0}}{k}\sin\delta_0 \overset{k\to 0}{=} \frac{\delta_0}{k} = -a \tag{2.28}$$

and the total cross section [Eq. (2.24)] looks like[9]

$$\sigma \overset{k\to 0}{=} 4\pi a^2 \ . \tag{2.29}$$

This means the scattering length determines the effective size of the scatterer[10] and that the scattering at low energies is spatially isotropic.

So far, we only made assumptions about the long-range decay of the interaction potential

[9] Keeping the next order term in the expansion in Eq. (2.28) would lead to the optical theorem being fulfilled.

[10] This result is four times the size of a classical scatterer with diameter a and would increase by another factor of two if one were to take indistinguishability of particles into account [170].

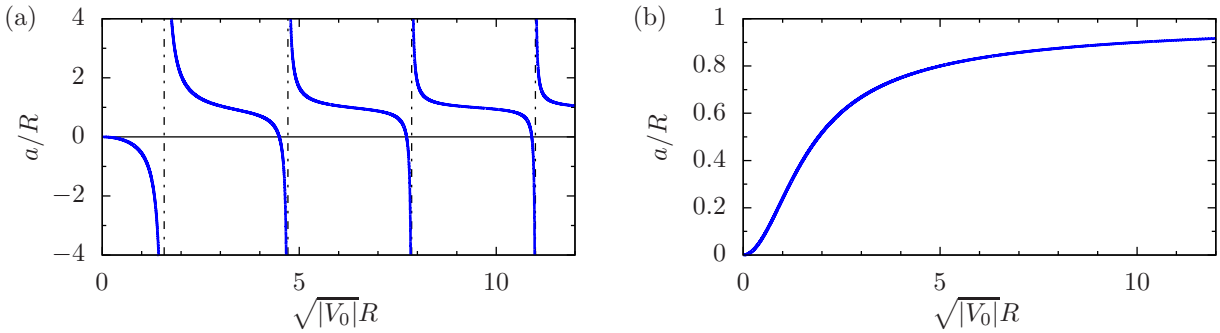

FIGURE 2.1: Scattering length a for square well potential $V(r) = V_0\,\Theta(R-r)$ in the zero-energy limit. (a) $V_0 < 0$: Attractive interactions lead to a scattering length that sensitively depends on the value of $\sqrt{V_0}R$. Vertical dashed lines mark the appearance of bound states in $V(r)$, which happen at $\sqrt{|V_0|}R = \frac{2n+1}{2}\pi$, where n is an integer. (b) $V_0 > 0$: Repulsive interactions lead to a positive scattering length a. In the limit of hard-sphere scattering, $\sqrt{V_0}R$ large, $a/R \to 1$.

and consequently our discussion was quite general. This also implies that the wavefunction in the far-field (or in the asymptotic region for two scattering particles) of different potentials can be identical for low-energy scattering. This motivates the introduction of a pseudo-potential, which replaces the true interatomic potential and simplifies calculations enormously while still producing exactly the same effective low-energy physics. Measurement of one single parameter, the s-wave scattering length, then allows one to describe the interactions with a simple microscopic (effective low-energy) Hamiltonian. We will come back to this point after discussing a specific potential, which will illustrate the general behavior of the s-wave scattering length and importantly, how the details of the true interatomic potential can lead to variations of the scattering length (which is directly related to the effective interaction strength of the pseudo-potential) over orders of magnitude, ranging from large negative to large positive values. For this, we investigate the s-wave scattering of a particle from a *spherically symmetric square well*, i.e. the potential reads $V(r) = V_0\,\Theta(R-r)$, with R the extent of the well and V_0 its strength. The radial s-wave Schrödinger equation [Eq. (2.11)] now reads

$$\left[\frac{\mathrm{d}^2}{\mathrm{d}r^2} + |V_0|\,\Theta(R-r)\right]u(r) = 0\,. \tag{2.30}$$

For the attractive square well, $V_0 < 0$, the solutions to Eq. (2.30) can be written as

$$u(r) \propto \begin{cases} \sin(kr), & r \leq R \\ (r-a), & r > R\,. \end{cases} \tag{2.31}$$

Continuity at the boundary leads to to

$$a = R - \frac{\tan(\sqrt{|V_0|}R)}{\sqrt{|V_0|}}\,, \tag{2.32}$$

which we plot in Fig. 2.1(a). The scattering length diverges at $\sqrt{|V_0|}R = \frac{2n+1}{2}\pi$, where n is an integer. At each of these values, an additional bound state appears for the deeper and deeper square well potential. In between, the scattering length vanishes.[11] In Fig. 2.1(b) we plot the s-wave scattering length for $V_0 > 0$. The scattering length is always positive, $a = R - \frac{\tanh(\sqrt{|V_0|}R)}{\sqrt{|V_0|}}$, and for large V_0 the scattering length goes to R (the cross-section looks like four times the classical hard-sphere radius).

The simple previous example showed that the scattering length sensitively depends on the exact combination of parameters of the interaction potential. Whenever a bound state was close to the continuum threshold, the scattering length diverged — a so-called shape resonance. The relation between a bound state with energy just below the scattering continuum and a large (positive) scattering length turns out to be general. But in experiments with ultracold gases it is very difficult to manipulate the true interatomic potential. Instead, the scattering length is tuned via *Feshbach resonances*, see e.g. Refs. [4, 170, 172, 174] and references therein, where the bound state is provided by different atomic configurations of the two particles. In experiments the atoms are confined by magneto-optical traps and usually in definite hyperfine levels. Consider an alkali atom: All electrons except one are in closed shells, so the relevant spin is that of the valence electron. In its ground state, the angular momentum of the electron is zero, and so the relevant quantum numbers for the hyperfine levels are the nuclear spin (and its projection) and the electron spin. Applying an external magnetic field leads to a Zeemann shift of hyperfine levels, and the latter depends on the total magnetic moment. This means that an external field can shift the energy levels

[11] For a figure of the radial wavefunction see Fig. 2, p.99 of Ref. [173].

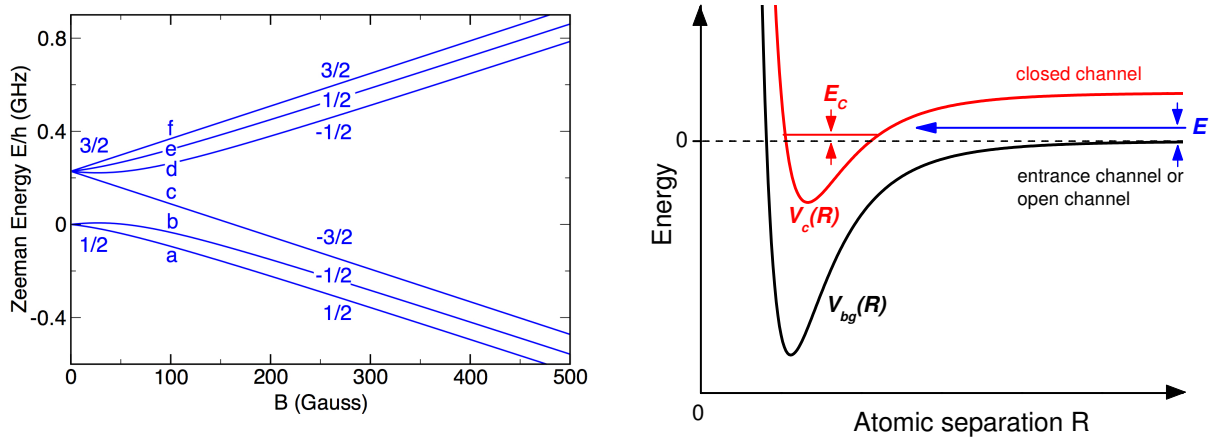

(a) (b)

FIGURE 2.2: (a) Zeeman splitting of hyperfine energy levels of lithium 6 in an external magnetic field B. The alkali atom is in its electronic ground state, and the hyperfine levels $f = 1/2$ and $f = 3/2$, where f is the total angular momentum quantum number. For non-zero external field, the two levels split up and the projection m of the total angular momentum along the field is a good quantum number (labelled by fractions on the right), in contrast to f, which is a good quantum number for zero field only. (b) Two-channel model of a Feshbach resonance. The atoms collide with energy E, which is close to zero for collisions in the ultracold regime. The closed channel (solid red line) corresponds to a different atomic configuration than the open channel (solid black line), and supports a bound state at energy E_C. If the bound-state energy is close to zero, a resonance occurs.

relative to each other. In Fig. 2.2(a), the dependence of the energy levels with external magnetic field is shown for lithium 6, a common choice of species for ultracold atom experiments.[12] For two well-separated atoms, i.e. in the asymptotic region, the total angular momentum is a good quantum number and different hyperfine levels do not mix. But inside the interaction region, i.e. when the two atoms are close to each other and thus are not well-described in terms of single entities, the total angular momentum is not conserved and the interatomic potential can lead to transitions during scattering events. If a certain atomic configuration supports a bound state, the energy of which is on resonance with the collision energy of the two atoms, the scattering length diverges, just as in the simple square-well scenario discussed earlier. This is shown in Fig. 2.2(b) for two channels.[13] The relation

[12] Note that this is a fermionic atom, but the energy level shifts in Fig. 2.2(a) are similar for other alkali atoms.

[13] We refer to a channel as an atomic configuration of the two atoms in the asymptotic region.

between the background scattering length a_{bg} (i.e. without coupling to a bound state) and the effective scattering length can be derived from a two-channel model[14] (or determined phenomenologically experimentally), which yields

$$a = a_{\mathrm{bg}}\Big(\frac{\Delta B}{B - B_0}\Big) \,, \tag{2.33}$$

where ΔB is the width and B_0 is the position of the resonance. This means that the effective interaction strength in ultracold atomic gases can be readily tuned over wide ranges. For diverging scattering lengths, the system doesn't have a typical length scale for interactions anymore and the physics becomes universal in this sense, see e.g. Ref. [175] (which also treats Efimov physics, i.e. three-body universality).

Inelastic processes

We here shortly comment on three-body recombination processes, since they play a prominent role in ultracold gases.[15] For potentials with bound states, molecule formation is possible and requires a third atom to be involved to carry away the binding energy of the pair. This usually leads to high kinetic energies and the molecule and the particle can escape the trap. For contact interactions this process is proportional to the probability to find three atoms at the same place in space. To avoid this undesirable reaction in general potentials, we need the density of the gas to be much smaller than the characteristic length scale of the interactions, the so-called diluteness condition $|a|n^{1/3} \ll 1$, where the scattering length a characterizes collisions at ultracold temperatures as we saw before.

2.1.3 From three spatial dimensions to one

The simplest model interaction potential, referred to as contact potential, reads

$$U(r) = g\delta(\vec{r}) \,, \tag{2.34}$$

[14] For more particles it is important that the three-body recombination rate is low, so there is no relaxation into deep bound states, which would lead to fast atom loss in the usual experimental set-ups. This is not the case for three-dimensional Bose Einstein condensates in general, opposed to fermionic systems (see e.g. [99]). However, the interactions are often small in typical Bose Einstein condensates.

[15] As we mentioned earlier, the atoms are usually trapped in a definite hyperfine state, so spin relaxation processes are possible. Collisions with the background gas of the (imperfect) vacuum lead to losses as well. For a general discussion of several inelastic processes, see Ref. [170].

where g is the interaction strength or coupling constant. In one spatial dimension, one can straight-forwardly substitute this potential into the Lippmann-Schwinger equation and define a one dimensional scattering length in analogy with the three dimensional case. This leads to $a_{1\mathrm{D}} = \frac{2\hbar^2}{\mu g}$. But the connection to the three dimensional scattering length is not clear from this and the important link with experimentally accessible quantities has been lost. To obtain this connection, it is necessary to perform scattering calculations in highly restricted geometries, such that the dynamics effectively takes place in one dimension. This was described in Ref. [176] and we shall outline the derivation here. For this purpose, it is necessary to regularize the pseudopotential [Eq. (2.34)] because its action on certain wavefunctions does not lead to physical scattering properties when $r \to 0$ in three spatial dimensions. The regularized potential reads

$$V(r) = g\delta(\vec{r})\frac{\partial}{\partial r}(r\cdot) \ , \tag{2.35}$$

where $(r\cdot)$ means that the wavefunction has to be multiplied by r before taking the derivative. This potential can be used in the reduced Schrödinger equation, meaning it reproduces the exact values for the energy, see e.g. Refs. [12, 177], provided that

$$g = \frac{2\pi\hbar^2}{\mu}a \ . \tag{2.36}$$

The need for this regularization operator arises from the fact the the radial part of the scattered wave behaves like $\frac{u(r)}{r}$ as we saw earlier. In combination with the δ-function, the regularization operator simply removes the short distance divergence of the scattered wave.[16] The discussion so far has been for two particles in vacuum, but it can be shown that the pseudo-potential method can be extended to many-body systems [12].

To get into the one-dimensional regime, consider the following situation [176]: Two atoms interact via the regularized pseudopotential (2.35) and are additionally confined in the x and y direction by a harmonic potential with trapping frequencies $\omega_\perp$. The center-of-mass

[16] See also discussion in footnote on p.125 of Ref. [170].

motion then decouples, and the z motion is free. The relative Hamiltonian then reads

$$\frac{\hat{p}_z^2}{2\mu} + g\delta(\vec{r})\frac{\partial}{\partial r}(r\cdot) + \hat{H}_\perp(\hat{p}_x, \hat{p}_y, x, y) \ , \tag{2.37}$$

where $\vec{r} = \vec{r}_2 - \vec{r}_1$ is the relative coordinate between the two atoms and the transverse Hamiltonian

$$\hat{H}_\perp(\hat{p}_x, \hat{p}_y, x, y) = \frac{\hat{p}_x^2 + \hat{p}_y^2}{2\mu} + \frac{\mu\omega_\perp^2(x^2+y^2)}{2} \ . \tag{2.38}$$

We assume the energy of the collision (i.e. the relative kinetic energy) is less than $\hbar\omega_\perp$ and the incident wave is in the ground state of the transverse Hamiltonian $\hat{H}_\perp$. Following the same procedure as in Sec. 2.1.1, we compare the asymptotic wavefunction with the wavefunction at short distances. Here, however, the short-distance form of the wavefunction has to be derived with care. Expanding the wavefunction onto the eigenstates of $\hat{H}_\perp$ with zero angular momentum, and then using the boundary condition of the pseudopotential (i.e. regular wavefunction for $r \to 0$), a closed analytic expression for the wavefunction can be derived [176]. Comparing this to the asymptotic wavefunction then gives the scattering phase shifts. In the low-energy limit, the scattering can be described by a *one dimensional δ–function potential* $V(r) = g_{1\mathrm{D}}\delta(r)$, where

$$g_{1\mathrm{D}} = -\frac{\hbar^2}{\mu a_{1\mathrm{D}}} = \frac{2\hbar^2 a}{\mu a_\perp^2}\Big(1 - C\frac{a}{a_\perp}\Big)^{-1} \ . \tag{2.39}$$

Here we introduced the one-dimensional scattering length $a_{1\mathrm{D}}$, $C = 1.46\ldots$ is a numerical constant, a is the three-dimensional scattering length, and $a_\perp = (\frac{\hbar}{\mu\omega_\perp})^{1/2}$ is related to the transverse confinement. The quantities in this expression are now experimentally accessible, allowing for a parameter free comparison of theoretical calculations with experimental results. Since $a_\perp$ enters the expression for $a_{1\mathrm{D}}$, the scattering length can be tuned by changing the trapping frequency of the transverse confinement, a so-called confinement induced resonance. The experimental realization of this has been reported in Ref. [178] and was utilized in Ref. [179] to abruptly change the effective interactions in a one-dimensional system of bosons from strongly repulsive to strongly attractive.

2.2 Theoretical tools for the one-dimensional Bose gas out of equilibrium

There are many different theoretical approaches to calculating properties of the one dimensional Bose gas, each with its advantages and drawbacks. Since we are interested in the far from equilibrium dynamics of strongly correlated one-dimensional bosonic systems with short-range interactions, we here shortly summarize some of them without claiming to be exhaustive and comment on their utilities and limitations.[17] For a thorough introduction and overview of non-equilibrium techniques in the context of quantum gases, we refer the reader to Ref. [180].

The conceptually simplest numerical method is exact diagonalization of the Hamiltonian in a suitable basis. For finite sized lattice models, the basis of the Hilbert space is finite and by obtaining all eigenstates of the Hamiltonian, any quantity of interest can in principle be computed, see e.g. Refs. [1, 62, 181]. Since the Hilbert space grows exponentially with particle number, this method is well suited for small systems. For continuous models, the Hilbert space is infinite dimensional, and a suitable truncation scheme for basis states has to be developed. For the Lieb–Liniger model with attractive interactions, this was done in Refs. [182–185] to access the low-energy properties of the system at relatively weak interactions around the quantum critical point.[18] For larger interaction strengths, on the other hand, this method quickly becomes prohibitive.

Another numerical method relying on the truncation of basis states is the multiconfigurational time-dependent Hartree method for bosons [180, 186], which uses an expansion of the wavefunction with time-dependent single-particle basis states and time-dependent coefficients, which themselves are variationally optimized. This method is well-suited to describe the dynamics of few-boson systems [187–189], but introduces an unphysical coupling of center-of-mass and relative motion that can lead to numerical problems for systems with attractive interactions [190], as well as a numerically prohibitive number of single particle

[17] Results for the ground state of the repulsively interacting Lieb–Liniger model are discussed in Sec. 3.4, while those for attractive interactions can be found in Sec. 5.4.

[18] In the mean-field limit, the one-dimensional Bose gas with attractive interactions exhibits a quantum phase transition from a uniform density state to a localized bright soliton at a critical interaction strength, cf. Ch. 5.

orbitals for strong interactions [188].

A powerful technique to simulate the dynamics of strongly correlated one-dimensional models are tensor network methods. For these, the Hilbert space is truncated to only contain the relevant sector in which the physics of interest happens. This is based on the fact that for gapped local Hamiltonians, the low-energy states obey an area-law for the entanglement entropy,[19] and these states only make up a very small fraction of the full Hilbert space, see e.g. Refs. [191–193]. Moreover, the time-evolution for these states is restricted to a relatively small part of the Hilbert space, making it possible to also implement non-equilibrium scenarios. However, since the entanglement entropy grows with time, more and more states have to be taken into account and the method eventually becomes inaccurate for a fixed truncation. For applications to dynamics in the Lieb–Liniger model, see e.g. Refs. [194, 195].

Phase-space methods map the density matrix to a quasi-probability distribution containing the full information of a system at hand. One can then map the time-evolution of a density matrix to the time evolution of a quasi-probability distribution [196, 197]. The advantage of this lies in the fact that generically, the time evolution of the phase space distribution, which is described by a generalized Fokker–Planck equation, can be mapped to stochastic differential equations. The latter can be solved with simple computational methods. The numerical problem thus shifts from the exponential size of the Hilbert space to sampling stochastic trajectories. Two common phase space formulations are the truncated Wigner approximation [180, 198] (and the related classical-field technique [180, 199]) and the positive P-representation [180, 197]. For general Hamiltonians involving interactions (i.e. Hamiltonians beyond quadratic), the mapping of the generalized Fokker–Planck to stochastic differential equations in the truncated Wigner approximation involves neglecting certain terms in the former. In general this is valid for systems that have a high occupation compared to the number of modes. The truncation is controlled in the sense that the error in time can, in principle, be bounded [200]. In the positive P-representation, the mapping between the Fokker–Planck equation and the stochastic differential equations is exact, however the method is only stable for short times. In practice, phase-space methods are not suited to access late-time dynamics or small systems.

Very recently, there has been progress on results of observables in the thermodynamic

[19] For ungapped Hamiltonians, there can be corrections.

limit. The numerical linked cluster expansion [201] gives access to the infinite time limit of the density matrix in the energy eigenbasis of a system, as well as thermal density matrices, but does not allow for calculations of finite-time dynamics.

Ref. [202] conjectured that the dynamics and relaxed value of certain local observables following an interaction strength quench are captured by a representative eigenstate of the postquench Hamiltonian and excitations around it — the so-called quench action approach [203]. The method was introduced for integrable models with Bethe ansatz solution,[20] where the overlaps of the initial state with the eigenstates of the Hamiltonian governing the time evolution can be computed in certain situations. These overlaps are the main ingredient in the quench action method, and are hard to calculate in general. However, if known they can be used to find the afore-mentioned representative eigenstate by means of a generalized thermodynamic Bethe ansatz equation. The equilibrium values of certain operators are then given as expectation values in this state, while the time-evolution is governed by states in the vicinity of it. For an application of the method to the Lieb–Liniger model, see Refs. [9, 10, 204–206].

In general, integrability-based methods make use of the various existing Bethe ansatz approaches. This thesis is concerned with the Lieb–Liniger model and its solution via the coordinate Bethe ansatz and we therefore give a detailed exposition of the subject in the next section. However, there are more Bethe ansatz based techniques and we briefly mention a powerful one here, the algebraic Bethe ansatz [207]. It also goes by the name quantum inverse scattering method, due to the parallels to the classical inverse scattering method. It is based on an abstract construction of a so-called transfer matrix to generate all local conserved charges at once. The Yang–Baxter algebra of this transfer matrix is then utilized to generate the eigenfunctions by applying certain algebraically constructed operators to a pseudo-vaccum state. The inverse problem consists of finding expressions for physical observables in terms of these algebraically constructed operators. Its value for non-equilibrium dynamics comes from a numerically convenient determinant expression for so-called form-factors [208], which are matrix elements of physical operators. As for the quench action method, the representation of the initial state in the eigenstates of the Hamiltonian governing the time-evolution is needed and is only known for some specific

[20] Although it is in principle not restricted to those [203].

examples [209–211].[21]

2.3 The Lieb–Liniger model and its solution via Bethe ansatz

Theoretical interest in the one-dimensional Bose gas with binary δ-function interactions preceded the derivation of its connection to experimental quantities [Sec. 2.1.3] by 35 years. In 1963, in their seminal paper E. Lieb and W. Liniger constructed the solutions of the N-particle Hamiltonian

$$\hat{H}_{\mathrm{LL}} = -\sum_{i=1}^{N} \frac{\partial^2}{\partial x_j^2} + 2c \sum_{1\leq i<j\leq N} \delta(x_j - x_i) \tag{2.40}$$

with the help of the Bethe ansatz, named after H. Bethe who developed the method to solve the one-dimensional spin-1/2 Heisenberg model [212]. Hamiltonian (2.40) constitutes the famous Lieb–Liniger model. Here and in the following, we set $\hbar = 1$ and the particle mass $m = 1/2$ for convenience (for a discussion of units, see e.g. the end of Sec. 4.3.2). It is instructive to start with the two-body problem, since it illustrates many aspects of the many-particle problem.

2.3.1 The two-body problem

For *non-interacting* systems, the time-independent Schrödinger equation reads

$$\Big(-\frac{\partial}{\partial x_1} - \frac{\partial}{\partial x_2} \Big)\psi = E\psi, \tag{2.41}$$

for which the solutions are plane waves. Let us consider the wave function in the *fundamental spatial sector* $\mathcal{R} : x_1 \leq x_2$. The wave function for $x_2 > x_1$ is then determined by Bose symmetry, $\psi(x_1, x_2) \equiv \psi(x_2, x_1)$. Then,

$$\psi = \mathcal{N} \mathrm{e}^{i(k_1 x_1 + k_2 x_2)}, \; E = k_1^2 + k_2^2, \tag{2.42}$$

[21] The Slavnov formula for overlaps of Bethe states doesn't work for states with non-equal interaction strength.

where $\mathcal{N}$ is a normalization constant to be determined once boundary conditions are introduced. The advantage of restricting the wave function to $\mathcal{R}$ lies in the fact that we did not explicitly have to symmetrize ψ. $k_{1,2}$ are the single particle momenta.
Introducing *interactions*, the time-independent Schrödinger equation reads

$$\Big(-\frac{\partial^2}{\partial x_1^2} - \frac{\partial^2}{\partial x_2^2} + 2c\delta(x_2 - x_1)\Big)\psi = E\psi, \tag{2.43}$$

where the interactions are repulsive for $c > 0$, and attractive for $c < 0$. If $x_1 \neq x_2$, then $\delta(x_2 - x_1) = 0$ and the particles do not interact. If $x_1 = x_2$, the following boundary condition on $\mathcal{R}$ should be fulfilled:

$$\Big(\frac{\partial}{\partial x_2} - \frac{\partial}{\partial x_1} - c\Big)\psi|_{x_2 = x_1 + 0} = 0. \tag{2.44}$$

This can be seen by transforming to relative coordinates[22]

$$r = \frac{x_2 - x_1}{2},\ R = \frac{x_1 + x_2}{2}. \tag{2.45}$$

The Hamiltonian is then

$$-\frac{1}{2}\frac{\partial^2}{\partial R^2} - \frac{1}{2}\frac{\partial^2}{\partial r^2} + c\delta(r) \tag{2.46}$$

and integrating the Schrödinger equation (2.43) around $r = 0$ leads to the following equation

$$\int_{-\epsilon}^{\epsilon} dr\Big[-\frac{1}{2}\frac{\partial^2}{\partial r^2}\psi(r, R) + c\delta(r)\psi(r, R)\Big] = \int_{-\epsilon}^{\epsilon} dr E\psi(r, R). \tag{2.47}$$

The center-of-mass motion is separable for translationally invariant problems, so the wavefunction is a product of two independent functions $\psi(r, R) = \psi(r)\chi(R)$. Taking the limit $\epsilon \to 0$, and utilizing Bose symmetry ($\psi(r) \equiv \psi(-r)$) we arrive at

$$-\frac{1}{2}\frac{\partial}{\partial r}\psi(r)\Big|_{r=0^-}^{r=0^+} + c\Psi(0) = 0, \tag{2.48}$$

[22] The reader might wonder about the slightly different choice of relative separation r here as opposed to the common $r' = x_2 - x_1$. Our choice ensures a symmetric factor in the kinetic part of the Hamiltonian, see Eq. (2.46) and makes it possible to factor out the total center-of-mass momentum for any number of particles with potentially different masses, see discussion in Appendix of Ref. [213].

which, upon resubstituting the original coordinates and utilizing Bose symmetry results in Eq. (2.44). Let us make the following ansatz for the wave function

$$\psi = a_1 \mathrm{e}^{i(\lambda_1 x_1 + \lambda_2 x_2)} + a_2 \mathrm{e}^{i(\lambda_2 x_1 + \lambda_1 x_2)}, \tag{2.49}$$

which is motivated by the fact that the solution should be a superposition of plane waves for $x_2 \neq x_1$, where the system is non-interacting, and that scattering of two identical particles in one dimension is very restrictive: momentum and energy conservation dictate that the particles can either exchange momenta, or just pass through each other.[23] Plugging this into Eq. (2.44) we obtain

$$(i\lambda_2 - i\lambda_1 - c)a_1 + (i\lambda_1 - i\lambda_2 - c)a_2 = 0 \iff \frac{a_1}{a_2} = \frac{i(\lambda_2 - \lambda_1) + c}{i(\lambda_2 - \lambda_1) - c}. \tag{2.50}$$

The λ_j here are free parameters of our ansatz, and generally not the single-particle momenta as in the non-interacting case. Writing Eq. (2.50) as

$$\frac{a_1}{a_2} = \mathrm{e}^{i\theta(\lambda_1 - \lambda_2)}, \ \theta(\lambda_1 - \lambda_2) = 2 \arctan \frac{\lambda_1 - \lambda_2}{c} \tag{2.51}$$

reveals that the relation between a_1 and a_2 is a pure phase factor, with θ the phase shift due to the scattering. Even though the λ are quasi-momenta, they determine the total momentum and energy of the system

$$\hat{P}\psi = \Big(-i\frac{\partial}{\partial x_1} - i\frac{\partial}{\partial x_2}\Big)\psi = (\lambda_1 + \lambda_2)\psi, \quad \hat{H}\psi = (\lambda_1^2 + \lambda_2^2)\psi. \tag{2.52}$$

Introducing *periodic boundary conditions* and keeping in mind that our wavefunction is defined on $\mathcal{R}$, i.e. $0 \leq x_1 \leq x_2 \leq L$, continuity requires

$$\begin{aligned} \psi(0, x_2) &= \psi(x_2, L) \\ \frac{\partial}{\partial x_1}\psi(x_1, x_2)\Big|_{x_1=0} &= \frac{\partial}{\partial x_1}\psi(x_2, x_1)\Big|_{x_1=L}, \end{aligned} \tag{2.53}$$

[23] We assume that momentum and energy conservation give two functionally independent conditions, so our ansatz has two parameters, λ_1 and λ_2.

and the same for x_2. Using our ansatz for the the wave function, Eq. (2.49), and the scattering factors obtained from the δ–function boundary condition, Eq. (2.50), we obtain

$$\mathrm{e}^{i\lambda_1 L} = \frac{\lambda_1 - \lambda_2 + ic}{\lambda_1 - \lambda_2 - ic}\,, \qquad \mathrm{e}^{i\lambda_2 L} = \frac{\lambda_2 - \lambda_1 + ic}{\lambda_2 - \lambda_1 - ic}\,. \tag{2.54}$$

Once these two simultaneous equations have been solved, we can plug the values of the rapidities into the equation for the wave function and the problem is (at least in principle) solved. The solutions to the so-called Bethe equations (2.54) depend on the sign of the interaction parameter c, and since the physical situation is very different for the attractive and repulsive case, we will discuss these two regimes separately.

Repulsive interactions ($c > 0$)

For repulsive interactions, the solutions of Eq. (2.54) are real numbers. To show this, assume the rapidities have an imaginary part, and assume $\Im(\lambda_1) > \Im(\lambda_2)$. Taking the absolute value of Eq. (2.54) leads to

$$\begin{aligned} |\mathrm{e}^{i\lambda_1 L}| &= \left|\frac{\lambda_1 - \lambda_2 + ic}{\lambda_1 - \lambda_2 - ic}\right| \geq 1 \;\Rightarrow\; \Im(\lambda_1) \leq 0\,, \\ |\mathrm{e}^{i\lambda_2 L}| &= \left|\frac{\lambda_2 - \lambda_1 + ic}{\lambda_2 - \lambda_1 - ic}\right| \leq 1 \;\Rightarrow\; \Im(\lambda_2) \geq 0\,. \end{aligned} \tag{2.55}$$

This contradicts our initial assumption and therefore the rapidities have to be real. Using the identities $\log(r\mathrm{e}^{i\theta}) = \log(r) + i\theta + 2\pi i n$, where n is an integer, and $\arctan z = \frac{1}{2}i[\log(1 - iz) - \log(1 + iz)]$, we can rewrite Eq. (2.54) as

$$\lambda_1 = \frac{2\pi}{L}m_1 - \frac{2}{L}\arctan\Big(\frac{\lambda_1 - \lambda_2}{c}\Big), \quad \lambda_2 = \frac{2\pi}{L}m_2 - \frac{2}{L}\arctan\Big(\frac{\lambda_2 - \lambda_1}{c}\Big), \tag{2.56}$$

where $m_j = n + \frac{N-1}{2}$. The m_j are in one-to-one correspondence with the rapidities λ_j [207].[24] The wavefunction is antisymmetric in the rapidities, which means that they cannot coincide, $\lambda_1 \neq \lambda_2$, and therefore the m_j are 'fermionic-like' quantum numbers. The ground state is therefore obtained by setting $m_j = \pm 1/2$. For infinitely strong interactions, $c \to \infty$, the arctan in Eq. (2.56) goes to zero and the rapidities are equal to the single-particle momenta

[24] This is handy for labeling states, because the rapidities λ_j are a function of c, whereas the m_j are fixed.

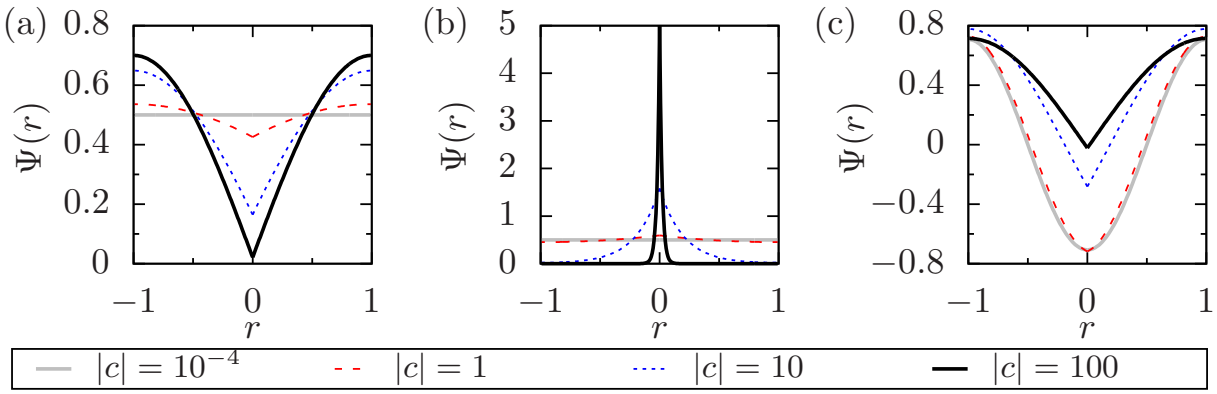

FIGURE 2.3: Relative wavefunction for $N = 2$ particles and system length $L = 2$ for several representative values of the interaction strength c. (a) Ground state wavefunction for repulsive interactions. (b) Ground state wavefunction for attractive interactions. (c) Wavefunction for the lowest scattering (super-Tonks) state for attractive interactions.

of free (spin-polarized) fermions. The wavefunction of the bosonic system in this so-called Tonks–Girardeau limit is identical to the absolute value of the fermionic system [214].[25] This implies that $\Psi(r = 0) = 0$, where r is the relative coordinate between the two particles. The behavior of the relative wavefunction at large but finite c is similar, see Fig. 2.3(a) ($c = 100$, solid black line). For lower values of the interaction strength, the cusp at $r = 0$ is less pronounced (recall Eq. (2.44): The derivative of $\Psi(r)$ at $r = 0$ has a jump equal to the value of $\Psi(0)$ times c), e.g. $c = 10$ (blue dotted line) and $c = 1$ (red dashed line). For very small values $c = 10^{-4}$ (horizontal grey line), the wave function approaches the constant line of the non-interacting case, $\Psi(c = 0, r) = L^{-N/2}$.

Attractive interactions ($c < 0$)

For attractive interactions, the solutions of the Bethe equations (2.54) allow for complex rapidities since for $c < 0$, Eqs. (2.55) have the inequalities reversed. We plot the relative wavefunction of the ground state in Fig. 2.3(b) for several representative interaction strengths c. For small values $c = -10^{-4}$ (horizontal grey line), the shape is similar to the afore-mentioned constant non-interacting case. For $c = -1$ (red dashed line), the wave function is slightly increased around the origin. For larger attractive values $c = -10$ (blue dotted line), the wavefunction becomes more sharply peaked around $r = 0$. This trend continues for even larger interaction strengths $c = -100$ (solid black line), signalling the

[25] As we will see in Sec. 3.4, this also applies to certain (but not all) correlation functions.

emergence of a tightly bound state. For strong attractive interactions,[26] the wavefunction can approximately be written

$$\Psi(r) \propto \mathrm{e}^{-|c|\,|r|/2}\,, \tag{2.57}$$

which is the exact ground state solution on the infinite line, $L \to \infty$ [213]. We will come back to the general structure of bound state solutions in the next section. For now, let us mention one particular excited state of the attractive Lieb–Liniger model, which for $|c|L \to \infty$ is the so-called super-Tonks state. This eigenstate has purely real rapidities and corresponds to a highly excited state. We plot the wavefunction for this state in Fig. 2.3(c). For strong attractive interactions $c = -100$ (black solid line), the wavefunction looks very much like that for the strongly repulsive case [solid black line in Fig. 2.3(a)]. This is no coincidence, as for $|c| \to \infty$, the energies and rapidities of the two states connect continuously [215–218] and this fact has been used to experimentally prepare the super-Tonks gas: Starting from strongly repulsive interaction strengths and instantly switching to attractive interactions utilizing a confinement induced resonance (cf. Sec. 2.1.3) this highly excited, metastable gas has been observed in Ref. [179]. For lower values of $c = -1$ (red dashed line) and $c = -10^{-4}$ (solid grey line), the wave function is very different from the repulsive case.

2.3.2 The coordinate Bethe ansatz for N particles and the Yang–Baxter equation

The previous discussion for two particles would have held for any short-ranged potential in the asymptotic region, as discussed in Sec. 2.1.1. Energy and momentum conservation give two independent conservation laws, and we have two rapidities for two particles. For three particles, scattering is more complicated and the general solution would contain a three-body scattering term, where only the total momentum and energy are fixed. For the special case of the Lieb–Liniger model, i.e. binary δ-potential interactions, it turns out that there are exactly N rapidities for N particles and the scattering of the system is non-diffractive [58]. Let us shortly outline this for the three-body case, before generalizing to N particles. Making the same ansatz as in Eq. (2.49), but with three rapidities and the

[26] Technically for large $|c|L$, but we keep the system length fixed to $L = 2$ for the two-particle case.

sum ranging over all 3! = 6 possible reorderings of the rapidities λ_j, the (unnormalized) wavefunction reads

$$\Psi_{N=3} = \sum_{\sigma} a(\sigma) \mathrm{e}^{i\sum_{j=1}^{N}\lambda_{\sigma(j)}x_j} \,, \tag{2.58}$$

where σ denotes a permutation of $\{1,2,3\}$. The cusp condition (2.44) now generalizes to six different cusp-conditions, three for $x_1 = x_2$ and three for $x_2 = x_3$ (recall that we are working in the fundamental spatial sector $x_1 \leq x_2 \leq x_3$), and we obtain six equations for the six $a(\sigma)$. They read

$$\begin{aligned}
&\frac{a(123)}{a(213)} = \mathrm{e}^{i\theta(\lambda_1-\lambda_2)} \,, \qquad \frac{a(123)}{a(132)} = \mathrm{e}^{i\theta(\lambda_2-\lambda_3)} \,, \qquad \frac{a(213)}{a(231)} = \mathrm{e}^{i\theta(\lambda_1-\lambda_3)} \,, \\
&\frac{a(132)}{a(312)} = \mathrm{e}^{i\theta(\lambda_1-\lambda_3)} \,, \qquad \frac{a(321)}{a(231)} = \mathrm{e}^{i\theta(\lambda_1-\lambda_2)} \,, \qquad \frac{a(321)}{a(312)} = \mathrm{e}^{i\theta(\lambda_2-\lambda_3)} \,,
\end{aligned} \tag{2.59}$$

where we used the definition of the scattering phase θ (2.51). Since every permutation can be decomposed into transpositions, there are two ways of connecting, for example, $a(123)$ and $a(321)$. The first one reads $(123) \to (213) \to (231) \to (321)$, while the second one reads $(123) \to (132) \to (312) \to (321)$. Importantly, Eqs. (2.59) lead to the same final scattering phase $\frac{a(123)}{a(321)} = \mathrm{e}^{i[\theta(32)+\theta(31)+\theta(21)]}$. This is the essence of the famous Yang–Baxter equation [58, 59]: The scattering of three particles can be decomposed into successive two-body events and the order of these does not matter. We depict this in Fig. 2.4 with the so-called star-triangle diagram: In Fig. 2.4(a), three particles, labelled with their corresponding Bethe rapidities λ_j scatter simultaneously.[27] In Fig. 2.4(b), the particle with rapidity λ_2 is slightly deplaced initially, leading to three consecutive two-body scattering events. The situation is the same in Fig. 2.4(c), with the scattering order interchanged. All three diagrams have the same amplitude in the asymptotic region.[28]

The results from the $N = 2$ and $N = 3$–particle cases extend to the N-particle sector. The general expression for the wavefunction on the fundamental spatial sector $\mathcal{R} : x_1 \leq x_2 \leq \cdots \leq x_N$ reads

$$\Psi(x_1,\ldots,x_N,\lambda_1,\ldots,\lambda_N) = \mathcal{N}\sum_{\sigma}(-1)^{[\sigma]}\prod_{1\leq k<j\leq N}[\lambda_{\sigma(j)}-\lambda_{\sigma(k)}-ic]\,\mathrm{e}^{i\sum_{j=1}^{N}\lambda_{\sigma(j)}x_j} \,, \tag{2.60}$$

[27] Take for example $x_1 < x_2 < x_3$ and $\lambda_1 > \lambda_2 > \lambda_3$ initially.

[28] The asymptotic region for a δ-function is everywhere but the origin. Let us remark that there are also long-range interacting models for which the Bethe ansatz is valid, see e.g. Ref. [55].

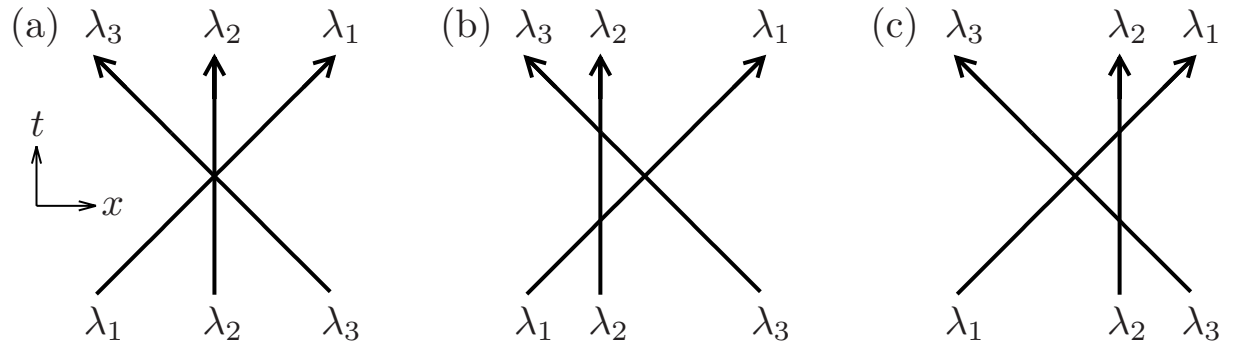

FIGURE 2.4: Space-time diagrams of possible scattering paths for $N = 3$ particles for taking $\lambda_1, \lambda_2, \lambda_3$ [denoted by (123)] into $\lambda_3, \lambda_2, \lambda_1$ [(321)]. (a) (123) $\to$ (321). (b) (123) $\to$ (213) $\to$ (231) $\to$ (321). (c) (123) $\to$ (132) $\to$ (312) $\to$ (321). These paths lead to the same scattering phase for the Lieb–Liniger model, i.e. they are equivalent, the essence of the Yang–Baxter relation.

where $\sum_\sigma$ extends over all $N!$ permutations of $\{1, 2, \ldots, N\}$, $\mathcal{N}$ is a normalization factor introduced below and $(-1)^{[\sigma]}$ is the sign of the permutation. Applying periodic boundary conditions leads to the Bethe equations, a set of N equations for N particles

$$\mathrm{e}^{\mathrm{i}L\lambda_j} = \prod_{l\neq j} \frac{(\lambda_j - \lambda_l) + \mathrm{i}c}{(\lambda_j - \lambda_l) - \mathrm{i}c} \,. \tag{2.61}$$

These equations are transcendental, so they have to be solved numerically in general. For repulsive interactions, it is convenient to write

$$\lambda_j = \frac{2\pi}{L} m_j - \frac{2}{L} \sum_{k=1}^{N} \arctan\left(\frac{\lambda_j - \lambda_k}{c}\right) \,, \tag{2.62}$$

where the m_j are in one-to-one correspondence with the rapidities λ_j [207]. The ground state is obtained by setting

$$m_j = j - \frac{N+1}{2}, \; j \in [1, 2, \ldots, N] \,. \tag{2.63}$$

All other combinations with *mutually distinct* m_j, where m_j are integers (half-integers) in the case of N odd (even), lead to allowed solutions of the Bethe equations [207, 219] and constitute excited states. We will come back to the excitation spectrum in the next section, when we consider the thermodynamic limit of the system. For finite systems, see e.g. Ref [220]. Importantly, the set of all corresponding eigenfunctions forms a complete

orthonormal basis for (the Bose-symmetric subspace of) the N-particle Hilbert space [219, 221]. The normalization constant reads [207]

$$\mathcal{N}_{\{\lambda_j\}} = \frac{\prod_{k>l}(\lambda_k - \lambda_l)}{\left\{N!\,\det\{M_{\{\lambda_j\}}\}\,\prod_{k>l}[(\lambda_k-\lambda_l)^2+c^2]\right\}^{1/2}}\,, \tag{2.64}$$

with $M_{\{\lambda_j\}}$ the $N\times N$ matrix with elements

$$\left[M_{\{\lambda_j\}}\right]_{kl} = \delta_{kl}\Big(L + \sum_{m=1}^{N}\frac{2c}{c^2+(\lambda_k-\lambda_m)^2}\Big) - \frac{2c}{c^2+(\lambda_k-\lambda_l)^2}. \tag{2.65}$$

In the eigenstate $|\{\lambda_j\}\rangle \equiv |\Psi(x_1,x_2,\ldots,x_N,\lambda_1,\lambda_2,\ldots,\lambda_N)\rangle$ the total energy and momentum are

$$E_{\{\lambda_j\}} = \sum_{j=1}^{N}\lambda_j^2, \qquad P_{\{\lambda_j\}} = \sum_{j=1}^{N}\lambda_j\,. \tag{2.66}$$

The parametrization (2.62) simplifies the discussion for the repulsive gas, but for the attractive gas it is more convenient to directly deal with Eq. (2.61). As we saw for the $N=2$ particle case, complex-valued rapidities are permitted solutions for attractive interactions and lead to bound states. For N particles, there are many of them and the general structure of the corresponding rapidities can be inferred from the following considerations. Following Ref. [222], let us consider the Bethe equation (2.61) for one complex rapidity $\lambda_\alpha \equiv \lambda + i\eta$ with λ,η real:

$$\mathrm{e}^{i\lambda L}\mathrm{e}^{-\eta L} = \prod_{\alpha\neq j}\frac{\lambda_\alpha-\lambda_j+ic}{\lambda_\alpha-\lambda_j-ic}. \tag{2.67}$$

For large L there are two possible scenarios depending on the sign of η:

$$\begin{aligned}\eta<0:&\quad \mathrm{e}^{-\eta L}\to\infty\\ \eta>0:&\quad \mathrm{e}^{-\eta L}\to 0.\end{aligned} \tag{2.68}$$

This means the right-hand side of Eq. (2.67) has to counter this exponentially large (small) term, and consequently there must be a second rapidity with $\lambda_\beta = \lambda - i\eta + ic + \mathcal{O}(\mathrm{e}^{-\eta L})$. This generalizes to more particles and the Bethe rapidities for attractive interactions organize themselves in strings with respect to the imaginary axis with deviations exponentially small

in system size. The ground state of the system has purely imaginary rapidities and is an N–particle bound state, and it is the only N–particle bound state of the system.[29] There are many possible ways to construct lower-order bound states, with unbound particles in a state having real rapidities. Each bound state in a given eigenstate (there can be many in one state) organizes in strings with respect to the imaginary part of the participating rapidities, all with exponentially small deviations in system size.

Neglecting string-deviations, the strings of various lengths behave like particles with total mass equal to the sum of the constituents, and one can deduce a reduced set of Bethe equations for the string centers and free particles in a state, the so-called Bethe-Takahashi equations [222, 223]. The completeness of the corresponding set of eigenfunctions is not proven and thus the procedure is referred to as the string-hypothesis.

The original finite-size Bethe solutions, however, are known to be complete for attractive interactions [224, 225]. For finite particle number N, the parameter characterizing the behavior of the system is cL, and thus for strong attractive interactions and finite L, the same conclusions of small deviations from the string solutions on the order $\mathrm{e}^{\mathrm{const.}\times cL}$ hold. As we will see in Chapter 5, this leads to complications in the numerical solution of the Bethe equations as well as the numerical calculation of correlation functions compared to the case of repulsive interactions. For small $|c|L$, the system shows significant deviations from the string solutions [226, 227].

2.3.3 The thermodynamic Bethe ansatz at zero temperature

The ground state energy of the Lieb–Liniger model with attractive interactions diverges in the usual thermodynamic limit $N, L \to \infty$, $n \equiv N/L$ fixed [213].[30] We shall therefore only consider the case of repulsive interactions, $c > 0$, where all the Bethe rapidities are purely

[29] With center-of-mass momentum zero. In our periodic geometry, adding $2\pi k/L$ (k an integer) to every rapidity in a given set corresponds to a center-of-mass shift which can be factored out in terms of a plane wave.

[30] The ground state energy $E_0 \propto N^3/L$, so one could think of taking the 'ultra-dilute' limit by keeping N^3/L constant, or by taking the limit $L \to \infty$ at finite N, which is non-trivial for attractive interactions [222, 228].

real.[31] Define a density of rapidities

$$\rho(\lambda) = \frac{1}{L(\lambda_{j+1} - \lambda_j)} \,, \tag{2.69}$$

where the difference of neighboring rapidities $(\lambda_{j+1} - \lambda_j)$ in the thermodynamic limit is of order L^{-1} [56] and therefore the rapidities become dense on the real axis. The finite-size Bethe equations (2.62) turn into an integral equation in the thermodynamic limit

$$\rho(\lambda) = \frac{1}{2\pi} + \frac{1}{2\pi} \int_{-k_F}^{k_F} \mathrm{d}\lambda' \rho(\lambda') \frac{2c}{c^2 + (\lambda - \lambda')^2} \,. \tag{2.70}$$

This is a linear Fredholm integral equation, and can be solved by numerical integration. Normalization requires

$$\int_{-k_F}^{k_F} \mathrm{d}\lambda' \rho(\lambda') = \frac{N}{L} \tag{2.71}$$

and for a given density determines the value of the Fermi momentum k_F, which is by definition the highest occupied rapidity in the ground state.[32]

Extending this formalism beyond the ground state to obtain the *excitation spectrum*, Lieb [231] introduced two sets of elementary excitations: Particle-like excitations (so-called Type I excitations), and hole-like (Type II) excitations. These excitations correspond to phonons (Type I) [231] and dark solitons (Type II) [211, 232–238]. The former is realized by adding a particle to the ground state of the Lieb–Liniger model, which has to be placed outside the Fermi zone, while the latter corresponds to taking away a particle inside the Fermi zone.[33] Adding a particle to the finite system will have an influence on all rapidities, since they are non-trivially coupled by the Bethe equations (2.62), underlining the concept of collective phenomena in one spatial dimension independent of the value of the interaction

[31] Recently, an integral equation for the ground state of the attractive gas for cLN constant has been derived [229]. Refs. [218, 230] considered a particular highly excited, meta-stable state of the attractive gas, the so-called super-Tonks gas. Since all the rapidities are real in this state, its properties can be described with the formalism of this section.

[32] It is customary to call this quantity Fermi momentum. To be precise, it is the Fermi rapidity, since only in the limit $c \to \infty$ the usual definition of $k_F = \pi n$ is recovered.

[33] This is different from the coordinate Bethe ansatz discussion before, where we were dealing with a fixed number of particles. Excitations are then given by moving one or several m_j around, but keeping the total number fixed. In the thermodynamic limit, these excitations are one-particle plus one-hole excitations. It can be shown that the energy and momentum are additive for these quantities [239], as long as one introduces a chemical potential for the change of particle number, so it is customary to simply focus on the two branches mentioned.

strength. To parameterize this shift in the thermodynamic limit, Lieb introduced the so-called shift or backflow function $F(\lambda, \lambda_p)$, where λ_p is the bare quasi-momentum of the particle added [231]. In the thermodynamic limit

$$F(\lambda|\lambda_p) = \frac{1}{2\pi}\int_{-k_F}^{k_F} \frac{2c}{c^2+(\lambda-\lambda')} F(\lambda'|\lambda_p)\mathrm{d}\lambda' - \frac{1}{\pi}\arctan\left(\frac{\lambda-\lambda_p}{c}\right) - \frac{1}{2}\,. \tag{2.72}$$

The change of momentum of the system is then given by

$$\Delta p(\lambda_p) = \lambda_p + \int_{-k_F}^{k_F} F(\lambda'|\lambda_p)\mathrm{d}\lambda' \tag{2.73}$$

and the change in energy by

$$\Delta\epsilon(\lambda_p) = \lambda_p^2 + \int_{-k_F}^{k_F} 2\lambda' F(\lambda'|\lambda_p)\mathrm{d}\lambda'\,, \tag{2.74}$$

The same considerations can be repeated for Type II (hole) excitations, where the bare hole quasi-momentum has to be inside the Fermi zone, leading to similar equations with different signs, cf. Refs. [207, 219, 223, 231]. Introducing a chemical potential to account for the change of particle number, one can define one-particle and one-hole excitation energies and momenta that are additive [207, 223, 239]. These quantities are the dressed momentum and energy of the system, i.e. exact many-body quantities with single-particle behavior determined by integral equations. Put differently, the integrable Lieb–Liniger model has stable quasi-particles that can be obtained by solving a set of integral equations. This allows for comparison to the universal, phenomenological low-energy Luttinger liquid theory [65, 240, 241], which does not specify the nature of its quasi-particles (fermionic or bosonic) beyond the linearized spectrum, see e.g. Refs. [242–244]. But the non-linearity is crucial for the correct description of, e.g., response functions, and taking input from the excitation spectrum of the Lieb–Liniger model has led to the development of nonlinear Luttinger liquid theory [242, 245, 246].

Recently, the excitations of the Lieb–Liniger model have been probed experimentally by Bragg spectroscopy [247, 248], and the contributions of the Type II branch to the dynamical structure factor, which does not have a counterpart in higher dimensions, has been revealed by comparing to numerical predictions obtained with algebraic Bethe ansatz based methods.

Since experiments in one-dimensional tubes necessarily break integrability, even if only weakly, the perfect elementary excitations (i.e. eigenstates of the many-body system) turn into long-lived quasi-particles (i.e. approximate eigenstates of the many-body system). This means that integrable models could shed light on physical processes beyond their exact applicability.

Finally, let us mention that the zero-temperature formalism introduced in this section can be extended to finite temperatures [207, 219, 223]. The idea in that case is to derive the entropy from the distribution of Bethe rapidities, which again leads to a set of integral equations.

3

A coordinate Bethe ansatz approach to the calculation of equilibrium and nonequilibrium correlations of the one-dimensional Bose gas

In Chapter 2, we introduced the Lieb–Liniger model and derived its solution in terms of energy eigenfunctions via the coordinate Bethe ansatz. In principle, the quantum-mechanical many-body problem is therefore solved. However, as we saw in Chapter 1, the quantities that are measured in a typical experiment are correlation functions like the momentum distribution in the case of the quantum Newton's cradle experiment [2] and the phase correlation function in the generalized Gibbs ensemble experiment [3]. Correlation functions are notoriously hard to calculate for strongly correlated systems, as we will outline in the introduction of the following publication. The scope of this chapter is to introduce a numerical method based on the coordinate Bethe ansatz to calculate matrix elements of operators in

Lieb–Liniger eigenstates exactly. This enables us to calculate correlation functions for equilibrium systems at zero and finite temperature, as well as dynamically evolving correlation functions following a preparation of the system in a nonequilibrium initial state on all time scales.

The following has been published in NJP [165] and is a verbatim reproduction.

3.1 Abstract

We use the coordinate Bethe ansatz to exactly calculate matrix elements between eigenstates of the Lieb–Liniger model of one-dimensional bosons interacting via a two-body delta-potential. We investigate the static correlation functions of the zero-temperature ground state and their dependence on interaction strength, and analyze the effects of system size in the crossover from few-body to mesoscopic regimes for up to seven particles. We also obtain time-dependent nonequilibrium correlation functions for five particles following quenches of the interaction strength from two distinct initial states. One quench is from the non-interacting ground state and the other from a correlated ground state near the strongly interacting Tonks-Girardeau regime. The final interaction strength and conserved energy are chosen to be the same for both quenches. The integrability of the model highly constrains its dynamics, and we demonstrate that the time-averaged correlation functions following quenches from these two distinct initial conditions are both nonthermal and moreover distinct from one another.

3.2 Introduction

The Lieb–Liniger model of a one-dimensional Bose gas with repulsive delta-function interactions is a paradigmatic example of an exactly solvable continuous, integrable many-body quantum system [56, 231]. In particular, it has served as the context for the development of theoretical tools that have subsequently been widely applied in the study of integrable systems, such as the so-called "thermodynamic Bethe ansatz" functional representation, which provides the exact equation of state, excitation spectrum [56, 231], and bulk parameters [219] of the system in the thermodynamic limit. However, the calculation of correlation

functions from the exact solutions provided by the Bethe ansatz is notoriously difficult.

At zero temperature, exact closed-form solutions for some equilibrium correlation functions are known in the Tonks–Girardeau limit of infinite interaction strength [214, 249–252]. This comparatively tractable limit also allows for some strong-coupling expansion results for large but finite interactions [252–255]. In the opposite weakly interacting quasi-condensate regime, a mean-field approach can be used to describe the system [256] and a Bogoliubov method can be used to determine the low-lying excitation spectrum [257], relying on small density fluctuations. Fewer results are available for intermediate interaction strengths, away from the strongly-interacting and weakly-interacting regimes. The development of the Luttinger liquid description of quantum fluids [240] and the related formalism of conformal field theory [258, 259] have lead to the prediction of power-law scaling for first-order correlations at large distances, with an exponent given in terms of the equation of state that is known exactly from the thermodynamic Bethe ansatz [241]. The algebraic Bethe ansatz provides a determinantal representation of correlations, from which their asymptotic behavior can be extracted [207]. More recently, exact expressions for local second- and third-order correlations [260–262], together with exact results for the one-body correlation function at asymptotically short distances [5] in terms of the equation of state have been derived.

Away from the asymptotic short- and long-range regimes, the behavior of correlation functions is less well known. For intermediate interaction strengths and arbitrary length scales one must resort to numerics to determine the correlation functions. Results for the latter have been obtained using numerical methodologies including quantum Monte Carlo [263, 264], and density matrix renormalization group approaches [265]. A recently developed, integrability-based approach combines the decomposition of correlation functions into sums over matrix elements (form factors) of certain simple operators between Bethe ansatz eigenstates [266, 267]. This approach has generated results, for example, for static and dynamical equilibrium correlations at zero and finite temperature for systems of up to $N \approx 100$ particles [268]. Other finite temperature results for correlation functions have been obtained using imaginary time stochastic gauge methods [269, 270], taking the non-relativistic limit of a relativistic field theory [271], utilizing Fermi–Bose mapping for the strongly interacting gas [254, 272, 273], employing perturbative expansions in temperature and interaction strength [274], as well as combining the thermodynamic Bethe ansatz with

the Hellmann–Feynman theorem [275].

Experiments with ultracold quantum gases are able to realize effectively one-dimensional systems by tightly confining the gas in two of the three spatial dimensions, either using optical lattice potentials or atom-chip traps [2, 39, 95, 96, 179, 247, 247, 248, 276–284]. These experiments are now probing the predictions of the Lieb–Liniger model. The configurability of quantum-gas experiments allows for so-called *quenches* of the system, in which Hamiltonian parameters of the system are abruptly changed, and thus for the study of the Lieb-Linger model out of equilibrium, providing even greater challenges for theory.

The dynamically evolving correlations of the Lieb–Liniger gas in nonequilibrium scenarios are currently a topic of significant interest, and a number of theoretical approaches have been applied. Notable examples include exact diagonalization under a low momentum cutoff [182–185, 285], mapping of the hard-core Tonks–Girardeau gas to free spinless fermions [62, 73, 286–291], phase-space methods [292], dynamic Bogoliubov-like approximations [293] and tensor-network methods [194, 195]. References [294–297] employed nonperturbative approximative functional-integral methods, while in Ref. [77] a dynamical Luttinger-liquid approach was taken. Other calculations make explicit use of the integrability of the system. These are based on various Bethe ansatz approaches, and include utilizing Fermi-Bose mapping [70, 71] and strong coupling expansions of the coordinate Bethe ansatz wave function [298–300], combining the algebraic Bethe ansatz with other numerical methods [209–211], and using the Yudson contour-integral representation for infinite-length systems [301, 302]. Recently, it was conjectured that the dynamics following an interaction strength quench are captured by a thermodynamic Bethe ansatz saddle point state and excitations around it — the so-called quench action approach [202, 204–206, 303, 304]. In the spirit of the methodology of Refs. [266, 305], Gritsev *et al.* [210] investigated a quench from $\gamma = 0 \to \infty$ by combining algebraic Bethe ansatz expressions for form factors with truncated sums over states, and employing Monte Carlo summation over the eigenstate components of the initial state.

In this paper we take a different approach, and calculate correlation functions of the Lieb-Linger model, both in and out of equilibrium, by calculating matrix elements between Lieb–Liniger eigenstates directly within the coordinate Bethe ansatz formalism. Given the known expressions for the coordinate-space forms of Lieb–Liniger eigenstates, we generate

symbolic expressions for matrix elements of operators between these states in terms of the Bethe rapidities. The numerically obtained values of the rapidities can then be substituted to yield essentially numerically exact values for the matrix elements.

In our previous work we applied this methodology to quenches from the ideal gas ground state to positive γ for up to $N = 5$ particles [166]. In Sec. 3.3 we provide the details of the methodology, and describe how it can be used to calculate the matrix elements of the Lieb–Liniger eigenstates. These symbolic expressions, and thus the computational cost of evaluating them, grow combinatorially with particle number, restricting the method to systems of only a few particles. However for small particle numbers $N \leq 7$ we obtain numerically exact results for ground-state correlations, which are described in Sec. 3.4. Our results demonstrate that local correlations in the strongly interacting regime are already close to their thermodynamic-limit values for these few-body to mesoscopic systems.

An additional advantage of our methodology is that it can also calculate overlaps between Lieb–Liniger eigenstates corresponding to *any* two interaction strengths, which allows us to study the dynamics of quenches of the interaction strength between arbitrary values. In Sec. 3.5 we utilize this property to study the effects of integrability on the relaxation of the Lieb-Liniger model following such a quench. In particular, we compare two nonequilibrium quench scenarios with the same final Hamiltonian and state energy, but beginning from starkly different initial states. Statistical mechanics would predict that the system would relax to the same thermal state in both cases, but due to the integrability of the Lieb-Linger model not only are the time-averaged states following the two quenches non-thermal, they are also distinct. After characterizing and comparing the nonequilibrium dynamics following both quenches, we conclude in Sec. 3.6.

3.3 Coordinate Bethe-ansatz methodology

3.3.1 Lieb–Liniger model eigenstates

The Lieb–Liniger model [56, 231] describes a system of N indistinguishable bosons subject to a delta-function interaction potential in a periodic one-dimensional (1D) geometry of length L. We work in units such that $\hbar = 1$ and the particle mass $m = 1/2$, and so the

Hamiltonian of this system reads

$$\hat{H} = -\sum_{i=1}^{N} \frac{\partial^2}{\partial x_i^2} + 2c \sum_{i<j}^{N} \delta(x_i - x_j), \tag{3.1}$$

where c is the interaction strength. The coordinate Bethe ansatz yields eigenstates $|\{\lambda_j\}\rangle$ of Hamiltonian (3.1) with spatial representation [207]

$$\zeta_{\{\lambda_j\}}(\{x_i\}) \equiv \langle\{x_i\}|\{\lambda_j\}\rangle = A_{\{\lambda_j\}} \sum_{\sigma} \exp\Big[i \sum_{m=1}^{N} x_m \lambda_{\sigma(m)}\Big] \prod_{k>l} \left(1 - \frac{ic\,\mathrm{sgn}(x_k - x_l)}{\lambda_{\sigma(k)} - \lambda_{\sigma(l)}}\right), \tag{3.2}$$

where the rapidities λ_j (or quasimomenta) are solutions of the Bethe equations

$$\lambda_j = \frac{2\pi}{L} m_j - \frac{2}{L} \sum_{k=1}^{N} \arctan\left(\frac{\lambda_j - \lambda_k}{c}\right). \tag{3.3}$$

The quantum numbers m_j are any N distinct integers (half-integers) in the case that N is odd (even) [219], and $\sum_\sigma$ denotes a sum over all $N!$ permutations $\sigma = \{\sigma(j)\}$ of $\{1, 2, \ldots, N\}$. The normalization constant reads [207]

$$A_{\{\lambda_j\}} = \frac{\prod_{k>l}(\lambda_k - \lambda_l)}{\left[N!\,\det\{M_{\{\lambda_j\}}\}\,\prod_{k>l}[(\lambda_k - \lambda_l)^2 + c^2]\right]^{1/2}}, \tag{3.4}$$

where $M_{\{\lambda_j\}}$ is the $N \times N$ matrix with elements

$$[M_{\{\lambda_j\}}]_{kl} = \delta_{kl}\Big(L + \sum_{m=1}^{N} \frac{2c}{c^2 + (\lambda_k - \lambda_m)^2}\Big) - \frac{2c}{c^2 + (\lambda_k - \lambda_l)^2}. \tag{3.5}$$

The rapidities determine the total momentum $P = \sum_{j=1}^{N} \lambda_j$ and energy $E = \sum_{j=1}^{N} \lambda_j^2$ of the system in each eigenstate. The ground state of the system corresponds to the set of N rapidities that minimize E and constitute the (pseudo-)Fermi sea of the 1D Bose gas [207]. The Fermi momentum

$$k_{\mathrm{F}} = \frac{2\pi}{L} \frac{N-1}{2} \tag{3.6}$$

is the magnitude of the largest rapidity occurring in the ground state in the Tonks–Girardeau limit of strong interactions [214]. The only parameter of the Lieb–Liniger model in the thermodynamic limit is the dimensionless coupling $\gamma \equiv c/n$, where $n \equiv N/L$ is the 1D density. In finite systems, physical quantities also depend on the particle number N (see, e.g., Sec. 3.4.3), whereas the length L of our system, and therefore also the density n, are arbitrary. Consequently, in this article we will specify both N and γ. Unless specified otherwise, we measure time in units of k_{F}^{-2}, energy in units of k_{F}^{2}, and length in units of k_{F}^{-1}.

3.3.2 Calculation of correlation functions and overlaps

As the eigenstates $|\{\lambda_j\}\rangle$ form a complete basis [221] for the state space of the Lieb–Liniger model, the expectation value $\langle\hat{O}\rangle_t = \mathrm{Tr}\{\hat{\rho}(t)\hat{O}\}$ of an arbitrary operator $\hat{O}$ in a Schrödinger-picture density matrix $\hat{\rho}(t)$ can be expressed as a sum of matrix elements of $\hat{O}$ between the states $|\{\lambda_j\}\rangle$. In particular, in a pure state $|\psi(t)\rangle = \sum_{\{\lambda_j\}} C_{\{\lambda_j\}}(t)|\{\lambda_j\}\rangle$ we have

$$\langle\hat{O}\rangle_t \equiv \langle\psi(t)|\hat{O}|\psi(t)\rangle = \sum_{\{\lambda_j\}}\sum_{\{\lambda'_j\}} C^*_{\{\lambda'_j\}}(t)C_{\{\lambda_j\}}(t)\langle\{\lambda'_j\}|\hat{O}|\{\lambda_j\}\rangle, \tag{3.7}$$

whereas in a statistical ensemble with density matrix $\hat{\rho}_{\mathrm{SE}} = \sum_{\{\lambda_j\}} \rho^{\mathrm{SE}}_{\{\lambda_j\}}|\{\lambda_j\}\rangle\langle\{\lambda_j\}|$, we find

$$\langle\hat{O}\rangle = \sum_{\{\lambda_j\}} \rho^{\mathrm{SE}}_{\{\lambda_j\}}\langle\{\lambda_j\}|\hat{O}|\{\lambda_j\}\rangle. \tag{3.8}$$

In this article, we focus in particular on the normalized m^{th}-order equal-time correlation functions

$$g^{(m)}(x_1,\ldots,x_m,x'_1,\ldots,x'_m;t) \equiv \frac{\left\langle\hat{\Psi}^\dagger(x_1)\cdots\hat{\Psi}^\dagger(x_m)\hat{\Psi}(x'_1)\cdots\hat{\Psi}(x'_m)\right\rangle}{\left[\langle\hat{n}(x_1)\rangle\cdots\langle\hat{n}(x_m)\rangle\langle\hat{n}(x'_1)\rangle\cdots\langle\hat{n}(x'_m)\rangle\right]^{1/2}}, \tag{3.9}$$

where $\hat{\Psi}^{(\dagger)}(x)$ is the annihilation (creation) operator for the Bose field and $\hat{n}(x) \equiv \hat{\Psi}^\dagger(x)\hat{\Psi}(x)$. Here and in the following we drop the time index t of the state vectors.

Since the Hamiltonian we consider in this article is translationally invariant along the periodic volume of length L, the mean density $\langle\hat{n}(x)\rangle \equiv n$ is constant in both time and space, and $g^{(m)}(x_1,\ldots,x_m,x'_1,\ldots,x'_m;t) = \langle\hat{\Psi}^\dagger(x_1)\cdots\hat{\Psi}^\dagger(x_m)\hat{\Psi}(x'_1)\cdots\hat{\Psi}(x'_m)\rangle/n^m$. The correla-

tion functions $g^{(m)}(x_1,\ldots,x_m,x'_1,\ldots,x'_m;t)$ can therefore be expressed as the expectation values of the operators $\hat{g}^{(m)}(x_1,\ldots,x_m,x'_1,\ldots,x'_m) \equiv \hat{\Psi}^\dagger(x_1)\cdots\hat{\Psi}^\dagger(x_m)\hat{\Psi}(x'_1)\cdots\hat{\Psi}(x'_m)/n^m$. We note that for the same reasons as above the matrix elements $\langle\{\lambda'_j\}|\hat{g}^{(m)}(x_1,\ldots,x_m,x'_1,\ldots,x'_m)|\{\lambda_j\}\rangle$ are invariant under global coordinate shifts $x \to x+d$ and thus, without loss of generality, we can set one of the spatial variables to zero. For the first-order correlation function, the matrix elements are

$$\begin{aligned}\langle\{\lambda'_j\}|\hat{g}^{(1)}(0,x)|\{\lambda_j\}\rangle &\equiv \langle\{\lambda'_j\}|\hat{\Psi}^\dagger(0)\hat{\Psi}(x)|\{\lambda_j\}\rangle \\ &= \frac{N}{n}\int dx_1\cdots dx_{N-1}\,\zeta^*_{\{\lambda'_j\}}(0,x_1,\ldots,x_{N-1})\,\zeta_{\{\lambda_j\}}(x,x_1,\ldots,x_{N-1}).\end{aligned} \tag{3.10}$$

The evaluation of the integral in Eq. (3.10) is complicated by the sign function in Eq. (3.2) and the associated nonanalyticities in $\zeta_{\{\lambda_j\}}(\{x_i\})$ where any two particle coordinates x_k and x_l coincide. However, we can use the Bose symmetry of the wave function $\zeta_{\{\lambda_j\}}(\{x_i\})$ to reexpress this matrix element as a sum of integrals

$$\begin{aligned}&\langle\{\lambda'_j\}|\hat{g}^{(1)}(0,x)|\{\lambda_j\}\rangle \\ &= \frac{N!}{n}\sum_{\ell=0}^{N-1}\int_{\mathcal{R}_{N-1,\ell}(x)} dx_1\cdots dx_{N-1}\,\zeta^*_{\{\lambda'_j\}}(0,x_1,\ldots,x_{N-1})\,\zeta_{\{\lambda_j\}}(x_1,\ldots,x_\ell,x,x_{\ell+1},\ldots,x_{N-1}),\end{aligned} \tag{3.11}$$

over the ordered domains [255]

$$\mathcal{R}_{M,j}(x): \quad 0 \le x_1 < \cdots < x_j < x < x_{j+1} < \cdots < x_M \le L. \tag{3.12}$$

Substituting the coordinate-space form [Eq. (3.2)] of the Lieb-Liniger eigenfunctions, we obtain

$$\begin{aligned}\langle\{\lambda'_j\}|\hat{g}^{(1)}(0,x)|\{\lambda_j\}\rangle = \frac{N!}{n}A_{\{\lambda_j\}}A^*_{\{\lambda'_j\}}\sum_\sigma\sum_{\sigma'}\prod_{j>k}\left(1-\frac{ic}{\lambda_{\sigma(j)}-\lambda_{\sigma(k)}}\right)\prod_{j'>k'}\left(1+\frac{ic}{\lambda'_{\sigma'(j')}-\lambda'_{\sigma'(k')}}\right) \\ \times\sum_{\ell=0}^{N-1}\exp(i\lambda_{\sigma(\ell+1)}x)\int_{\mathcal{R}_{N-1,\ell}(x)}dx_1\cdots dx_{N-1}\exp\left(i\sum_{m=1}^{N-1}(\lambda_{\sigma^{(\ell+1)}(m)}-\lambda'_{\sigma'(m+1)})x_m\right),\end{aligned} \tag{3.13}$$

where $\sigma^{(\ell+1)} = (\sigma(1), \ldots, \sigma(\ell), \sigma(\ell+2), \ldots, \sigma(N))$. The matrix elements of the second-order correlation operator $\hat{g}^{(2)}(0,x) \equiv \hat{\Psi}^\dagger(0)\hat{\Psi}^\dagger(x)\hat{\Psi}(x)\hat{\Psi}(0)/n^2$ are similarly given by

$$\langle\{\lambda'_j\}|\hat{g}^{(2)}(0,x)|\{\lambda_j\}\rangle = \frac{N!}{n^2} A_{\{\lambda_j\}} A^*_{\{\lambda'_j\}} \sum_\sigma \sum_{\sigma'} \prod_{j>k} \Big(1 - \frac{ic}{\lambda_{\sigma(j)} - \lambda_{\sigma(k)}}\Big) \prod_{j'>k'} \Big(1 + \frac{ic}{\lambda'_{\sigma'(j')} - \lambda'_{\sigma'(k')}}\Big)$$
$$\times \sum_{\ell=0}^{N-2} \exp\big(i(\lambda_{\sigma(\ell+2)} - \lambda'_{\sigma'(\ell+2)})x\big) \int_{\mathcal{R}_{N-2,\ell}(x)} dx_1 \cdots dx_{N-2} \exp\left(i \sum_{m=1}^{N-2} (\lambda_{\sigma^{(1,\ell+2)}(m)} - \lambda'_{\sigma'^{(1,\ell+2)}(m)}) x_m\right), \tag{3.14}$$

where $\sigma^{(1,\ell+2)} = (\sigma(2), \ldots, \sigma(\ell+1), \sigma(\ell+3), \ldots, \sigma(N))$ and $\sigma'^{(1,\ell+2)}$ is defined analogously in terms of the elements of σ'. In the limit $x \to 0$ this expression simplifies somewhat, and in general the matrix elements of the local m^{th}-order correlation operator $\hat{g}^{(m)}(0) \equiv [\hat{\Psi}^\dagger(0)]^m [\hat{\Psi}(0)]^m / n^m$ are given by the expression

$$\langle\{\lambda'_j\}|\hat{g}^{(m)}(0)|\{\lambda_j\}\rangle = \frac{N!}{n^m} A_{\{\lambda_j\}} A^*_{\{\lambda'_j\}} \sum_\sigma \sum_{\sigma'} \prod_{j>k} \Big(1 - \frac{ic}{\lambda_{\sigma(j)} - \lambda_{\sigma(k)}}\Big) \prod_{j'>k'} \Big(1 + \frac{ic}{\lambda'_{\sigma'(j')} - \lambda'_{\sigma'(k')}}\Big)$$
$$\times \sum_{\ell=0}^{N-m} \int_{\mathcal{R}_{N-m}} dx_1 \cdots dx_{N-m} \exp\left(i \sum_{n=1}^{N-m} (\lambda_{\sigma(m+n)} - \lambda'_{\sigma'(m+n)}) x_n\right), \tag{3.15}$$

where the domain $\mathcal{R}_M : 0 \le x_1 < x_2 < \cdots < x_M \le L$. We note, moreover, that Eqs. (3.13)–(3.15) include as degenerate cases the diagonal matrix elements (cf. Ref. [255]) appropriate to the calculation of correlations in the ground state (Sec. 3.4) and in statistical ensembles (Sec. 3.5).

The calculation of correlation functions from Eqs. (3.13)–(3.15) involves the evaluation of integrals of the general form

$$\int_{\mathcal{R}_{M,\ell}(x)} dx_1 \cdots dx_M \exp\left(i \sum_{m=1}^{M} \kappa_m x_m\right) = \int_x^L dx_M e^{i\kappa_M x_M}$$
$$\times \int_x^{x_M} dx_{M-1} e^{i\kappa_{M-1} x_{M-1}} \cdots \int_x^{x_{\ell+2}} dx_{\ell+1} e^{i\kappa_{\ell+1} x_{\ell+1}} \int_0^x dx_\ell e^{i\kappa_\ell x_\ell} \int_0^{x_\ell} dx_{\ell-1} e^{i\kappa_{\ell-1} x_{\ell-1}} \cdots \int_0^{x_2} dx_1 e^{i\kappa_1 x_1}, \tag{3.16}$$

where (for the repulsive interactions $c > 0$ considered in this article) the κ_m are real numbers. A single closed form for this integral does not exist, as in general one or more κ_m may vanish,

and this must be handled separately from the case of $\kappa_m \neq 0$. However, given knowledge of the *particular* sets of rapidities $\{\lambda_j\}$ and $\{\lambda'_j\}$ (and permutations σ and σ'), and thus of the locations of zero exponents $\kappa_m = 0$ in Eq. (3.16), each individual integral of this form can be reduced to an algebraic expression in terms of $\{\kappa_m\}$. More specifically, each successive integration $\int dx_m$ yields a term (involving, in general, x_{m+1}) arising from the primitive integral [306]

$$\begin{aligned}\int dx\, x^p e^{ikx} &= -(i/k)^{p+1}\Gamma(p+1,-ikx) \\ &= -p!(i/k)^{p+1}e^{ikx}\sum_{s=0}^{p}\frac{(-ikx)^s}{s!},\end{aligned} \tag{3.17}$$

in the case that κ_m is nonzero, or from $\int dx\, x^p$ otherwise. In our calculations, the construction of algebraic expressions for the integrals occurring in Eqs. (3.13)–(3.15) in terms of the rapidities λ_j is efficiently performed by a simple computer algorithm that accounts for and combines the symbolic terms that arise from these successive reductions. We note that, e.g., each matrix element $\langle\{\lambda'_j\}|\hat{g}^{(1)}(0,x)|\{\lambda_j\}\rangle$ is a sum of N integrals over $(N-1)$-dimensional domains and that the integrand in each case comprises $(N!)^2$ terms [255], illustrating the dramatically increasing computational cost of evaluating correlation functions with increasing N. Nevertheless, the explicit closed-form expression for the integral produced by our algorithm can be evaluated to obtain a numerically exact result by substituting in the values of the rapidities. The latter are obtained by solving Eq. (3.3) numerically using Newton's method, starting in the Tonks–Girardeau regime of strong interactions $\gamma \gg 1$ and iteratively progressing to smaller values of γ using initial guesses given by linear extrapolation of the solutions at stronger interaction strengths.

We note that this algorithmic approach also provides for the efficient and accurate calculation of the overlaps $\langle\{\lambda_j\}|\{\mu_j\}\rangle$ between eigenstates of Hamiltonian (3.1) corresponding to different values of γ, which we make use of in our analysis of nonequilibrium dynamics in Sec. 3.5. In particular, the overlap between an arbitrary eigenstate $|\{\lambda_j\}\rangle$ of $\hat{H}$ at a finite interaction strength $\gamma > 0$ and the noninteracting ground state $|0\rangle$, with constant spatial

representation $\langle\{x_i\}|0\rangle = L^{-N/2}$, is simply given by

$$\langle\{\lambda_j\}|0\rangle = \frac{N!}{L^{N/2}} A_{\{\lambda_j\}} \sum_{\sigma} \prod_{j>k} \left(1 + \frac{ic}{\lambda_{\sigma(j)} - \lambda_{\sigma(k)}}\right) \int_{\mathcal{R}_N} dx_1 \cdots dx_N \exp\left(-i \sum_{n=1}^{N} \lambda_{\sigma(n)} x_n\right), \tag{3.18}$$

which can easily be evaluated semi-analytically using our algorithm. In practice we find that the results we obtain for the overlaps from our evaluation of Eq. (3.18) agree with the recently derived closed-form expressions for these quantities [204, 307–309], which imply in particular that $\langle\{\lambda_j\}|0\rangle \propto 1/\lambda_j^2$ as any $\lambda_j \to \infty$.

3.4 Ground-State Correlation Functions

As a first application of our methodology we calculate the correlation functions of the Lieb–Liniger model in the ground state for up to $N = 7$ particles. In this case, we need to evaluate only the diagonal elements of Eqs. (3.13)–(3.15) in the ground-state wave function, thereby obtaining exact algebraic expressions for correlation functions in terms of the ground-state rapidities, which are themselves determined to machine precision (Sec. 3.3.2). The ground-state correlations of the Lieb–Liniger model have been considered extensively in previous works (see Refs. [310, 311] and references therein), and we compare our exact mesoscopic results to those obtained with various other methods and approximations, for finite system sizes as well as in the thermodynamic limit. This allows us to clarify the utility and limitations of calculations, such as ours here and in Ref. [166], that involve only small particle numbers.

3.4.1 First-order correlations

We begin by considering the first-order correlation function $g^{(1)}(x) \equiv g^{(1)}(0, x)$ in the ground state of the Lieb–Liniger model. In Fig. 3.1(a) we plot $g^{(1)}(x)$ for $N = 7$ particles for a range of interaction strengths γ, which exhibits the expected decrease in spatial phase coherence with increasing γ [241]. As is well known, true long-range order, $\lim_{x\to\infty} g^{(1)}(x) = n_0 > 0$ [312, 313], is prohibited in an interacting homogeneous 1D Bose gas in the thermodynamic

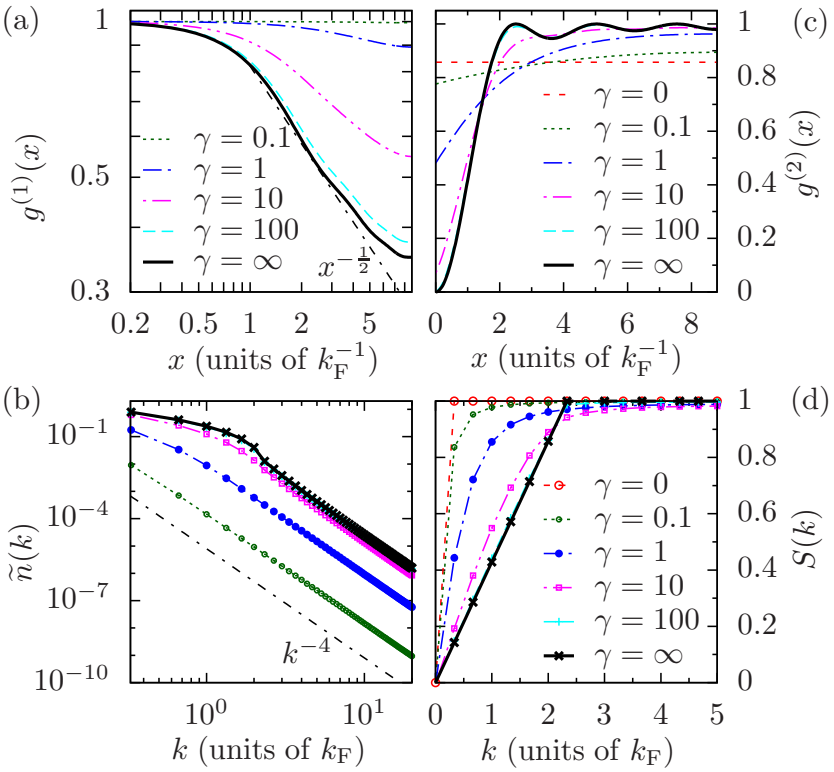

FIGURE 3.1: (Color online) One- and two-body correlations in the Lieb–Liniger ground state, for $N = 7$ particles. (a) Non-local first-order coherence $g^{(1)}(x)$. The black dot-dashed line indicates the asymptotic long-range behavior $g^{(1)}(x) \propto |x|^{-1/2}$ of a Tonks–Girardeau gas in the thermodynamic limit. (b) Corresponding zero-temperature momentum distribution $\widetilde{n}(k_j)$. The black dot-dashed line indicates the universal high-momentum power-law scaling $\widetilde{n}(k) \propto k^{-4}$ common to all positive interaction strengths [5]. (c) Non-local second-order coherence $g^{(2)}(x)$. (d) Corresponding static structure factor $S(k)$.

limit, even at zero temperature (see Ref. [311] and references therein). Indeed the Lieb–Liniger system is quantum critical at zero temperature, and the asymptotic long-range behavior of $g^{(1)}(x)$ is a power-law decay (so-called *quasi*-long-range order) [207].

This power-law scaling of $g^{(1)}(x)$ is only expected to be realized at separations x large compared to the healing length $\xi = 1/\sqrt{\gamma}$ and, in a finite periodic geometry such as we consider here, is curtailed by the finite extent L of the system (see, e.g., Ref. [241]). Indeed, for $\gamma = 0.1$, the power-law decay is not visible in our finite-sized calculation, although as the interaction strength γ increases $g^{(1)}(x)$ exhibits behavior consistent with power-law decay over an increasingly large range of x, see Fig. 3.1(a). In particular, for $\gamma \gtrsim 10$, our results for $g^{(1)}(x)$ seem to converge toward the asymptotic scaling of the Tonks–Girardeau limit (black dot-dashed line) with increasing γ.

Due to the translational invariance of our system, the first-order correlations of the

Lieb–Liniger ground state are encoded in the momentum distribution

$$\widetilde{n}(k_j) = n \int_0^L dx\, e^{-ik_j x} g^{(1)}(x), \tag{3.19}$$

which, in our finite periodic geometry, is only defined for discrete momenta $k_j = 2\pi j/L$, with j an integer. In Fig. 3.1(b) we plot the momentum distributions $\widetilde{n}(k_j)$ corresponding to the first-order correlation functions $g^{(1)}(x)$ shown in Fig. 3.1(a). The first feature that we note in Fig. 3.1(b) is that for all interaction strengths, $\widetilde{n}(k)$ exhibits a power-law decay $\widetilde{n}(k) \propto k^{-4}$ (dot-dashed black line) at high momenta. This is a universal result for delta-function interactions in one dimension [5, 305, 314] (and indeed also in higher dimensions [315]). The effects of the finite extent L of the system on the first-order correlations are again evident in this momentum-space representation. For $\gamma = 0.1$, no deviation from the $\propto k^{-4}$ scaling is observed for the smallest (nonzero) momenta k_j that can be resolved in the periodic geometry. For larger values of the interaction strength, $\widetilde{n}(k)$ departs from the $\propto k^{-4}$ scaling at increasingly large values of k with increasing γ, and develops a hump at momenta near k_{F} for $\gamma \gtrsim 10$ [305]. We note that although the small-k behavior of $\widetilde{n}(k)$ tends towards the $\propto k^{-1/2}$ scaling exhibited by the Tonks–Girardeau gas in the thermodynamic limit, the rounding off of the power-law decay of $g^{(1)}(x)$ as $x \to L/2$ precludes $\widetilde{n}(k)$ from reaching the known asymptotic $k \to 0$ behavior in our finite geometry.

3.4.2 Second-, third-, and fourth-order correlations

In Fig. 3.1(c), we present the nonlocal second-order coherence $g^{(2)}(x) \equiv g^{(2)}(0, x, x, 0)$, which provides a measure of density-density correlations, for $N = 7$ particles at a range of interaction strengths γ. In the limiting case of an ideal gas ($\gamma = 0$), the ground state of the system is a Fock state of N particles in the zero-momentum single-particle mode, and the second-order coherence $g^{(2)}_{\gamma=0}(x) = 1 - N^{-1}$ (horizontal dashed line) is therefore independent of x. As the interaction strength γ is increased, the second-order coherence is increasingly suppressed at zero spatial separation and correspondingly enhanced at separations $x \gtrsim 2k_{\mathrm{F}}^{-1}$. Oscillations in $g^{(2)}(x)$ develop at finite x as the system enters the strongly interacting regime $\gamma \gg 1$ [207, 254] and, in particular, for $\gamma = 100$ (dashed cyan line), our numerical results are practically indistinguishable from the exact Tonks–Girardeau limit result (solid black

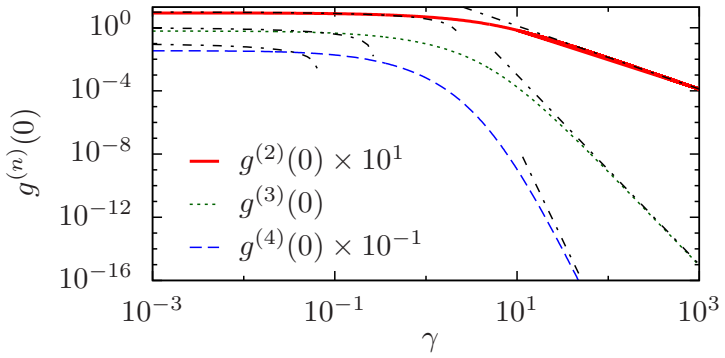

FIGURE 3.2: (Color online) Interaction-strength dependence of the local second-, third- and fourth-order coherence in the Lieb–Liniger ground state, for $N = 7$ particles. To aid visibility, we plot $g^{(2)}(0)$ scaled by a factor of 10^1, and $g^{(4)}(0)$ scaled by a factor of 10^{-1}. Dot-dashed lines indicate asymptotic weak- ($\gamma \ll 1$) and strong-coupling ($\gamma \gg 1$) expressions for $g^{(2)}(0)$, $g^{(3)}(0)$ and $g^{(4)}(0)$ in the thermodynamic limit (see text).

line) [214].

An alternative representation of the second-order correlations of the ground state is given by the static structure factor $S(k)$, which is related to $g^{(2)}(x)$ by [256]

$$S(k_j) = 1 + n \int_0^L dx\, e^{-ik_j x} \left[g^{(2)}(x) - 1 \right]. \tag{3.20}$$

In Fig. 3.1(d) we present the structure factors $S(k)$ corresponding to the correlation functions $g^{(2)}(x)$ shown in Fig. 3.1(c). For all values of γ, $S(0) = 0$ due to particle-number conservation and translational invariance. In the ideal-gas limit (red circles) $S(k_j) = 1$ for all nonzero k_j. In the opposite limit of a Tonks–Girardeau gas

$$S_{\gamma=\infty}(k_j) = \begin{cases} \frac{|k_j|(1-N^{-1})}{2k_{\mathrm{F}}} & |k_j| \leq 2k_{\mathrm{F}} \\ 1 & |k_j| > 2k_{\mathrm{F}}, \end{cases} \tag{3.21}$$

which tends, in the thermodynamic limit, to the well-known result (see, e.g., Ref. [254]) $S(k) = |k|/2k_{\mathrm{F}}$ for $|k| \leq 2k_{\mathrm{F}}$, and $S(k) = 1$ for $|k| > 2k_{\mathrm{F}}$. Just as for $g^{(2)}(x)$, we observe that for $\gamma = 100$ (cyan plus symbols), our numerical results for $S(k)$ are almost identical to the known exact expression [Eq. (3.21)] for the Tonks–Girardeau limit (black crosses). For smaller values of γ our mesoscopic results for $S(k)$ appear consistent with those of Refs. [263, 266], obtained using quantum Monte Carlo and algebraic-Bethe ansatz techniques, respectively.

We now focus in more detail on local correlation functions. We note that the local second-order coherence has recently been proposed as a measure of quantum criticality in the 1D boson system [316], while the local third-order correlations have received increasing attention both in theory [317] and experiment [282, 318–320]. The local fourth-order correlations for the Lieb–Liniger model have also been investigated [321]. In Fig. 3.2, we plot the local second-order coherence $g^{(2)}(0)$ (solid red line), together with the local third-order coherence $g^{(3)}(0) = \langle[\hat{\Psi}^\dagger(0)]^3[\hat{\Psi}(0)]^3\rangle/n^3$ (dotted green line), and the local fourth-order coherence $g^{(4)}(0) = \langle[\hat{\Psi}^\dagger(0)]^4[\hat{\Psi}(0)]^4\rangle/n^4$ (dashed blue line) for $N = 7$ particles and a broad range of interaction strengths γ. For comparison, we also plot the asymptotic results obtained in the Bogoliubov limit of weak interactions ($\gamma \to 0$) in the thermodynamic limit [257, 260] (left-hand dot-dashed lines). The numerical results for small γ are broadly comparable to these thermodynamic-limit results. However, for the small particle numbers considered here, the suppression of $g^{(2)}(0)$, $g^{(3)}(0)$, and $g^{(4)}(0)$ due to interactions in the limit of small γ is overshadowed by the suppression due to the finite population of the system [262]. At larger γ, the effects of interactions dominate, and the numerical results converge closely to the appropriate strong-coupling expressions [260] (right-hand dot-dashed lines). We note, therefore, that the local correlations of the Lieb–Liniger ground state, and particularly their scaling with γ, appear to be quite insensitive to the infrared cutoff imposed by the finite extent of our system in the strongly interacting regime $\gamma \gg 1$.

3.4.3 System-size dependence

The results we have obtained so far indicate that, as expected, the small size of our system leads to corrections to correlation functions as compared to their known asymptotic forms in the thermodynamic limit. However, our results also suggest that the effects of finite system size are comparatively less important for local correlations, particularly in the limit of large interaction strengths $\gamma \gg 1$. To further elucidate the potential significance of finite-size effects in our calculations of nonequilibrium dynamics [166], here we give a brief characterization of the dependence of correlation functions of the Lieb–Liniger ground state on the particle number N at a fixed value of the interaction strength γ.

Specifically we consider the case for $\gamma = 10$, as this value places the system in the

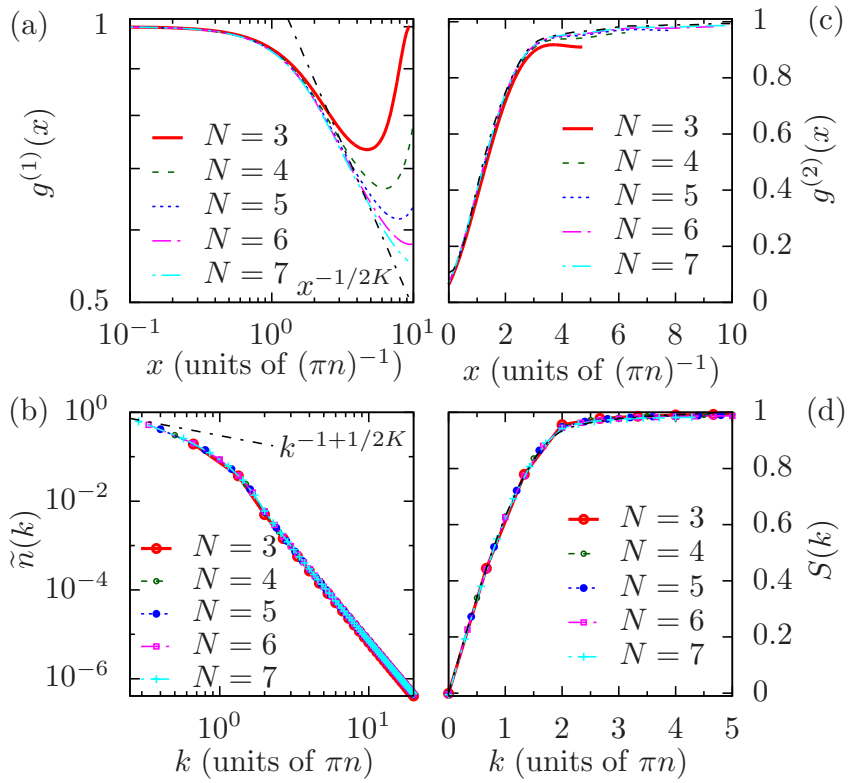

FIGURE 3.3: (Color online) Dependence of first- and second-order correlations in the Lieb–Liniger ground state on particle number N for $\gamma = 10$. (a) First-order correlation function $g^{(1)}(x)$. (b) Corresponding momentum distribution function $\widetilde{n}(k_j)$. Black dot-dashed lines in (a) and (b) indicate the asymptotic infrared scaling of $g^{(1)}(x)$ and $\widetilde{n}(k)$, respectively, with Luttinger parameter $K = 1.40$ (see text). (c) Second-order correlation function $g^{(2)}(x)$. (d) Corresponding static structure factor $S(k)$. The black dot-dashed lines in (c) and (d) represent the phenomenological expressions of Ref. [6] for $g^{(2)}(x)$ and $S(k)$ in the thermodynamic limit, respectively.

strongly interacting regime $\gamma \gg 1$ (which appears less sensitive to finite-size effects than the weakly interacting regime $\gamma \lesssim 1$), while still exhibiting significant deviations from the Tonks–Girardeau limit (see, e.g., Ref. [254]). Whereas elsewhere in this paper we quote momenta (lengths) in units of k_{F} (k_{F}^{-1}), in comparing results between systems with different particle numbers N we quote momenta (lengths) in units of πn [$(\pi n)^{-1}$], so as to avoid a potentially misleading dependence of the unit of length on N [cf. Eq. (3.6)].

In Fig. 3.3(a) we plot $g^{(1)}(x)$ for particle numbers $N = 3, 4, 5, 6$, and 7. For small x, the curves fall nearly perfectly on one line. The same behavior can be observed for the large-k tail of the corresponding momentum distribution $\widetilde{n}(k)$, which we plot in Fig. 3.3(b). Indeed, at larger momenta $k \gtrsim 2\pi n$, $\widetilde{n}(k)$ appears to exhibit a rapid collapse to a single curve with increasing N [5, 322]. However, the differences in $\widetilde{n}(k)$ are so small that they can not be seen

in Fig. 3.3(b). For small momenta, our choice of units implies an increasing resolution with increasing particle number, specifically $k_1 = 2\pi/L \times (\pi n)^{-1} = 2/N$. However, this lowest resolvable momentum seems to fall on one line for increasing particle number, indicating that the infrared behavior of large systems can be at least partly accessed by our mesoscopic system sizes.

Luttinger-liquid theory predicts a long-range power-law decay $g^{(1)}(x) \propto |x|^{-1/2K}$, where the Luttinger parameter K can be calculated from the thermodynamic limit of the Bethe ansatz solution (see, e.g., Refs. [207, 241] and references therein). For our parameters we have $K = 1.40$, implying an asymptotic scaling $g^{(1)}(x) \propto |x|^{-0.357}$ [black dot-dashed line in Fig. 3.3(a)]. This corresponds to a power-law behavior $\widetilde{n}(k) \propto |k|^{-1+1/2K} = |k|^{-0.643}$ [241] [dot-dashed line in Fig. 3.3(b)] for small momenta. We note that this infrared scaling is a true many-body effect and as such does not show up for $N = 2$ particles. Indeed, one can show analytically that, for $N = 2$, the momentum distribution $\widetilde{n}(k) \propto (\lambda_1^2 - k^2)^{-2}$ and thus k^{-4} is the highest power in the series expansion of $\widetilde{n}(k)$.

In Fig. 3.3(c) we plot the nonlocal second-order coherence $g^{(2)}(x)$ for $\gamma = 10$ and $N = 3, 4, 5, 6,$ and 7. The corresponding static structure factor $S(k)$ is shown in Fig. 3.3(d). In Fig. 3.3(d) we also plot (black dot-dashed line) the form of $S(k)$ resulting from the phenomenological expression proposed in Ref. [6] (see also Ref. [323]). This expression involves the limiting dispersions and edge exponents of the Lieb–Liniger model, which we obtain by numerically solving the appropriate integral equations [231, 245]. We also plot the corresponding prediction for $g^{(2)}(x)$ (black dot-dashed line) in Fig. 3.3(c). We note that the numerical results for our mesoscopic systems are, in general, rather close to the phenomenological thermodynamic-limit expressions even for the relatively small particle numbers considered here.

3.5 Application to nonequilibrium dynamics

We now apply our methodology to the nonequilibrium dynamics of the Lieb–Liniger model. Specifically, we consider the evolution of a system, initially prepared in the ground state of Hamiltonian (3.1) with interaction strength γ_0, following an abrupt change, at time $t = 0$, of the interaction strength to a distinct value $\gamma \neq \gamma_0$ — a so-called "interaction quench".

The evolution of the system following such a quench is generated by Hamiltonian (3.1) with interaction strength γ, which we denote by $\hat{H}(\gamma)$ hereafter. The time-evolving state is given at all times $t > 0$ by

$$|\psi(t)\rangle = \sum_{\{\lambda_j\}} C_{\{\lambda_j\}} \mathrm{e}^{-iE_{\{\lambda_j\}}t} |\{\lambda_j\}\rangle, \tag{3.22}$$

where $|\{\lambda_j\}\rangle$ are the eigenstates of $\hat{H}(\gamma)$ with energies $E_{\{\lambda_j\}}$, and $C_{\{\lambda_j\}} \equiv \langle\{\lambda_j\}|\psi_0\rangle$ are the overlaps of the $|\{\lambda_j\}\rangle$ with the initial state $|\psi_0\rangle$. The expectation value of an arbitrary operator $\hat{O}$ in the state $|\psi(t)\rangle$ is given by

$$\langle\hat{O}\rangle_t \equiv \langle\psi(t)|\hat{O}|\psi(t)\rangle = \sum_{\{\lambda_j\}} \sum_{\{\lambda'_j\}} C^*_{\{\lambda'_j\}} C_{\{\lambda_j\}} \, \mathrm{e}^{i(E_{\{\lambda'_j\}} - E_{\{\lambda_j\}})t} \, \langle\{\lambda'_j\}|\hat{O}|\{\lambda_j\}\rangle. \tag{3.23}$$

We use the methodology described in Sec. 3.3 to evaluate both the overlaps $C_{\{\lambda_j\}}$ and the matrix elements $\langle\{\lambda'_j\}|\hat{O}|\{\lambda_j\}\rangle$ that appear in Eq. (3.23).

One of the features of our methodology is that it allows us to describe quenches between arbitrary interaction strengths. In this paper we consider two interaction-strength quenches, from different initial interaction strengths γ_0, to a common final value of the coupling γ. Specifically, we consider a quench from the non-interacting limit $\gamma_0 = 0$ (similar to those previously studied in Refs. [7, 73, 166, 204, 210, 324–326]) and a quench from the correlated ground state obtained for a strong interaction strength $\gamma_0 = 100$. As $\hat{H}(\gamma)$ is time independent following the quench, energy is conserved during the dynamics. We choose the final interaction strength after the two quenches such that the postquench energy is the same in both cases.

The statistical description of the dynamics of sufficiently ergodic systems is usually based on the assumption that the energy is the sole integral of motion, such that the equilibrium system is entirely determined by its energy. If this would be the case for our system, the two quenches would lead to the same equilibrium state. However, the dynamics according to the integrable Lieb–Liniger Hamiltonian are strongly constrained by the conserved quantities other than the total energy. By performing two different quenches to the same final Hamiltonian and energy, we investigate the effects of integrability on the postquench evolution of the Lieb–Liniger system.

The conserved energy following the quench is the energy of the system at time $t = 0^+$,

$$E_{\gamma_0\to\gamma} \equiv \langle\psi(0^+)|\hat{H}(\gamma)|\psi(0^+)\rangle = E_{\mathrm{G}}(\gamma_0) + (\gamma-\gamma_0)\frac{dE_{\mathrm{G}}(\gamma)}{d\gamma}\Big|_{\gamma_0} \tag{3.24}$$

where $E_{\mathrm{G}}(\gamma_0)$ is the energy of the ground state $|\psi_0\rangle$ of the initial Hamiltonian $\hat{H}(\gamma_0)$ and we used the well-known result $g_\gamma^{(2)}(0) = n^{-2}N^{-1}dE_{\mathrm{G}}(\gamma)/d\gamma$ [260], which implies that $E_{\gamma_0\to\gamma}$ is given by following the tangent to the curve $E_{\mathrm{G}}(\gamma)$ at γ_0 out to γ. Here, $g_{\gamma_0}^{(2)}(0) \equiv \langle\psi_0|\hat{g}^{(2)}(0)|\psi_0\rangle$ is the local second-order coherence in the initial state. In the case of a quench from the noninteracting ground state ($\gamma_0 = 0$), Eq. (3.24) reduces to the simple expression $E_{0\to\gamma} = (N-1)n^2\gamma$ [166, 194], implying that the energy imparted to the system during the quench diverges as $\gamma\to\infty$ [73]. By contrast, in a quench from the Tonks–Girardeau limit $\gamma_0\to\infty$ to a finite interaction strength γ the final energy is bounded from above, $E_{\infty\to\gamma} \leq E_{\mathrm{G}}(\infty)$, by the ground-state energy of the Tonks–Girardeau gas. Nevertheless, according to Eq. (3.24), a final interaction strength $0 < \gamma^* < 100$ such that $E_{100\to\gamma^*} = E_{0\to\gamma^*}$ does exist.

Here, we consider quenches of $N = 5$ particles, and determine this final interaction strength to machine precision, inferring a value $\gamma^* = 3.7660\ldots$ from numerical solutions for the energy and local second-order coherence of the ground state at finite γ (Sec. 3.4.2). We note that although the overlaps $C_{\{\lambda_j\}}$ of the initial state $|\psi_0\rangle$ with the eigenstates of $\hat{H}(\gamma^*)$ can be calculated analytically in the case of the quench from $\gamma_0 = 0$ [307–309], for the quench from $\gamma_0 = 100$ no closed-form expressions for these quantities are known, and thus their numerical values must be determined using the semi-analytical methodology described in Sec. 3.3.2.

An important summary of the postquench expectation value of an operator [Eq. (3.23)] is provided by the time-averaged value

$$\overline{O} = \lim_{\tau\to\infty}\frac{1}{\tau}\int_0^\tau dt\,\langle\psi(t)|\hat{O}|\psi(t)\rangle. \tag{3.25}$$

Neglecting degeneracies in the spectrum of $\hat{H}(\gamma^*)$ (see discussion in Appendix 3.7.2), such averages are given by the expectation values $\langle\hat{O}\rangle_{\mathrm{DE}} = \mathrm{Tr}\{\hat{\rho}_{\mathrm{DE}}\hat{O}\}$ of operators $\hat{O}$ in the

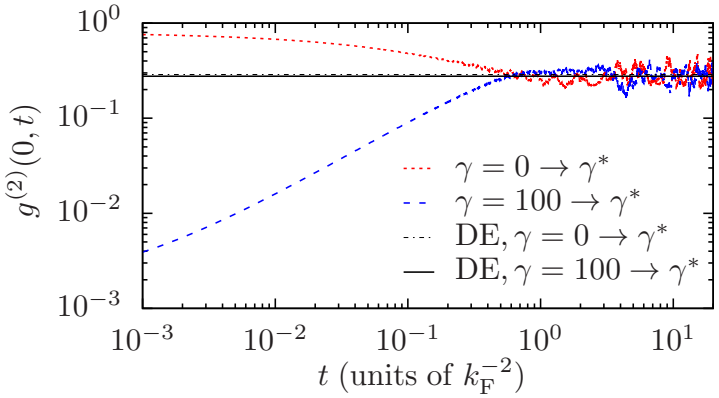

FIGURE 3.4: (Color online) Time evolution of local second-order correlations for $N = 5$ particles following quenches of the interaction strength to a final value $\gamma^* = 3.7660\ldots$ from initial values $\gamma_0 = 0$ (red dotted line) and $\gamma_0 = 100$ (blue dashed line). The horizontal solid (dot-dashed) line indicates the prediction of the diagonal ensemble for $g^{(2)}(0)$ for the quench from $\gamma_0 = 100$ ($\gamma_0 = 0$).

density matrix

$$\hat{\rho}_{\mathrm{DE}} = \sum_{\{\lambda_j\}} |C_{\{\lambda_j\}}|^2 |\{\lambda_j\}\rangle\langle\{\lambda_j\}| \tag{3.26}$$

of the diagonal ensemble [1, 327].

Formally, the sums in Eq. (3.22),(3.23), and (3.26) range over an infinite number of eigenstates $|\{\lambda_j\}\rangle$, and thus the basis over which $|\psi(t)\rangle$ is expanded must be truncated in our numerical calculations. By only including eigenstates with an absolute initial-state overlap $|C_{\{\lambda_j\}}|$ larger than some threshold, we consistently neglect small contributions to correlation functions from weakly occupied eigenstates and minimize the truncation error for a given basis size. We quantify this truncation error by the violations of the normalization and energy sum rules, as we discuss in Appendix 3.7.1.

3.5.1 Evolution of two-body correlations

In Fig. 3.4 we plot the time evolution of the local second-order coherence $g^{(2)}(0,t)$ for $N = 5$ particles following quenches of the interaction strength from initial values $\gamma_0 = 0$ (red dotted line) and $\gamma_0 = 100$ (blue dashed line) to the common final value γ^*. For the quench from the noninteracting initial state ($\gamma_0 = 0$), as time evolves the local second-order coherence decays from its initial value $g^{(2)}(0, t = 0) = 1 - N^{-1}$ before settling down to fluctuate about the diagonal-ensemble expectation value $g^{(2)}_{\mathrm{DE}}(0)$ (horizontal dot-dashed line). This behavior is consistent with results obtained for similar quenches of the interaction strength from zero

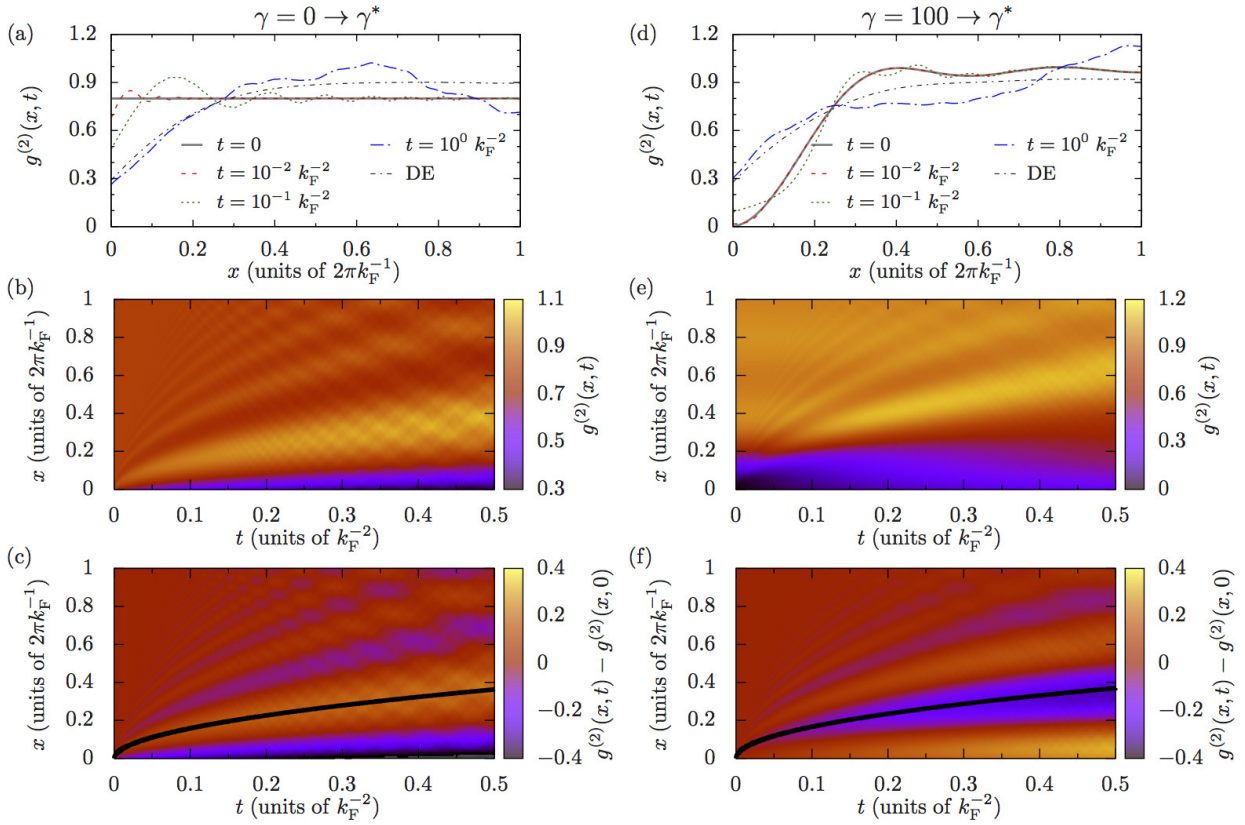

FIGURE 3.5: (Color online) Time evolution of the nonlocal second-order coherence function $g^{(2)}(x,t)$ following quenches of the interaction strength to γ^* from initial values [(a),(b),(c)] $\gamma_0 = 0$ and [(d),(e),(f)] $\gamma_0 = 100$. All data is for $N = 5$ particles. [(a),(d)] Correlation function $g^{(2)}(x,t)$ at four representative times t. Black dot-dashed lines indicate the predictions of the diagonal ensemble for the equilibrium form of this function. [(b),(e)] Evolution of coherence $g^{(2)}(x,t)$ and [(c),(f)] change in coherence $g^{(2)}(x,t) - g^{(2)}(x,t=0)$ for short times $t \leq 0.5k_F^{-2}$. Black lines in (c) and (f) indicate power-law fits to the position $x(t)$ of the first extremum of the correlation wave, which yield $x \propto t^{0.516\pm0.012}$ and $x \propto t^{0.496\pm0.005}$ for quenches from $\gamma_0 = 0$ and $\gamma_0 = 100$, respectively.

to a positive value in Ref. [166]. For the quench from $\gamma_0 = 100$, the value of $g^{(2)}(0)$ in the initial "fermionized" state is $g^{(2)}(0) \approx 10^{-3}$. In this case $g^{(2)}(0,t)$ rises as time progresses, and then exhibits somewhat irregular oscillations about $g^{(2)}_{\rm DE}(0)$ (horizontal solid line). We observe that the decay (growth) of $g^{(2)}(0,t)$ to its diagonal-ensemble value and the onset of irregular oscillations about this value occur on comparable time scales in the two quenches.

We note that the predictions of the diagonal ensemble for the local second-order coherence $g^{(2)}_{\rm DE}(0)$ are very similar for the two quenches, despite the significant difference between the values of $g^{(2)}(0)$ in the two initial states. However, they are clearly distinct — $g^{(2)}_{\rm DE}(0)$ for the quench from the noninteracting state is in fact larger than that for the quench from the correlated state by an amount ≈ 0.0125, demonstrating that the system retains some

memory of its initial state in the long time limit as is expected for an integrable system. We analyze this difference in more detail in Sec. 3.5.3.

We now turn our attention to the time evolution of the full non-local second-order correlation function $g^{(2)}(x,t)$. In Fig. 3.5(a) we show the dependence of $g^{(2)}(x,t)$ on separation x for the quench from the noninteracting initial state at four representative times. [Note that the upper limit $x = 2\pi k_{\mathrm{F}}^{-1}$ of the x axis in Fig. 3.5(a) corresponds to $x = L/2$ in the present case of $N = 5$ particles.] At $t = 0$ (horizontal solid line), the second-order coherence has the constant form of the noninteracting ground state. At short times (e.g., $t = 0.01\, k_{\mathrm{F}}^{-2}$, red dashed line) a minimum in $g^{(2)}(x)$ develops at zero separation, together with the corresponding maximum required by the conservation of $\int_0^L dx\; g^{(2)}(x,t)$ [194]. As time progresses a wave pattern of maxima and minima develops and propagates away from the origin (e.g., $t = 0.1\, k_{\mathrm{F}}^{-2}$, green dotted line). By time $t = 1\, k_{\mathrm{F}}^{-2}$ (blue dot-dashed line), the distinct maxima and minima of $g^{(2)}(x,t)$ have broadened in such a way that they are no longer clearly distinguishable and the correlation function agrees reasonably well with its diagonal-ensemble form (black dot-dashed line) for small separations $x \lesssim 0.25 \times 2\pi k_{\mathrm{F}}^{-1}$. In Fig. 3.5(b) we show the full space and time dependence of $g^{(2)}(x,t)$ following a quench from $\gamma_0 = 0$, which gives a more complete picture of the development of a correlation wave at short length scales and its propagation to larger values of x as time progresses. The correlation wave we observe here is consistent with the results of previous investigations of the dynamics following the sudden introduction of repulsive interactions in an initially noninteracting gas [73, 194, 210, 292, 328].

In Fig. 3.5(d) we plot the spatial form of $g^{(2)}(x,t)$ for the quench from $\gamma_0 = 100$ at the same four representative times considered in Fig. 3.5(a). Despite the obvious distinction that the initial ($t = 0$, solid grey line) correlation function is in the fermionized regime with $g^{(2)}(0) \ll 1$, the behavior of $g^{(2)}(x,t)$ for this quench is qualitatively similar to that observed for the quench from $\gamma_0 = 0$, in that at early times (e.g., $t = 0.01 k_{\mathrm{F}}^{-2}$, red dashed line), deviations from $g^{(2)}(x, t = 0)$ occur only at small separations $x \ll 2\pi k_{\mathrm{F}}^{-1}$. Moreover, as time evolves and $g^{(2)}(0,t)$ increases towards $g^{(2)}_{\mathrm{DE}}(0)$, larger modulations of $g^{(2)}(x,t)$ about its initial functional form develop (e.g., $t = 0.1 k_{\mathrm{F}}^{-2}$, green dotted line). At later times (e.g., $t = 1 k_{\mathrm{F}}^{-2}$, blue dot-dashed line), $g^{(2)}(x,t)$ is close to $g^{(2)}_{\mathrm{DE}}(x)$ at small separations $x \lesssim 0.25 \times 2\pi k_{\mathrm{F}}^{-1}$, but exhibits large excursions away from it at larger x. In Fig. 3.5(e) we

plot the full space and time dependence of $g^{(2)}(x,t)$ following the quench from $\gamma_0 = 100$. Although the behavior of $g^{(2)}(x,t)$ here obviously differs from that following a quench from the noninteracting initial state [Fig. 3.5(b)], with the "fermionic" depression around $x = 0$ lessening rather than growing in magnitude, a similar pattern of propagating correlation waves in $g^{(2)}(x,t)$ can again be seen.

The correlation-wave pattern common to both quenches is more clearly exhibited by the *change* $g^{(2)}(x,t) - g^{(2)}(x,0)$ in the correlation function following the quench, which we plot in Figs. 3.5(c) and 3.5(f). This representation of the postquench second-order coherence of the system reveals a remarkably similar pattern of propagating waves in both cases, although the maxima and minima of the two wave patterns are inverted relative to one another. Fitting a power law to the position $x(t)$ of the first propagating extremum of each of the two correlation waves, we find $x \propto t^{0.516\pm0.012}$ for the quench from $\gamma_0 = 0$ and $x \propto t^{0.496\pm0.005}$ for the quench from $\gamma_0 = 100$, which we indicate by the solid black lines in Figs. 3.5(c) and 3.5(f). These power-law trajectories are consistent with the "telescoping" $x \propto t^{1/2}$ behavior obtained for a quench $\gamma = 0 \to \infty$ in Ref. [73], and for quenches from finite repulsive interactions to the noninteracting limit in Ref. [329] (see also Ref. [72]). The small scale features on top of the main propagating extrema differ for the two quenches, with fast oscillations appearing more pronounced for the quench $\gamma = 0 \to \gamma^*$ in Fig. 3.5(c). Even though hardly visible in Fig. 3.5(f), they are still present for the quench from $\gamma = 100 \to \gamma^*$, but due to the different distribution of overlaps in the final basis compared to the quench from $\gamma_0 = 0$ (cf. Sec. 3.5.3), they contain more high-frequency components and therefore the fine structure differs.

3.5.2 Time-averaged correlations

We now compare the time-averaged second-order correlation functions following the two quenches with the form of this function that would be obtained if, following the quench, the system relaxed to thermal equilibrium. As in Ref. [166] we make use of the canonical ensemble, for which the density matrix is given by

$$\hat{\rho}_{\mathrm{CE}} = Z_{\mathrm{CE}}^{-1} \sum_{\{\lambda_j\}} \mathrm{e}^{-\beta E_{\{\lambda_j\}}} \, |\{\lambda_j\}\rangle\langle\{\lambda_j\}|, \tag{3.27}$$

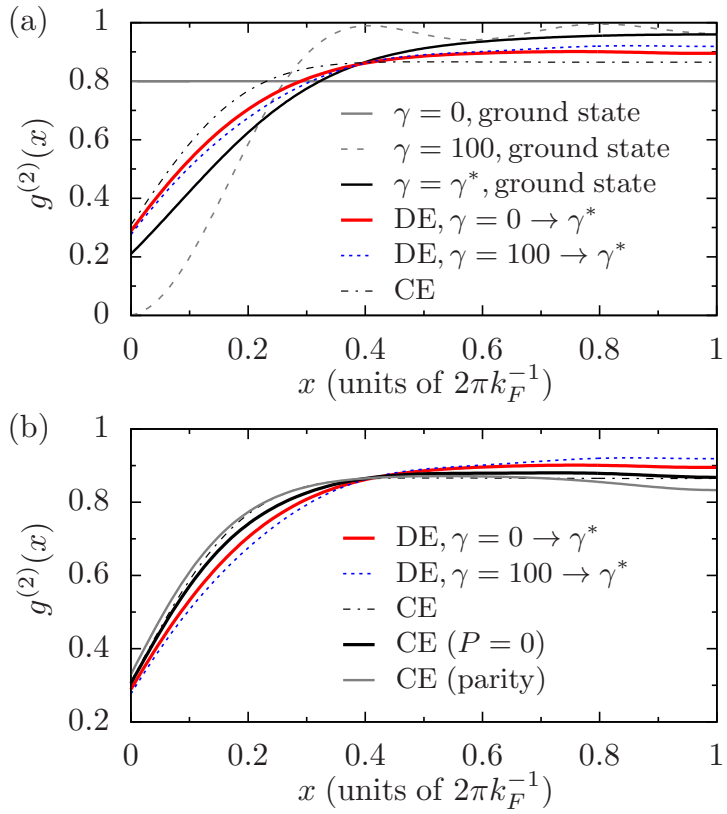

FIGURE 3.6: (Color online) Time-averaged second-order correlation functions following quenches of the interaction strength to $\gamma^* = 3.7660\ldots$ from initial values $\gamma_0 = 0$ (red solid line) and $\gamma_0 = 100$ (blue dotted line). Results are for $N = 5$ particles. (a) The correlation functions $g^{(2)}(x)$ in the initial states with $\gamma_0 = 0$ (horizontal solid line) and $\gamma_0 = 100$ (grey dashed line), as well as for the ground state at $\gamma = \gamma^*$ (solid black line) are also indicated for comparison. The black dot-dashed line corresponds to the thermal value of the correlation function following relaxation, as predicted by the canonical ensemble (see text). (b) Comparison of the time-averaged second order correlation functions to the various ensembles defined in the text: The standard canonical ensemble (black dot-dashed line), the canonical ensemble restricted to zero-momentum eigenstates (black solid line), and the canonical ensemble restricted to parity-invariant states (grey solid line).

where the partition function $Z_{\mathrm{CE}} = \sum_{\{\lambda_j\}} \exp(-\beta E_{\{\lambda_j\}})$. The inverse temperature β is determined implicitly by fixing the mean energy in the state $\hat{\rho}_{\mathrm{CE}}$ to the common postquench energy, i.e., $\mathrm{Tr}\{\hat{\rho}_{\mathrm{CE}} \hat{H}(\gamma^*)\} = E_{0\to\gamma^*}$. The sum in Eq. (3.27), like that in Eq. (3.26), formally ranges over an infinite number of eigenstates. We therefore truncate this sum by applying a cutoff in energy, as described in Appendix 3.7.1.

In Fig. 3.6(a) we plot the second-order correlation function $g^{(2)}_{\mathrm{CE}}(x) = \mathrm{Tr}\{\hat{\rho}_{\mathrm{CE}}\, \hat{g}^{(2)}(0,x)\}$ in the canonical ensemble (black dot-dashed line), along with the diagonal-ensemble predictions $g^{(2)}_{\mathrm{DE}}(x)$ for the quenches from $\gamma_0 = 0$ (red solid line) and from $\gamma_0 = 100$ (blue dotted line). For comparison we also plot the correlation functions in the initial states with $\gamma_0 = 0$

(horizontal line), $\gamma_0 = 100$ (grey dashed line), as well as the ground state for $\gamma = \gamma^*$ (solid black line). For the quench from $\gamma_0 = 0$, the time-averaged value $g^{(2)}_{\mathrm{DE}}(0)$ is smaller than the corresponding thermal value $g^{(2)}_{\mathrm{CE}}(0)$, consistent with the results of Refs. [7, 166, 204]. In fact $g^{(2)}_{\mathrm{DE}}(x)$ is suppressed below $g^{(2)}_{\mathrm{CE}}(x)$ over a range of separations $x \lesssim 0.4 \times 2\pi k_{\mathrm{F}}^{-1}$. Correspondingly, $g^{(2)}_{\mathrm{DE}}(x) > g^{(2)}_{\mathrm{CE}}(x)$ at larger separations x due to particle number and momentum conservation. For the quench $\gamma = 100 \to \gamma^*$, the diagonal-ensemble coherence function $g^{(2)}_{\mathrm{DE}}(x)$ is similar in shape to that of the quench from $\gamma_0 = 0$. However, it is somewhat smaller at $x = 0$, and correspondingly larger at large x. This indicates some memory of the initial state preserved by the dynamics of the integrable Lieb–Liniger system [62, 303]. Despite these differences, on the whole both functions $g^{(2)}_{\mathrm{DE}}(x)$ are comparable to $g^{(2)}_{\mathrm{CE}}(x)$ (cf. also Ref. [194]). We note, however, that they are also both reasonably close to the ground state result for $g^{(2)}(x)$ at interaction strength γ^* (solid black line), although the local value $g^{(2)}_{\mathrm{DE}}(0)$ for both quenches is much closer to the thermal value than the ground state value.

Since the system is in its ground state before the quench for both $\gamma_0 = 0$ and $\gamma_0 = 100$, and the total momentum operator $\hat{P}$ commutes with the Hamiltonian, the postquench states at γ^* only have support on eigenstates with total momentum $P = 0$. Furthermore, the spatially structureless initial state at $\gamma_0 = 0$ implies additional parity-invariance ($\{\lambda_j\} = \{-\lambda_j\}$) in Bethe rapidity space for the postquench eigenstates [307–309]. Thus an interesting question to ask is if we constructed a canonical density matrix (3.27) restricted to $P = 0$ states, or one further restricted to parity-invariant states (which are a subset of the $P = 0$ states), would these yield better agreement with the diagonal ensemble predictions for the quenches? We have performed these constructions with the temperature in both cases fixed via the postquench energy in the same way as for the canonical ensemble, cf. Eq. (3.27) and the following text.

In Fig. 3.6(b), we plot the resulting second-order correlation function $g^{(2)}_{\mathrm{CE}}(x) = \mathrm{Tr}\{\hat{\rho}_{\mathrm{CE}}\, \hat{g}^{(2)}(0, x)\}$ for the standard canonical ensemble (black dot-dashed line), as well as in the restricted $P = 0$ ensemble (solid black line), and the parity-invariant ensemble (solid grey line). We also include the diagonal-ensemble predictions $g^{(2)}_{\mathrm{DE}}(x)$ for the quenches from $\gamma_0 = 0$ (red solid line) and from $\gamma_0 = 100$ (blue dotted line). It can be seen that the restricted ensembles give results for the correlation function that are quite close to the standard canonical ensemble,

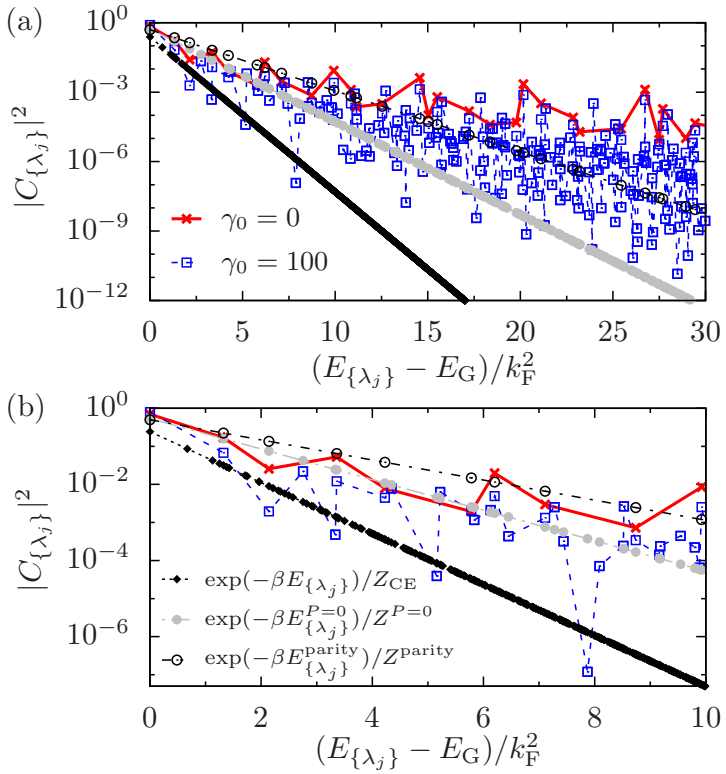

FIGURE 3.7: (Color online) (a) Populations $|C_{\{\lambda_j\}}|^2$ of eigenstates with energies $E_{\{\lambda_j\}}$ following quenches to $\gamma^* = 3.7660\ldots$ from $\gamma_0 = 0$ (red crosses) and $\gamma_0 = 100$ (blue squares). Note that the y-axis is plotted on a logarithmic scale. For the quench from $\gamma_0 = 100$, additional non-parity-invariant states appear in degenerate, parity-conjugate pairs and since their contributions is identical, the points lie on top of each other. The black dotted line with filled black circles represents the populations $\exp(-\beta E_{\{\lambda_j\}})/Z_{CE}$ of eigenstates with energies $E_{\{\lambda_j\}}$ for the canonical ensemble. The grey line with grey filled circles, and the black dashed line with empty black circles are the corresponding results for the $P = 0$ restricted ensemble, and the parity-restricted ensemble, respectively. (b) Low-energy part of (a).

and are no closer to the diagonal ensemble results.

3.5.3 Contributions to relaxed correlation functions

The relaxation of the nonlocal correlations $g^{(2)}(x,t)$ takes place on a similar time scale to that of the local coherence $g^{(2)}(0,t)$ for both of the quenches considered here. This should be contrasted with, e.g., the behavior following a quench from the noninteracting limit to $\gamma = 100$ reported in Ref. [166], in which $g^{(2)}(0,t)$ decays rapidly and the development and propagation of correlation waves occurs over a significantly longer time scale. We identify the absence of a significant separation of the time scales of local and nonlocal evolution here as a consequence of the fact that only a small number of eigenstates contribute significantly

to the postquench dynamics (cf. Ref. [166] and references therein). Indeed, we find that the purity $\Gamma_{\mathrm{DE}} \equiv \mathrm{Tr}\{(\hat{\rho}_{\mathrm{DE}})^2\}$ of the diagonal-ensemble density matrix takes values ≈ 0.52 for the quench $\gamma = 0 \to \gamma^*$ and ≈ 0.63 for the quench $\gamma = 100 \to \gamma^*$, indicating rather weak participation of the eigenstates $|\{\lambda_j\}\rangle$ in the dynamics. The difference in the purities can largely be attributed to the somewhat greater occupation of the ground state of $\hat{H}(\gamma^*)$ following the quench from the $\gamma = 100$ initial state.

To further illustrate the difference in the final states, in Fig. 3.7 we plot the occupations of eigenstates with energy $E_{\{\lambda_j\}}$ for the quenches from $\gamma_0 = 0$ (red crosses) and $\gamma_0 = 100$ (blue squares). For the quench from $\gamma_0 = 100$, significantly more eigenstates have occupations above a given threshold than in the case of $\gamma_0 = 0$, resulting in a much larger basis size in this case. However, the occupation of the ground state of $\hat{H}(\gamma^*)$ is somewhat larger for the quench from $\gamma_0 = 100$ than for $\gamma_0 = 0$, and the low-lying excited states are comparatively weakly occupied for $\gamma_0 = 100$, cf. Fig. 3.7(b). This result is reasonably intuitive, as the ground state for $\gamma = \gamma^*$ is moderately correlated, and will be more similar to the $\gamma = 100$ than the $\gamma = 0$ ground state. The distribution of normalization over eigenstates $|\{\lambda_j\}\rangle$ is thus more sharply "localized" on the ground state in this case, resulting in the somewhat larger value of the purity Γ_{DE} following this quench.

For comparison, we also plot the occupations of the three ensembles introduced in Sec. 3.5.2 in Fig. 3.7. The restrictions lead to a reduction in available eigenstates for any given energy-window, and correspondingly the temperature of the canonical ensemble is smaller than that of the $P = 0$ ensemble, which is in turn smaller than that of the parity-invariant ensemble. The occupations of eigenstates for the quench from $\gamma_0 = 0$ (red crosses) and from $\gamma_0 = 100$ (blue squares) are suggestive of power-law decay at high energies. For small energies on the other hand, Fig. 3.7(b) shows that the functional form is not incompatible with exponential decay.

3.6 Conclusions

We have described a method to calculate matrix elements between eigenstates of the Lieb–Liniger model of one-dimensional delta-interacting bosons. This method is based on the coordinate Bethe ansatz, which generates a complete set of energy eigenfunctions for any

fixed coupling strength. This allows us to obtain overlaps between eigenstates of different Hamiltonians, as well as expressions for correlation functions. By introducing periodic boundary conditions, we obtained expressions amenable to numerical evaluation. We applied our methodology to the evaluation of first-, second-, third-, and fourth-order correlation functions in the ground state of the Lieb–Liniger model for various values of the interparticle interaction strength. Our results indicate that although the correlations of the system are in general distorted by the small system size, finite-size effects become increasingly less significant with increasing interaction strength and decreasing spatial separation.

Out of equilibrium, we investigated the dynamics of relaxation after a quantum quench of the interparticle interaction strength towards a non-thermal steady state. Starting from two different initial states, we quenched to a common final interaction strength γ^* chosen in such a way that both postquench energies were the same. Our calculations reveal a similar relaxation process for the second-order coherence $g^{(2)}(x,t)$ for both initial states: the build-up of correlations on short interparticle distances and their propagation through the system as time progresses. The time-averaged second-order correlation functions in both cases disagreed with the prediction for thermal equilibrium and were biased, relative to one another, towards their pre-quench forms — an intuitive result given the integrability of the system. In the future it would be interesting to study quenches from other initial states with the same final energy to explore how the memory of the initial state is manifest in different situations.

Although our method is restricted to small system sizes due to computational complexity and here only applied to five particles out of equilibrium, we were able to obtain the dynamical evolution as well as time-averaged correlation functions to high precision. Finally we note that the evaluation of matrix elements of the Lieb–Liniger model with this method is not restricted to real-valued Bethe rapidities, opening the door to investigating the nonequilibrium dynamics of attractively interacting systems (where the rapidities become complex-valued) and that following quenches from more complex initial states.

3.7 Supplement

3.7.1 Basis-set truncation

The Hilbert space of the Lieb–Liniger model is infinite dimensional, and therefore the sums in Eqs. (3.22), (3.23), and (3.26) must be truncated for numerical purposes. Here, we provide details of the truncation scheme for the two different initial states we considered in Sec. 3.5, and explain how we quantify the error resulting from this truncation.

For the quench from $\gamma_0 = 0$, the initial state $|\psi_0\rangle$ only has nonzero overlap with eigenstates $|\{\lambda_j\}\rangle$ of $\hat{H}(\gamma^*)$ that are parity invariant (i.e., eigenstates for which $\{\lambda_j\} = \{-\lambda_j\}$) and, *a fortiori*, have zero total momentum P [325]. The strongly-correlated initial state of the quench from $\gamma_0 = 100$ similarly has zero overlap with eigenstates $|\{\lambda_j\}\rangle$ with nonzero total momentum, but in this case states contributing to $|\psi(t)\rangle$, and thus $\hat{\rho}_{\mathrm{DE}}$, need not be parity-invariant in general. For $\gamma_0 = 0$ our results for the overlaps agree with recently obtained analytical expressions [308, 309], which predict real positive overlaps, given the phase convention implicit in Eq. (3.2), for quenches to $\gamma > 0$. For $\gamma_0 = 100$, we find that the overlaps are still real, but are no longer restricted to positive values.

We briefly summarize our procedure to determine the cutoff here — see Appendix A of Ref. [166] for an extended discussion for the case of parity-invariant states. It can be shown [219] that the solutions $\{\lambda_j\}$ of the Bethe equations (3.3) are in one-to-one correspondence with the numbers m_j that appear in Eq. (3.3). This allows us to uniquely label states by the set $\{m_j\}$. Without loss of generality, we order the numbers m_j such that $m_1 > m_2 > \cdots > m_{N-1} > m_N$, and we only need consider states for which $\sum_j m_j = 0$, corresponding to zero total momentum P. We specialize hereafter to the case $N = 5$, which is the largest N for which we consider the dynamics in this article. The states can be grouped into families, labelled by m_1. We have found empirically that within each such family, the eigenstate $(m_1, 1, 0, -1, -m_1)$ has the largest absolute overlap $|\langle\{\lambda_j\}|\psi_0\rangle|$ with the initial state, for both initial states we consider ($\gamma_0 = 0$ and $\gamma_0 = 100$). Furthermore, this overlap is larger than that of the most significantly contributing eigenstate $(m_1 + 1, 1, 0, -1, -m_1 - 1)$ of the following family $(m_1 + 1)$. We therefore construct the basis by considering in turn each family m_1 and including all states within that family for which the overlap with the initial state exceeds our chosen threshold value $C_{\min}$. Eventually, for some value of m_1, even

the eigenstate $(m_1, 1, 0, -1, -m_1)$ has overlap with $|\psi_0\rangle$ smaller than the threshold, at which point all states that meet the threshold have been accounted for.

We note that the Lieb–Liniger model has an infinite number of conserved charges $[\hat{Q}^{(m)}, \hat{H}(\gamma)] = 0$; $m = 0, 1, 2, \ldots$, with eigenvalues given by $\hat{Q}^{(m)}|\{\lambda_j\}\rangle = \sum_{l=1}^{N} \lambda_l^m |\{\lambda_j\}\rangle$. However, for a quench from $\gamma_0 = 0$ their expectation values in the diagonal ensemble $\langle \hat{Q}^{(m)} \rangle_{\mathrm{DE}}$ diverge for all even $m \geq 4$ [308, 309]. Our numerical results suggest that this is also the case for quenches from $\gamma_0 > 0$ (indeed, they diverge for almost all states but eigenstates [330, 331]). For all odd values m, the expectation values of the corresponding conserved charges $\hat{Q}^{(m)}$ are identically zero for our initial states and quench protocol. Thus, the only nontrivial and regular conserved quantities are the particle number ($m = 0$) and energy ($m = 2$). As in Ref. [166], we quantify the saturation of the normalization and energy sum rules by the sum-rule violations

$$\Delta N = 1 - \sum_{\{\lambda_j\}} |C_{\{\lambda_j\}}|^2, \tag{3.28}$$

$$\Delta E = 1 - \frac{1}{E_{\gamma_0 \to \gamma}} \sum_{\{\lambda_j\}} |C_{\{\lambda_j\}}|^2 \sum_{l=1}^{N} (\lambda_l)^2, \tag{3.29}$$

respectively, where $E_{\gamma_0 \to \gamma}$ is the exact postquench energy [Eq. (3.24)]. We note that the calculation of time-dependent observables involves a double sum over $\{\lambda_j\}$, and is therefore more numerically demanding than the calculation of expectation values in the DE. Moreover, the calculation of the local coherence $g^{(2)}(0, t)$ is much less demanding than that of the full nonlocal $g^{(2)}(x, t)$. We therefore use different thresholds C_{min}, resulting in different basis sizes and sum-rule violations, in the calculation of $g^{(2)}(0, t)$, $g^{(2)}(x, t)$, and $g^{(2)}_{\mathrm{DE}}(x)$, as indicated in Table 3.1. We note that the energy sum rule is in general less well satisfied than the normalization sum rule, due to the $\propto \lambda^{-4}$ tail of the diagonal-ensemble distribution of eigenstates [166]. We find also that both sum rules are less well satisfied for the quench $\gamma = 100 \to \gamma^*$, despite the truncation procedure described above resulting in more than five times as many basis states being employed in its solution than are used in the quench $\gamma = 0 \to \gamma^*$.

For expectation values in the CE [Eq. (3.27)], we truncate the basis by retaining all states with energies below some cutoff E_{cut}. The inverse temperature β is then chosen to minimize

TABLE 3.1: Basis-set sizes and sum-rule violations for full non-local, time-evolving second-order coherence $g^{(2)}(x,t)$, for local, time-evolving second-order coherence $g^{(2)}(x=0,t)$, and for time-averaged second-order coherence $g^{(2)}_{\mathrm{DE}}(x)$ following quenches from $\gamma_0 = 0$, and $\gamma_0 = 100$ to $\gamma^* = 3.7660\ldots$.

γ_0	Type[a]	$C_{\min}$	No. states	ΔN	$\Delta E/k_{\mathrm{F}}^2$
0	$g^{(2)}(x,t)$	5×10^{-5}	673	7×10^{-7}	6×10^{-3}
0	$g^{(2)}(0,t)$	1×10^{-5}	1704	7×10^{-8}	3×10^{-3}
0	$g^{(2)}_{\mathrm{DE}}(x)$	1×10^{-6}	6282	2×10^{-9}	8×10^{-4}
100	$g^{(2)}(x,t)$	5×10^{-5}	3704	4×10^{-6}	4×10^{-2}
100	$g^{(2)}(0,t)$	1×10^{-5}	10473	5×10^{-7}	3×10^{-2}
100	$g^{(2)}_{\mathrm{DE}}(x)$	1×10^{-6}	43918	2×10^{-8}	2×10^{-3}

[a] Occupations of the $g^{(2)}_{\mathrm{DE}}(x)$ basis set are used in the calculation of Γ_{DE} (Sec. 3.5.3).

the energy sum-rule violation ΔE. The normalization sum rule is fulfilled by construction. Since all states (not only those with zero momentum) contribute to this sum, the number of eigenstates involved in canonical-ensemble calculations is much larger than that in diagonal-ensemble calculations. For the canonical-ensemble correlation function plotted in Fig. 3.6 we used an energy cutoff of $3.2\times10^2\,k_{\mathrm{F}}^2$, which yields a basis of 2.1×10^6 eigenstates $|\{\lambda_j\}\rangle$. We checked that this cutoff is sufficiently large to ensure saturation of $g^{(2)}_{\mathrm{CE}}(x)$ (Fig. 3.6). For the ensemble restricted to $P=0$ eigenstates [Fig. 3.6(b)], we used an energy cut-off of $6.4\times10^5\,k_{\mathrm{F}}^2$, corresponding to 44530 eigenstates, while for the parity-invariant ensemble we used an energy cut-off of $8.5\times10^6\,k_{\mathrm{F}}^2$, corresponding to 64204 eigenstates.

3.7.2 Time-averaged correlation functions and the diagonal ensemble

The time-averaged expectation value [Eq. (3.25)] of an operator $\hat{O}$ can be expressed as an expectation $\overline{O} = \mathrm{Tr}\{\overline{\hat{\rho}}\,\hat{O}\}$ in the time-averaged density matrix

$$\begin{aligned}\overline{\hat{\rho}} &\equiv \lim_{\tau\to\infty}\frac{1}{\tau}\int_0^\tau dt\,|\psi(t)\rangle\langle\psi(t)| \\ &= \sum_{\{\lambda_j\}}|C_{\{\lambda_j\}}|^2|\{\lambda_j\}\rangle\langle\{\lambda_j\}| + \sum_{\{\lambda_j\}\neq\{\lambda'_j\}}\delta_{E_{\{\lambda_j\}},E_{\{\lambda'_j\}}}C^*_{\{\lambda'_j\}}C_{\{\lambda_j\}}|\{\lambda_j\}\rangle\langle\{\lambda'_j\}|\,. \end{aligned} \tag{3.30}$$

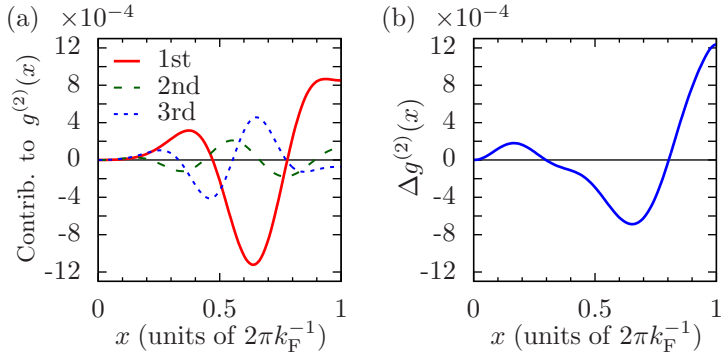

FIGURE 3.8: (Color online) Contributions of degenerate energy eigenstates to the time-averaged second-order correlation function following a quench from $\gamma_0 = 100$ to $\gamma^* = 3.7660\ldots$ for $N = 5$ particles. (a) Contributions $C_{\{\lambda_j\}}C^*_{\{-\lambda_j\}}\langle\{-\lambda_j\}|\hat{g}^{(2)}(0,x)|\{\lambda_j\}\rangle + \text{c.c.}$ of off-diagonal matrix elements corresponding to the three largest weights $C_{\{\lambda_j\}}C^*_{\{-\lambda_j\}}$. (b) Total contribution of degenerate energy eigenstates.

The first term in Eq. (3.30) is simply the diagonal-ensemble density matrix $\hat{\rho}_{\text{DE}}$ [Eq. (3.26)], to which $\overline{\hat{\rho}}$ reduces in the absence of degeneracies in the spectrum of $\hat{H}(\gamma)$. This is the case for the quench from $\gamma_0 = 0$, as the only eigenstates of $\hat{H}(\gamma^*)$ with nonvanishing overlaps with $|\psi_0\rangle$ in this case are the parity-invariant states $|\{\lambda_j\}\rangle$ with $\{\lambda_j\}=\{-\lambda_j\}$, which are nondegenerate (see Ref. [166] and references therein). By contrast, in a quench from $\gamma_0 > 0$, $|\psi(t)\rangle$ has support on non-parity-invariant states $|\{\lambda_j\}\rangle$, which are degenerate with their parity conjugates $|\{-\lambda_j\}\rangle$.

In general such degeneracies can have observable consequences for time-averaged expectation values [327]. However, as can be seen from Fig. 3.8, the correction to $g^{(2)}_{\text{DE}}(x)$ due to the contributions of degenerate eigenstates in the case of the quench from $\gamma_0 = 100$ is small. It is straightforward to show that the elements $\langle\{-\lambda_j\}|\hat{g}^{(2)}(0)|\{\lambda_j\}\rangle$ of the local second-order coherence between parity-conjugate states must vanish due to symmetry considerations. At larger separations x, the matrix elements between these pairs of states are nonzero, as illustrated in Fig. 3.8(a). However, these contributions are small compared to the diagonal-ensemble result $g^{(2)}_{\text{DE}}(x)$, and indeed the total contribution of all parity-conjugate states in our finite-basis description [Fig. 3.8(b)] would yield a barely visible correction to the function $g^{(2)}_{\text{DE}}(x)$ plotted in Fig. 3.6. We note also that the substitution of $\hat{\rho}_{\text{DE}}$ for the time-averaged density matrix $\overline{\hat{\rho}}$ introduces negligible error in the calculation of the purity of this matrix (Sec. 3.5.3).

4

Relaxation dynamics of the Lieb–Liniger gas following an interaction quench: A coordinate Bethe-ansatz analysis

In this chapter, we focus on the interaction quench scenario introduced in Chapter 3 in more detail. Starting from the ideal gas ground state, we investigate the temporal evolution of the system for several representative postquench interaction strengths and relate the relaxation dynamics of certain nonlocal correlation functions to the relaxation of the system via dephasing of the many-body energy eigenstates (cf. Fig. 1.1). We also consider the relaxation time-scales for local and nonlocal quantities, for which a unified theoretical framework has not been developed yet. In order to see if we can extract predictions for physical quantities beyond the small system sizes we consider, we perform a finite-size scaling analysis for relaxed correlation functions.

This is a verbatim reproduction of a publication, reprinted with permission from Physical Review A **91**, 023611 (2015) [166].

4.1 Abstract

We investigate the relaxation dynamics of the integrable Lieb–Liniger model of contact-interacting bosons in one dimension following a sudden quench of the collisional interaction strength. The system is initially prepared in its noninteracting ground state and the interaction strength is then abruptly switched to a positive value, corresponding to repulsive interactions between the bosons. We calculate equal-time correlation functions of the nonequilibrium Bose field for small systems of up to five particles via symbolic evaluation of coordinate Bethe-ansatz expressions for operator matrix elements between Lieb–Liniger eigenstates. We characterize the relaxation of the system by comparing the time-evolving correlation functions following the quench to the equilibrium correlations predicted by the diagonal ensemble and relate the behavior of these correlations to that of the quantum fidelity between the many-body wave function and the initial state of the system. Our results for the asymptotic scaling of local second-order correlations with increasing interaction strength agree with the predictions of recent generalized thermodynamic Bethe-ansatz calculations. By contrast, third-order correlations obtained within our approach exhibit a markedly different power-law dependence on the interaction strength as the Tonks–Girardeau limit of infinitely strong interactions is approached.

4.2 Introduction

Experiments in ultracold atomic physics offer the opportunity to study many-body quantum systems that are well isolated from their environment and exhibit dynamical evolution on observable time scales. Moreover, the excellent control of trapping geometries now attainable in experiments allows for the near-direct realization of idealized models of condensed-matter systems [99]. In particular, experiments on degenerate Bose gases in quasi-one-dimensional trapping geometries approach the conditions assumed in the Lieb–Liniger (LL) model [56, 231] of indistinguishable bosons in one dimension (1D) interacting via a point

interparticle potential [176, 311, 332, 333]. The LL model plays an important role in the literature as a comparatively transparent, prototypical example of the class of quantum integrable models [55, 207], which admit formal solutions in terms of the Bethe ansatz [212]. Experimental investigations of nonequilibrium dynamics with ultracold atoms have demonstrated the breakdown of conventional thermalization in quasi-1D Bose gases [2, 39, 95, 96]. These observations have fueled a rapidly growing program of theoretical research into the role of conservation laws in constraining the nonequilibrium dynamics of integrable systems in particular and the mechanisms of relaxation and origins of thermal equilibrium in isolated quantum systems in general [18, 19, 64].

Theoretical works on the relaxation of integrable quantum systems initially focused on the class of spin chains and other interacting 1D systems that can be solved by a Jordan-Wigner transformation [66] to a system of noninteracting fermions [62, 70, 71, 74–76, 80, 286–290, 334–338]. More recently, workers in this area have focused increasingly on the nonequilibrium dynamics and relaxation of the more general class of integrable quantum systems (such as the LL model) that can be solved by Bethe ansatz [212] but do not admit a mapping to noninteracting degrees of freedom [209, 211, 294–302, 339–346]. The quantum quench consisting of an abrupt change of the interparticle interaction strength of the LL model has recently emerged as an important test bed for theories of relaxation of such systems. Such a scenario may be realized experimentally by making use of confinement-induced resonances [176, 178, 347]. In this article we undertake calculations within the coordinate Bethe-ansatz formalism to investigate the dynamics following a quench of the interaction strength in small LL systems of at most five particles.

Results for the relaxation dynamics of the LL model following an interaction-strength quench have previously been obtained in the limiting cases of quenches to the noninteracting limit [72, 329] and to the opposite Tonks–Girardeau (TG) limit of infinitely strong interactions [73, 205, 210, 348], where the dynamics are governed by free-particle propagation. For quenches to finite interaction strengths, the relaxation dynamics have been investigated using a range of techniques, including exact diagonalization within a truncated momentum-mode basis [285], quasiexact numerical simulations of lattice discretizations of the model [194, 292], and nonperturbative approximations derived using functional-integral

techniques [294–297]. [1] A finite-size scaling analysis [349] of expectation values in energy eigenstates of the LL model indicated that the eigenstate thermalization hypothesis [1, 24, 25] holds for this model in the weak sense [350] only, implying the absence of thermalization following a quench. A recently proposed generalization of the thermodynamic Bethe ansatz (TBA) [351, 352] was used in Ref. [7] to obtain the predictions of the nonthermal generalized Gibbs ensemble (GGE) [60–62] for the relaxed state following an interaction-strength quench. This generalized TBA also forms the basis for the so-called quench-action variational approach [202, 303], which was used in Ref. [8] to predict the dynamical evolution of correlation functions following such a quench. We note also studies of related nonequilibrium scenarios such as a quench to the so-called super-Tonks regime [179, 216] of strong attractive interactions [195, 218] and a coherent splitting [96] of the LL gas [327]. In higher dimensionalities, interaction quenches of Bose systems have been investigated within Bogoliubov-based [293, 328, 353–356] theoretical descriptions, motivated in part by recent experiments on interaction-strength quenches in 2D [357] and 3D [358] Bose gases.

In this article we undertake calculations within the coordinate Bethe-ansatz formalism to characterize the dynamics of the LL model following an interaction-strength quench. Our methodology is based on the symbolic evaluation of overlaps and matrix elements between LL eigenstates in terms of the rapidities that label them. The rapidities themselves are obtained by numerical solution of the appropriate Bethe equations. Computational expense limits our calculations to small particle numbers $N \leq 5$. However, our approach in terms of the exact eigenstates of the LL Hamiltonian explicitly respects the integrability of the model, in contrast to works that make use of lattice discretizations [194, 292] of the LL Hamiltonian or explicit momentum-space cutoffs [285]. Moreover, our approach allows us to calculate infinite-time averages of observables, i.e., expectation values in the so-called diagonal ensemble (DE) [1], in contrast to quasiexact numerical schemes that can only follow the relaxation dynamics for short time periods [194, 292].

We observe clear signs of relaxation of the system to the DE in our results for dynamically evolving correlation functions, even for the small system sizes we consider. In partic-

[1] References [294–297] consider a Gaussian correlated initial state characterized by an occupation number distribution over (single-particle) momentum modes. This corresponds to an incoherent mixture of the ground and excited energy eigenstates of the ideal Bose gas.

ular, we calculate the time evolution of the momentum distribution of the Bose gas, which is not easily accessible within other Bethe-ansatz-based approaches [73], and find results qualitatively consistent with the results of functional-integral calculations of the relaxation dynamics [294–297]. [1] Our results for the second-order coherence function reveal the propagation of correlation waves, as previously observed in simulations of quenches within lattice discretizations of the LL model [194, 292] and quenches to the TG limit [73, 210]. Our numerical approach in terms of the N-particle energy eigenstates of the LL Hamiltonian also allows us to calculate the quantum fidelity between the time-evolved state of the system following the quench and the initial state, which decays over time as the eigenstate dephasing that underlies the relaxation dynamics [1] takes place. We find, in particular, that the behavior of this fidelity is qualitatively similar to that of nonlocal quantities such as the occupation of the zero-momentum single-particle mode, indicating that these experimentally relevant quantities provide effective probes of the eigenstate dephasing of the N-body system.

Our results for correlation functions in the DE are complementary both to exact analytic results for the stationary-state correlations following a quench to the TG limit [73] and to the predictions of generalized thermodynamic ensembles for the equilibrium correlations following quenches to finite interaction strengths [7, 8]. For large interaction strengths, our results for the momentum distribution and static structure factor appear to be approaching the known TG-limit results [73]. Moreover, our results for second-order correlations in the DE corroborate the predictions of Refs. [7, 8] for the generalized equilibrium state of the system. In particular, our DE results for local second-order correlations are consistent with the power-law scaling with interaction strength predicted by Refs. [7, 8]. By contrast, however, we find that the power law with which local third-order correlations in the DE scale with interaction strength is markedly different from that predicted by these previous works, suggesting that further investigation of these correlations is necessary.

This article is organized as follows. Section 4.3 contains a brief review of the LL model and the coordinate Bethe-ansatz approach to its solution, and outlines our methodology for the calculation of correlation functions within this formalism. In Sec. 4.4 we present results on the time evolution of dynamical correlation functions following a quench of the interaction strength from the noninteracting limit to a finite repulsive value. Section 4.5

compares the relaxed-state correlation functions, as described by the DE, to the predictions of conventional statistical mechanics and other theoretical approaches to the interaction-strength quench scenario. In Sec. 4.6 we summarize our results and present our conclusions.

4.3 Methodology

4.3.1 Lieb–Liniger model eigenstates

The LL model [56, 231] describes a system of N indistinguishable bosons subject to a delta-function pairwise interparticle interaction potential in a periodic 1D geometry. In this article we work in units such that $\hbar = 1$ and the particle mass $m = 1/2$, and so the first-quantized Hamiltonian for this system can be written

$$\hat{H} = -\sum_{i=1}^{N} \frac{\partial^2}{\partial x_i^2} + 2c \sum_{i<j}^{N} \delta(x_i - x_j), \tag{4.1}$$

where c is the interaction strength. Hereafter, we restrict our attention to the case of non-negative interaction strengths $c \geq 0$. The solution of Hamiltonian (4.1) by Bethe ansatz was first described by Lieb and Liniger [56, 231], and a detailed discussion of this approach can be found in Ref. [207]. For the reader's convenience, we provide a brief review of the method here.

Due to the symmetry of the Bose wave function $\psi(\{x_i\})$ under the exchange of particle labels, it is (irrespective of the boundary conditions of the geometry) completely determined by its form on the fundamental permutation sector,

$$\mathcal{R}: \quad x_1 \leq x_2 \leq \cdots \leq x_{N-1} \leq x_N, \tag{4.2}$$

of the configuration space. Where all coordinates x_j are distinct, the interaction term in Hamiltonian (4.1) vanishes and the corresponding Schrödinger equation is that of a system of free particles. Where two coordinates x_j and x_{j+1} coincide, the delta-function interaction

potential can be recast as a boundary condition,

$$\left[\left(\frac{\partial}{\partial x_{j+1}} - \frac{\partial}{\partial x_j}\right) - c\right]_{x_{j+1}=x_j} \psi(\{x_i\}) = 0, \tag{4.3}$$

on the spatial derivatives of the wave function. The solution then proceeds by the substitution of the unnormalized ansatz (valid on $\mathcal{R}$ only)

$$\psi(\{x_i\}) = \sum_{\sigma} a(\sigma) \exp\Big[i \sum_{m=1}^{N} x_m \lambda_{\sigma(m)}\Big] , \tag{4.4}$$

where $\sum_\sigma$ denotes a sum over all $N!$ permutations $\sigma = \{\sigma(j)\}$ of $\{1, 2, \ldots, N\}$. Demanding that $\psi(\{x_i\})$ be an eigensolution of the Schrödinger equation corresponding to Hamiltonian (4.1) then yields the general expression

$$a(\sigma) = \prod_{k>l} \left(1 - \frac{ic}{\lambda_{\sigma(k)} - \lambda_{\sigma(l)}}\right) \tag{4.5}$$

for the phase factors $a(\sigma)$ that encode the effects of interactions between the particles. The quantities λ_j are termed the rapidities, or quasimomenta of the Bethe-ansatz wave function. Imposing that the system be confined to a spatial domain of length L and subject to periodic boundary conditions $\psi(\{x_1, \ldots, x_i + L, \ldots, x_N\}) = \psi(\{x_1, \ldots, x_i, \ldots, x_N\})$ yields the set of N Bethe equations [56, 231]

$$\lambda_j = \frac{2\pi}{L} m_j - \frac{2}{L} \sum_{k=1}^{N} \arctan\left(\frac{\lambda_j - \lambda_k}{c}\right) \tag{4.6}$$

for the rapidities λ_j, where the "quantum numbers" m_j are any N distinct integers (half-integers) in the case that N is odd (even) [219].

Extending Eq. (4.4) outside of the ordered sector $\mathcal{R}$ of the periodic domain using Bose symmetry, each set $\{\lambda_j\}$ of N distinct rapidities obtained as a particular solution of the Bethe equations (4.6) defines a normalized eigenstate $|\{\lambda_j\}\rangle$ of Hamiltonian (4.1), with

spatial representation

$$\zeta_{\{\lambda_j\}}(\{x_i\}) \equiv \langle\{x_i\}|\{\lambda_j\}\rangle = A_{\{\lambda_j\}} \sum_{\sigma} \exp\Big[i \sum_{m=1}^{N} x_m \lambda_{\sigma(m)}\Big] \prod_{k>l} \Big(1 - \frac{ic\,\mathrm{sgn}(x_k - x_l)}{\lambda_{\sigma(k)} - \lambda_{\sigma(l)}}\Big), \quad (4.7)$$

where the normalization constant [207]

$$A_{\{\lambda_j\}} = \frac{\prod_{k>l}(\lambda_k - \lambda_l)}{\big\{N!\,\det\{M_{\{\lambda_j\}}\}\,\prod_{k>l}[(\lambda_k - \lambda_l)^2 + c^2]\big\}^{1/2}}\,, \quad (4.8)$$

with $M_{\{\lambda_j\}}$ the $N \times N$ matrix with elements

$$\big[M_{\{\lambda_j\}}\big]_{kl} = \delta_{kl}\Big(L + \sum_{m=1}^{N} \frac{2c}{c^2 + (\lambda_k - \lambda_m)^2}\Big) - \frac{2c}{c^2 + (\lambda_k - \lambda_l)^2}. \quad (4.9)$$

The set of all such eigenfunctions forms a complete orthonormal basis for (the Bose-symmetric subspace of) the N-particle Hilbert space on which Hamiltonian (4.1) acts [221]. In the eigenstate $|\{\lambda_j\}\rangle$ the total energy,

$$E_{\{\lambda_j\}} = \sum_{j=1}^{N} \lambda_j^2, \quad (4.10)$$

and total momentum,

$$P_{\{\lambda_j\}} = \sum_{j=1}^{N} \lambda_j, \quad (4.11)$$

of the system, and indeed an infinite set of quantities $Q^{(m)}_{\{\lambda_j\}} \equiv \sum_{j=1}^{N} (\lambda_j)^m$ that are conserved under the action of the Hamiltonian (4.1), are specified completely by the set $\{\lambda_j\}$ of rapidities that label the state. In particular, the ground state of the system corresponds to the set of N rapidities that minimize Eq. (4.10) and constitute the (pseudo-)Fermi sea of the 1D Bose gas [207].

In this work we obtain ground- and excited-state solutions to Eq. (4.6) numerically using a standard Newton solver. The numerical solution is significantly aided by the fact that the Jacobian matrix corresponding to Eq. (4.6) takes a simple analytical form [219]. In practice, we exploit the fact that in the TG limit $c \to \infty$ the rapidities $\{\lambda_j\}$ are simply the single-particle momenta of a system of free spinless fermions [207] to obtain initial guesses

for the rapidities in the strongly interacting regime $c \gg 1$. We then obtain solutions for the rapidities $\{\lambda_j\}$ at successively smaller values of c, providing the root-finding algorithm in each case with an initial guess for these quantities obtained from linear extrapolation of the converged solutions found at stronger interaction strengths.

4.3.2 Calculation of correlation functions

Throughout this article, we present results on the m^{th}-order equal-time correlation functions

$$G^{(m)}(x_1,\ldots,x_m,x'_1,\ldots,x'_m;t) \equiv \left\langle \hat{\Psi}^\dagger(x_1)\cdots\hat{\Psi}^\dagger(x_m)\hat{\Psi}(x'_1)\cdots\hat{\Psi}(x'_m)\right\rangle, \tag{4.12}$$

where $\langle\cdots\rangle \equiv \mathrm{Tr}\{\hat{\rho}(t)\cdots\}$ denotes an expectation value in a Schrödinger-picture density matrix $\hat{\rho}(t)$, and $\hat{\Psi}^{(\dagger)}(x)$ is the annihilation (creation) operator for the Bose field. Formally, the corresponding normalized correlation functions are

$$g^{(m)}(x_1,\ldots,x_m,x'_1,\ldots,x'_m;t) \equiv \frac{G^{(m)}(x_1,\ldots,x_m,x'_1,\ldots,x'_m;t)}{\left[\langle\hat{n}(x_1)\rangle\cdots\langle\hat{n}(x_m)\rangle\langle\hat{n}(x'_1)\rangle\cdots\langle\hat{n}(x'_m)\rangle\right]^{1/2}},$$

where $\hat{n}(x) \equiv \hat{\Psi}^\dagger(x)\hat{\Psi}(x)$. We note, however, that in the nonequilibrium scenarios we consider in this article both the initial state of the system and the Hamiltonian that generates its time evolution are translationally invariant (modulo the finite extent L of the periodic geometry). Thus, the mean density $\langle\hat{n}(x)\rangle \equiv n$ is constant in both time and space, and $g^{(m)}(x_1,\ldots,x_m,x'_1,\ldots,x'_m;t) = G^{(m)}(x_1,\ldots,x_m,x'_1,\ldots,x'_m;t)/n^m$. In the remainder of this article we consider the forms of these correlation functions both in a pure (time-dependent) state $|\psi(t)\rangle$, in which case

$$\begin{aligned} g^{(m)}(x_1,\ldots,x_m,x'_1,\ldots,x'_m;t) &= \frac{1}{n^m}\langle\psi(t)|\hat{\Psi}^\dagger(x_1)\cdots\hat{\Psi}^\dagger(x_m)\hat{\Psi}(x'_1)\cdots\hat{\Psi}(x'_m)|\psi(t)\rangle \\ &= N!\int_0^L \frac{dx_{m+1}\cdots dx_N}{n^m(N-m)!}\psi^*(x_1,\ldots,x_m,x_{m+1},\ldots,x_N,t)\psi(x'_1,\ldots,x'_m,x_{m+1},\ldots,x_N,t) \end{aligned} \tag{4.13}$$

and in a statistical ensemble with density matrix $\hat{\rho}_{\rm SE} \equiv \sum_{\{\lambda_j\}} \rho^{\rm SE}_{\{\lambda_j\}} |\{\lambda_j\}\rangle\langle\{\lambda_j\}|$, in which case

$$g^{(m)}_{\rm SE}(x_1,\ldots,x_m,x'_1,\ldots,x'_m) = \frac{1}{n^m}{\rm Tr}\{\hat{\rho}_{\rm SE}\hat{\Psi}^\dagger(x_1)\cdots\hat{\Psi}^\dagger(x_m)\hat{\Psi}(x'_1)\cdots\hat{\Psi}(x'_m)\}$$
$$= \frac{1}{n^m}\sum_{\{\lambda_j\}}\rho^{\rm SE}_{\{\lambda_j\}}\langle\{\lambda_j\}|\hat{\Psi}^\dagger(x_1)\cdots\hat{\Psi}^\dagger(x_m)\hat{\Psi}(x'_1)\cdots\hat{\Psi}(x'_m)|\{\lambda_j\}\rangle, \tag{4.14}$$

where the matrix elements of field-operator products are given in first-quantized form by Eq. (4.13) upon replacing $\psi(\{x_i\},t) \to \zeta_{\{\lambda_j\}}(\{x_i\})$. The evaluation of such integrals can then be performed semianalytically, following the approach of Ref. [255]. For this purpose, we developed a symbolic integration algorithm, which will be presented elsewhere [165]. We note also that translational invariance of the state $|\psi(t)\rangle$ (or $\hat{\rho}_{\rm SE}$) also implies that the correlation functions $g^{(m)}(x_1,\ldots,x_m,x'_1,\ldots,x'_m)$ are invariant under global coordinate shifts $x \to x+d$, and thus $g^{(1)}(x,y) \equiv g^{(1)}(0,y-x)$, etc. We focus, in particular, on the first-order correlation function $g^{(1)}(x) \equiv g^{(1)}(0,x)$, the second-order correlation function $g^{(2)}(x) \equiv g^{(2)}(0,x,x,0)$, and the local third-order coherence $g^{(3)}(0) = \langle[\hat{\Psi}^\dagger(0)]^3[\hat{\Psi}(0)]^3\rangle/n^3$.

We note that as we work in units $\hbar = 2m = 1$, time (energy) has dimensions of (inverse) length squared. Although our results depend explicitly on the number of particles N in our system, the extent L of our periodic geometry, and consequently the density $n \equiv N/L$ of the Bose gas, is arbitrary. Following Ref. [56] we absorb the density into the dimensionless interaction-strength parameter $\gamma = c/n$. In the thermodynamic limit $N,\ L \to \infty$ at constant n, the interaction strength γ is the only parameter of the LL theory. However, in our finite system, the particle number N must also be specified. We hereafter quote the strength of interactions in our calculations in terms of γ. The Fermi momentum $k_F = (2\pi/L)(N-1)/2$, which is the magnitude of the largest rapidity occurring in the ground state in the TG limit [207], is a convenient unit of inverse length and so we often specify lengths in units of k_F^{-1}, energies in units of k_F^2, and times in units of k_F^{-2}.

4.4 Dynamics following an interaction-strength quench

We now investigate the nonequilibrium dynamics of the LL model following a sudden change (quench) of the interparticle interaction strength γ. We focus, in particular, on a quench

of a system initially in the ground state $|\psi_0\rangle$ of Hamiltonian (4.1) in the limit of vanishing interaction strength [7, 8, 73, 194, 210]. We note that the corresponding spatial wave function of this initial state is simply a constant,

$$\psi_0(\{x_i\}) = \langle\{x_i\}|\psi_0\rangle = L^{-N/2}, \tag{4.15}$$

and, e.g., the spatial correlation functions $g^{(1)}_{\gamma=0}(x) = 1$ and $g^{(2)}_{\gamma=0}(x) = 1 - 1/N$ in this state are also constants. At $t = 0$, we discontinuously change the interaction strength to a finite final value $\gamma > 0$. The ensuing time evolution of the state is governed by the LL Hamiltonian $\hat{H}$ [Eq. (4.1)] with interaction strength γ. As $\hat{H}$ is time-independent following the quench, energy is conserved during the dynamics. This conserved energy is the energy of the system at time $t = 0^+$,

$$E \equiv \langle\psi(0^+)|\hat{H}|\psi(0^+)\rangle = (N-1)n^2\gamma, \tag{4.16}$$

which is easily derived by noting that the state $|\psi(0^+)\rangle$ immediately following the quench is simply the (homogeneous) prequench wave function $|\psi_0\rangle$, in which the kinetic-energy component of Hamiltonian (4.1) vanishes and in which the interaction energy is determined by the local second-order coherence $[g^{(2)}_{\gamma=0}(0)]$ of the state.

Formally, the time-evolving wave function is given at all times $t > 0$ by

$$|\psi(t)\rangle = \sum_{\{\lambda_j\}} C_{\{\lambda_j\}} e^{-iE_{\{\lambda_j\}}t}|\{\lambda_j\}\rangle, \tag{4.17}$$

where the sum is over all eigenstates $|\{\lambda_j\}\rangle$ of $\hat{H}$, and the $C_{\{\lambda_j\}} \equiv \langle\{\lambda_j\}|\psi_0\rangle$ are the overlaps between the initial state $|\psi_0\rangle$ and these eigenstates, which we calculate from their coordinate-space representations $\zeta_{\{\lambda_j\}}(\{x_i\})$ [165]. [2] We note, however, that only those states $|\{\lambda_j\}\rangle$ that have zero total momentum, $\sum_j \lambda_j = 0$ [cf. Eq. (4.11)], and are parity invariant (for which the rapidities $\{\lambda_j\}$ can be enumerated such that $\lambda_j = -\lambda_{N+1-j}; \quad j = 1, 2, \ldots, N$)

[2] We note that the authors of Ref. [218] similarly evaluated overlaps of post-quench eigenstates with the initial state in their study of a quench from the TG regime to the so-called super-Tonks regime [216] of strong attractive interactions. However, their investigations focused primarily on the overlap of the initial state with the super-Tonks eigenstate itself, and did not consider the time-dependent dynamics of the system explicitly.

have nonzero overlaps with the initial state $|\psi_0\rangle$, as discussed in Refs. [7, 325].

We primarily characterize the nonequilibrium dynamics of the system by the evolution of its equal-time correlation functions (Sec. 4.3.2). These are calculated by noting that the time evolution of the expectation value of an arbitrary operator $\hat{O}$ in the time-dependent state $|\psi(t)\rangle$ is given by

$$\langle\hat{O}(t)\rangle \equiv \langle\psi(t)|\hat{O}|\psi(t)\rangle = \sum_{\{\lambda_j\}}\sum_{\{\lambda'_j\}} C^*_{\{\lambda'_j\}} C_{\{\lambda_j\}} e^{i(E_{\{\lambda'_j\}}-E_{\{\lambda_j\}})t} \langle\{\lambda'_j\}|\hat{O}|\{\lambda_j\}\rangle. \tag{4.18}$$

The matrix elements $\langle\{\lambda'_j\}|\hat{O}|\{\lambda_j\}\rangle$ of observables are calculated in a similar manner to the overlaps $C_{\{\lambda_j\}}$, as we will discuss in Ref. [165]. The computational expense incurred in evaluating these matrix elements increases exponentially with the particle number N, placing a strong practical constraint on the system sizes we can describe with our coordinate Bethe-ansatz approach. In the remainder of this article, unless otherwise specified, we always consider a quench of $N = 5$ particles.

Assuming that all energies $E_{\{\lambda_j\}}$ of the contributing eigenstates $|\{\lambda_j\}\rangle$ are nondegenerate, the (infinite-)time average of Eq. (4.18) is

$$\langle\hat{O}\rangle_{\mathrm{DE}} = \lim_{\tau\to\infty}\frac{1}{\tau}\int_0^\tau dt\,\langle\psi(t)|\hat{O}|\psi(t)\rangle = \sum_{\{\lambda_j\}} |C_{\{\lambda_j\}}|^2 \langle\{\lambda_j\}|\hat{O}|\{\lambda_j\}\rangle, \tag{4.19}$$

which we identify as the expectation value of $\hat{O}$ in the density matrix,

$$\hat{\rho}_{\mathrm{DE}} = \sum_{\{\lambda_j\}} |C_{\{\lambda_j\}}|^2 |\{\lambda_j\}\rangle\langle\{\lambda_j\}|, \tag{4.20}$$

of the DE [1]. A finite system such as we consider here does not exhibit true relaxation, in which the instantaneous density matrix of the system (and therefore all observables) becomes stationary in the long-time limit $t \to \infty$, but will instead exhibit recurrences [359, 360]. However, the dephasing of the energy eigenstates is expected to lead, quite generically, to observables fluctuating about reasonably well-defined mean values consistent with the DE predictions [1]. Numerical results for a number of systems indicate that the relative magnitude of these fluctuations scales towards zero with increasing system size and thus that observables relax to the predictions of the DE in the thermodynamic limit (see, e.g.,

Refs. [181, 288, 361]). Establishing whether the LL system relaxes to the DE following an interaction-strength quench in the thermodynamic limit is beyond the scope of this article. We therefore simply regard the DE defined by Eq. (4.20) as the ensemble appropriate to describe the relaxed state of our finite-sized system.

We note that formally the sums in Eqs. (4.17)–(4.20) range over an infinite number of LL eigenstates. In practice, we include only a finite number of eigenstates in our calculations and thus truncate the sums in Eqs. (4.17)–(4.20). As we discuss in Appendix 4.7.1, we retain all eigenstates $|\{\lambda_j\}\rangle$ that have (absolute) overlap with $|\psi_0\rangle$ greater than some threshold value. The accuracy of our results can then be quantified by considering the saturation of the sum rules associated with the normalization (cf. Ref. [209]) and energy of the wave function $|\psi(t)\rangle$ (see Appendix 4.7.1).

4.4.1 First-order correlations

We begin our characterization of the nonequilibrium dynamics of the LL system following the quench by considering the first-order (or one-body) correlations of the system. As the translational invariance of the initial state $|\psi_0\rangle$ is preserved under the evolution generated by $\hat{H}$, the first-order correlations are at all times completely described by the momentum distribution

$$\widetilde{n}(k,t) = n \int_0^L dx\, e^{-ikx} g^{(1)}(x,t). \tag{4.21}$$

We note that, in our finite periodic geometry, the single-particle momentum k is quantized and takes discrete values $k_j = 2\pi j/L$, where j is an integer. In the initial state, all particles occupy the ground (zero-momentum) single-particle orbital [i.e., $\widetilde{n}(0, t = 0^-) \equiv N$], and at times $t > 0$ the presence of finite interparticle interactions $\gamma > 0$ induces partial redistribution of this population over single-particle modes with finite momenta $|k| > 0$. The ensuing dynamics of the momentum distribution have previously been considered in the nonequilibrium field-theoretical studies of the dynamics of the LL model presented in Refs. [294–297], whereas in later works the focus has been set primarily on the second-order (density-density) correlations [8, 72, 194, 210]. Exceptions can be found in Refs. [7, 73], which presented results for $g^{(1)}(x)$ in the stationary state following a quench to the TG limit (in which case the Bose-Fermi mapping and Wick's theorem can be used to simplify

the calculation significantly) and in Ref. [205], which details the calculation of the dynamical evolution of $g^{(1)}(x,t)$ in the same TG-limit quench scenario.

In Fig. 4.1(a) we plot the evolution of the occupations of the first ten non-negative momentum modes, $\widetilde{n}(k_j,t)$ $(j=0,1,\ldots,9)$, following a quench to $\gamma=100$. In the limit $t\to 0^+$, the occupations of all nonzero momentum modes rise at a common k-independent rate, due to the purely local nature of the delta-function interaction potential, which corresponds to a momentum-independent coupling [295]. As time progresses, the zero-momentum occupation $\widetilde{n}(0,t)$ correspondingly decreases, and the occupation of each nonzero momentum mode k_j levels off and fluctuates about its DE value $\widetilde{n}_{\mathrm{DE}}(k_j)$ [see Eq. (4.19)], which we indicate in Fig. 4.1(a) for the first three non-negative momenta k_j $(j=0,1,2)$ (horizontal solid lines). The time evolution of the momentum distribution shown in Fig. 4.1(a) is similar to the results obtained with functional-integral field-theory methods [294–297]. In particular, the populations of higher momentum modes stop increasing and settle to their DE values (about which they fluctuate) more rapidly than those of lower momentum modes, indicating that nonlocal first-order correlations relax increasingly rapidly on decreasing length scales (cf., e.g., Refs. [39, 294–296, 355]). We note, however, that the momentum distribution here, similarly to that observed for a quench to the strongly interacting regime in Ref. [297], appears to evolve directly to a stationary state, without exhibiting any intermediary period of quasistationary relaxation such as that observed for quenches to weak interaction strengths in Refs. [294–296].

Qualitatively similar evolution is observed for any value of the final interaction strength γ, but both the form of the DE momentum distribution $\widetilde{n}_{\mathrm{DE}}(k_j)$ and the time scales on which mode occupancies reach their DE values depend strongly on γ. A useful summary statistic by which to compare the relaxation of first-order correlations between quenches is the occupation $\widetilde{n}(0,t)$ of the zero-momentum mode, the dynamical evolution of which we plot in Fig. 4.1(b) for $\gamma=1,\ 10$, and 100. We note that in the case $\gamma=1$, $\widetilde{n}(0,t)$ exhibits near-monochromatic oscillations over time. For a larger interaction strength $\gamma=10$, the zero-momentum occupation $\widetilde{n}(0,t)$ first crosses $\widetilde{n}_{\mathrm{DE}}(0)$ earlier (at time $t\approx 0.7\,k_F^{-2}$), after which it exhibits less regular, more intricately structured fluctuations about $\widetilde{n}_{\mathrm{DE}}(0)$. In the quench to the Tonks regime ($\gamma=100$), the DE value is first reached even earlier (at time $t\approx 0.4\,k_F^{-2}$), and we note also that the fluctuations of $\widetilde{n}(0,t)$ around $\widetilde{n}_{\mathrm{DE}}(0)$ are, in general,

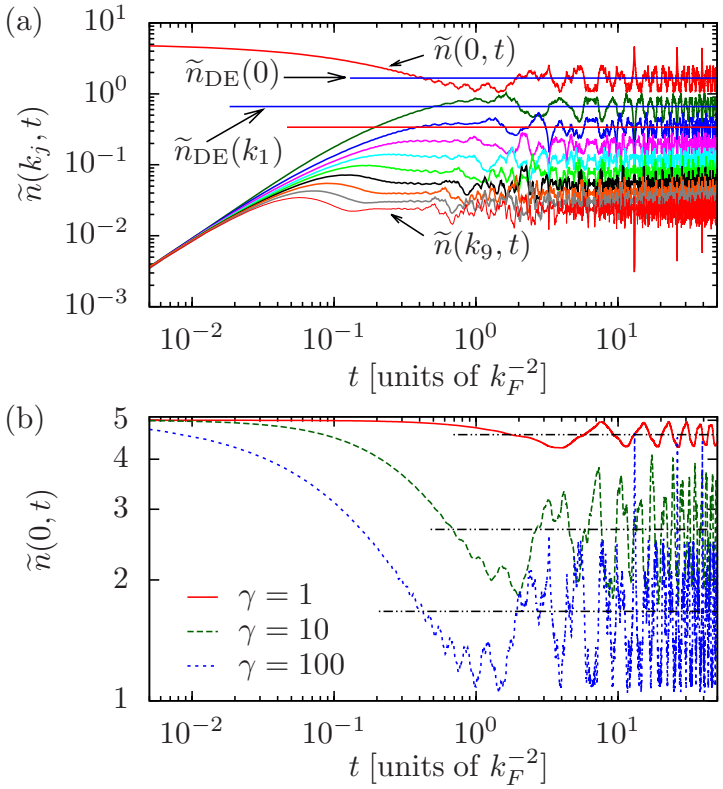

FIGURE 4.1: (a) Time evolution of the occupations of the first ten non-negative momentum modes, $\widetilde{n}(k_j,t)$ ($j = 0, 1, \ldots, 9$), for $N = 5$ particles following a quench of the interaction strength from zero to $\gamma = 100$. Horizontal solid lines indicate the equilibrium values $\widetilde{n}_{\rm DE}(k_j)$ predicted by the DE, for the first three non-negative momentum modes. (b) Time evolution of the zero-momentum occupation $\widetilde{n}(0,t)$ following quenches of $N = 5$ particles to $\gamma = 1$, 10, and 100. The horizontal dot-dashed lines indicate the corresponding DE values $\widetilde{n}_{\rm DE}(0)$.

somewhat smaller than those observed in the quench to $\gamma = 10$, although in this case $\widetilde{n}(0,t)$ also exhibits near-complete revival peaks, in which it returns close to its initial value.

4.4.2 Second-order correlations

We now extend our characterization of the relaxation dynamics of the LL system to the second-order (or two-body) correlations of the Bose field. We focus first on the local second-order coherence $g^{(2)}(0,t)$, the time evolution of which we plot in Fig. 4.2 for $\gamma = 1, 10$, and 100. Similarly to $\widetilde{n}(0,t)$, as time evolves the local second-order coherence decays from its initial value $g^{(2)}(0,t=0) = 1 - N^{-1}$ before settling down to fluctuate about the prediction $g^{(2)}_{\rm DE}(0)$ of the diagonal ensemble. In the case $\gamma = 1$, $g^{(2)}(0,t)$ decays over a time scale similar to that over which the corresponding zero-momentum occupation $\widetilde{n}(0,t)$ decays and subsequently exhibits similar near-regular oscillations about its DE value $g^{(2)}_{\rm DE}(0)$

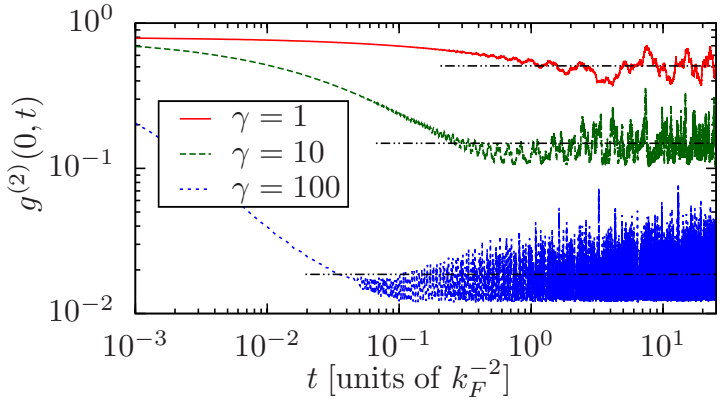

FIGURE 4.2: Time evolution of the local second-order coherence $g^{(2)}(0,t)$ following quenches of the interaction strength to $\gamma = 1, 10$, and 100 for $N = 5$ particles. Horizontal dot-dashed lines indicate the corresponding equilibrium values $g^{(2)}_{\mathrm{DE}}(0)$ predicted by the DE.

[cf. Fig. 4.1(b)]. As the final interaction strength γ increases, $g^{(2)}(0,t)$ reaches its time-averaged value $g^{(2)}_{\mathrm{DE}}(0)$ increasingly rapidly, and this value itself decreases. We note that although this behavior is qualitatively consistent with that observed for the zero-momentum occupation in Fig. 4.1(b), at large final interaction strengths $g^{(2)}(0,t)$ decays to its DE value much more rapidly than the nonlocal quantity $\widetilde{n}(0,t)$.

In Fig. 4.3 we present the time evolution of the full nonlocal second-order correlation function $g^{(2)}(x,t)$ for a quench to $\gamma = 100$. Figure 4.3(a) shows the dependence of this function on the separation x at four representative times. At time $t = 0$, $g^{(2)}(x)$ has the x-independent form appropriate to the noninteracting ground state (black horizontal line). By time $t = 5 \times 10^{-3}\, k_F^{-2}$ (red solid line) the local second-order coherence $g^{(2)}(0,t)$ has decreased to $\approx 7 \times 10^{-2}$, and $g^{(2)}(x,t)$ exhibits a maximum at a finite spatial separation and a decaying oscillatory structure past this maximum. The appearance of such an *increase* in $g^{(2)}(x,t)$ at some finite x is required by conservation of the integrated second-order correlation function $\int_0^L dx\, g^{(2)}(x,t)$ (which itself follows from conservation of particle number and total momentum during the evolution) [194]. By time $t = 5 \times 10^{-2}\, k_F^{-2}$ (blue dotted line) the maximum in $g^{(2)}(x,t)$ and the smaller subsidiary maxima and minima that accompany it have propagated to larger separations. The oscillations in $g^{(2)}(x)$ appear quite distorted at time $t = 5 \times 10^{-1}\, k_F^{-2}$ (green dashed line), though the broad envelope of this function is at this time comparable to the DE prediction for the equilibrium form of $g^{(2)}(x)$ (black dot-dashed line). The formation and propagation of such a "correlation wave" was previously

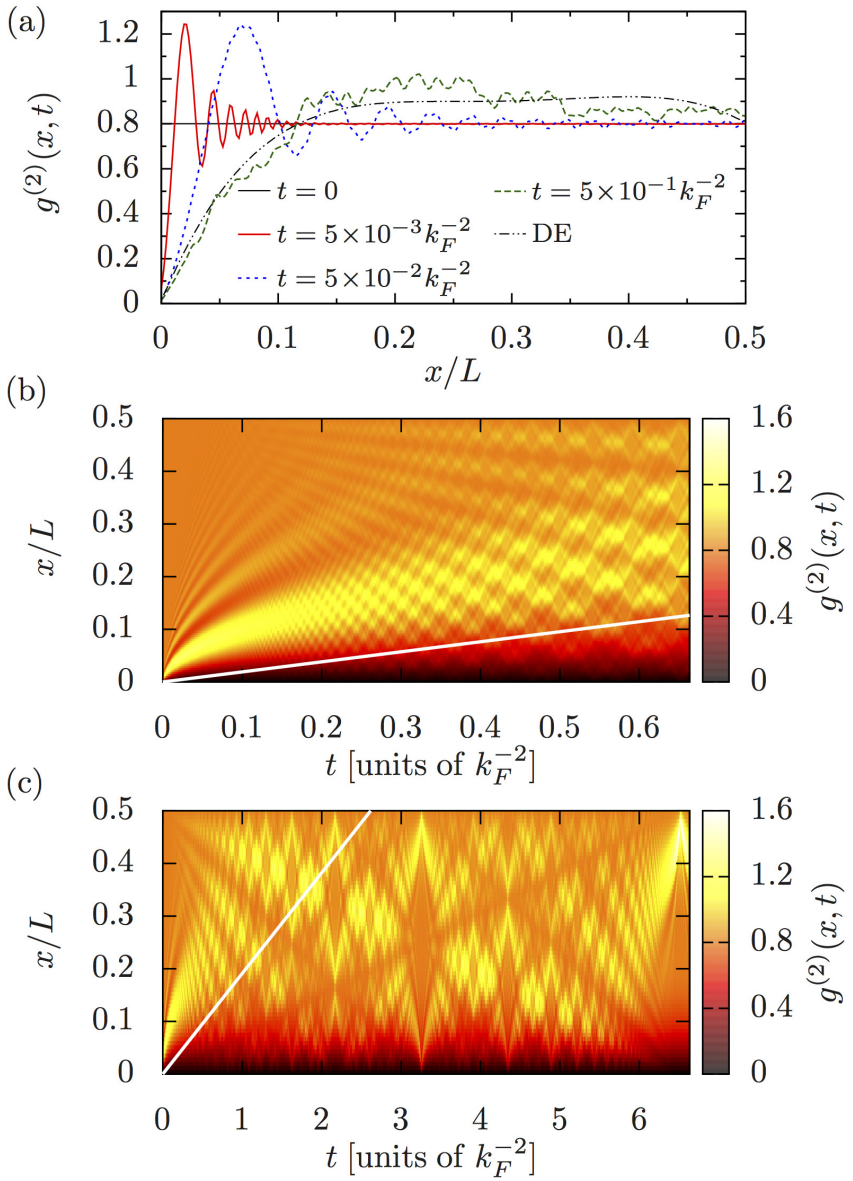

FIGURE 4.3: Time evolution of the nonlocal second-order coherence $g^{(2)}(x,t)$ following a quench of $N = 5$ particles to $\gamma = 100$. (a) Correlation function $g^{(2)}(x)$ at four representative times. The black dot-dashed line indicates the prediction of the DE for the equilibrium form of this function. (b) Evolution of $g^{(2)}(x,t)$ for short times $t \leq \pi/5\, k_F^{-2}$ and (c) longer times $t \leq 2\pi\, k_F^{-2}$. The white solid lines in (b) and (c) indicate the trajectory $x = v_s t$ of a particle propagating away from the origin at the zero-temperature speed of sound v_s of the LL system with interaction strength $\gamma = 100$ (see text).

observed in phase-space [292] and matrix-product-state [194] simulations of quenches from zero to finite γ within a Bose-Hubbard lattice discretization of the LL model and in Bethe-ansatz-based simulations of a quench of the continuous gas to the TG limit $\gamma \to \infty$ [210]. [3]

Figure 4.3(b) gives a more complete picture of the evolution of $g^{(2)}(x,t)$ following the quench. We observe that the oscillations in this function initially propagate rapidly, but then slow and disperse as time progresses. By time $t = 0.6\,k_F^{-2}$ the primary maximum of $g^{(2)}(x,t)$ has dispersed to a width comparable to $L/2$, though additional modulations, due to interference between oscillations propagating in opposite directions around the periodic geometry, have by this time destroyed any meaningful distinction between the (initially well-resolved) individual maxima and minima of the correlation wave. Nevertheless, the behavior of $g^{(2)}(x,t)$ at early times $t \lesssim 0.5\,k_F^{-2}$ is consistent with analytical results for a quench to the TG limit recently obtained in Ref. [73], which found that the maxima of the correlation wave propagate with an algebraically decaying velocity $v \propto 1/\sqrt{t}$. On longer time scales [Fig. 4.3(c)] $g^{(2)}(x,t)$ exhibits a more complicated structure. In particular, $g^{(2)}(x,t)$ appears crisscrossed by a number of solitonlike "density" dips. The slowest of these propagates at approximately 40% of the speed of sound $v_s = 2\pi(1-4/\gamma)N/L = 2.4\,k_F$ [56, 231, 241] [4] of a zero-temperature system with interaction strength $\gamma = 100$ [indicated by white solid lines in Figs. 4.3(b) and 4.3(c)]. This slowest-moving dip is accompanied by similar depressions propagating at integer multiples of its velocity—although the more rapidly moving dips are less well resolved in Fig. 4.3(c). We discuss the significance of this particular set of velocities further in Sec. 4.4.3.

We now consider an alternative characterization of the time development of second-order correlations in the system, given by the instantaneous structure factor [256]

$$S(k,t) = 1 + n\int_0^L dx\; e^{-ikx}\left[g^{(2)}(x,t) - 1\right]. \tag{4.22}$$

We note that particle-number conservation and translational invariance imply that $S(0,t) =$

[3] We note that Refs. [72, 329] discussed the appearance of similar propagating correlation waves following quenches of interacting bosons in 1D to zero interaction strength, in which case the evolution of $g^{(2)}(x,t)$ is determined exactly by the propagation of free bosons from the correlated initial state.

[4] We quote the speed of sound here in units of the Fermi wave vector k_F of our finite-sized system (Sec. 4.3.2), which differs from the Fermi wave vector $k_F^{(\infty)} = n\pi$ in the thermodynamic limit by an $O(1/N)$ correction. We note that this finite-size correction is here much larger than the $O(1/\gamma)$ strong-coupling correction to the TG-limit speed of sound.

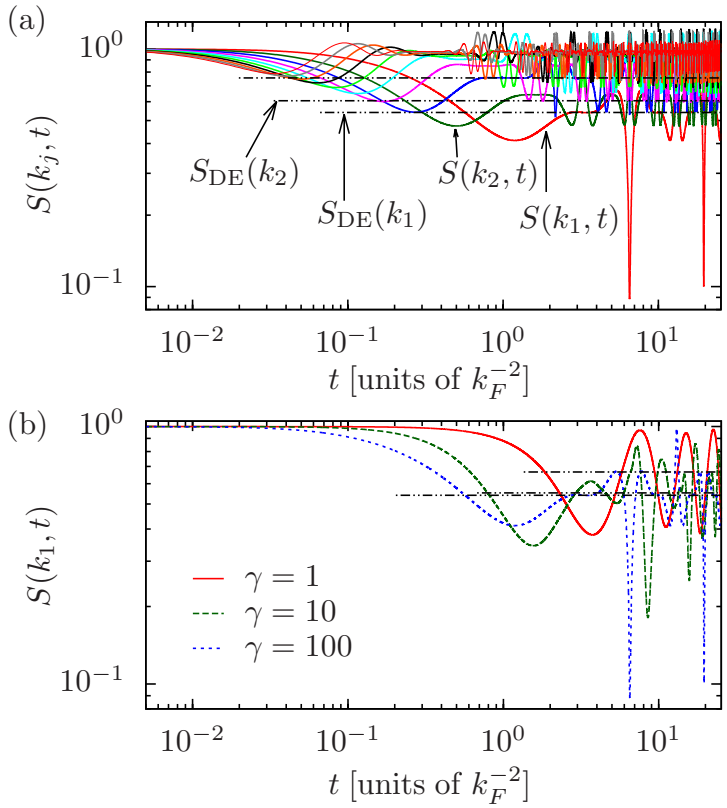

FIGURE 4.4: Time evolution of the structure factor for $N = 5$ particles. (a) Components of the structure factor at the first ten positive momenta, $S(k_j, t)$ ($j = 1, 2, \ldots, 10$), for a quench to $\gamma = 100$. Horizontal dot-dashed lines indicate the DE values $S_{\rm DE}(k_j)$ for $j = 1, 2$, and 3 (bottom to top). (b) First positive-momentum component $S(k_1, t)$ of the structure factor, for $\gamma = 1, 10$, and 100. Horizontal dot-dashed lines indicate the DE values $S_{\rm DE}(k_1)$ for $\gamma = 1, 10$, and 100 (top to bottom).

0 at all times t. In Fig. 4.4(a) we therefore plot the time development of the structure factor, evaluated at the first ten positive wave vectors k_j ($j = 1, 2, \ldots, 10$) in our finite periodic geometry, for a quench to $\gamma = 100$.

We note that the behavior of the individual components $S(k_j, t)$ of the structure factor is opposite to that of the occupations $\widetilde{n}(k_j, t)$ of nonzero momentum modes k_j for this quench [Fig. 4.1(a)], in that the $S(k_j, t)$ begin at unity and decay towards their DE values $S_{\rm DE}(k_j, t)$ as time progresses. Moreover, in contrast to the momentum occupations $\widetilde{n}(k_j, t)$ ($j > 0$), which initially rise uniformly, the components $S(k_j, t)$ of the structure factor at distinct momenta k_j decay at distinct rates even in the limit $t \to 0^+$. However, just as observed for the momentum distribution, components of the structure factor at higher momenta reach their first turning points and settle (with large fluctuations) around their DE values more rapidly than those components at lower momenta. In particular, $S(k_1, t)$ is the last

component to reach its turning point and, in general, fluctuates more slowly about its time-averaged value $S_{\mathrm{DE}}(k_1)$ than higher-momentum components, although its oscillations include large excursions towards zero and unity. This can be seen more clearly in Fig. 4.4(b), where we compare the time evolution of $S(k_1, t)$ (which we take as a simple summary measure for the evolution of the structure factor) for quenches to $\gamma = 1, 10$, and 100. Similarly to $\widetilde{n}(0, t)$, the structure-factor component $S(k_1, t)$ exhibits approximately monochromatic oscillations for the quench to $\gamma = 1$. Moreover, $S(k_1, t)$ first crosses its DE value sooner, and exhibits progressively less-regular oscillations, with increasing γ. We observe that for $\gamma = 100$, the component $S(k_1, t)$ exhibits a large fluctuation towards zero at time $t \approx 6.51\, k_F^{-2}$. Considering Fig. 4.3(c), we see that this time also corresponds to that at which the solitonlike correlation dip in $g^{(2)}(x, t)$ that emerges following the quench, propagating at a velocity $\approx 1.0\, k_F$, reaches $x = L/2$. A large fluctuation of $S(k_1, t)$ to a value close to unity occurs at time $t \approx 13.1\, k_F^{-2}$, coinciding with the quasirecurrence of $\widetilde{n}(0, t)$ in Fig. 4.1(a), and a second fluctuation of $S(k_1, t)$ towards zero (somewhat smaller than the first) occurs at time $t \approx 19.9\, k_F^{-2}$, indicating a (quasi-)regular pattern of large fluctuations in the correlations of the system.

4.4.3 Fidelity

So far our characterizations of the nonequilibrium dynamics of the LL model have considered only the one- and two-body correlations of the system. We now consider a quantity that allows us to characterize the relaxation of the system in the N-body state space of the LL model: the quantum fidelity [362]. The fidelity provides a measure of "closeness" between two quantum states and, when evaluated between a pure state $|\chi\rangle$ and an arbitrary (pure or mixed) density matrix $\hat{\sigma}$, takes the form $F(|\chi\rangle, \hat{\sigma}) = \langle\chi|\hat{\sigma}|\chi\rangle$. We note first that the fidelity

$$F_{\mathrm{DE}} = \langle\psi(t)|\hat{\rho}_{\mathrm{DE}}|\psi(t)\rangle = \sum_{\{\lambda_j\}} |C_{\{\lambda_j\}}|^4 \tag{4.23}$$

between the time-evolving state $|\psi(t)\rangle$ and the DE density matrix is time independent, as $\hat{\rho}_{\mathrm{DE}}$ is (by definition) diagonal in the energy eigenbasis of $\hat{H}$ and therefore invariant under the action of the time-displacement operator $\hat{U}(t) = \sum_{\{\lambda_j\}} \exp(-iE_{\{\lambda_j\}}t)|\{\lambda_j\}\rangle\langle\{\lambda_j\}|$. In

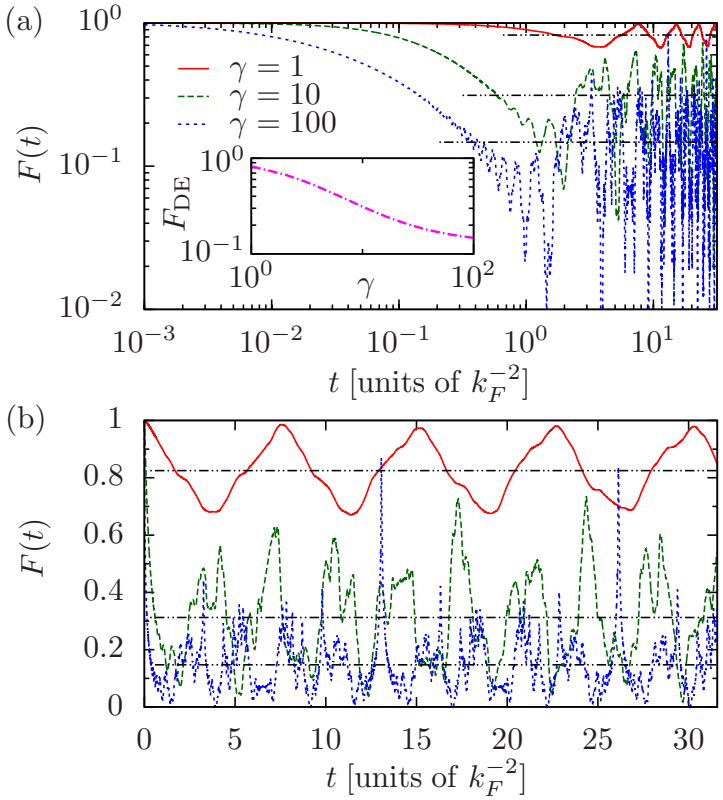

FIGURE 4.5: (a) Fidelity $F(t)$ between time-evolving state $|\psi(t)\rangle$ and initial state $|\psi_0\rangle$. Horizontal dot-dashed lines indicate the corresponding DE values $F_{\rm DE}$. Inset: Fidelity $F_{\rm DE}$ between DE density matrix $\hat{\rho}_{\rm DE}$ and initial state $|\psi_0\rangle$ (i.e., IPR of $|\psi_0\rangle$ in the eigenstates of $\hat{H}$) as a function of γ. (b) The same data as (a) on a linear scale.

fact, the fidelity $F_{\rm DE}$ is simply the inverse participation ratio (IPR) [363] of the initial state $|\psi_0\rangle$ in the energy eigenbasis of $\hat{H}$.

We characterize the dynamics of the time-evolving state vector $|\psi(t)\rangle$ in the N-body Hilbert space by the fidelity between $|\psi(t)\rangle$ and the initial state $|\psi_0\rangle$ of the system:

$$F(t) = |\langle\psi_0|\psi(t)\rangle|^2 = \sum_{\{\lambda_j\}}\sum_{\{\lambda'_j\}} |C_{\{\lambda_j\}}|^2 |C_{\{\lambda'_j\}}|^2 e^{i(E_{\{\lambda_j\}} - E_{\{\lambda'_j\}})t}. \tag{4.24}$$

This quantity provides a characterization of the dephasing of energy eigenstates that underlies the relaxation of the system to the DE [1]. We note in particular that, in the absence of degeneracies in the energy spectrum, the time average of the fidelity $\lim_{\tau\to\infty}(1/\tau)\int_0^\tau dt\, F(t) = F_{\rm DE}$ (see, e.g., Ref. [364] and references therein).

In Fig. 4.5(a) we plot the fidelity $F(t)$ as a function of time for $N = 5$ particles and final interaction strengths $\gamma = 1, 10$, and 100. We observe that for each value of γ, the evolution

of $F(t)$ is qualitatively similar to the corresponding evolution of the zero-momentum occupation $\widetilde{n}(0,t)$ [Fig. 4.1(b)]. For the quench to $\gamma = 1$, the fidelity exhibits near-monochromatic oscillations around its DE value. We observe that for this quench, the IPR $F_{\mathrm{DE}} \approx 0.83$, implying that few eigenstates contribute significantly to the DE (note that $F_{\mathrm{DE}} \to 1$ in the limit that $\hat{\rho}_{\mathrm{DE}}$ is pure). In fact, for the quench to $\gamma = 1$, the two most highly occupied energy eigenstates, with populations $n^{(0)} = |C^{(0)}|^2 \approx 0.903$ and $n^{(1)} = |C^{(1)}|^2 \approx 0.073$, account for the majority of the norm of $|\psi(t)\rangle$, with more highly excited states accounting for the remaining $\approx 2.5\%$. Thus, the postquench system can be regarded to a good approximation as a superposition of the ground state and the lowest-lying excited state that has finite overlap with $|\psi_0\rangle$, yielding a monochromatic oscillation in $F(t)$ with a period $t_1 = 2\pi/(E^{(1)} - E^{(0)}) \approx 7.52\, k_F^{-2}$, which indeed appears consistent with the primary frequency component of $F(t)$ for this quench. This behavior is straightforward to understand, as the finite extent of the system induces a finite-size gap in the excitation spectrum. As we discuss in Appendix 4.7.2, this gap strongly suppresses the excitation of the system in quenches to small values of γ, yielding effectively two-level dynamics.

As the final interaction strength γ increases, the IPR F_{DE} of $|\psi_0\rangle$ in the eigenstates of $\hat{H}$ decreases significantly [inset to Fig. 4.5(a)]. For $\gamma = 10$, we find $F_{\mathrm{DE}} \approx 0.31$, and in this case $F(t)$ is a strongly irregular function, composed of many frequency components, and more clearly exhibits a rapid initial decay [see the linear plot of $F(t)$ in Fig. 4.5(b)], followed by (large) fluctuations about its temporal mean F_{DE}. We note that this decay of $F(t)$ towards F_{DE} has a simple physical interpretation. As F_{DE} is the average of the fidelities between $|\psi(t)\rangle$ and the eigenstates $|\{\lambda_j\}\rangle$ of $\hat{H}$, weighted by their populations in $\hat{\rho}_{\mathrm{DE}}$, when $F(t) = F_{\mathrm{DE}}$ the state $|\psi(t)\rangle$ is equally close to $|\psi_0\rangle$ as it is to a typical state in the DE, indicating a loss of "memory" of the initial state.

For $\gamma = 100$, the IPR ($F_{\mathrm{DE}} \approx 0.15$) and the typical magnitude of the fluctuations of $F(t)$ about it are again smaller than for $\gamma = 10$. Moreover, the evolution of $F(t)$ appears even more irregular in this case. However, although the typical fluctuations of $F(t)$ are comparatively small, we note that $F(t)$ also exhibits sharp, sudden fluctuations towards values ≈ 0.8, and indeed closer to unity than the largest fluctuations exhibited by $F(t)$ for $\gamma = 10$. We identify the appearance of these quasirecurrences as resulting from the proximity of the system to the TG limit $\gamma \to \infty$ [344]. As γ is increased towards the TG

limit, the spectrum of $\hat{H}$ approaches that of free fermions in the periodic ring geometry, which yields perfect recurrences of the initial state on comparatively short time scales, due to the commensurability of eigenstate energies. In particular, in the TG limit the energies of eigenstates contributing to the DE are all integer multiples of $\delta\varepsilon = 2k_1^2 \equiv 8\pi^2/L^2$ (where the factor of 2 is due to the restriction to parity-invariant eigenstates), yielding a recurrence time $t_r^{(\mathrm{TG})} = 2\pi/\delta\varepsilon = L^2/4\pi$. For the quenches we consider here with $N = 5$, the Fermi momentum $k_F = 4\pi/L$, and thus $t_r^{(\mathrm{TG})} = 4\pi\, k_F^{-2}$. We therefore expect the sharp quasirevival evident in $F(t)$ at $t \approx 13.1\, k_F^{-2}$ to shift to earlier times and increase in magnitude as γ is increased, ultimately becoming a perfect recurrence [$F(t_r^{(\mathrm{TG})}) = 1$] in the TG limit. [5] This insight also helps us to understand the appearance of the solitonic dip in $g^{(2)}(x,t)$ [Fig. 4.3(c)] traveling at $\approx 40\%$ of the speed of sound v_s: Complete recurrence of the system at time $t_r^{(\mathrm{TG})}$ would imply a minimum speed $v_{\mathrm{min}} = L/t_r^{(\mathrm{TG})}$ that any (persistent) disturbance in the nonlocal correlation functions of the system can travel at, in order that it returns to its starting position when the recurrence occurs. For $N = 5$ the minimum velocity $v_{\mathrm{min}} = k_F$, whereas the Fermi velocity and speed of sound (in the TG limit) $v_F = 2.5\, k_F$. [6] We therefore interpret the slow-moving density depression in Fig. 4.3(c) as a precursor to a solitonic disturbance propagating at v_{min} in the TG limit and the more rapidly moving dips as traveling at integer multiples of this velocity. [7] We note also that as the thermodynamic limit is approached (i.e., increasing N at fixed density), the recurrence time diverges like N^2 and the minimum velocity vanishes like $1/N$; i.e., the discrete spectrum of permitted velocities becomes a continuum.

[5] To leading order in the strong-coupling expansion, each rapidity in a parity-invariant set $\lambda_j = (1 - 2/\gamma)k_j$, where k_j is its value in the TG limit (see, e.g., Ref. [255]). Thus, for large but finite γ, eigenstate energies are somewhat smaller than their values in the TG limit, and the (quasi-)recurrence time is therefore somewhat longer than the exact recurrence time of the TG system.

[6] We quote the speed of sound here in units of the Fermi wave vector k_F of our finite-sized system (Sec. 4.3.2), which differs from the Fermi wave vector $k_F^{(\infty)} = n\pi$ in the thermodynamic limit by an $O(1/N)$ correction. We note that this finite-size correction is here much larger than the $O(1/\gamma)$ strong-coupling correction to the TG-limit speed of sound.

[7] We note that the ratio of the minimum velocity v_{min} to the Fermi velocity v_F depends, in general, on the particle number N. We have found that for $N = 4$, density dips propagate at velocities consistent with integer multiples of v_{min}, which correspond to integer multiples of $v_F/2$.

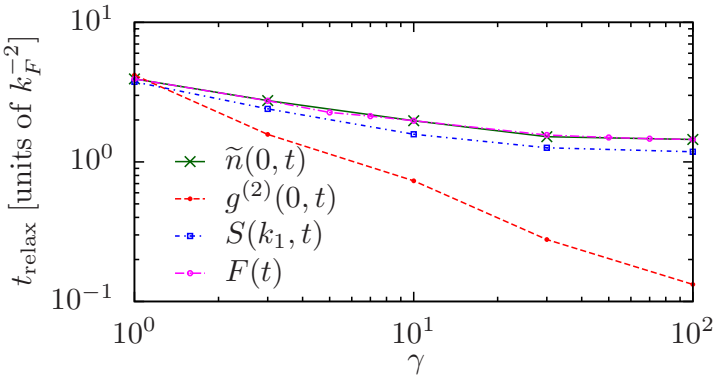

FIGURE 4.6: Relaxation time scales (defined by the first crossing of the DE value; see text) for the zero-momentum occupation $\widetilde{n}(0,t)$, local second-order coherence $g^{(2)}(0,t)$, first nonzero momentum component $S(k_1,t)$ of the instantaneous structure factor, and fidelity $F(t)$, for a quench of $N=5$ particles.

4.4.4 Relaxation time scales

Our results for first- and second-order correlations of the LL system following the quench, together with the fidelity $F(t)$ between the state at time t and the initial state, indicate that our finite-size calculations exhibit behavior consistent with the notion of relaxation of a quantum system due to the dephasing of energy eigenstates [1], at least for large final interaction strengths $\gamma \gg 1$. Here we consider the dependence of the time scales over which these quantities relax on γ. We note that in our finite-size calculations, quantities do not, in general, show decay over sufficiently long time scales that particular functional forms (such as exponential or power-law decay) can be fitted to extract relaxation rates (or exponents). We therefore simply associate, with each quantity we consider, a relaxation time defined as the time at which that quantity first reaches its time-averaged (DE) value. In this manner we extract from the results of our calculations relaxation times t_{relax} for the zero-momentum occupation $\widetilde{n}(0,t)$, local second-order coherence $g^{(2)}(0,t)$, structure-factor component $S(k_1,t)$, and fidelity $F(t)$. We plot these relaxation times t_{relax} as functions of the final interaction strength γ in Fig. 4.6.

It is clear from this figure that (as we have noted in Sec. 4.4.2) the local second-order coherence $g^{(2)}(0,t)$ relaxes much more quickly than $\widetilde{n}(0,t)$, aside from the strongly finite-size limited case $\gamma = 1$. Moreover, the relaxation time for the local quantity $g^{(2)}(0,t)$ decreases steadily with increasing γ (consistent with the results of Ref. [194]), whereas the relaxation time for the nonlocal quantity $\widetilde{n}(0,t)$ appears to saturate to a limiting value $\sim 1.5\,k_F^{-2}$ as

$\gamma \to \infty$. We note also that the relaxation time of the fidelity $F(t)$ is essentially equal to that of $\widetilde{n}(0,t)$ at each γ. The relaxation time of $S(k_1,t)$ is, for each value of γ, somewhat smaller than that of $F(t)$ and $\widetilde{n}(0,t)$, though inspection of Fig. 4.4 suggests that this discrepancy arises due to the functional form of $S(k_1,t)$, which is perhaps not ideally suited to our particular definition of $t_{\rm relax}$.

As the decay of the fidelity $F(t)$ quantifies the dephasing of the energy eigenstates $|\{\lambda_j\}\rangle$ of the system, we regard its evolution as the fundamental characterization of relaxation in our unitarily evolving system. Our results here indicate that the relaxation of nonlocal quantities such as $\widetilde{n}(0,t)$ and $S(k_1,t)$ is directly associated with the relaxation of $F(t)$ and that these experimentally relevant quantities serve as effective probes of the relaxation of the N-particle quantum system as a whole. Finally in this section, we note that, on general principles, the time taken for $\widetilde{n}(0,t)$ to relax to its DE value should diverge with the time taken for correlations to traverse the system extent, which is $\propto N$ at fixed density n. This should be contrasted with both the $\propto N^2$ scaling of the (quasi-)recurrence time scale and the essentially system-size-independent time scale for the relaxation of $g^{(2)}(0,t)$, which is determined by local physical mechanisms [194].

4.5 Comparison of relaxed state to thermal equilibrium

In this section we compare the correlations of the relaxed state of the system described by the DE with those that would be obtained if, following the quench, the system relaxed to thermal equilibrium. Construction of the microcanonical ensemble is hampered by the small system size, combined with the sparse spectrum of the integrable LL Hamiltonian (4.1), which make it difficult to identify an appropriate microcanonical energy "window" encompassing many energy eigenstates while remaining narrow compared to the mean (postquench) energy E [Eq. (4.16)]. We therefore consider the canonical ensemble (CE). The density matrix of the CE is given by

$$\hat{\rho}_{\rm CE} = Z_{\rm CE}^{-1} \sum_{\{\lambda_j\}} e^{-\beta E_{\{\lambda_j\}}} |\{\lambda_j\}\rangle\langle\{\lambda_j\}|, \tag{4.25}$$

where the inverse temperature β is defined implicitly by $Z_{\mathrm{CE}}^{-1}\sum_{\{\lambda_j\}}\exp(-\beta E_{\{\lambda_j\}})E_{\{\lambda_j\}} = E$ and the partition function $Z_{\mathrm{CE}} = \sum_{\{\lambda_j\}}\exp(-\beta E_{\{\lambda_j\}})$. It is important to note that the only constraint (beyond that of fixed particle number) imposed in the CE is the conservation of the mean energy. Thus, in contrast to the definition of $\hat{\rho}_{\mathrm{DE}}$ in Eq. (4.20), the sum in Eq. (4.25) formally runs over all N-particle eigenstates $|\{\lambda_j\}\rangle$, regardless of parity and including those with nonzero values of the total momentum defined in Eq. (4.11). [8] Similarly to our calculations of DE expectation values, in practice we construct expectation values in the CE from a finite set of eigenstates, though we note that for a given level of accuracy their calculation requires us to include many more eigenstates than are required in the calculation of expectation values in the DE density matrix $\hat{\rho}_{\mathrm{DE}}$, as we discuss in Appendix 4.7.1.

4.5.1 Momentum distribution

In Fig. 4.7(a) we plot the DE momentum distribution $\widetilde{n}_{\mathrm{DE}}(k)$ for quenches of $N = 5$ particles to final interaction strengths $\gamma = 1, 10$, and 100, along with the corresponding momentum distributions $\widetilde{n}_{\mathrm{CE}}(k)$ predicted by the CE. Figure 4.7(b) shows the same momentum distributions on a logarithmic scale and reveals that for all interaction strengths, both $\widetilde{n}_{\mathrm{DE}}(k)$ and $\widetilde{n}_{\mathrm{CE}}(k)$ exhibit a power-law decay $\widetilde{n}(k) \propto k^{-4}$ (black dotted line) at high momenta. [9] This scaling behavior is a universal consequence of short-ranged two-body interactions in 1D [5, 305, 314] and indeed in higher dimensions [315, 365].

In the weakly excited case (Appendix 4.7.2) of a quench to $\gamma = 1$, the DE (red solid line) and CE (red dot-dashed line) momentum distributions appear similar, with the zero-momentum occupation $\widetilde{n}_{\mathrm{DE}}(0)$ being only slightly larger than the corresponding CE value and the occupations $\widetilde{n}(k_{\pm 1})$ of the smallest magnitude nonzero momenta being somewhat

[8] Although one could consider more refined definitions of the CE that are restricted so as to involve only states that have finite overlap with the initial state—e.g., states with zero total momentum or strictly parity-invariant states—we have found that these refined CE definitions do not yield correlation functions that agree more closely with the DE results. Therefore, for clarity, we simply take as our "reference" thermal ensemble the most common definition of CE, in which, at fixed particle number N, all conservation laws other than conservation of energy are ignored.

[9] We note that the accuracy with which we can resolve correlations at high values of k is ultimately limited by the density of the (Cartesian) position-space grid on which we calculate correlation functions. We stress that this effective "momentum cutoff" is independent of the size of the basis set used in our nonequilibrium calculations and does not affect the propagation of the LL solution following the quench, but merely limits the accuracy with which we can extract correlations from the solutions. In practice, we always choose the Cartesian grid density to be sufficiently high that the characteristic $\propto k^{-4}$ scaling of the high-momentum tail is observed over a broad range of momenta.

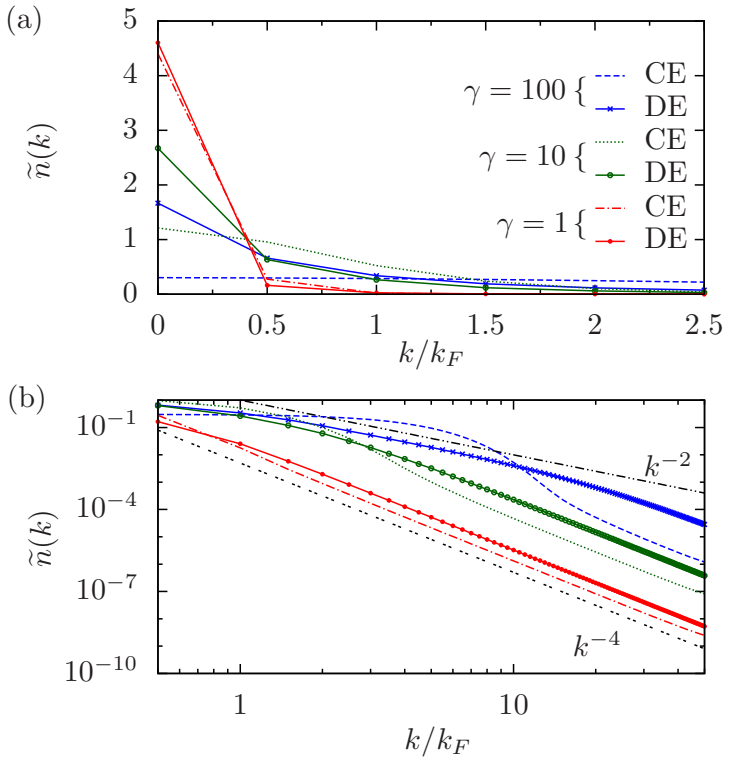

FIGURE 4.7: (a) Comparison of equilibrium momentum distributions $\widetilde{n}_{\mathrm{DE}}(k)$ and $\widetilde{n}_{\mathrm{CE}}(k)$ predicted by the DE and CE, respectively, for an interaction-strength quench of $N = 5$ particles. (b) The same momentum distributions on a double-logarithmic scale. The black dotted line indicates the universal $\propto k^{-4}$ power-law scaling [5] observed at high momenta k. For strong interactions, a power-law decay $\propto k^{-2}$ (black dot-dashed line) emerges at intermediate momenta.

smaller in the DE than in the CE. From Fig. 4.7(b) we observe that in this case both the DE momentum distribution and that of the CE deviate from the $\propto k^{-4}$ power-law scaling (black dotted line) only at the smallest nonzero momenta resolvable in the finite periodic geometry. In the relaxed (DE) state, our system is too small to observe the nontrivial long-wavelength behavior of the LL model for comparatively weak interactions $\gamma \lesssim 1$. In fact, many low-lying excitations of the LL system that would be excited by a quench to $\gamma = 1$ in an infinite system are not present in our finite-sized system. As a result our system is only weakly excited above the ground state of $\hat{H}$ by the quench and the relaxation dynamics associated with the dephasing of energy eigenstates are not observed. This results, in particular, in the near-monochromatic oscillations of $\widetilde{n}(0,t)$ for this quench, as discussed in Sec. 4.4.3 and Appendix 4.7.2.

We note from Fig. 4.7(a) that the zero-momentum occupation $\widetilde{n}_{\mathrm{DE}}(0)$ in the DE and the prediction $\widetilde{n}_{\mathrm{CE}}(0)$ of the CE for this quantity both decrease significantly with increasing

final interaction strength γ. However, the decrease in $\widetilde{n}_{\mathrm{CE}}(0)$ with increasing γ is much more pronounced than the corresponding decrease in $\widetilde{n}_{\mathrm{DE}}(0)$, and $\widetilde{n}_{\mathrm{DE}}(0)$ therefore exceeds $\widetilde{n}_{\mathrm{CE}}(0)$ by an increasingly large margin as γ increases. Figure 4.7(a) also reveals conspicuous differences, at larger values of γ, between the width and the shape of $\widetilde{n}_{\mathrm{DE}}(k)$ and those of $\widetilde{n}_{\mathrm{CE}}(k)$. In particular, $\widetilde{n}_{\mathrm{DE}}(k)$ remains convex on $k \geq 0$ for all considered final interaction strengths, whereas $\widetilde{n}_{\mathrm{CE}}(k)$ develops an increasingly broad concave hump at small k (cf. Ref. [273]) with increasing γ. For $\gamma = 100$ the width (half width at half maximum) of the CE momentum distribution is much greater than k_F, whereas $\widetilde{n}_{\mathrm{DE}}(k)$ is comparatively sharply peaked around $k = 0$. We observe from Fig. 4.7(b) that a scaling $\propto k^{-2}$ (black dot-dashed line) emerges at intermediate momenta for $\gamma \sim 100$. This same power-law scaling has been obtained analytically [73] in the singular limit of a quench to the TG limit of infinitely strong interactions, where it was found to persist in the limit $k \to \infty$. By contrast, the universal $\propto k^{-4}$ scaling of the momentum distribution at large k [5, 314, 315] is always observed in the quenches to finite final interaction strengths γ that we consider here.

We remark that at comparatively low temperatures, such that the LL system is in the quantum-degenerate regime, the known asymptotic form of the thermal-equilibrium first-order correlation function $g^{(1)}(x)$ at large separations x is an exponential decay [241, 311, 366], corresponding to a Lorentzian functional form for $\widetilde{n}(k)$ at small k. At increasingly higher temperatures, the effects of both interactions and particle statistics eventually become negligible, and $g^{(1)}(x)$ becomes Gaussian with width given by the thermal de Broglie wavelength (see, e.g., Ref. [272]), corresponding to a Gaussian momentum distribution $\widetilde{n}(k)$ that becomes increasingly broad with increasing temperature. Although Fig. 4.7 indicates that $\widetilde{n}_{\mathrm{CE}}(k)$ is consistent with these known thermal-equilibrium results, the momentum distributions $\widetilde{n}_{\mathrm{DE}}(k)$ we observe here show a qualitatively distinct behavior. In particular, for $\gamma = 100$, the Gaussian form of $\widetilde{n}_{\mathrm{CE}}(k)$ demonstrates that the energy imparted to the system by the quench, if redistributed during relaxation so as to agree with the principles of conventional statistical mechanics, would heat the system to temperatures far above quantum degeneracy. By contrast, the DE momentum distribution $\widetilde{n}_{\mathrm{DE}}(k)$ appears to retain the Lorentzian-like character expected for the LL model at nonzero but small temperatures, such that quantum-degeneracy effects remain significant. We note also that the coefficient $\lim_{k\to\infty} k^4 \widetilde{n}(k)$ of the high-momentum tail (i.e., the Tan contact [5, 314, 315]) in the DE is

always larger than that in the CE. In the case of $\gamma = 1$ this coefficient is larger in the DE as compared to the CE by a factor of approximately two, and its value in the DE exceeds that in the CE by an increasingly large factor as γ increases, being more than an order of magnitude larger in the case of $\gamma = 100$.

4.5.2 Second-order correlations

In Fig. 4.8(a) we plot the predictions $g^{(2)}_{\mathrm{DE}}(x)$ of the DE for the equilibrium second-order correlations of the postquench system, along with the corresponding predictions $g^{(2)}_{\mathrm{CE}}(x)$ of the CE for this quantity. For $\gamma = 1$ the nonlocal real-space correlation function $g^{(2)}_{\mathrm{DE}}(x)$ [small red circles in Fig. 4.8(a)] is similar to the CE form $g^{(2)}_{\mathrm{CE}}(x)$ (red dot-dashed line), and both are comparable to the form of $g^{(2)}(x)$ found for $\gamma \lesssim 1$ at zero temperature in previous works [6, 263, 264, 274], consistent with the weak excitation of the system observed in the behavior of the momentum distribution (Sec. 4.5.1) for this final interaction strength. We note that both the local second-order coherence $g^{(2)}_{\mathrm{DE}}(0)$ in the DE and that in the CE decrease significantly as γ is increased. However, the "Friedel" oscillations of wavelength $\sim 1/k_F$ that appear in $g^{(2)}(x)$ for strong interaction strengths $\gamma \gg 1$ at zero temperature [207, 254, 274] are not seen in either the DE or the CE predictions for the equilibrium second-order coherence at large values of γ. Indeed for $\gamma = 10$ and 100 the results for $g^{(2)}_{\mathrm{DE}}(x)$ are qualitatively similar to the behavior of the second-order coherence in the high-temperature fermionization regime [261, 274, 275], consistent with the results of the lattice-model simulations of Ref. [194] and studies of quenches to the TG limit [7, 8, 73, 210]. We note, however, that the dip in the second-order correlation function about $x = 0$ is significantly wider in the DE than in the CE for $\gamma = 10$ and 100. Moreover, for these large final interaction strengths the function $g^{(2)}_{\mathrm{DE}}(x)$ is not completely flat outside the central "fermionic" dip at small x and, in fact, as the separation x approaches the midpoint $L/2$ of the periodic geometry, the second-order coherence exhibits a small secondary dip to a value lower than the roughly constant value of $g^{(2)}_{\mathrm{DE}}(x)$ at intermediate separations. We have found that this feature is highly sensitive to the particle number N, varying between a small dip (as seen here) and a small peak for odd and even values of N, respectively, and we therefore identify it as a finite-size artifact that should gradually vanish with increasing system size.

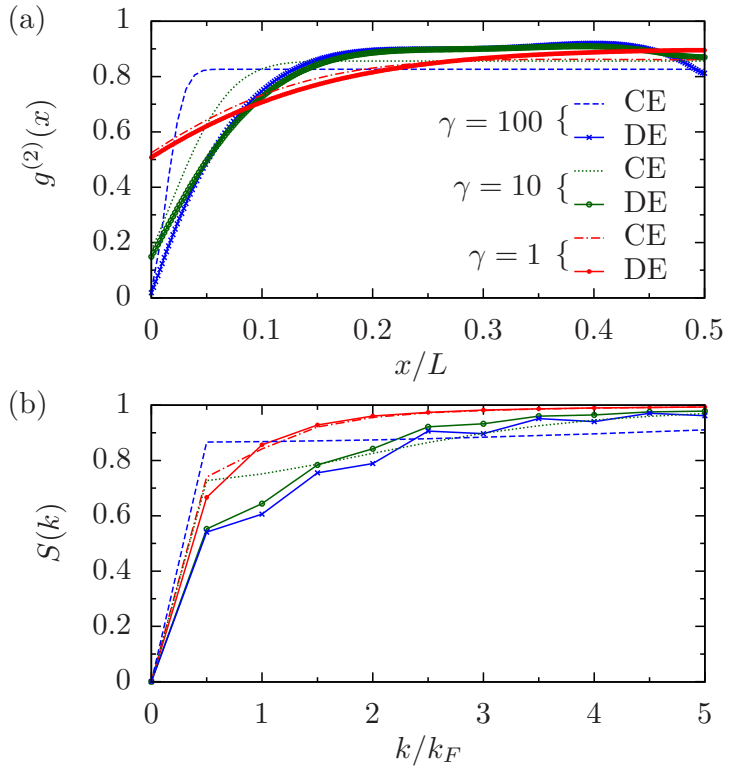

FIGURE 4.8: Second-order correlations in the DE for quenches of $N = 5$ particles to $\gamma = 1, 10$, and 100. (a) Second-order correlation function $g^{(2)}_{\mathrm{DE}}(x)$ and (b) corresponding structure factor $S_{\mathrm{DE}}(k_j)$. The legend is the same for both panels and is indicated in (a).

Figure 4.8(b) shows the DE predictions for the equilibrium structure factors $S_{\mathrm{DE}}(k)$ obtained from the correlation functions $g^{(2)}_{\mathrm{DE}}(x)$ plotted in Fig. 4.8(a) via Eq. (4.22), along with the corresponding CE structure factors $S_{\mathrm{CE}}(k)$. Unsurprisingly, for $\gamma = 1$ this representation of the second-order correlations in the DE is also similar to the predictions of the CE, whereas for both of the larger values of γ we consider, the DE prediction $S_{\mathrm{DE}}(k)$ differs markedly from $S_{\mathrm{CE}}(k)$ and also from the corresponding zero-temperature form of the structure factor (see, e.g., Refs. [6, 266]). In particular, the DE predictions for these structure factors have smaller magnitudes at small momenta $k \lesssim k_F$ than the corresponding CE structure factors. We note that our results for the equilibrium static structure factor following the quench are at least qualitatively similar to those of Refs. [8, 73], aside from the obvious distinction that the characteristic γ-independent value $S(0) = 1/2$ obtained in Ref. [8] is precluded in our calculations by particle-number conservation, which imposes $S_{\mathrm{DE}}(0) = 0$. [10]

[10] In fact, our results in Fig. 4.8(b) are not inconsistent with the structure factor exhibiting the limiting

4.5.3 Local correlations

We now compare the DE values $g^{(2)}_{\rm DE}(0)$ and $g^{(3)}_{\rm DE}(0)$ of the local second- and third-order correlation functions, respectively, to the predictions of the CE for these quantities. The dramatically reduced computational expense involved in calculating local correlation functions, as compared to nonlocal correlation functions such as $g^{(1)}(x)$ and $g^{(2)}(x)$, allows us to pursue our investigations to much larger values of γ than we have considered so far while maintaining a comparable level of accuracy (see Appendix 4.7.1). We therefore present in Fig. 4.9 results for $g^{(2)}_{\rm DE}(0)$ and $g^{(3)}_{\rm DE}(0)$ for final interaction strengths up to $\gamma = 10^3$.

In Fig. 4.9(a) we plot $g^{(2)}_{\rm DE}(0)$ for $N = 2, 3, 4$, and 5 particles (solid lines, bottom to top), together with the thermal-equilibrium values $g^{(2)}_{\rm CE}(0)$ obtained in the canonical ensemble, for $N = 3$ and 4 particles (red triangles and green circles, respectively). We observe that both ensembles predict $g^{(2)}(0)$ to exhibit behavior consistent with power-law decay $\propto 1/\gamma$ at large values of γ, though for any given value of γ and particle number N, the DE result $g^{(2)}_{\rm DE}(0)$ is somewhat smaller than $g^{(2)}_{\rm CE}(0)$. This behavior is consistent with the results of the generalized TBA calculations of Refs. [7, 8], which both predict an asymptotic form $g^{(2)}_{\rm GTBA}(0) \sim 8/(3\gamma)$ (black dot-dashed line) for the local second-order coherence following a quench of the LL-model interaction strength from zero to γ. As noted in Ref. [7], this prediction for the equilibrium postquench value of $g^{(2)}(0)$ has the same power-law scaling exponent as the corresponding prediction $g^{(2)}_{\rm GCE}(0) \sim 4/\gamma$ of the grand-canonical ensemble [7, 261] [11] (black dotted line), but a significantly smaller prefactor. We note not only that $g^{(2)}_{\rm DE}(0)$ here exhibits the same $\propto 1/\gamma$ scaling as $g^{(2)}_{\rm CE}(0)$ and that its prefactor is indeed smaller, but also that our results for $g^{(2)}_{\rm DE}(0)$ and $g^{(2)}_{\rm CE}(0)$ appear to be scaling towards the asymptotic predictions of Ref. [7, 8] for $g^{(2)}(0)$ in the generalized statistical ensembles considered in those works and the grand-canonical ensemble, respectively, as the particle number N is increased.

We now turn our attention to the local third-order correlation functions $g^{(3)}_{\rm DE}(0)$ and

behavior $\lim_{k\to 0} S_{\rm DE}(k) = 1/2$ in the thermodynamic limit [i.e., $S_{\rm DE}(k_1) \equiv S_{\rm DE}(2\pi/L) \to 1/2$ as $L \to \infty$ at fixed density n], which would agree with the thermodynamic-limit calculation of Ref. [8] aside from the singular point $k = 0$.

[11] For large γ, the spectrum of the LL Hamiltonian (4.1) approaches that of a system of free spinless fermions in 1D, for which (at fixed N) the mean energy $E \propto T$ in the limit of large T. Combining this with the linear dependence of the postquench system energy [Eq. (4.16)] on the final interaction strength γ and the analytic predictions $g^{(2)}(0) \propto T/\gamma^2$ and $g^{(3)}(0) \propto T^3/\gamma^6$ [261] appropriate to the high-temperature fermionization regime, we find $g^{(2)}_{\rm th}(0) \propto \gamma^{-1}$ and $g^{(3)}_{\rm th}(0) \propto \gamma^{-3}$.

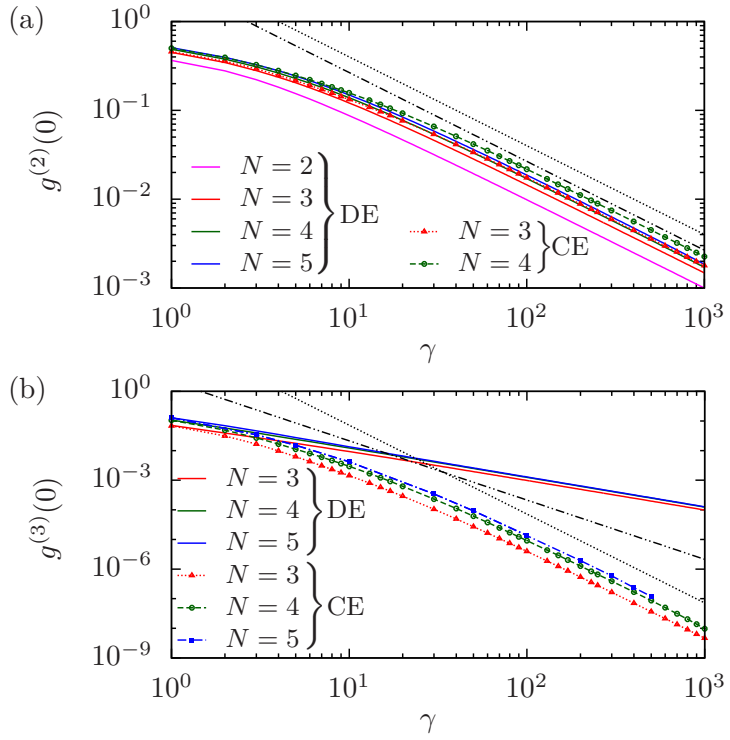

FIGURE 4.9: Comparison of equilibrium values of local correlation functions predicted by the DE and the CE. (a) Local second-order coherence functions $g^{(2)}_{\mathrm{DE}}(0)$ and $g^{(2)}_{\mathrm{CE}}(0)$. (b) Local third-order coherence functions $g^{(3)}_{\mathrm{DE}}(0)$ and $g^{(3)}_{\mathrm{CE}}(0)$. In both panels, black dotted and dot-dashed lines indicate thermodynamic-limit predictions for the corresponding correlation functions obtained in the grand-canonical ensemble and the generalized TBA calculations of Refs. [7, 8], respectively (see text).

$g^{(3)}_{\mathrm{CE}}(0)$, which we plot in Fig. 4.9(b) for $N = 3, 4$, and 5 particles (solid lines and symbols, respectively). We observe that for all three particle numbers, the behavior of $g^{(3)}_{\mathrm{DE}}(0)$ is consistent with power-law scaling $\propto \gamma^{-1}$ at large γ, in pronounced disagreement with the prediction $g^{(3)}_{\mathrm{GTBA}}(0) \sim 32/(15\gamma^2)$ of Refs. [7, 8] (black dot-dashed line). By contrast, the results of our CE calculations appear to be scaling towards the grand-canonical prediction[11] $g^{(3)}_{\mathrm{GCE}}(0) \sim 72/\gamma^3$ (black dotted line) with increasing N.

Although we employ a sufficiently large basis of LL eigenstates in our calculation of DE expectation values that the values of the local coherences appear reasonably insensitive to the precise number of states we use, the accuracy of our results for the local coherences is inevitably limited by this eigenstate "cutoff" (see Appendix 4.7.1). However, we stress that the local correlation function $g^{(3)}(0)$ is [like $g^{(2)}(0)$] non-negative in any LL eigenstate $|\{\lambda_j\}\rangle$, and raising the cutoff to include some or all of the weakly occupied eigenstates

omitted in our numerical calculation of this quantity could therefore only *increase* its value. Moreover, the total occupation of neglected eigenstates in our DE calculations increases with increasing γ (Appendix 4.7.1). Thus, we expect our calculated value of $g^{(3)}_{\mathrm{DE}}(0)$ to increasingly *underestimate* the exact value of this quantity with increasing γ; i.e., the scaling $g^{(3)}_{\mathrm{DE}}(0) \propto \gamma^{-1}$ shown in Fig. 4.9(b) should constitute an *upper* bound to the rate at which $g^{(3)}_{\mathrm{DE}}(0)$ scales to zero, whereas the prediction of Refs. [7, 8] vanishes even more rapidly. Of course, our results here are for strongly finite-sized systems of at most $N = 5$ particles, and the reader might expect that the discrepancy between $g^{(3)}_{\mathrm{DE}}(0)$ and the results of Refs. [7, 73] should disappear in the thermodynamic limit. However, results for local correlation functions at zero temperature [165, 262] and our results for $g^{(2)}_{\mathrm{DE}}(0)$ [Fig. 4.9(a)] both suggest that local correlations, and in particular their scaling with interaction strength, become increasingly insensitive to finite-size effects as the TG limit is approached. We note that the power-law behavior $g^{(3)}_{\mathrm{GTBA}}(0) \propto \gamma^{-2}$ obtained in the calculations of Ref. [7, 8] lies in between the thermal scaling $g^{(3)}_{\mathrm{GCE}}(0) \propto \gamma^{-3}$ and the result $g^{(3)}_{\mathrm{DE}}(0) \propto \gamma^{-1}$ of our DE calculations. We remark that this may be an indication that the GGE and quench-action calculations of Refs. [7] and [8], respectively, only partially account for the constraints to which the integrable LL system is subject. The origin of this discrepancy remains an important question for future study.

4.6 Summary

We have investigated the dynamics of the Lieb–Liniger model of 1D contact-interacting bosons following a sudden quench of the interaction strength from zero to a positive value. We computed the long-time evolution of systems containing up to five particles by expanding the time-evolving pure-state wave function of the postquench system over a truncated basis consisting of all energy eigenstates with (absolute) overlap with the initial state of the system larger than a chosen threshold. These overlaps, and the matrix elements of observables between energy eigenstates, were obtained by symbolic evaluation of the corresponding coordinate-space integrals in terms of the rapidities that label the states, which were themselves obtained as numerical solutions of the appropriate Bethe equations.

We found that for quenches to comparatively small final interaction strengths ($\gamma \lesssim 1$),

observables exhibit near-monochromatic oscillations. We identified this as a consequence of the gap in the energy spectrum induced by the finite size of the system, which severely suppresses the excitation of the system for small values of the final interaction strength, resulting in quasi-two-level system dynamics. For stronger interaction strengths, we observed results for the first- and second-order correlations consistent with the relaxation of the integrable many-body system due to the dephasing of the N-particle energy eigenstates. We also observed the propagation of correlation waves in the second-order correlations of the system, which are related to density modulations. We found that the behavior of the fidelity between the initial (prequench) state and the state at time t following the quench is qualitatively similar to that of nonlocal quantities such as the occupation of the zero-momentum single-particle mode, indicating that these experimentally relevant quantities provide effective probes of the eigenstate dephasing of the N-body system. Local correlations, however, decay much more rapidly and do not necessarily reflect the relaxation of the system as a whole.

We assessed the character of correlations in the relaxed state by comparing diagonal-ensemble correlations to those of the canonical ensemble, in which only the conservation of energy and normalization are taken into account. In particular, we observed that for quenches to large γ, the relaxed state of the system exhibits a momentum distribution consistent with the asymptotically Lorentzian form expected for the Lieb–Liniger model at low-temperature thermal equilibrium. This is in stark contrast to the canonical-ensemble prediction for the relaxed postquench state, which yields a Gaussian momentum distribution consistent with temperatures well above quantum degeneracy. Our calculations also indicate that in the Tonks–Girardeau limit $\gamma \to \infty$ the local second-order coherence $g^{(2)}_{\mathrm{DE}}(0)$ scales towards zero with the same power law as the corresponding correlation function in the canonical ensemble (i.e., like $1/\gamma$), but with a smaller prefactor, consistent with the results of Refs. [7, 8]. However, although our results for the local third-order coherence in the canonical ensemble are consistent with the expected behavior of a thermal system, our results for $g^{(3)}(0)$ in the nonthermal diagonal ensemble show a scaling $\propto \gamma^{-1}$, slower than both the $\propto \gamma^{-3}$ scaling expected for a thermal state and the $\propto \gamma^{-2}$ scaling predicted by the generalized thermodynamic Bethe-ansatz calculations of Refs. [7, 8]. Whether this discrepancy is merely a consequence of the finite size of our system or is indicative of

subtleties not captured in the methodologies of Refs. [7, 8] is an important question for further study.

4.7 Supplement

4.7.1 Basis-set truncation

Expression (4.17) for $|\psi(t)\rangle$ [and, consequently, Eqs. (4.18)–(4.20) derived from it] involves a sum $\sum_{\{\lambda_j\}}$ over all zero-momentum, parity-invariant states $|\{\lambda_j\}\rangle$. In principle, there are an infinite number of such states that contribute to the sum. However, in practical numerical calculations, we must truncate the sum to a finite number of terms in some manner. The accuracy of our calculations based on this truncated sum can then be quantified by the sum rules satisfied by the conserved quantities of the system. We focus primarily on the normalization sum rule $\sum_{\{\lambda_j\}} |C_{\{\lambda_j\}}|^2 = 1$ (cf. Ref. [209]).

In our calculations we include all states $|\{\lambda_j\}\rangle$ for which the absolute overlap $|\langle\{\lambda_j\}|\psi_0\rangle|$ with the initial state [Eq. (4.15)] is larger than some threshold value. Our approach exploits the fact that the solutions $\{\lambda_j\}$ of the Bethe equations (4.6) are in one-to-one correspondence [219] with the (half-)integers $\{m_j\}$ that appear in Eq. (4.6). As the states $|\{\lambda_j\}\rangle$ are parity invariant, we can choose to label the rapidities such that $\lambda_j = -\lambda_{N+1-j}$, where $\lambda_1 > \lambda_2 > \cdots > \lambda_N$. Then we can label the states simply by $(m_1, m_2, \ldots, m_{\lfloor (N+1)/2 \rfloor})$, where $\lfloor x \rfloor$ denotes the integer part of x. We specialize hereafter to the case $N = 5$, which is the largest N for which we consider the dynamics in this article. Our approach reduces in a natural way to the cases of $N \leq 4$. The states can be grouped into families labeled by $m_1 = 2, 3, \ldots$, where within each family the second quantum number can assume values $1 \leq m_2 < m_1$ (and $m_3 = 0$). We have found from our explicit evaluation of the overlaps [165] that $|\langle\{\lambda_j\}|\psi_0\rangle|$ decreases monotonically with increasing m_2 within each family m_1 and, moreover, that the first member $(m_1, 1, 0)$ of each family m_1 has a larger (absolute) overlap with $|\psi_0\rangle$ than the first member $(m_1 + 1, 1, 0)$ of the next family [8, 165, 307–309]. [12] We therefore construct the basis by considering in turn each family m_1 and including all states within that family for which the overlap with the initial state exceeds our chosen threshold value. Eventually, for some value of m_1, even the first state $(m_1, 1, 0)$ of the family has overlap with $|\psi_0\rangle$ smaller than the threshold, at which point all states that meet the overlap threshold have been exhausted. The basis so constructed therefore comprises the $\mathcal{N}$ states

[12] In practice, we find that the results we obtain for the overlaps from our method [165] agree with the recently derived analytical expressions for these quantities [8, 307–309], which imply, in particular, that $\langle\{\lambda_j\}|\psi_0\rangle \sim 1/\lambda_j^2$ as any $\lambda_j \to \infty$.

TABLE 4.1: Basis-set sizes and sum-rule violations for time-evolving correlations and statistical-ensemble expectation values. Energy cutoff $E_{\rm cut}$ applies only for CE calculations, and the CE density matrix defined in Eq. (4.25) automatically satisfies the normalization sum rule.

γ	Type [a]	No. states	ΔN	ΔE	$E_{\rm cut}/k_F^2$
1	$\langle\hat{O}(t)\rangle$	1221	5×10^{-8}	2×10^{-3}	N/A
1	DE	6770	4×10^{-10}	5×10^{-4}	N/A
1	CE	3.7×10^{6}	N/A	2×10^{-7}	4.0×10^{2}
10	$\langle\hat{O}(t)\rangle$	1221	7×10^{-6}	2×10^{-2}	N/A
10	DE	6770	8×10^{-8}	5×10^{-3}	N/A
10	CE	3.7×10^{6}	N/A	8×10^{-6}	4.0×10^{2}
100	$\langle\hat{O}(t)\rangle$	1221	10^{-3}	2×10^{-1}	N/A
100	DE	6770	3×10^{-5}	5×10^{-2}	N/A
100	CE	3.7×10^{6}	N/A	8×10^{-6}	4.0×10^{2}

[a] Fidelities $F(t)$ are calculated from the DE basis sets.

with the largest overlap with $|\psi_0\rangle$ and thus minimizes the violation $\Delta N = 1-\sum_{\{\lambda_j\}}|C_{\{\lambda_j\}}|^2$ of the normalization sum rule for this basis size.

For an integrable system such as we consider here, the normalization is just one of an infinite number of sum rules defined by the conserved quantities $Q^{(m)} = \sum_j(\lambda_j)^m$ of the LL Hamiltonian (4.1). However, all the odd charges $Q^{(2n+1)}$, with n an integer, are zero by the constraint to parity-invariant states. Moreover, even charges $Q^{(2n)}$ with $2n \geq 4$ are formally singular [7], diverging as any rapidity $\lambda_k \in \{\lambda_j\}$ is increased toward infinity. Thus, the only nontrivial and regular conserved quantity other than the normalization is the energy $\langle\hat{H}\rangle = \sum_{\{\lambda_j\}}|C_{\{\lambda_j\}}|^2\sum_k(\lambda_k)^2$ [cf. Eq. (4.10)]. We note that this quantity converges as $1/\lambda_j$, which is much slower than the $\propto 1/\lambda_j^3$ convergence of the normalization. We characterize the saturation of this sum rule by the energy sum-rule violation $\Delta E = (E-\sum_{\{\lambda_j\}}|C_{\{\lambda_j\}}|^2\sum_k(\lambda_k)^2)/E$, where E is the exact postquench energy [Eq. (4.16)]. As a consequence of the slow convergence of the energy with increasing basis-set size, the energy sum rule is, in general, less well satisfied in our calculations than the normalization sum rule.

We note also that the evaluation of time-dependent observables [Eq. (4.18)] involves a double summation over $\{\lambda_j\}$ and is thus more numerically demanding than the calculation of correlations in the DE [Eq. (4.19)], for which only a single sum occurs (i.e., only diagonal elements contribute). An exception is the time-evolving fidelity $F(t)$, which can be written

TABLE 4.2: Basis-set sizes and sum-rule violations for the local correlation functions plotted in Fig. 4.9.

N	Type	No. states	ΔN [a]	ΔE [a]	E_{cut}/k_F^2
3	DE	10^4	10^{-8}	2×10^{-2}	N/A
3	CE	3.9×10^5	N/A	10^{-6}	4.8×10^3
4	DE	9.5×10^4	3×10^{-6}	5×10^{-3}	N/A
4	CE	3.2×10^6	N/A	10^{-6}	1.6×10^3
5	DE	1.9×10^5	5×10^{-6}	5×10^{-2}	N/A
5	CE	5.9×10^6	N/A	5×10^{-7}	4.8×10^2 [b]

[a] Sum-rule discrepancies quoted are those for $\gamma = 10^3$ ($\gamma = 5 \times 10^2$ for ΔE in the $N = 5$ CE).
[b] For quenches to $\gamma < 50$, cutoff energy $E_{\mathrm{cut}} = 4.0 \times 10^2\, k_F^2$.

as the modulus square of a single sum over eigenstates [cf. Eq. (4.24)]. We list the sizes of the basis sets employed in our calculations, together with the resulting violations ΔN and ΔE of the norm and energy sum rules, respectively, in Table 4.1. For expectation values in the CE [Eq. (4.25)], the truncation of the basis set is most appropriately performed by retaining all states with energy E below some cutoff energy E_{cut}. The inverse temperature β is then chosen as that which, within a prescribed tolerance level, minimizes the energy sum-rule violation ΔE. In this case, the sum is not restricted to parity-invariant, or even zero-momentum, states. However, the weights of states in the ensemble decrease exponentially with energy, and we have found that the energy cutoffs used in our CE calculations, which we also list in Table 4.1, are sufficiently large to ensure saturation of the momentum distributions plotted in Fig. 4.7.

The results for the local second- and third-order correlation functions presented in Fig. 4.9 constitute a more demanding test of numerical accuracy, due to the large values of γ considered. We list the sizes of the basis sets used in these calculations and the resulting sum-rule violations in Table 4.2.

4.7.2 Post-quench energy and finite-size gap

In Fig. 4.10 we plot the postquench energy E [Eq. (4.16)] as a function of the final interaction strength γ (blue dotted line). For comparison, we also plot the energy $E^{(0)}(\gamma)$ of the (N-particle) ground state of the LL Hamiltonian (4.1) with interaction strength γ (red solid

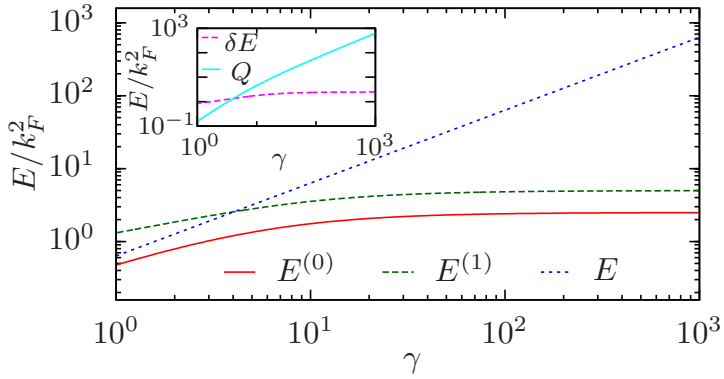

FIGURE 4.10: Energy of a system of $N = 5$ particles following a quench of the interaction strength from zero to $\gamma > 0$. For comparison, the energy $E^{(0)}$ of the ground state of $\hat{H}$ and the energy $E^{(1)}$ of the lowest-lying excited state of $\hat{H}$ that has finite overlap with the initial state $|\psi_0\rangle$ are also shown. Inset: Heat Q added to the system by the quench and the energy gap δE between the ground state and the lowest-lying state that has finite overlap with the initial state (see text).

line). The difference between these two energies, $Q \equiv E - E^{(0)}(\gamma)$, can be identified as the heat added to the system by the quench [367], which we plot in the inset to Fig. 4.10 (cyan solid line).

We note that although the excitation spectrum of the LL system is gapless in the thermodynamic limit, in a finite-sized system a gap of order $1/L$ [207] (and thus $\sim 1/N$ at fixed density) between the energies of the ground state and the lowest-lying excited state(s) appears. In Fig. 4.10 we plot (green dashed line) the energy $E^{(1)}$ of the lowest-lying state that has finite overlap with the initial state (see Sec. 4.4). We observe that the gap $\delta E = E^{(1)} - E^{(0)}$ between this energy and that of the ground state is $\sim 2k_F^2$ for the system sizes we consider (magenta dashed line in inset to Fig. 4.10). We note that for large $\gamma \gg 1$, the heat Q added to the system is much larger than the finite-size gap δE, whereas for $\gamma \lesssim 10$ the two energies are comparable, and for $\gamma \sim 1$, the gap is, in fact, larger than the added heat Q. It is clear, therefore, that in this regime the system can only be weakly excited above the ground state of $\hat{H}$ by the quench, due to the presence of the finite-size gap. Thus, in quenches to $\gamma = 1$, we observe almost purely monochromatic oscillations of observables, as many low-lying excitations of the formally gapless system are not present in the finite geometry and the dynamics of the system are dominated by the two most highly occupied eigenstates of $\hat{H}$. By contrast, for large values of $\gamma \gtrsim 10$, the finite-size gap is relatively small compared to the energy imparted to the system during the quench, and as a result many energy eigenstates contribute significantly to the postquench dynamics. Thus, for

quenches to large values of γ many states are available to realize the eigenstate-dephasing picture of relaxation dynamics, consistent with the results of our calculations. [13]

[13] We note that this implies that the crossover from regular to irregular dynamics observed in the calculation of Berman *et al.* [285] and interpreted by those authors as accompanying the onset of beyond-mean-field correlations is also a finite-size artifact.

5

Correlations and quench dynamics of the one-dimensional Bose gas with attractive interactions via the coordinate Bethe ansatz

So far, our focus has been on the dynamics and relaxation of the Lieb–Liniger model with repulsive interactions. In this chapter, we apply the methodology developed in Chapter 3 to the attractively interacting gas. There has been renewed interest in the properties of the system with attractive interactions from two different communities: First, it was suggested that a black hole can be described as a system of gravitons trapped at a quantum critical point, which maps onto the one-dimensional Bose gas with attractive interactions [368, 369]. The latter has a quantum critical point at a certain interaction strength, marking the emergence of a bright soliton. Second, the solution to the Kardar-Parisi-Zhang equation for the noisy growth of a one-dimensional interface can be mapped onto a random-directed polymer prob-

lem [370], whose generating function can be mapped onto the Lieb–Liniger model with attractive interactions [371]. For certain initial conditions, the overlaps of the ideal gas ground state with the interacting system following an interaction quench are needed [325, 372].

In the context of ultracold gases, the Bethe ansatz solution can provide insight into the properties of quantum bright solitons [373, 374]. However, few studies of correlation functions beyond the mean-field level exist in the literature, partly due to the additional complexities compared to the repulsively interacting system due to the nature of Bethe ansatz eigenstates.

The following is a draft of a manuscript about to be uploaded to the arxiv preprint server.

5.1 Abstract

We study the Lieb–Liniger model of a one-dimensional gas of bosons interacting via an attractive delta-function potential using the coordinate Bethe ansatz. We consider the case of a finite-size ring, which in the mean-field limit exhibits a quantum phase transition between a uniform density ground state and a bright soliton as the interactions become increasingly attractive. Firstly, we calculate the zero-temperature correlation functions for seven particles in the vicinity of the critical point, and compare our results with the predictions of mean-field theory. Secondly, we consider the dynamics of a system of four particles undergoing a quench from the ideal-gas ground state to increasingly attractive interactions. We characterize the time-evolution of correlation functions and their infinite-time limit, and contrast these quantities to the corresponding ones obtained for quenches to repulsive interactions of the same magnitude. The difference in these quantities is traced back to bound states of the attractively interacting gas.

5.2 Introduction

The near perfect isolation and exquisite experimental control possible for many system parameters in ultra-cold atomic gases has enabled the experimental study of nonequilibrium dynamics of closed many-body quantum systems [99]. A number of different trapping geome-

tries have lead to the realization of one-dimensional systems [2, 39, 95, 96, 179, 247, 248, 276–284], which are well described by the paradigmatic exactly solvable Lieb–Liniger model of point-like interacting bosons [56, 176, 231]. The integrability of the model means that the powerful methods of the Bethe ansatz in its various forms become available for its study [56, 207, 219, 223, 231].

One of the simplest methods of taking the system out of equilibrium is to perform an instantaneous change of a parameter in the Hamiltonian – a so-called quench. Several authors have considered the dynamics of repulsively interacting systems, where one particularly well-studied scenario is an interaction quench starting from the zero-temperature ideal gas [7, 73, 165, 166, 204, 210, 324–326]. There have been fewer studies of the one-dimensional Bose gas with *attractive* interactions.

The ground state wave function for the attractive 1D Bose gas on the infinite line was constructed by McGuire [213] and consists of a single bound state of all the particles. For systems with finite spatial extent, the coordinate Bethe ansatz provides solutions in terms of quasi-momenta (or rapidities), which for attractive interactions are generally complex-valued. Correlation functions of the ground state in a hard-wall trap for up to four particles were studied in Ref. [375]. Since the energy of the ground state is proportional to $-N^3$, where N is the particle number, a proper thermodynamic limit with $N, L \to \infty$ and fixed density $n = N/L$ does not exist [56, 223, 376]. However, the zero-density limit $L \to \infty$, $N = const$ is well defined and non-trivial for attractive interactions. In this limit, some correlation functions are accessible with algebraic Bethe-ansatz methods [222, 228]. An alternative large-system limit is given by $N \to \infty$ in a finite ring of circumference L. In fact, in the Bogoliubov limit $g \to 0$, $N \to \infty$, $gN = const$, a mean-field Gross–Pitaevskii description of the finite circumference system is valid, and predicts the appearance of a localized bright-soliton state beyond some threshold interaction strength [182, 377]. This has been interpreted as evidence for spontaneous breaking of translational symmetry in the infinite-N, finite-L limit [182, 184]. However, Bogoliubov theory predicts a diverging depletion in the vicinity of the crossover, invalidating the mean-field description in this regime [182]. A many-body analysis for finite N reveals a smooth crossover between the uniform condensate state and a correlated state with solitonic correlations, as expected in a finite system [182–185, 378]. Such an analysis also indicates that the gap at the crossover

point vanishes like $N^{-1/3}$ [182]. The Bogoliubov-theory prediction of a vanishing gap at the crossover point in the semiclassical $N \to \infty$ limit is thus regained. The crossover to the correlated state has therefore been interpreted [182] as a kind of effective quantum phase transition in the finite-L system, though it should be stressed that this crossover cannot be considered a finite-system precursor of a true quantum phase transition, as no true thermodynamic limit exists.

In a full many-body quantum-mechanical treatment, eigenstates respect the symmetry of their Hamiltonian, but contain solitonic structure in (pair) correlations. Therefore, localized bright solitons can be constructed from superpositions of certain exact many-body wave functions [373, 374, 379], which are given by the Bethe ansatz [56, 213, 231]. Recently, an integral equation for the density of Bethe rapidities of the ground state for particle number $N \to \infty$, valid across the phase transition point, has been derived and signatures of the phase transition were observed in the density of rapidities [229]. Bright-soliton-like structures have also been observed experimentally in elongated quantum gases [380–386].

A particular *non-equilibrium* scenario for the attractive 1D Bose gas was proposed in Refs. [215, 216] and subsequently realized experimentally in the group of Nägerl [179]. The experiment began by preparing the ground state at strong repulsive interactions, before suddenly switching the interactions to be strongly attractive using a confinement-induced resonance [176]. In doing so a metastable state was created, the so-called super-Tonks gas [215–218, 387]. The metastability of the system is due to the fact that the super-Tonks state is a highly excited eigenstate of the Lieb–Liniger model with "fermonized" character [217], and the preparation of this state is very efficient because the overlap between the Tonks–Girardeau state and the super-Tonks state is very large for large attractive interactions [218, 387]. This comparatively tractable case also allows for a Luttinger liquid description [388], as well as numerical studies with algebraic Bethe-ansatz [388] and tensor-network methods [195]. Local correlation functions can be determined by combining the equation of state of the super-Tonks gas with the Hellmann–Feynman theorem [218], and also in the non-relativistic limit of a relativistic field theory (sinh–Gordon model) [230].

There are fewer results available for more general interaction quench scenarios of the one-dimensional Bose gas with attractive interactions. References [301, 302] introduced a Bethe-ansatz method for calculations of dynamical correlation functions for a few particles and in

the infinite-volume limit, which is based on the Yudson contour-integral representation and puts the system in the strongly interacting regime away from the phase transition [229]. Recently, the local second-order correlation function in the relaxed state following a quench from the ideal-gas ground state to attractive interactions was calculated. This was done for the entire range of attractive interactions in the thermodynamic limit[1] [9, 10] using the quench-action method [202, 203]. Within this approach, the relaxed value of certain observables can be calculated in a single representative eigenstate of the system. This eigenstate was found in Refs. [9, 10] by means of a generalized thermodynamic Bethe Ansatz. Invoking the Hellmann–Feynman theorem, the authors found an expression for the stationary local second-order coherence in terms of an infinite number of coupled integral equations, which they solved numerically by truncation.

In the present work we make use of the coordinate Bethe-ansatz based approach of Refs. [165, 166], which enables us to calculate the stationary and dynamical values of several correlation functions for system sizes up to seven particles. We provide a brief summary of the Lieb-Liniger model in Sec. 5.3 and provide definitions of the correlation functions we evaluate. We also discuss the numerical complications for the attractively interacting gas due to complex Bethe rapidities, and explain how we solve them, as well as the limitations they impose. In Sec. 5.4, we calculate the ground state correlation functions for up to seven particles for values of the interaction strength in the vicinity of the quantum phase transition. We also consider the strongly interacting regime for four particles. In Sec. 5.5, we compute several nonequilibrium correlation functions following an interaction quench from zero to attractive values, for up to four particles, covering the weakly interacting regime below and above the mean-field transition point, as well as the strongly interacting regime. We also compare the dynamics to that of a system following an interaction quench to repulsive interactions of the same magnitude. In Sec. 5.6 we present results on correlation functions within the diagonal ensemble, before concluding in Sec. 5.7.

[1] The quench deposits a finite amount of energy in the system and therefore the thermodynamic limit is well-defined in this case.

5.3 Methodology

5.3.1 Lieb–Liniger model

The Lieb–Liniger model [56, 231] describes a system of N indistinguishable bosons subject to a delta-function interaction potential in a one-dimensional geometry. The Hamiltonian is

$$\hat{H} = -\sum_{i=1}^{N} \frac{\partial^2}{\partial x_i^2} + 2c \sum_{i<j}^{N} \delta(x_i - x_j), \tag{5.1}$$

where c is the interaction strength, and we have set $\hbar = 1$ and the particle mass $m = 1/2$. The interactions are attractive for $c < 0$, and repulsive for $c > 0$. The solutions of Hamiltonian (5.1) in the ordered spatial permutation sector R_p ($x_1 \leq x_2 \leq \cdots \leq x_N$) are given by the coordinate Bethe ansatz in the form [207]

$$\zeta_{\{\lambda_j\}}(\{x_i\}) \equiv \langle \{x_i\} | \{\lambda_j\} \rangle = A_{\{\lambda_j\}} \sum_{\sigma} (-1)^{[\sigma]}\, a(\sigma)\, \exp\Big[i \sum_{m=1}^{N} x_m \lambda_{\sigma(m)} \Big] \tag{5.2}$$

where the sum runs over all permutations $\sigma = \{\sigma(1), \sigma(2), \cdots, \sigma(N)\}$ of $\{1, 2, \cdots, N\}$, $(-1)^{[\sigma]}$ denotes the sign of the permutation and the scattering factors

$$a(\sigma) = \prod_{k>l} \left(\lambda_{\sigma(k)} - \lambda_{\sigma(l)} - ic \right). \tag{5.3}$$

The sets $\{\lambda_j\}$ are the so-called Bethe rapidities. The normalization constant $A_{\{\lambda_j\}}$ is given by [207]

$$A_{\{\lambda_j\}} = \left[N!\, \det\{M_{\{\lambda_j\}}\} \prod_{k>l} [(\lambda_k - \lambda_l)^2 + c^2] \right]^{-1/2}, \tag{5.4}$$

where $M_{\{\lambda_j\}}$ is the $N \times N$ matrix with elements

$$[M_{\{\lambda_j\}}]_{kl} = \delta_{kl} \Big(L + \sum_{m=1}^{N} \frac{2c}{c^2 + (\lambda_k - \lambda_m)^2} \Big) - \frac{2c}{c^2 + (\lambda_k - \lambda_l)^2}. \tag{5.5}$$

Applying periodic boundary conditions leads to a set of N equations for N particles, the so-called Bethe equations

$$\mathrm{e}^{iL\lambda_j} = \prod_{l \neq j} \frac{(\lambda_j - \lambda_l) + ic}{(\lambda_j - \lambda_l) - ic}, \tag{5.6}$$

where L is the length of the system. The rapidities determine the total momentum $P = \sum_{j=1}^{N} \lambda_j$ and energy $E = \sum_{j=1}^{N} \lambda_j^2$ of the system in each eigenstate. The ground state of the system for attractive interactions is an N–body bound state (the finite-system analogue of the McGuire cluster state [213]) and has purely imaginary rapidities [226, 227]. All eigenstates corresponding to bound states have some Bethe rapidities with imaginary component. This is in contrast to the repulsively interacting system ($c > 0$), for which the solutions to the Bethe equations (5.6) are characterized by purely real rapidities $\{\lambda_j\}$. The latter are usually parameterized by a set of quantum numbers $\{m_j\}$, which for $c \to +\infty$ are proportional to $\{\lambda_j\}$, see e.g. Ref. [207]. For the attractively interacting gas, it is more convenient to enumerate the solutions of the Bethe equations (5.6) with their corresponding N ideal-gas (i.e. $c = 0$) quantum numbers $\{n_j\}$, where $k_j = 2\pi n_j/L$ are the free single-particle momenta [226].[2] By convention we order the $\{n_j\}$ of an eigenstate from largest to smallest.[3] In this paper, where we consider ground state correlations and quenches from the ideal-gas ground state, we only need to consider eigenstates that are parity invariant, i.e. where $n_j = -n_{N+1-j}$ for $j \in [1, N]$. Thus, we can label all eigenstates by $\lfloor N/2 \rfloor$ quantum numbers, where $\lfloor \dots \rfloor$ is the floor function, which by convention we choose to be the non-negative values (for odd N, $n_{(N+1)/2} = 0$).

Interactions in the Lieb–Liniger model are characterized by the dimensionless coupling $\gamma \equiv c/n$, where $n = N/L$ is the 1D density, which in the thermodynamic limit for repulsive interactions is the only parameter at zero temperature. In finite systems, physical quantities also depend on the particle number N, whereas the length L of our system is arbitrary. Therefore, we use the finite-system definition of the Fermi momentum $k_F = (2\pi/L)(N-1)/2$, which is the largest rapidity in the ground state for $c \to +\infty$, and measure time in units of k_F^{-2}, energy in units of k_F^2, and length in units of k_F^{-1}.

[2] The energy of an eigenstate with $\{n_j\}$ for $c \to 0^-$ connects to the energy of the eigenstate with $\{m_j^{(0)} + n_j\}$ for $c \to 0^+$. Here, $\{m_j^{(0)}\}$ are the ground state quantum numbers for $c > 0$.

[3] In slight abuse of notation, we keep using curly brackets as delimiters, even though $\{n_j\}$ is technically a tupel.

5.3.2 Correlation functions

The static and dynamic behavior of the Lieb-Linger gas can be characterized by the normalized m^{th}-order correlation functions

$$g^{(m)}(x_1,\ldots,x_m,x_1',\ldots,x_m';t) \equiv \frac{\left\langle \hat{\Psi}^\dagger(x_1)\cdots\hat{\Psi}^\dagger(x_m)\hat{\Psi}(x_1')\cdots\hat{\Psi}(x_m')\right\rangle}{\left[\langle\hat{n}(x_1)\rangle\cdots\langle\hat{n}(x_m)\rangle\langle\hat{n}(x_1')\rangle\cdots\langle\hat{n}(x_m')\rangle\right]^{1/2}}, \tag{5.7}$$

where $\hat{\Psi}^{(\dagger)}(x)$ is the annihilation (creation) operator for the Bose field, the density operator $\hat{n}(x) \equiv \hat{\Psi}^\dagger(x)\hat{\Psi}(x)$, and $\langle\cdots\rangle \equiv \mathrm{Tr}\{\hat{\rho}(t)\cdots\}$ denotes an expectation value with respect to a Schrödinger-picture density matrix $\hat{\rho}(t)$. Due to the translational invariance of the system the density is constant (i.e. $\langle\hat{n}(x)\rangle \equiv n$), and the correlation functions are invariant under global coordinate shifts $x \to x + d$. Without loss of generality, we therefore set one of the spatial coordinates to zero and focus on the first-order correlation function $g^{(1)}(x) \equiv g^{(1)}(0,x)$, the second-order correlation function $g^{(2)}(x) \equiv g^{(2)}(0,x,x,0)$, and the local third-order coherence $g^{(3)}(0) = \langle[\hat{\Psi}^\dagger(0)]^3[\hat{\Psi}(0)]^3\rangle/n^3$. We also consider the momentum distribution

$$\widetilde{n}(k) = n\int_0^L dx\; e^{-ikx}g^{(1)}(x). \tag{5.8}$$

The periodic boundary conditions lead to quantized single-particle momenta $k_j = 2\pi j/L$, where j is an integer.

For a system in a pure state $|\psi(t)\rangle$, Eq. (5.7) reads

$$\begin{aligned} g^{(m)}(x_1,\ldots,x_m,x_1',\ldots,x_m';t) &= \frac{1}{n^m}\langle\psi(t)|\hat{\Psi}^\dagger(x_1)\cdots\hat{\Psi}^\dagger(x_m)\hat{\Psi}(x_1')\cdots\hat{\Psi}(x_m')|\psi(t)\rangle \\ &= N!\int_0^L \frac{dx_{m+1}\cdots dx_N}{n^m(N-m)!}\psi^*(x_1,\ldots,x_m,x_{m+1},\ldots,x_N,t)\psi(x_1',\ldots,x_m',x_{m+1},\ldots,x_N,t)\,. \end{aligned} \tag{5.9}$$

By expressing the wave function $\psi(\{x_j\},t)$ in terms of Lieb–Liniger eigenstates $\zeta_{\{\lambda_j\}}(\{x_i\})$ (5.2), we can calculate the integrals in Eq. (5.9) semi-analytically with the methodology of Ref. [165]. This also allows for calculation of the norm (5.4) and the evaluation of the overlaps of the initial state with Lieb–Liniger eigenstates necessary for our nonequilibrium calculations in Sec. 5.5. In Sec. 5.6, we consider the relaxed system in terms of the diagonal ensemble [1]

density matrix $\hat{\rho}_{\mathrm{DE}} \equiv \sum_{\{\lambda_j\}} \rho^{\mathrm{DE}}_{\{\lambda_j\}} |\{\lambda_j\}\rangle\langle\{\lambda_j\}|$, in which case Eq. (5.7) reads

$$\begin{aligned} g^{(m)}_{\mathrm{DE}}(x_1,\ldots,x_m,x'_1,\ldots,x'_m) &= \frac{1}{n^m}\mathrm{Tr}\{\hat{\rho}_{\mathrm{DE}}\hat{\Psi}^\dagger(x_1)\cdots\hat{\Psi}^\dagger(x_m)\hat{\Psi}(x'_1)\cdots\hat{\Psi}(x'_m)\} \\ &= \frac{1}{n^m}\sum_{\{\lambda_j\}}\rho^{\mathrm{DE}}_{\{\lambda_j\}}\langle\{\lambda_j\}|\hat{\Psi}^\dagger(x_1)\cdots\hat{\Psi}^\dagger(x_m)\hat{\Psi}(x'_1)\cdots\hat{\Psi}(x'_m)|\{\lambda_j\}\rangle \\ &= N!\sum_{\{\lambda_j\}}\rho^{\mathrm{DE}}_{\{\lambda_j\}}\int_0^L \frac{dx_{m+1}\cdots dx_N}{n^m(N-m)!}\,\zeta^*_{\{\lambda_j\}}(x_1,\ldots,x_m,x_{m+1},\ldots,x_N,t) \\ &\qquad\qquad \times\zeta_{\{\lambda_j\}}(x'_1,\ldots,x'_m,x_{m+1},\ldots,x_N,t)\,. \end{aligned} \tag{5.10}$$

5.3.3 Numerical considerations

For repulsive interactions, the solutions to the Bethe equations (5.6) are characterized by purely real rapidities λ_j, and finding these numerically is relatively straightforward, see e.g. Ref. [166]. However, for attractive interactions solutions with complex rapidities are possible, and the associated Yang-Yang action of the problem is nonconvex (see e.g. Ref. [222]), which complicates the root-finding procedure. We start our root-finding routine close to $\gamma = 0$, where the rapidities $\{\lambda_j\}$ are close to the corresponding free-particle momenta corresponding to $\{n_j\}$. Advancing in small steps to more negative values of γ using linear extrapolation leads to good convergence of the rapidities to machine precision with a Newton method with adaptive step size and trust region.

Eigenstates with complex rapidities arrange themselves in so-called string patterns in the complex plane for large values of $|c|L$, with deviations from these strings exponentially small in system length L [223, 226]. For these, some of the scattering phases $a(\sigma)$ in Eq. (5.3) become smaller and smaller for increasing $|\gamma|$, canceling the huge exponential factor to give a finite result. Naive evaluation of the wave function would therefore lead to numerical inaccuracies due to catastrophic cancellations as soon as the string deviations are of the order of machine precision. This problem can be overcome by using the Bethe equations (5.6) to rewrite the problematic factors in $a(\sigma)$ in terms of exponentials, therefore optimizing the expressions for floating-point calculations, cf. Appendix 5.8.2. For $N = 4$ and $L = 4$, this enables us to calculate correlation functions for attractive interaction strength values up to $|\gamma| \approx 40$. For larger values of $|\gamma|$, the bound states become increasingly localized, leading to factors in Eq. (5.2) that are too large to be represented with standard double-precision

floating point arithmetic. We could in principle use high-precision arithmetic to overcome this problem.[4] However, to address the physics of interest in this work, double precision arithmetic is sufficient and allows us to investigate the system from the weakly interacting regime all the way up to the strongly interacting regime.

5.4 Ground state correlation functions

The ground state correlation functions of the one-dimensional Bose gas with attractive interactions have so far been investigated in the mean-field regime [182, 377, 389] and with quantum-mechanical methods [182–185, 378, 390]. A lattice approximation was considered in Ref. [391]. For system length $L \to \infty$, studies include [177, 376, 379, 392], while in Ref. [375] correlation functions for up to $N = 4$ particles under hard-wall boundary conditions were calculated within the coordinate Bethe ansatz. Refs. [222, 228] calculated the dynamic structure factor to first order in the string deviations based on the algebraic Bethe ansatz. Here, we investigate the correlation functions for finite system length L and periodic boundary conditions exactly. We compare these with the mean-field solution for $N = 7$ particles in the vicinity of the quantum phase transition $-0.7 \leq \gamma \leq 0$, before considering the more strongly attractive system up to $\gamma = -40$ for $N = 4$ particles.

5.4.1 Correlations near the critical point

In Fig. 5.1, we plot the first- and second-order coherence functions for the ground state for $N = 7$ particles for a range of γ. Fig. 5.1(a) shows the first-order coherence $g^{(1)}(x)$ in the spatial domain. For translationally invariant and particle-number conserving systems, $g^{(1)}(x = 0) \equiv 1$ for all γ. For $\gamma = -0.1$ (red dashed line), the proximity to the non-interacting gas results in a nearly constant $g^{(1)}(x)$. For more attractive values of γ, $g^{(1)}(x)$ begins to decay towards zero at larger distances. For $\gamma = -0.7$ (pink dot-dashed line), $g^{(1)}(x)$ comes close to zero for $x = 3\pi k_F^{-1}$, which corresponds to $x = L/2$ in our units. [Due to the periodic nature of our geometry, $g^{(1)}(x)$ is symmetric around $x = L/2$, and we

[4] In fact, for $N = 4$ the eigenstate with $\{n_j\} = \{1, 0\}$ has two rapidities which are nearly identical and we need to utilize high-precision arithmetic for calculations involving this specific set, see Appendix 5.8.2 for details.

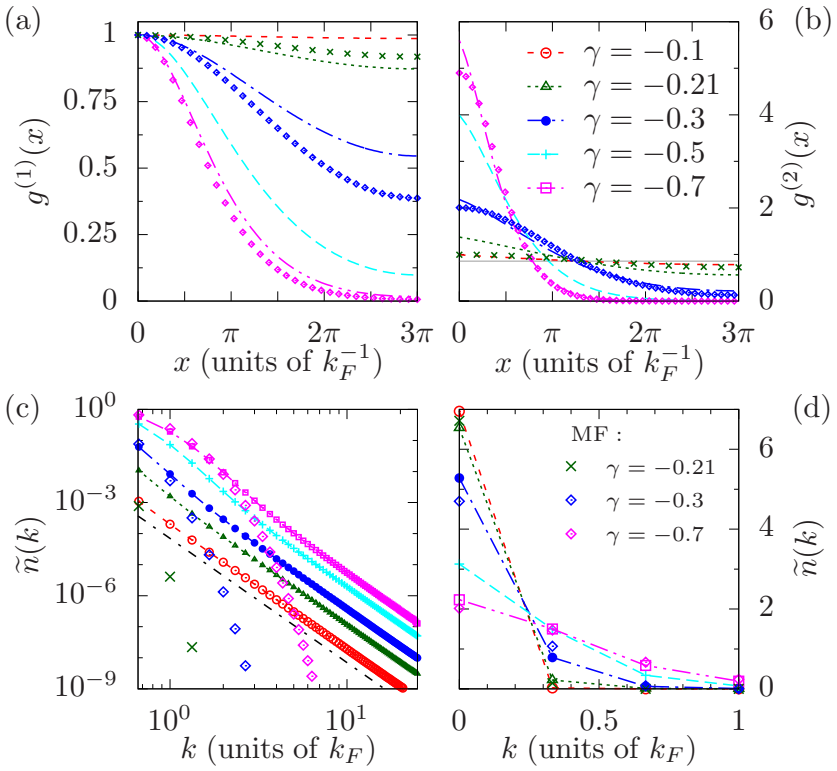

FIGURE 5.1: Ground state correlation functions for $N = 7$ particles and interaction strengths of $\gamma = -0.1$, -0.21, -0.3, -0.5, and -0.7. For comparison, we also plot the mean-field correlation functions for $\gamma = -0.21$ (green crosses), $\gamma = -0.3$ (blue diamonds), and $\gamma = -0.7$ (pink diamonds). The mean-field critical value is $\gamma_{\rm cr} \simeq 0.2$. (a) First-order coherence $g^{(1)}(x)$ in the spatial domain. (b) Second-order coherence $g^{(2)}(x)$. The horizontal line indicates the result for the non-interacting gas with $\gamma = 0$. (c) Momentum distribution $\widetilde{n}(k)$. Black dot-dashed line indicates $\propto k^{-4}$ scaling. (d) Momentum distribution $\widetilde{n}(k)$ for small momenta on linear scale.

therefore only show $g^{(1)}(x)$ up to this point.]

As discussed in the introduction, mean-field theory predicts a quantum phase transition[5] from a flat mean-field wave function to a localized bright-soliton state at $\gamma_{\rm cr} = -\pi^2/N^2 \simeq -0.201$ [182, 184, 229, 377]. For our exact quantum-mechanical treatment of the translationally invariant (and particle number conserving) system, the density is necessarily constant. However, the signature of the bright soliton-like state can be found in the first-order correlation function. Due to the finite size of the system the transition is smeared out, but there is clearly a significant change in $g^{(1)}(x)$ between $\gamma = -0.1$ [red dashed line in Fig. 5.1(a)] and $\gamma = -0.3$ (blue dot-dashed line). In the mean-field approximation, the many-body wave function is approximated by a symmetrized (Hartree–Fock) product of single particle wavefunctions, which amounts to neglecting two-body (and higher) correlations between

[5] For a discussion of spontaneous symmetry breaking in finite volumes, see the Appendix of Ref. [184].

particles [177, 393]. In this approximation, which becomes exact in the infinite N limit, correlation functions for the small system sizes we consider here are easy to compute numerically, see Appendix 5.8.1 for details.

At the critical point, the mean-field wave function is nearly perfectly uniform, leading to a nearly constant $g^{(1)}(x)$. We therefore compare our exact results to the mean-field solution at $\gamma = -0.21$ (green crosses) and find that close to the critical point, the exact solution (green dotted line) is slightly more localized. For $\gamma = -0.3$, i.e. further from the critical point, the mean-field solution (blue diamonds) is more localized than the exact solution (blue dot-dashed line). Even further from the critical point at $\gamma = -0.7$, the mean-field solution (pink diamonds) and the exact $g^{(1)}(x)$ (pink dot-dot-dashed line) agree quite closely.

In Fig. 5.1(c), we plot the momentum distribution $\widetilde{n}(k)$ corresponding to the first-order correlations shown in Fig. 5.1(a). [For translationally invariant systems $\widetilde{n}(k_j, t) \equiv \widetilde{n}(-k_j, t)$ and hence we only plot positive momenta in the following.] For $\gamma = -0.1$ (red empty circles), the finite extent of our small system leads to $\widetilde{n}(k) \propto k^{-4}$ for all momenta $k_j \geq 1k_F$. For all other values of γ, the k^{-4}-scaling is still present for high momenta. This is the universal large-momentum behavior for systems with short-range interactions [5, 314, 315]. For increasingly attractive interactions, $\gamma = -0.21$ (green triangles), the lowest non-zero momentum modes start to deviate from the $\propto k^{-4}$ scaling. For larger values of $-\gamma$, the deviations extend further in momentum, and a broad hump develops. This can be more clearly seen in Fig. 5.1(d), where we plot the momentum distribution for low momenta $k \leq 1k_F$ on a linear scale. For $\gamma = -0.1$ (red empty circles), the zero-momentum mode is close to its ideal-gas value of $\widetilde{n}(k = 0) = N$. For larger attractive values of γ, the zero-momentum mode occupation decreases and the first couple of non-zero momentum modes increase visibly, leading to a broad distribution for $\gamma = -0.7$ (pink empty squares).

The ground-state mean-field momentum distributions in Fig. 5.1(c) do not show the k^{-4}-scaling for large k. Close to the critical point at $\gamma = -0.21$, the exact $\widetilde{n}(k)$ (green dotted line) and the mean-field solution (green crosses) are clearly different away from $k = 0$. For larger attractive values of γ, however, the momentum distributions start to agree better for the lowest three modes, e.g. at $\gamma = -0.3$ (blue diamonds for mean-field solution, blue dot-dashed line for exact solution). This is even more pronounced for $\gamma = -0.7$, where the lowest six modes of the exact solution (pink dot-dot-dashed line) agree well with the

mean-field solution (pink diamonds), before the k^{-4} tail of the exact momentum distribution takes over.

In Fig. 5.1(b), we plot the second-order coherence $g^{(2)}(x)$ for the same range of γ as before. For $\gamma = -0.1$ (red dashed line), $g^{(2)}(x)$ is close to the ideal-gas value $g^{(2)}_{\gamma=0}(x) = 1 - 1/N$ (horizontal grey line). For $\gamma = -0.21$ (green dotted line), $g^{(2)}(x)$ is increased over the ideal-gas value at distances $x \lesssim 1.3\pi k_F^{-1}$ and correspondingly decreased at larger distances. This behavior is even more pronounced for $\gamma = -0.3$ (blue dot-dashed line), and the trend continues for larger attractive values of γ, where there is significant bunching of particles.

Comparing the exact results to the mean-field solutions, we again observe a clear difference near the critical point at $\gamma = -0.21$, where the exact solution (green dotted line) is more localized than the mean-field solution (green crosses). For $\gamma = -0.3$, the exact solution (blue dot-dashed line) has a slightly increased value at zero separation compared to the mean-field solution (blue diamonds), but away from the origin the latter is marginally broader. For $\gamma = -0.7$, the local value $g^{(2)}(0)$ of the exact solution (pink dot-dot-dashed line) is again slightly larger than the mean-field value (pink diamonds). Away from the origin, $x \gtrsim \pi/4\, k_F^{-1}$, the mean-field and exact distribution show very good agreement.

5.4.2 Correlations for strongly interacting systems

In Fig. 5.2, we plot the first-, second- and third-order correlation functions of the ground state for $N = 4$ particles and for a larger range of values of the interaction strength $-2 \geq \gamma \geq -40$. For $N = 4$, the mean-field critical interaction strength is $\gamma_{\mathrm{cr}} \simeq -0.617$. Fig. 5.2(a) shows the first-order coherence $g^{(1)}(x)$. For increasing attractive interactions, $g^{(1)}(x)$ shows that the soliton-like state is increasingly localized. This can also be observed in momentum space, Fig. 5.2(c), where the corresponding momentum distributions $\widetilde{n}(k)$ become broader, much more so than in the repulsive regime (cf., e.g., Ref. [165]). For comparison, we also plot the mean-field correlation functions for $\gamma = -40$ in Figs. 5.2(a),(c) (grey diamonds). The spatial first-order coherences agree well, with the mean-field solution being slightly more localized than the exact solution. This leads to a slightly broader mean-field momentum distribution for low values of k. Nevertheless, the two momentum distributions agree very

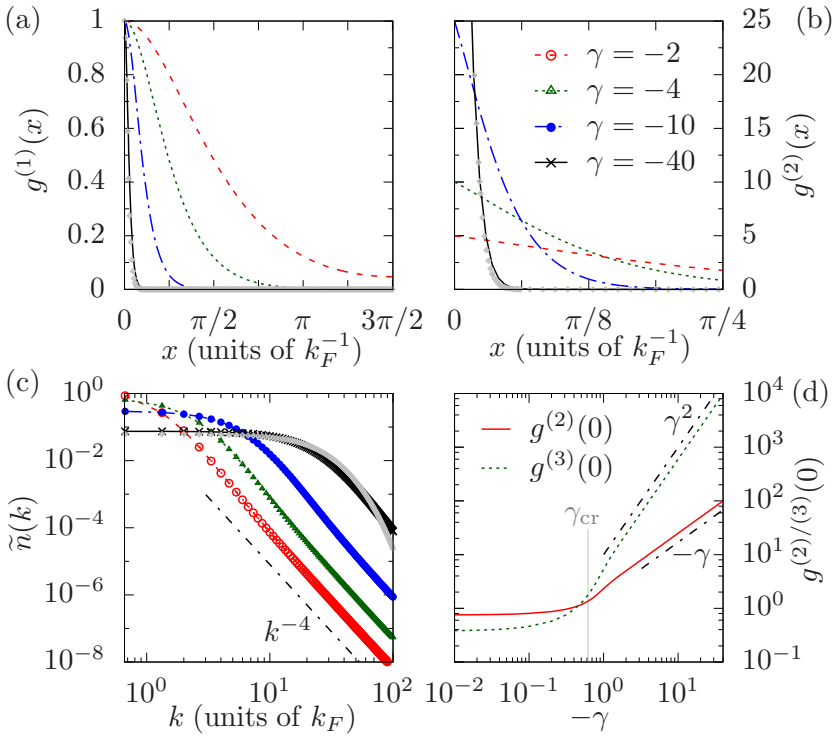

FIGURE 5.2: Ground state correlation functions for $N = 4$ particles and interaction strengths $\gamma = -2$, -4, -10 and -40. (a) First order coherence $g^{(1)}(x)$. (b) Second order coherence $g^{(2)}(x)$ up to $x = \pi/4\ k_F^{-1}$. The local value for $\gamma = -40$, $g^{(2)}(x) = 100$, exceeds the shown range. (c) Momentum distribution $\widetilde{n}(k_j)$. Grey diamonds correspond to mean-field solution for $\gamma = -40$. (d) Local second and third order coherence $g^{(2)}(0)$ and $g^{(3)}(0)$, respectively, for a wide range of γ. Black dot-dashed lines indicate power-law scaling, proportional to $-\gamma$ (lower line) and γ^2.

well over a wide range of momenta up to $k \simeq 30k_F$, where the universal k^{-4}-scaling of the exact momentum distribution takes over.

Fig. 5.2(b) shows the second order coherence $g^{(2)}(x)$ for distances up to $x = \pi/4\ k_F^{-1}$ (which corresponds to $x = L/12$). We again observe that the system is more tightly bound for increasingly attractive interactions. The local value for $\gamma = -40$ (solid black line) is $g^{(2)}(x = 0) = 100$ and not shown in our plots to keep larger distance features visible. The mean-field solution for $\gamma = -40$ (grey diamonds) again shows good agreement with the exact solution away from the origin (the local value is again slightly suppressed).

Fig. 5.2(d) shows the local second- and third-order coherence for a wide range of interaction strengths. For small values of γ, the values are close to the ideal-gas limit, $g^{(2)}(0) = 1 - 1/N = 0.75$ and $g^{(3)}(0) = n^3N(N-1)(N-2)N^{-3} = 0.375$ [262]. In the vicinity of the mean-field quantum phase transition point (indicated by vertical grey line), both $g^{(2)}(0)$ and $g^{(3)}(0)$ start to increase significantly. For larger attractive values of γ, we

observe a linear scaling of the second-order coherence $g^{(2)}(0) \propto -\gamma$ and a quadratic scaling of the third-order coherence $g^{(3)}(0) \propto \gamma^2$, which we indicate by the black dot-dashed lines in Fig. 5.2(d). The scaling of $g^{(2)}(0) \propto -\gamma$ can be understood by noting that the McGuire cluster energy scales as $E_G \propto -n^2\gamma^2$ [213], and $g^{(2)}_\gamma(0) = n^{-2}N^{-1}dE_G(\gamma)/d\gamma$ [260]. The increase of the local second- and third-order correlation functions for large attractive interactions is in stark contrast to the behavior of these quantities for strongly repulsive interactions, for which $g^{(2)}_{\gamma>0}(0) \propto \gamma^{-2}$ and $g^{(3)}_{\gamma>0}(0) \propto \gamma^{-6}$ [165, 260].

To summarize, the exact finite-system correlation functions we considered show crossover behavior around the mean-field critical value, with characteristic changes happening at slightly smaller values of γ. At stronger interactions, the mean-field correlation functions agree surprisingly well with our small-system results. This does not apply to quantities being dictated by two-body correlations, i.e. the large momentum behavior of the momentum distribution and the local pair correlations [5, 314, 315].

5.5 Dynamics following an interaction quench

In this section we investigate the dynamical evolution of the interacting Lieb–Liniger gas following an interaction quench for $N = 4$ particles at time $t = 0$. The system is initially taken to be in the ideal-gas ground state, for which the wave function is constant in space, $\psi_0(\{x_i\}) = \langle\{x_i\}|\psi_0\rangle = L^{-N/2}$. Formally, the state of the system at time $t > 0$ is given by

$$|\psi(t)\rangle = \sum_{\{\lambda_j\}} C_{\{\lambda_j\}}\, \mathrm{e}^{-iE_{\{\lambda_j\}}t}|\{\lambda_j\}\rangle\ , \tag{5.11}$$

where $C_{\{\lambda_j\}} \equiv \langle\{\lambda_j\}|\psi_0\rangle$ are the overlaps of the initial state with the Lieb–Liniger eigenstates $|\{\lambda_j\}\rangle$ at the post-quench interaction strength γ, and $E_{\{\lambda_j\}}$ are the corresponding energies. The evolution of equal-time correlation functions (Sec. 5.3.2) is calculated by noting that the time evolution of the expectation value of an arbitrary operator $\hat{O}$ in the time-dependent state $|\psi(t)\rangle$ is given by

$$\langle\hat{O}(t)\rangle \equiv \langle\psi(t)|\hat{O}|\psi(t)\rangle = \sum_{\{\lambda_j\}}\sum_{\{\lambda'_j\}} C^*_{\{\lambda'_j\}}C_{\{\lambda_j\}}e^{i(E_{\{\lambda'_j\}}-E_{\{\lambda_j\}})t}\langle\{\lambda'_j\}|\hat{O}|\{\lambda_j\}\rangle. \tag{5.12}$$

The matrix elements $\langle\{\lambda'_j\}|\hat{O}|\{\lambda_j\}\rangle$ and overlaps $C_{\{\lambda_j\}}$ are calculated with the method described in Ref. [165].

Numerically it is necessary to truncate the infinite sum in Eq. (5.12), and our procedure is analogous to that described in Appendix A of Ref. [166]. We include all eigenstates for which the populations $|C_{\{\lambda_j\}}|^2$ are larger than some threshold value, thereby minimizing the normalization sum-rule violation $\Delta N = 1 - \sum_{\{\lambda_j\}} |C_{\{\lambda_j\}}|^2$ for any given value of the cut-off. The smallest cut-off we use in this work is $|C_{\{\lambda_j\}}|^2 \geq 10^{-8}$ for calculations of $\widetilde{n}(k_j, t)$ and $g^{(2)}(x, t)$ for interaction strength quenches to $\gamma = -40$, leading to a sum-rule violation of $\Delta N = 9 \times 10^{-6}$. All other correlation functions are calculated with a cut-off $|C_{\{\lambda_j\}}|^2 \geq 10^{-10}$, and the sum-rule violations are correspondingly smaller. We have checked that increasing the cut-off does not visibly alter any of our results.

5.5.1 Influence of bound states following a quench

Before considering the dynamics following a quench to attractive interactions, we first look at the populations of the Lieb-Linger eigenstates for the post-quench Hamiltonian. Comparing these distributions to those for quenches to repulsive interactions helps provide an understanding of the contribution of bound states to the dynamics.

In Fig. 5.3 we plot the populations $|C_{\{\lambda_j\}}|^2$ of several representative eigenstates following a quench of the interaction strength from zero to γ for a wide range of interactions. [Recall that for $N = 4$ there are two independent n_j to be specified, which we quote for each eigenstate.] For attractive interactions, Fig. 5.3(a), several bound states have significant populations for small values of $-\gamma \lesssim 5$. The ground state $\{n_j\} = \{0, 0\}$ (red solid line), which is a four-particle bound state, and the three particle bound state $\{n_j\} = \{1, 0\}$ (green dotted line) are most important for quenches to $-\gamma \lesssim 4$. However their populations decrease rapidly for increasingly attractive values of γ.

At intermediate $-\gamma \approx 5$, two-body bound states start to dominate the populations [e.g. the states with $\{n_j\} = \{2, 0\}$ (blue dot-dashed line) and $\{n_j\} = \{1, 1\}$ (pink dot-dot-dashed line)]. For increasing attractive values of γ, gas-like states with no bound state component start to become more important [e.g. $\{n_j\} = \{3, 1\}$ (black solid line) and $\{n_j\} = \{4, 1\}$ (pink dotted line)]. Indeed, at $\gamma \approx -24$, the population of the super-Tonks state

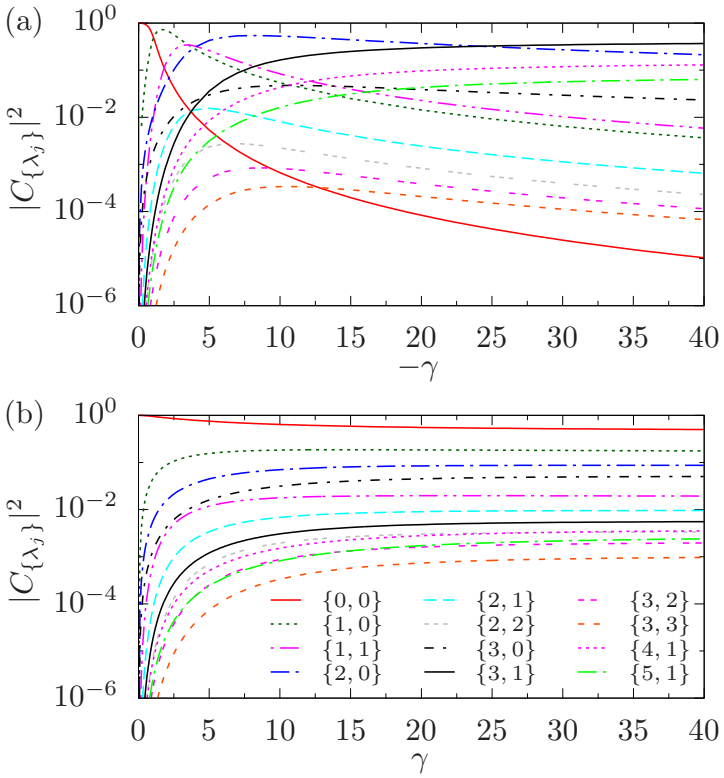

FIGURE 5.3: Populations $|C_{\{\lambda_j\}}|^2$ of the lowest energy eigenstates for quenches of the interaction strength from zero to γ and $N = 4$ particles. (a) Populations for attractive post-quench interaction strengths. All states except those with $\{n_j\} = \{3, 1\}$, $\{4, 1\}$ and $\{5, 1\}$ contain bound states. (b) Populations for repulsive post-quench interactions strengths for comparison with (a).

$\{n_j\} = \{3, 1\}$ — the lowest-energy gas-like state at strong interactions — begins to dominate (black solid line). However, the two-body bound state with $\{n_j\} = \{2, 0\}$ (blue dot-dashed line) still has a significant population in the strongly interacting regime.[6] Consequently, we expect bound states to influence the dynamical evolution of correlation functions following a quench from the ideal gas for all attractive interaction strengths. Comparing the populations of eigenstates for attractive post-quench interactions to those for repulsive interactions, Fig. 5.3(b), we can see that there is significantly less structure due to the absence of bound states.

Further understanding of quenches to attractive interactions is provided by Fig. 5.4, where we make a more detailed comparison of the eigenstate populations $|C_{\{\lambda_j\}}|^2$ for quenches from the ideal-gas ground state to attractive and repulsive interactions with $\gamma = \pm 40$ for $N = 4$ particles. We see that there are additional families of populations for the attractive

[6] We note that this state has an energy of $E/n^2 = -798.6$, which is very close to the energy of the two-particle McGuire cluster state, $E/n^2 = -\gamma^2/2 = -800$ [213].

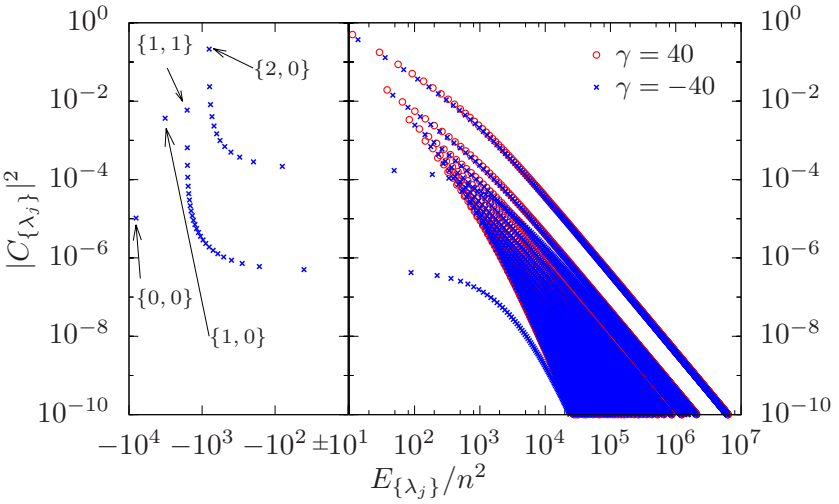

FIGURE 5.4: Comparison of populations of eigenstates in the post-quench basis for quenches from the ideal gas ground state to $\gamma = -40$ (blue crosses) and $\gamma = +40$ (red circles) for $N = 4$ particles. To display negative energies on a logarithmic scale, we mirror the energy axis around $E_{\{\lambda_j\}}/n^2 = 10$, plotting the populations of eigenstates with negative energy on the left and those with positive energy on the right. Four exemplary bound states with negative energy are labelled with their (ideal gas) quantum numbers, and are described further in the main text.

gas (blue crosses that extend to negative energies) that are not present for the repulsive gas (red circles). These are due to the four different types of bound states as we describe below.

The first two types are the ground state $\{n_j\} = \{0, 0\}$ at $E/n^2 \approx -8000$, $|C_0|^2 \approx 10^{-5}$ which is a four-body bound state, and the the first parity-invariant excited state $\{n_j\} = \{1, 0\}$ at $E/n^2 \approx -3200$, $|C_1|^2 \approx 3.7 \times 10^{-3}$ which is a three-body bound state. We note that the parity invariance of eigenstates for quenches from the initial ideal gas restricts the appearance of bound states with more than two bound particles to only these states.

The third type is the eigenstate with $\{n_j\} = \{2, 0\}$, which has two bound particles and two free particles, and is the first in a family of similar states whose populations decrease gradually for higher excitations $\{2 + l, 0\}$ (l positive integer).

The fourth type is represented by the eigenstate with $\{n_j\} = \{1, 1\}$ contains two two-particle bound states, and again is the first in a whole family with decreasing populations for higher excitations $\{1 + l, 1 + l\}$ and $\{1 + l, l\}$ (l positive integer), which contribute alternatingly. For larger l, the two two-body bound states have higher "center-of-mass"-momenta with opposite sign (recall that only eigenstates with total momentum $P = 0$ contribute), and at some point the corresponding energy dominates over the binding energy of the bound states.

We can see from Fig. 5.4 that the distribution of populations over eigenstates with purely real rapidities are very similar for quenches to $\gamma = \pm 40$, aside from a shift in energy and a small decrease in populations for the attractive gas to accommodate the additional bound states that arise. For comparison, the number of eigenstates with populations $|C_{\{\lambda_j\}}|^2 \geq 10^{-10}$ is 7815 (7462) for the attractive (repulsive) gas. The shift in energy can be explained by noting that for $\gamma = \pm 40$, the system is in the strongly interacting regime and the Bethe rapidities of scattering states (i.e. states with no bound particles) can be obtained by a strong-coupling expansion around the Tonks–Girardeau limit of infinitely strong interactions (see e.g. Ref. [255]). This yields $\lambda_j \approx (1 - \frac{2}{\gamma})k_j$, where k_j are the Tonks–Girardeau values.

Finally, we note that the scattering eigenstates that are physically identical as $\gamma \to \pm\infty$ do not have the same ideal-gas quantum numbers, due to the appearance of the bound states on the attractive side [195]. For example, for $N = 4$ particles, the ground state for repulsive interactions, $\{n_j\} = \{0, 0\}$, maps to the super-Tonks state with $\{n_j\} = \{3, 1\}$ on the attractive side.

5.5.2 Dynamics of local correlations

We now consider the dynamics following the quench. In Fig. 5.5(a) we plot the local second-order coherence $g^{(2)}(x = 0, t)$ for $N = 4$ particles following a quench from $\gamma = 0$ to four representative interaction strengths. Initially, $g^{(2)}(0, t = 0) = 1 - 1/N = 0.75$ (see e.g. Ref. [166]). For a quench to $\gamma = -0.5$ (pink dot-dashed line), $g^{(2)}(0, t)$ shows nearly monochromatic oscillatory behavior. This is similar to the behavior of quenches to small repulsive interactions analyzed in Ref. [166]: Because the post-quench energy $E \equiv \langle\psi(0^+)|\hat{H}|\psi(0^+)\rangle = (N - 1)n^2\gamma$ [166, 195] is small compared to the energy spacing for the small system size, the dynamics is dominated by the ground state and first (parity-invariant) excited state. The value of $g^{(2)}(0)$ in the former is close to the ideal-gas value for $\gamma = -0.5$, cf. Sec. 5.4. For a quench to $\gamma = -2$ (blue dashed line), $g^{(2)}(0, t)$ rises from its initial value before settling in to fluctuate about a much larger average value. The main shape is dominated by two frequencies, originating from the energy difference of the strongly occupied three-body bound state with the ground state, and the energy difference of the former state with the two-body bound state with $\{n_j\} = \{1, 1\}$, cf. Fig. 5.3.

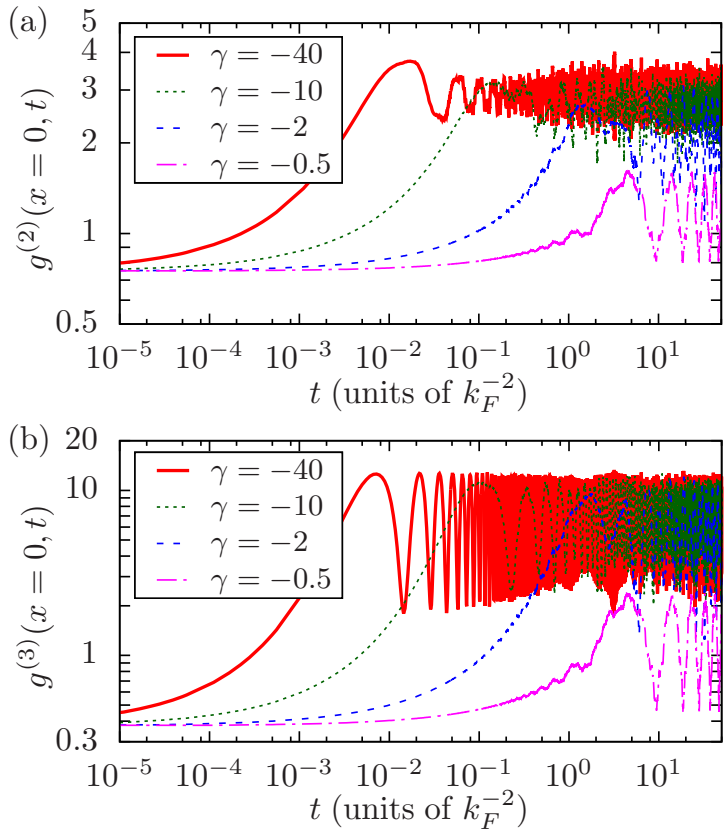

FIGURE 5.5: Time evolution of local correlation functions following a quench of the interaction strength from zero to $\gamma = -0.5$, -2, -10 and -40 for $N = 4$ particles. (a) Local second-order coherence $g^{(2)}(x = 0, t)$. (b) Local third-order coherence $g^{(3)}(x = 0, t)$.

For quenches to $\gamma = -10$ (green dotted line), $g^{(2)}(0, t)$ again rises from its initial value before settling to fluctuate somewhat irregularly about a greatly increased average value. For $\gamma = -40$ (solid red line), the system is dominated by the super-Tonks and first two-body bound state, cf. Fig. 5.3, and the dominant frequency in the oscillations at early times matches the energy difference of these two eigenstates. At later times, the shape of $g^{(2)}(0, t)$ is more irregular, but the large oscillations due to the two dominant eigenstates persist.

In Fig. 5.5(b) we plot the local third-order coherence $g^{(3)}(x = 0, t)$ for $N = 4$ particles following a quench from $\gamma = 0$ to the same four representative interaction strengths as before. Initially, $g^{(3)}(0, t = 0) = n^3 N(N-1)(N-2)N^{-3} = 0.375$ [262]. For low post-quench interaction strengths, $\gamma = -0.5$ (pink dot-dashed line) and $\gamma = -2$ (blue dashed line), the evolution is similar to that of $g^{(2)}(x = 0, t)$ for the same interaction strengths. For larger attractive values of the post-quench interaction strength, on the other hand, the shape of $g^{(3)}(0, t)$ is more regular compared to $g^{(2)}(x = 0, t)$. For $\gamma = -10$ (green dotted line) and

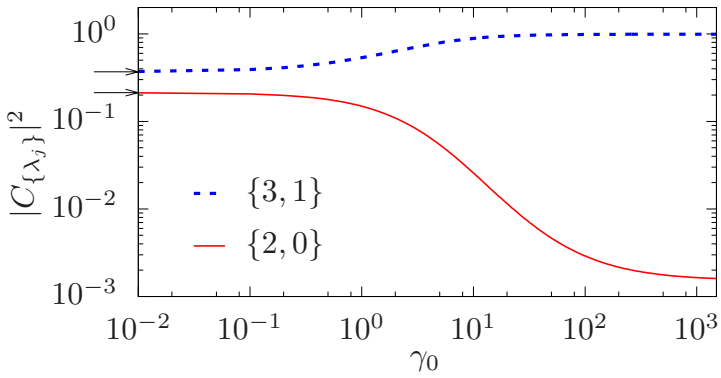

FIGURE 5.6: Populations $|C_{\{\lambda_j\}}|^2$ of the super-Tonks state ($\{n_j\} = \{3,1\}$) and the dominant two-body bound state ($\{n_j\} = \{2,0\}$, see text) for quenches from the interacting ground state at $\gamma_0 > 0$ to $\gamma = -40$ for $N = 4$ particles. The black arrows indicate the populations for the quench from the ideal gas ground state.

$\gamma = -40$ (solid red line), $g^{(3)}(0,t)$ is dominated by a single frequency, given by the energy difference between the two-body bound state with $\{n_j\} = \{2,0\}$ and the three-body bound state. The initial rise of both $g^{(2)}(0,t)$ and $g^{(3)}(0,t)$ occurs on increasing shorter time-scales for larger attractive post-quench interaction strengths. This time scale is proportional to γ^2, and is due to bound states. The large increase of both $g^{(2)}(0,t)$ and $g^{(3)}(0,t)$ is in stark contrast to the decay of the same quantities following quenches to repulsive interactions [166] due to the "fermionization" of the system.

The metastability of the super-Tonks state in the experiment of Ref. [179] is due to the "fermonized" nature of this state. Additionally, the overlap of the repulsive ground state with the super-Tonks state is very large for large interaction strengths. Therefore, the experimental preparation via a quick interaction strength ramp from large repulsive interactions to large attractive values puts the system predominantly in the super-Tonks gas and bound states are hardly excited at all [179, 195, 218, 387]. This is in contrast to our results for quenches from the ideal-gas initial state, where bound states lead to largely increased values of both $g^{(2)}(0)$ and $g^{(3)}(0)$, which in turn would lead to strong particle losses in experiments [179, 319, 394].

To investigate how the populations of the two most dominant eigenstates (cf. Fig. 5.3) are influenced by the initial state, we find the (correlated) ground state $|\psi_0\rangle$ of the system at $\gamma_0 > 0$ and then compute the populations of the eigenstates for a quench to $\gamma = -40$. In Fig. 5.6, we plot the populations $|\langle\{2,0\}|\psi_0\rangle|^2$ and $|\langle\{3,1\}|\psi_0\rangle|^2$ of the aforementioned two-

body bound state and the super-Tonks state, respectively, for a wide range of initial values γ_0 and $N = 4$ particles. Starting in the strongly interacting regime $\gamma = 10^3$, the overlap between the initial (Tonks–Girardeau) state and the super-Tonks state is very close to one. As γ_0 is decreased, the population of the super-Tonks gas decreases, and the population of the bound state increases correspondingly. At $\gamma_0 \approx 1$, the values are already near their corresponding ideal-gas initial-state values (indicated by black arrows on the left-hand side). Consequently, we expect the values of $g^{(2)}(0,t)$ and $g^{(3)}(0,t)$ to be much smaller for quenches from initial values of $\gamma_0 \gtrsim 10$ compared to the non-interacting initial state.

5.5.3 Dynamics of the momentum distribution

We now turn our attention to the dynamics of nonlocal correlations. In Fig. 5.7 we plot the time evolution of the momentum mode occupations $\widetilde{n}(k_j,t)$ [cf. Eq. (5.8)] for the first six non-negative momentum modes k_j ($j = 0,1,\ldots,5$) following a quench from the ideal gas ground state and for $N = 4$ particles. Initially, all particles occupy the zero-momentum single-particle orbital $\widetilde{n}(k_j, t = 0) = N\delta_{j0}$ appropriate to the ideal-gas ground state. At times $t > 0$, the quenched interaction leads to a redistribution of this population over single-particle modes with nonzero momenta. At very early times, all nonzero modes rise with the same rate, independent of k. This is due to the local nature of the interaction potential, which corresponds to a momentum-independent interaction [295]. This applies to all post-quench interaction strengths γ, but the time scale at which deviations from this behavior first appear is dependent on γ.

For quenches to $\gamma = -2$, Fig. 5.7(a), the nonzero modes start to level off and fluctuate around a constant average value. This happens earlier for modes corresponding to larger momenta, indicating that non-local correlations settle earlier on shorter length scales [39]. The main shape of $\widetilde{n}(k_0,t)$ is dictated by two frequency components, corresponding to the energy difference of the same states as for local correlation functions.

In Fig. 5.7(b), we plot the same quantity, i.e. $\widetilde{n}(k_j,t)$ for the first six modes and $N = 4$ particles, but for quenches of the interaction strength from zero to $\gamma = -10$. The initial rise of all non-zero modes happens on shorter time-scales than for $\gamma = -2$. For later times, $\widetilde{n}(k = 0,t)$ oscillates around an average value with a frequency given by the energy

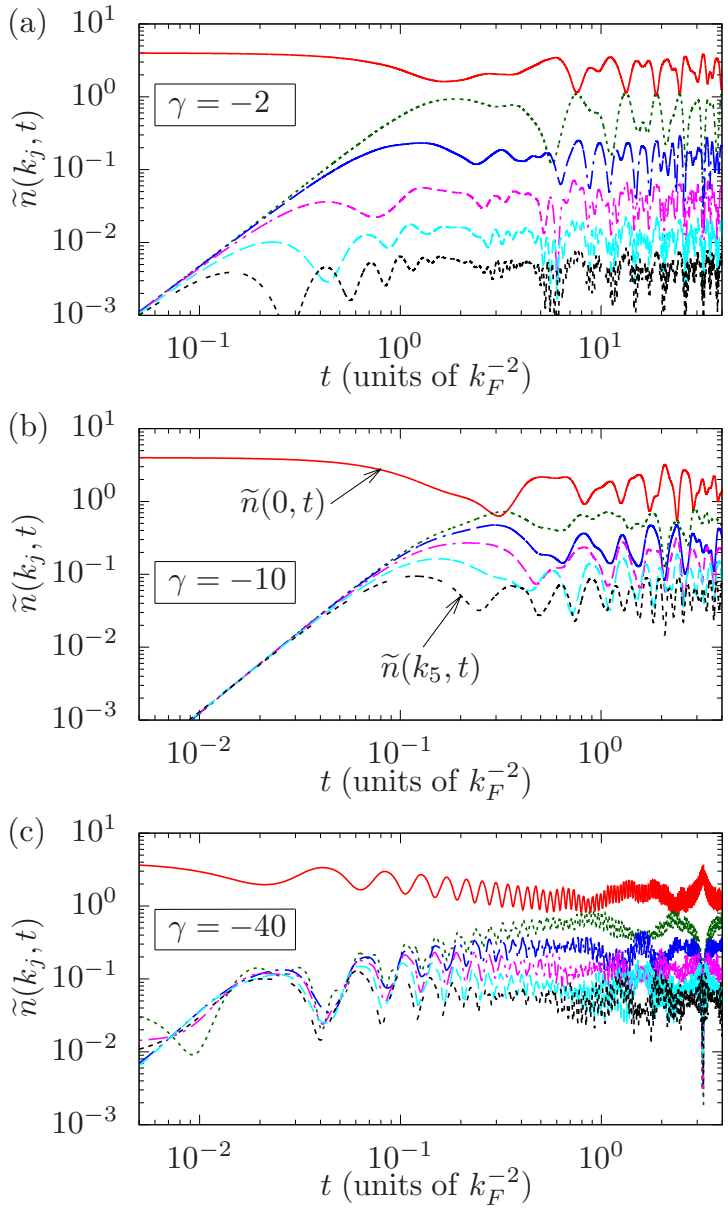

FIGURE 5.7: Time evolution of the momentum occupations $\widetilde{n}(k_j,t)$ of the first six (non-negative) momentum modes k_j $(j = 0,1,\ldots,5)$ for $N = 4$ particles and for a quench of the interaction strength from zero to (a) $\gamma = -2$, (b) $\gamma = -10$ and (c) $\gamma = -40$. Note the different time-scale of (a) compared to (b), (c).

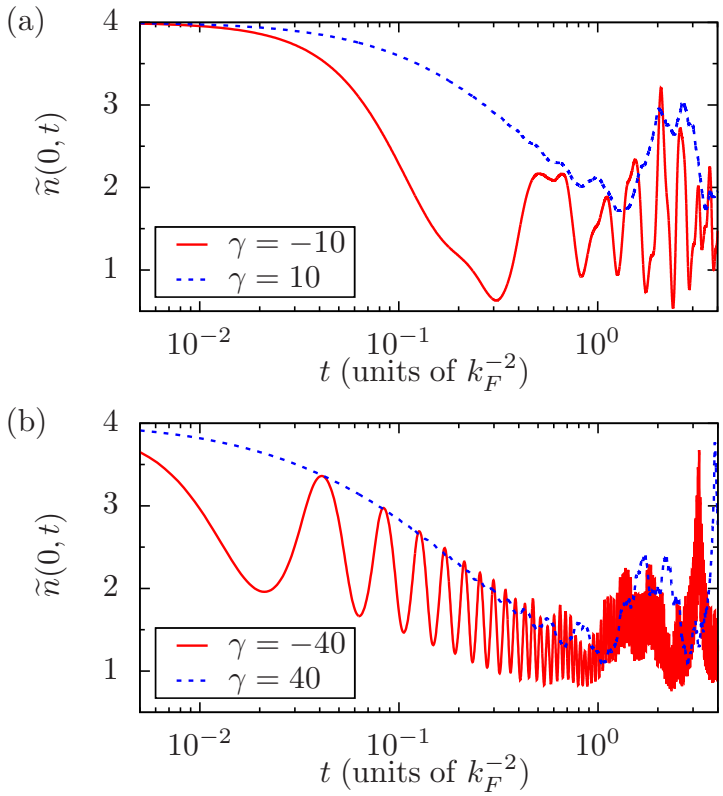

FIGURE 5.8: Time-evolution of the zero-momentum mode occupation $\widetilde{n}(k_j = 0, t)$ for $N = 4$ particles and quenches of the interactions strength from zero to attractive and repulsive values of the same magnitude. (a) Post-quench interaction strengths of $\gamma = -10$ (red solid line) and $\gamma = +10$ (blue dashed line). (b) Post-quench interaction strengths of $\gamma = -40$ (red solid line) and $\gamma = +40$ (blue dashed line).

difference of the super-Tonks state with $\{n_j\} = \{3, 1\}$ and the two-body bound state with $\{n_j\} = \{2, 0\}$. For a quench to $\gamma = -40$, Fig. 5.7(c), all modes exhibit fast oscillations at a single frequency given by the energy difference of the super-Tonks and the same two-body bound state as previously, imposed on top of an overall irregular shape.

We note that the dynamics of the envelope of $\widetilde{n}(k_j, t)$ exhibits similar behavior as for the quenches to strong repulsive interactions described in Ref. [166]. This can be more clearly seen in Fig. 5.8, where we compare $\widetilde{n}(k = 0, t)$ for quenches from the ideal gas to repulsive and attractive interaction strengths of the same magnitude. In Fig. 5.8(a), we plot the time-evolution of the zero-momentum mode occupation $\widetilde{n}(0, t)$ for a quench from $\gamma = 0$ to $\gamma = -10$ (solid red line) and $\gamma = 10$ (blue dashed line). This also applies for quenches to $\gamma = \pm 40$, Fig. 5.8(b), but the oscillations for quenches to $\gamma = -40$ (solid red line) are faster than for quenches to $\gamma = -10$. The reason for this behavior is that the properties of the many-body wave functions following a quench to large positive or negative γ are very similar,

aside from the additional presence of two-body bound states for attractive interactions, as demonstrated in Fig. 5.4. The oscillations seen in the momentum-mode occupations are due to the interference between the dominant super-Tonks state with $\{n_j\} = \{3, 1\}$ and the two-body bound state with $\{n_j\} = \{2, 0\}$.

Additionally we observe a partial revival in $\widetilde{n}(0, t)$ for quenches to $\gamma = \pm 40$. This revival is due to the system at $\gamma = 40$ being close to the Tonks–Girardeau limit of infinitely strong interactions, where the spectrum of the repulsive Lieb–Liniger model is identical to that of free fermions [214]. This also applies to the scattering states of the attractive system. For $\gamma = \infty$, this would lead to recurrences at integer multiples of $t_{\mathrm{rev}} = 3.5 k_F^{-2}$ [166] due to the commensurability of eigenstate energies [344]. The slight shift between attractive and repulsive behavior is due to γ^{-1} corrections to the Bethe rapidities, cf. Sec. 5.5.1. Consequently, the revival time gets shifted to later times for repulsive interactions [166], and to shorter times for attractive interactions, and this is indeed what we observe in Fig. 5.7(b), where $t_{\mathrm{rev}} \approx 3.2 k_F^{-2}$ for the attractive gas compared to $t_{\mathrm{rev}} \approx 3.9 k_F^{-2}$ for the repulsive gas.

5.5.4 Dynamics of non-local correlations

We now consider the evolution of the full non-local second-order coherence $g^{(2)}(x, t)$. In Fig. 5.9 we plot the behavior of this quantity for an interaction quench from zero to $\gamma = -40$ for $N = 4$ particles.

Figure 5.9(a) shows $g^{(2)}(x)$ for four representative times. Initially, $g^{(2)}(x) = 1 - 1/N$ (horizontal line). At $t = 0.01 k_F^{-2}$ (red dashed line), the local value is already very much enhanced, $g^{(2)}(0, t = 0.01 k_F^{-2}) \approx 3.5$, cf. Fig. 5.5(a). [Due to the large difference of $g^{(2)}(x)$ for $x \lesssim 0.02 \times (2\pi k_F^{-1})$, we do not show the short-range behavior in order to keep the fine structure at larger distances visible.] At separations $x \approx 0.1 \times (2\pi k_F^{-1})$, a maximum builds up due to particle-number and momentum conservation, while at larger distances $g^{(2)}(x)$ exhibits a decaying oscillatory structure. As time progresses, this maximum propagates further away from the origin and broadens, e.g. $t = 0.1 k_F^{-2}$ (green dotted line) and $t = 0.25 k_F^{-2}$ (blue dot-dashed line), and the overall distribution gets more distorted.

The initial build-up of correlations and their propagation through the system can be more

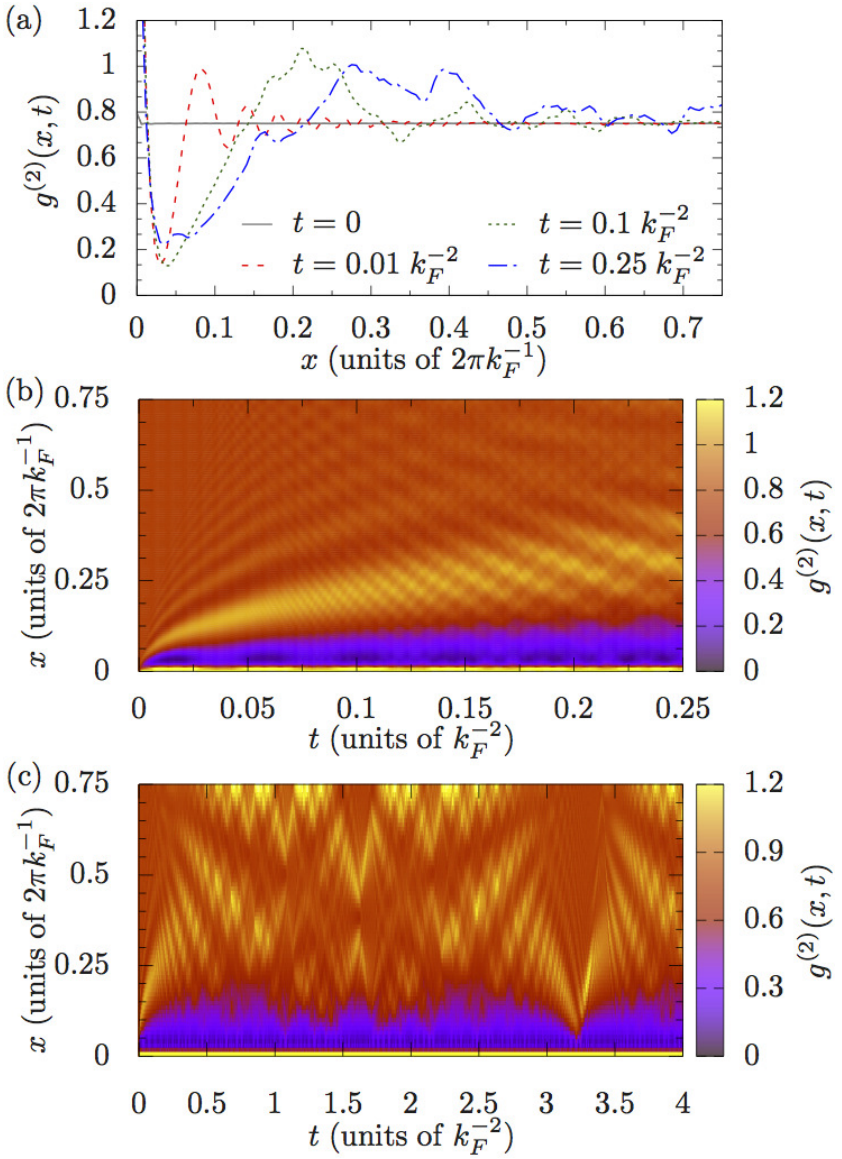

FIGURE 5.9: Time-evolution of the nonlocal second-order coherence function $g^{(2)}(x,t)$ following a quench from the ideal gas ground state to $\gamma = -40$ for $N = 4$ particles. (a) Correlation function $g^{(2)}(x)$ at four representative times. (b) Evolution of $g^{(2)}(x,t)$ for short times $t \leq 0.25\, k_F^{-2}$ and (c) longer times $t \leq 4\, k_F^{-2}$. Note that $g^{(2)}(x,t)$ for $x \lesssim 0.02 \times (2\pi k_F^{-1})$ is not resolved on the chosen color scale in order to preserve the visibility of the long-range features. The local value oscillates between $g^{(2)}(0,t) \approx 2$ and 4, cf. Sec. 5.5.2.

clearly seen in Fig. 5.9(b), where we plot the time-evolution of $g^{(2)}(x,t)$. The propagation of the first maximum is given by $x(t) \propto t^{0.5}$, which was also observed for quenches from the same initial state to strongly repulsive interactions [73, 166]. [Note that $g^{(2)}(x=0,t)$ is again not resolved on the density scale in order that the longer range behavior is visible.] Fig. 5.9(c) shows $g^{(2)}(x,t)$ for longer times up to $t = 4k_F^{-2}$. The overall structure is more complicated, with several soliton-like correlation dips propagating through the system [166] and a revival of $g^{(2)}(x,t=0)$ at $t \approx 3.2k_F^{-2}$. Besides the largely increased value at small distances, the shape of $g^{(2)}(x,t)$ is strikingly similar to our results in Ref. [166] for quenches from the same non-interacting ground state to repulsive interaction strengths.

In summary, for quenches from the ideal gas ground state to attractive values of γ, bound states significantly influence the dynamics of correlation functions for all post-quench interaction strengths. For large attractive values of γ, these bound states are highly localized and therefore only influence correlation functions sensitive to local features.

5.6 Time-averaged correlations

A closed quantum mechanical system prepared in a pure state will remain in a pure state for all time. However, for a non-degenerate post-quench energy spectrum, as is the case here (cf. Refs. [165, 166]), the time-averaged expectation value of any operator $\hat{O}$ is characterized by the matrix elements of dephased eigenstates

$$\langle \hat{O} \rangle_{\mathrm{DE}} = \lim_{\tau\to\infty} \frac{1}{\tau} \int_0^\tau dt\, \langle \psi(t)|\hat{O}|\psi(t)\rangle = \sum_{\{\lambda_j\}} |C_{\{\lambda_j\}}|^2 \langle \{\lambda_j\}|\hat{O}|\{\lambda_j\}\rangle, \tag{5.13}$$

which can be viewed as the expectation value of $\hat{O}$ in the diagonal-ensemble density matrix [1]

$$\hat{\rho}_{\mathrm{DE}} = \sum_{\{\lambda_j\}} |C_{\{\lambda_j\}}|^2 |\{\lambda_j\}\rangle\langle\{\lambda_j\}| \,. \tag{5.14}$$

If correlation functions relax at all, it has to be to the corresponding diagonal ensemble value [19]. Although we expect rather large fluctuations around these stationary values for system sizes as small as those considered here, we expect these fluctuations to decrease with

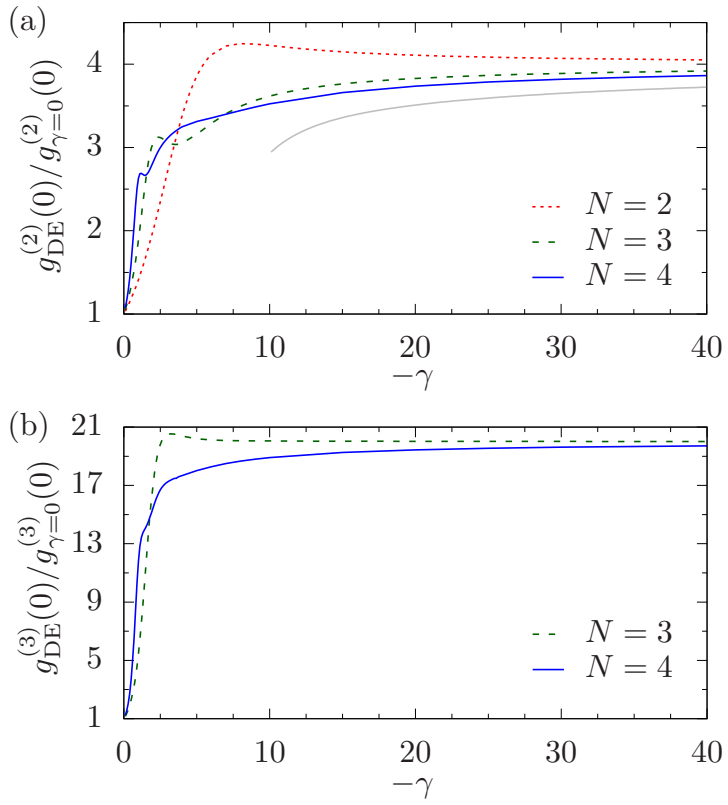

FIGURE 5.10: Diagonal ensemble value of local correlation functions following quenches of the interaction strength from zero to γ for different particle numbers. (a) Local second-order coherence normalized by the corresponding ideal gas values, $g^{(2)}_{\mathrm{DE}}(0)/g^{(2)}_{\gamma=0}(0)$, for quenches to γ for particle numbers $N = 2, 3, 4$. The solid grey line is the quench-action strong-coupling thermodynamic-limit prediction for $g^{(2)}_{\mathrm{DE}}(0)$ [9, 10]. (b) Local third-order coherence normalized by the corresponding ideal gas values, $g^{(3)}_{\mathrm{DE}}(0)/g^{(3)}_{\gamma=0}(0)$, for quenches to γ and particle numbers $N = 3, 4$.

increasing system size. However, establishing this behavior is beyond the scope of the current work and we will simply consider the diagonal ensemble as the appropriate description of stationary observables. In the following we consider the time-averaged properties of the quenched system.

5.6.1 Local correlations

In Fig. 5.10(a), we plot the diagonal-ensemble value of the local second coherence $g^{(2)}_{\mathrm{DE}}(0)$, normalized to its non-interacting initial value, following an interaction quench from zero to γ for particle numbers $N = 2$, 3, and 4. For very small values $\gamma \approx 0$, $g^{(2)}_{\mathrm{DE}}(0)$ is very close to its ideal-gas initial value. Away from $\gamma = 0$, $g^{(2)}_{\mathrm{DE}}(0)$ quickly increases for all particle numbers. For values between $-\gamma \approx 1$ and 8, the local second-order coherence $g^{(2)}_{\mathrm{DE}}(0)$ displays a "hump"

that occurs at smaller attractive values of γ for larger particle number N. For $N = 4$ particles (solid blue line), the location of the hump coincides with the point at which eigenstates other than the ground state start to contribute significantly, cf. Fig. 5.3. Specifically, the value at $-\gamma = 1$, where $g^{(2)}_{\mathrm{DE}}(0)$ displays a local maximum, agrees with the crossing of the three-particle bound state with $\{n_j\} = \{1, 0\}$ and the ground state according to Fig. 5.3. The local minimum of $g^{(2)}_{\mathrm{DE}}(0)$ at $-\gamma = 1.5$ coincides with the maximum population of this three-particle bound state, and as soon as the population of this state starts to decrease, $g^{(2)}_{\mathrm{DE}}(0)$ begins to increase monotonically with increasing $|\gamma|$.

For large attractive values of γ, the local second-order coherence tends to a constant value $g^{(2)}_{\mathrm{DE}}(0)/g^{(2)}_{\gamma=0}(0) \approx 4$, which is much larger than the ideal gas and super-Tonks values [230] (the latter being larger than the Tonks values, but still strongly suppressed). The scaling of $g^{(2)}_{\mathrm{DE}}(0)$ with particle number seems to be consistent with the thermodynamic-limit strong-coupling value obtained to third order in $1/\gamma$ in Ref. [9, 10], indicated by the solid grey line.

Using the quench-action approach [202] in the thermodynamic limit, Ref. [9, 10] found that $g^{(2)}_{\mathrm{DE}}(0) = 2$ for $\gamma \to 0^-$. Our methodology does not recover this result for small attractive values of γ, as our small system sizes lead to a finite-size gap for excitations and therefore the energy added by the quench is small in this case. Additionally, eigenstates with more than four bound particles are absent in our calculations and for low post-quench values of γ they contribute significantly [9, 10], see also Fig. 5.3. For larger attractive values of γ, however, bound states with more than two particles are strongly suppressed and we expect our results to be less influenced by finite-size effects [165].

In Fig. 5.10(b), we plot the diagonal ensemble value of the local third coherence $g^{(3)}_{\mathrm{DE}}(0)$, normalized to its non-interacting initial value, following an interaction quench from zero to γ for particle numbers $N = 3$ and 4. The qualitative behavior is similar to that of $g^{(2)}_{\mathrm{DE}}(0)$, with a hump at low $-\gamma$ moving to lower attractive interactions for higher particle number. For strong interactions, $g^{(3)}_{\mathrm{DE}}(0)$ also tends to a constant value that is much larger than the initial value. If this result persists in the thermodynamic limit is an important open question, since a large value of $g^{(3)}_{\mathrm{DE}}(0)$ entails strong atom losses in experiments with ultracold gases [319, 394].

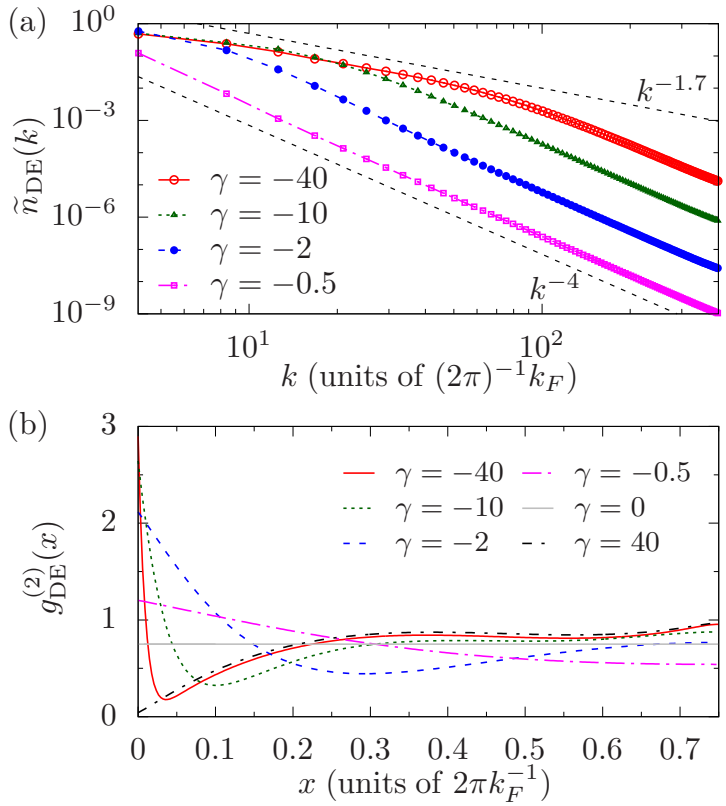

FIGURE 5.11: Diagonal-ensemble correlation functions for quenches from $\gamma = 0$ to $\gamma = -0.5$, -2, -10, and -40 for $N = 4$ particles. (a) Momentum distribution $\widetilde{n}_{\mathrm{DE}}(k)$. Black dashed lines indicate scaling of $k^{-1.7}$ (upper line) and k^{-4}. (b) Second-order coherence $g^{(2)}_{\mathrm{DE}}(x)$. The grey horizontal line marks the initial value $g^{(2)}_{\mathrm{DE}}(x, t = 0)$.

5.6.2 Non-local correlations

In Fig. 5.11(a) we plot the momentum distribution $\widetilde{n}_{\mathrm{DE}}(k)$ in the diagonal ensemble for $N = 4$ particles and for several post-quench interaction strengths γ. At high momenta and for all interaction strengths γ, $\widetilde{n}_{\mathrm{DE}}(k)$ exhibits a scaling of $\widetilde{n}_{\mathrm{DE}}(k) \propto k^{-4}$. This behavior is due to the universal character of short-range two-body interactions [5, 314, 315]. For $\gamma = -0.5$ (pink squares), the functional form of $\widetilde{n}_{\mathrm{DE}}(k)$ is nearly perfectly given by this k^{-4} scaling, and only the three lowest resolvable modes in our finite periodic system deviate slightly.

For a quench to $\gamma = -2$ (blue filled circles), the low-momentum part of $\widetilde{n}_{\mathrm{DE}}(k)$ starts to deviate more strongly from the k^{-4} scaling, and the distribution seems to get wider at low momenta. This low-k "hump" broadens with increasing post-quench interaction strength. This is qualitatively similar to the results for quenches to repulsive values of

γ [166]. However, for $\gamma = -40$ (red circles), a scaling of $\widetilde{n}_{\mathrm{DE}}(k) \propto k^{-1.7}$ emerges for momenta between $k \approx 1\times((2\pi)^{-1}k_F)$ and $5\times((2\pi)^{-1}k_F)$. This scaling is different from the behavior of $\widetilde{n}_{\mathrm{DE}}(k)$ for quenches to the Tonks–Girardeau limit of an infinitely strong repulsive interaction strength, where analytical calculations yield $\widetilde{n}_{\mathrm{DE}}(k) \propto k^{-2}$ [73]. Similarly as here, for finite but strong repulsive interactions, the scaling of $\widetilde{n}_{\mathrm{DE}}(k) \propto k^{-2}$ becomes more and more pronounced over larger ranges of intermediate k [166].

In Fig. 5.11(b), we plot the second-order coherence $g^{(2)}_{\mathrm{DE}}(x)$ in the diagonal ensemble for several post-quench interaction strengths γ. For comparison, we also plot the constant form $g^{(2)}(x, t = 0) = 1 - 1/N$ appropriate to the ideal gas (horizontal line). The first feature we notice is that for all values of the post-quench interaction strength, $g^{(2)}_{\mathrm{DE}}(x)$ is increased at short distances compared to its initial value. For the quench to $\gamma = -0.5$ (pink dot-dashed line), $g^{(2)}_{\mathrm{DE}}(x)$ decreases monotonically for larger distances. For $\gamma = -2$ (blue dashed line), $g^{(2)}_{\mathrm{DE}}(x)$ exhibits a local minimum at finite distance $x \approx 0.3 \times (2\pi k_F^{-1})$, before increasing again at larger distances. This behavior can also be observed for $\gamma = -10$ (green dotted line), where the minimum in $g^{(2)}_{\mathrm{DE}}(x)$ moves to smaller distances $x \approx 0.1 \times (2\pi k_F^{-1})$ and becomes more pronounced. This trend continues for quenches to larger attractive values of the interactions strength. For $\gamma = -40$ (solid red line), the minimum is located at $x \approx 0.03 \times (2\pi k_F^{-1})$ and its magnitude is again decreased compared to the quench to $\gamma = -10$. The large increased value of $g^{(2)}_{\mathrm{DE}}(0)$ and the minimum at larger distances is a signature of bound states, which become more strongly bound at larger attractive values of the post-quench interaction strength. The behavior past this minimum is consequently dominated by scattering states for strong attractive interactions, and indeed the shape of $g^{(2)}_{\mathrm{DE}}(x)$ for distances $x \gtrsim 0.03 \times (2\pi k_F^{-1})$ is nearly identical for quenches to $\gamma = -40$ and $\gamma = +40$ (black dot-dashed line). The increase of $g^{(2)}_{\mathrm{DE}}(x)$ for $x \gtrsim 0.6\times(2\pi k_F^{-1})$ is a finite-size effect [166].

5.7 Conclusions

We have investigated the static and nonequilibrium correlation functions of the one-dimensional Bose gas with attractive interactions within the Lieb–Liniger model. Our computational method is based on the coordinate Bethe ansatz and was found to be more demanding

for attractive interactions compared to repulsive interactions for large values of the interaction strength due to ever-smaller string deviations of the rapidities. Nevertheless, we were able to calculate first-, second-, and third-order correlation functions of the ground state for up to seven particles and a wide range of attractive interactions. We observed the emergence of bright soliton-like behavior for increasing attractive interaction strengths in relative-coordinate correlation functions, with the shape of the latter agreeing closely with the corresponding mean-field bright soliton solutions.

We also calculated the dynamics of the correlation functions following a quench of the interaction strength, starting from the non-interacting gas ground state to several representative values γ for up to four particles. For small post-quench interaction strengths of $\gamma \approx -0.5$, the energy deposited in the system by the quench was found to be on the order of the energy gap of the system, and consequently excitations are strongly suppressed. This resulted in correlation functions exhibiting quasi two-level dynamics. For quenches to more attractive values of the interaction strength, local correlation functions were found to increase on short time scales, while for longer times the correlations functions settled to fluctuate around a constant value, substantially increased compared to the initial value. For quenches to large attractive interaction strengths, single-frequency oscillations on top of an overall irregular behavior were observed, with the oscillations persisting at late times. The oscillatory behavior also arose in the momentum distribution for large post-quench interactions strengths. The reason for these was linked to the contribution of bound states in the many-body wave function.

For quantities not influenced by short-distance features, such as the second-order coherence away from the origin, the relaxation dynamics for quenches to strong interactions is remarkably similar to that of a system following a quench to repulsive interactions of the same magnitude, where the system relaxes due to dephasing of the (many-body) energy eigenstates. The same behavior was observed for the relaxed correlation functions in the infinite time limit. The relaxed values of local correlation functions, on the other hand, were very much increased compared to their repulsively interacting counterparts. The scaling of both the relaxed local second- and third-order coherence with post-quench interaction strength were consistent with a constant value much larger than the initial value in the limit of infinitely strong attractive interactions. For the local second-order coherence, the scaling

with particle number was consistent with a recently obtained value at strong interactions.

5.8 Supplement

5.8.1 Mean-field correlation functions

In this appendix we describe how we obtained the mean-field results for comparison with the Lieb-Liniger results plotted in Figs. 5.1, 5.2. The solution of the 1D Gross–Pitaevskii equation is (see e.g. Refs. [182, 389])

$$\Psi_{\mathrm{GP}}(\theta,\theta_0)=\begin{cases}\sqrt{\frac{1}{2\pi}}, & |\gamma^{(r)}|\le|\gamma_{\mathrm{cr}}^{(r)}|\\ \sqrt{\frac{K(m)}{2\pi E(m)}}\mathrm{dn}\Big(\frac{K(m)}{\pi}(\theta-\theta_0)\Big|m\Big), & \text{else}\end{cases} \tag{5.15}$$

where $\theta\in[0,2\pi)$ is the angular variable on the ring (the radius is incorporated in the interaction strength), θ_0 is the center of the soliton and we assumed periodic boundary conditions $\Psi_{\mathrm{GP}}(0)=\Psi_{\mathrm{GP}}(2\pi)$. The functions $K(m)$ and $E(m)$ are the complete elliptic integrals of the first and second kind, respectively, and $\mathrm{dn}(x|m)$ is one of the Jacobian elliptic functions. The parameter $m\in[0,1]$ is fixed by the solution to

$$K(m)E(m)=\frac{\pi^2\gamma^{(r)}}{2}, \tag{5.16}$$

where $\gamma^{(r)}=\frac{cNL}{2\pi^2}$ in our units and the phase transition occurs at $\gamma_{\mathrm{cr}}^{(r)}=-0.5$.

The approximation leading to the Gross–Pitaevski equation is that the many-body wave function is a product over single-particle wave functions $\Psi(\theta_1,\ldots,\theta_N)=\prod_{j=1}^N\Psi_{\mathrm{GP}}(\theta_j,\theta_{0,j})$, which depend on the center of mass variable $\theta_{0,j}$ (5.15). Following Ref. [393], we restore the translational symmetry of the wave function via a symmetrized Hartree-Fock ansatz

$$\Psi(\theta_1,\ldots,\theta_N)=\frac{1}{\sqrt{2\pi}}\int_0^{2\pi}d\Theta\prod_{j=1}^N\Psi_{\mathrm{GP}}(\theta_j,\Theta). \tag{5.17}$$

The normalized correlation functions are then given by

$$g^{(1)}(\theta,\theta')=\frac{G^{(1)}(\theta,\theta')}{\sqrt{G^{(1)}(\theta,\theta)G^{(1)}(\theta',\theta')}},\qquad g^{(2)}(\theta,\theta')=\frac{G^{(2)}(\theta,\theta')}{G^{(1)}(\theta,\theta)G^{(1)}(\theta',\theta')}, \tag{5.18}$$

where

$$G^{(1)}(\theta,\theta') = \frac{N}{2\pi}\int_0^{2\pi} \mathrm{d}\Theta\ \Psi^*_{\mathrm{GP}}(\theta,\Theta)\Psi_{\mathrm{GP}}(\theta',\Theta), \tag{5.19}$$

and similarly

$$G^{(2)}(\theta,\theta') = \frac{N(N-1)}{2\pi}\int_0^{2\pi} \mathrm{d}\Theta\ \Psi^*_{\mathrm{GP}}(\theta,\Theta)\Psi_{\mathrm{GP}}(\theta,\Theta)\Psi^*_{\mathrm{GP}}(\theta',\Theta)\Psi_{\mathrm{GP}}(\theta',\Theta). \tag{5.20}$$

5.8.2 Details of numerical algorithm involving bound states

Eigenstates with complex rapidities arrange themselves in so-called string patterns in the complex plane for large values of $|c|L$, with deviations from these strings being exponentially small in the system size [223, 226]. This results in numerical problems for the methodology of Ref. [165], as illustrated for the $N = 2$ particle ground state in the following. The Bethe rapidities for intermediate and large $|c|L$ in this case read

$$\lambda_j = \pm i\frac{c}{2} + i\delta_j\ , \tag{5.21}$$

where the minus (plus) sign applies to λ_1 (λ_2) by convention (recall that $c < 0$). The string deviations $\delta_j \propto \mathrm{e}^{const\times L}$. The (unnormalized) two-particle wave-function reads

$$\begin{aligned}\zeta(x_1,x_2) &= (\lambda_2-\lambda_1-ic)\mathrm{e}^{i(\lambda_1 x_1+\lambda_2 x_2)} - (\lambda_1-\lambda_2-ic)\mathrm{e}^{i(\lambda_2 x_1+\lambda_1 x_2)}\\ &\equiv -i\Big((2\lambda+c)\mathrm{e}^{\lambda r} + (2\lambda-c)\mathrm{e}^{-\lambda r}\Big)\ ,\end{aligned} \tag{5.22}$$

where in the last step we defined the relative coordinate $r = x_2 - x_1$ and $\lambda = \lambda_1/i = -\lambda_2/i$. In light of Eq. (5.21), the first term in the last line is a product of a very small number $(2\lambda + c)$ and a very large one ($\mathrm{e}^{\lambda r}$) away from $r = 0$. The former is a difference of two numbers that are nearly equal, leading to catastrophic cancellations in double-precision floating-point arithmetic. But since $2\lambda + c \equiv 2\delta_1$, and we can express δ_1 with the help of Eq. (5.6), we can replace this critical factor in Eq. (5.22) with

$$\delta_1 \equiv 2\lambda + c = \mathrm{e}^{-\lambda L}(2\lambda - c). \tag{5.23}$$

The last term is now amenable to numerical evaluation. This procedure can be extended to $N > 2$, as described below for parity invariant states for $N = 3$ and 4 particles.

$N = 3$ particles

There are two parity-invariant eigenstates with complex rapidities for $N = 3$, and the following factors have to be replaced:

- The ground state is a three-body bound state with imaginary rapidities and $\lambda_2 = 0$. For small string deviations, the factor $\lambda_2 - \lambda_1 - ic \equiv -\lambda_1 - ic$ needs to be replaced. The Bethe equation for λ_1 is

$$e^{i\lambda_1 L} = \frac{\lambda_1 + ic}{\lambda_1 - ic} \frac{2\lambda_1 + ic}{2\lambda_1 - ic}, \tag{5.24}$$

  which can be written as

$$-(\lambda_1 + ic) = -\mathrm{e}^{i\lambda_1 L}(\lambda_1 - ic)\frac{2\lambda_1 - ic}{2\lambda_1 + ic}. \tag{5.25}$$

- First excited parity invariant state. Here, the rapidities λ_1, λ_3 are real up to the "phase crossover" point [226], after which they are imaginary. The critical factor to be replaced is $-2\lambda_1 - ic$. Using Eq. (5.25) leads to

$$-(2\lambda_1 + ic) = -\mathrm{e}^{i\lambda_1 L}(2\lambda_1 - ic)\frac{\lambda_1 - ic}{\lambda_1 + ic}. \tag{5.26}$$

$N = 4$ particles

For $N = 4$ particles, an infinite number of parity-invariant bound states contribute to the post-quench dynamics, and they can be grouped into the following categories, cf. Sec. 5.5.1.

- The ground state with $\{n_j\} = \{0, 0\}$. Define $\lambda_j := \Im(\lambda_j)$, since the rapidities are purely imaginary. Plugging this into Eq. (5.6) leads to the following two equations.

$$\mathrm{e}^{-\lambda_1 L} = \frac{\lambda_1 - \lambda_2 + c}{\lambda_1 - \lambda_2 - c} \frac{\lambda_1 + \lambda_2 + c}{\lambda_1 + \lambda_2 - c} \frac{2\lambda_1 + c}{2\lambda_1 - c}, \tag{5.27}$$

$$\mathrm{e}^{-\lambda_2 L} = \frac{\lambda_2 - \lambda_1 + c}{\lambda_2 - \lambda_1 - c} \, \frac{\lambda_2 + \lambda_1 + c}{\lambda_2 + \lambda_1 - c} \, \frac{2\lambda_2 + c}{2\lambda_2 - c} \, . \tag{5.28}$$

There are two critical factors: $|\lambda_1| - |\lambda_2| - |c|$ and $2|\lambda_2| - |c|$. Define $\lambda_1, \lambda_2 > 0$. Rewriting Eq. (5.27) leads to

$$\lambda_1 - \lambda_2 + c = \mathrm{e}^{-|\lambda_1| L}(|\lambda_1| - |\lambda_2| + |c|) \frac{|\lambda_1| + |\lambda_2| + |c|}{|\lambda_1| + |\lambda_2| - |c|} \, \frac{2|\lambda_1| + |c|}{2|\lambda_1| - |c|} =: \alpha \, . \tag{5.29}$$

Equation (5.28) can be expressed as

$$2\lambda_2 + c = \mathrm{e}^{-|\lambda_2| L}(-\alpha) \frac{|\lambda_2| + |\lambda_1| + |c|}{|\lambda_2| + |\lambda_1| - |c|} \, \frac{2|\lambda_2| + |c|}{|\lambda_2| - |\lambda_1| - |c|} \, , \tag{5.30}$$

where α is the first critical factor defined in Eq. (5.29).

- The three-body bound state with $\{n_j\} = \{1, 0\}$. This is the first parity invariant excited state and has real rapidities λ_1 and λ_4 that tend to zero for large attractive values of cL. Following Ref. [325], Appendix B, we can reparameterize the rapidities in this case via their deviations $\delta = \mathrm{e}^{-|c|L/2}$ from the string solution

$$\begin{aligned} \lambda_1 &= \delta\alpha \, , \\ \lambda_2 &= -ic + i\delta^2\beta \, . \end{aligned} \tag{5.31}$$

Plugging this into the Bethe equations (5.6), Ref. [325] obtained

$$\begin{aligned} \alpha &= \sqrt{12}\,|c| \, , \\ \beta &= 6Lc^2 \, . \end{aligned} \tag{5.32}$$

We found it necessary to utilize high-precision arithmetic for numerical calculations involving this eigenstate. To obtain correspondingly precise Bethe rapidities for large attractive values of γ, we use Eqs. (5.32) as the starting point for our root-finding algorithm.

- Eigenstates with $\{n_j\} = \{n, 0\}$ for all integers $n \geq 2$. λ_1 is real, λ_2 imaginary, and the

critical factor is $2|\lambda_2| - |c|$. Rewrite the Bethe equation for λ_2 and define $\lambda = -i\lambda_2$:

$$\mathrm{e}^{-\lambda L} = \frac{\lambda_1 - i(\lambda + c)}{\lambda_1 - i(\lambda - c)} \frac{\lambda_1 + i(\lambda + c)}{\lambda_1 + i(\lambda - c)} \frac{2\lambda + c}{2\lambda - c} \,. \tag{5.33}$$

Define $\lambda, \lambda_1 > 0$, rewrite

$$2\lambda + c = \mathrm{e}^{-|\lambda| L}(2|\lambda| + |c|) \frac{|\lambda_1| - i(|\lambda| + |c|)}{|\lambda_1| - i(|\lambda| - |c|)} \frac{|\lambda_1| + i(|\lambda| + |c|)}{|\lambda_1| + i(|\lambda| - |c|)} \,. \tag{5.34}$$

- Eigenstates with $\{n_j\} = \{n, n\}$ for all integers $n \geq 1$. The Bethe rapidities are complex and satisfy $\lambda_1 = \lambda_2^*$. Rewrite the first Bethe equation using the following definitions: $\Re(\lambda_1) \equiv \Re(\lambda_2) =: \delta$ and $\Im(\lambda_1) \equiv -\Im(\lambda_2) =: \lambda$.

$$\mathrm{e}^{i\delta L}\mathrm{e}^{\lambda L} = \frac{2\lambda + c}{2\lambda - c} \frac{2\delta + ic}{2\delta - ic} \frac{2\delta + i(2\lambda + c)}{2\delta + i(2\lambda - c)} \,, \tag{5.35}$$

The critical factor is $2|\lambda| - |c|$. Define $\delta, \lambda > 0, c < 0$, so we need to replace $2\lambda + c$ in Eq. (5.35). Straightforward manpulation of Eq. (5.35) leads to

$$2\delta(2\lambda + c) + i(2\lambda + c)^2 = \mathrm{e}^{i\delta L}\mathrm{e}^{-\lambda L} \frac{(2\lambda - c)(2\delta + i(2\lambda - c))(2\delta + ic)}{2\delta - ic}. \tag{5.36}$$

For two complex numbers to be equal, both the real and imaginary part have to be equal, so we can focus on the real part here, which leads to

$$(2\lambda + c) = \frac{2|\lambda| + |c|}{2|\delta|} \mathrm{e}^{-|\lambda| L} \Re \left[(2|\delta| + i(2|\lambda| + |c|)) \frac{2|\delta| + i|c|}{2|\delta| - i|c|} \mathrm{e}^{i|\delta| L} \right]. \tag{5.37}$$

- Eigenstates with $\{n_j\} = \{n, n-1\}$ for all integers $n \geq 2$. For $|c| < |c_{\mathrm{crit}}|$, the Bethe rapidities are real. Here, c_{crit} is a n-dependent "phase crossover" point [226]. Past that point, they turn into complex numbers and are complex conjugates of each other, $\lambda_1 = \lambda_2^*$, and this case is equivalent to the preceding one.

Extending this procedure to $N > 4$ particles is possible, but the number of factors that have to be considered increases rapidly.

6

Periodic driving of the interaction strength in the Lieb–Liniger model

The interaction quench scenario utilized in the previous chapters is conceptually the simplest protocol to take a system out of equilibrium. Due to the integrability of the Lieb–Liniger model, we found that the system following a quench does not thermalize, but still relaxes to a steady state. In this chapter, we ask the question if periodically changing the interaction strength of the post-quench Hamiltonian changes this behavior, and if so in what way. Specifically, we quench from the non-interacting ground state to some final repulsive value of the interaction strength, and then periodically modulate the interaction strength around that value. Due to the driving, the energy of the system is not conserved, and integrability is broken. The time-averaged interaction strength over one period is equal to the constant value of the quench scenario of Chapters 3, 4, allowing us to compare the dynamics of the driven and undriven system.

One question at hand is if we see a crossover from relaxation to a generalized Gibbs ensemble to a true thermal state. If so, does this happen instantly, i.e. for arbitrarily weak perturbations, or is there some kind of remembrance of (quasi-) conserved constants of motions? In classical systems, the famous KAM theorem gives a mathematical answer to these questions, as discussed in the introduction to this thesis. However, until now no quantum analogue has been identified [91, 395]. Generic (ergodic) quantum systems subject to periodic driving are believed to continuously absorb energy from the driving and thermalize at infinite temperature [26, 150, 151, 163]. However, recent numerical studies have found parameter regimes for certain models for which the heating is very slow [148, 156, 396, 397]. The change from one regime to the other happens at a finite threshold of the driving frequency [148, 156, 396]. For integrable models mappable to a quadratic Hamiltonian, Refs. [161, 162] found that the system synchronizes with the driving and that the steady state can be described by a periodic generalized Gibbs ensemble. A periodicaly-driven-system analogue of prethermalization [93] was observed in Refs. [153, 156, 160]. Most of these studies are performed for locally bounded Hilbert spaces, but two recent studies for continuous systems found threshold behavior [396], as well as absence of infinite heating for all parameters [397]. For locally unbounded Hilbert spaces the infinite-temperature state is trivial, and should be readily identifiable in our work.

We proceed by summarizing Floquet theory in Sec. 6.1, which is the standard tool to study time-periodic systems. Combining this with the coordinate Bethe ansatz approach developed in Chapter 3 enables us to calculate nonequilibrium and time-averaged correlation functions by expressing the time evolution operator in Lieb–Liniger basis states and diagonalizing it numerically, as detailed in Sec. 6.2. In Sec. 6.3 we present results on the nonequilibrium dynamics and time-averaged second-order coherence, energy and fidelity for two and three particles. We also analyze the Floquet energy spectrum. In Sec. 6.4, we discuss the numerical difficulties that arise when approximating the infinite-dimensional Floquet basis by a finite subset. Finally, we conclude in Sec. 6.5.

6.1 Floquet theory for time-periodic systems

For quantum-mechanical systems described by a Hamiltoninan with generic time-dependence, the powerful tools of time-independent quantum mechanics are not available due to the fact that the Hamiltonian at two different times does not commute. However, for a *time-periodic* Hamiltonian $\hat{H}(t) \equiv \hat{H}(t+T)$, Floquet theory states that a complete set of solutions to the time-dependent Schrödinger equation

$$i\frac{\partial}{\partial t}|\Psi(t)\rangle = \hat{H}(t)|\Psi(t)\rangle \tag{6.1}$$

is given by the so-called Floquet states [100–103]

$$|F_j(t)\rangle = \mathrm{e}^{-i\epsilon_j t}|\Phi_j(t)\rangle \ , \tag{6.2}$$

where the real numbers ϵ_j are the so-called Floquet quasi-energies and $|\Phi_j(t)\rangle$ are the Floquet modes which obey the system's time periodicity

$$|\Phi_j(t+T)\rangle = |\Phi_j(t)\rangle \ . \tag{6.3}$$

This is in complete analogy with the space-periodic case, where the solution of the Schrödinger equation is given by Bloch's theorem [104]. The ambiguity of the quasimomentum of the space-periodic case carries over to the quasienergy of the time-periodic case, and we will always work in the first Brioullin zone such that $\epsilon_j \in [-\pi/T, \pi/T]$. In further analogy, one can show that extending the Hilbert space to include time, and then simultaneously diagonalizing the Hamiltonian and the time translation operator, gives the Floquet states, which therefore form a common basis of $\hat{H}$ and the time-translation operator. In doing so, the time-dependent problem is turned into an effective time-independent one in the extended Hilbert space, and the powerful methods of standard time-independent quantum mechanics can be applied. However, computationally it is more convenient for us to obtain the Floquet modes by diagonalizing the time-evolution operator $\hat{U}(t+T,t)$ over one period, defined by $\hat{U}(t+T,t)|\Psi(t)\rangle = |\Psi(t+T)\rangle$. This can be seen as follows. Acting with $\hat{U}(t+T,t)$ on the

Floquet states yields

$$\hat{U}(t+T,t)|F_j(t)\rangle = |F_j(t+T)\rangle \ , \tag{6.4}$$

which, using Eq. (6.2) and the time-periodicity of the Floquet modes, yields

$$\hat{U}(t+T,t)|\Phi_j(t)\rangle = \mathrm{e}^{-i\epsilon_j T}|\Phi_j(t)\rangle \ . \tag{6.5}$$

This is an eigenvalue equation and can be utilized to find the Floquet modes at a given time t. If we are only interested in stroboscobic times $t = nT$, where n is an integer, the time-evolution operator is given by

$$\hat{U}(nT,0) \equiv [\hat{U}(T,0)]^n \ . \tag{6.6}$$

This means that given an appropriate basis, diagonalizing $\hat{U}(T,0)$ leads to the system at stroboscopic times being described by the n-th power of a diagonal matrix, which is trivial to compute. Eq. (6.6) holds because we can expand $\hat{U}(t,0)$ in the basis of Floquet states $|F_j(t)\rangle$ and use their definition [Eq. (6.2)] to obtain

$$\hat{U}(t,0) = \sum_j \mathrm{e}^{-i\epsilon_j t}|\Phi_j(t)\rangle\langle\Phi_j(0)| \ , \tag{6.7}$$

which for one period T becomes

$$\hat{U}(T,0) = \sum_j \mathrm{e}^{-i\epsilon_j T}|\Phi_j(0)\rangle\langle\Phi_j(0)| \tag{6.8}$$

due to the periodicity of Floquet modes. For $t = nT$, using the resolution of identity (at $t = 0$) n times proves Eq. (6.6). With the knowledge of ϵ_j and $|\Phi_j(0)\rangle$, any state $|\Psi(T)\rangle$ at time T can be expanded as

$$\begin{aligned} |\Psi(T)\rangle &= \sum_j \langle F_j(T)|\Psi(T)\rangle \ |F_j(T)\rangle = \sum_j \langle\Phi_j(T)|\Psi(T)\rangle \ |\Phi_j(T)\rangle \\ &= \sum_j \langle\Phi_j(0)|\hat{U}(T,0)|\Psi(0)\rangle \ |\Phi_j(0)\rangle \ . \end{aligned} \tag{6.9}$$

Using the spectral resolution for $\hat{U}$ [Eq. (6.8)] yields

$$|\Psi(T)\rangle = \sum_j \mathrm{e}^{-i\epsilon_j T}\langle\Phi_j(0)|\Psi(0)\rangle\ |\Phi_j(0)\rangle\,. \tag{6.10}$$

Furthermore, utilizing Eq. (6.6) leads to

$$|\Psi(nT)\rangle = \sum_j \mathrm{e}^{-i\epsilon_j nT}\langle\Phi_j(0)|\Psi(0)\rangle\ |\Phi_j(0)\rangle\,. \tag{6.11}$$

For arbitrary times t, we can write $t = \delta t + nT$ with $0 < \delta t < T$ to obtain [103]

$$\hat{U}(t,0) = \hat{U}(\delta t,0)\hat{U}(nT,0) \equiv \hat{U}(\delta t,0)[\hat{U}(T,0)]^n\,. \tag{6.12}$$

For a generic state, this leads to

$$|\Psi(nT+\delta t)\rangle = \sum_j \mathrm{e}^{-i\epsilon_j nT}\langle\Phi_j(0)|\Psi(0)\rangle\ \mathrm{e}^{-i\epsilon_j \delta t}|\Phi_j(\delta t)\rangle\,. \tag{6.13}$$

Importantly, the coefficients of any initial state in the Floquet basis are time-independent, the time-dependence being incorporated in the basis states. In numerical calculations, time is restricted to discrete points. In order to find $|\Phi_j(\delta t)\rangle$, one can either make use of the eigenvalue equation (6.5) for every point δt, or use $\hat{U}(\delta t,0)$ to propagate $|\Phi_j(0)\rangle$ up to the desired time point.

6.2 Setup

The setup we will consider in the remainder of this chapter is depicted in Fig. 6.1. The system is initially prepared in the noninteracting ground state with structureless spatial representation $\langle\{x_j\}|\Psi(0)\rangle = L^{-N/2}$. At time $t = 0$, the interaction strength is instantaneously changed from zero to γ_1 and the system is governed by the Lieb–Liniger Hamiltonian $\hat{H}_1 = -\sum_j \partial_{x_j}^2 + 2c_1 \sum_{l>j} \delta(x_l - x_j)$ at interaction strength $c_1 = \gamma_1 n_{1\mathrm{D}}$, with density $n_{1\mathrm{D}} = N/L$.[1] The system is left to evolve under the influence of Hamiltonian $\hat{H}_1$ up until t_1, at which point we change the Hamiltonian instantaneously to $\hat{H}_2$, where the interaction

[1] As done throughout this thesis, we set $\hbar = 1$ and the particle mass $m = 1/2$.

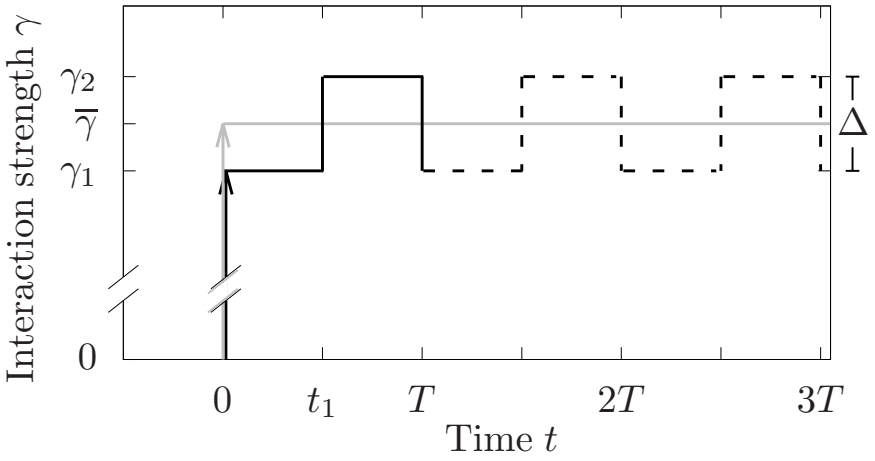

FIGURE 6.1: Time-periodic Hamiltonian (solid black line for first driving period, after that black dashed line) with period T and amplitude $\Delta = \gamma_2 - \gamma_1$ after an initial interaction quench from the non-interacting ground state at time $t = 0$. The time-averaged Hamiltonian of the driven system is given by the time-independent post-quench Hamiltonian at interaction strength $\overline{\gamma}$ (horizontal grey line).

strength is $\gamma_2 = \gamma_1 + \Delta$. For times $t_1 < t < T$ the systems is governed by Hamiltonian $\hat{H}_2$. This first period is marked by the solid black line in Fig. 6.1. If we now choose to repeat this protocol in time (marked by the black dashed line for the second and third period), the full time-dependent Hamiltonian (after the initial quench) reads

$$\hat{H} = \begin{cases} \hat{H}_1 & \text{for} \quad nT \leq t < (2n+1)t_1 \\ \hat{H}_2 & \text{for} \quad (2n+1)t_1 \leq t < (n+1)T \ , \end{cases} \tag{6.14}$$

where n is a non-negative integer. The system is time-periodic with period T, $\hat{H}(t) = \hat{H}(t+T)$, and we can therefore employ Floquet theory to solve for the time-evolution in terms of Lieb–Liniger eigenstates. For comparison, we also plot the time-averaged interaction strength (horizontal grey line), which corresponds to the interaction quench scenario considered in Chapters 3, 4. As indicated in Fig. 6.1, we only consider the case $t_1 = T/2$ in this work. However, the theory we develop does not rely on that, opening up the possibility of studying the effect of breaking time-reversal symmetry in the future. The time evolution operator over a single period is given by $\hat{U}(T,0) = \mathrm{e}^{-iH_2(T-t_1)}\mathrm{e}^{-iH_1t_1}$ and we proceed by explicitly writing down $\hat{U}(T,0)$ in the basis of Lieb–Liniger eigenstates.

6.2.1 Time-evolution over one period: finding $\hat{U}(T,0)$

Independent of the initial state,[2] our protocol can be described by two interaction quenches between Lieb–Liniger Hamiltonians $\hat{H}_1$ and $\hat{H}_2$ within each period T, and consists of the following steps:

(I) Evolution of basis states at interaction strength γ_1 from time $t_0 \equiv 0$ to t_1.

(II) Interaction strength quench from γ_1 to γ_2 at time t_1.

(III) Evolution of basis states at interaction strength γ_2 from time t_1 up to $t_2 = T$.

(IV) Interaction strength quench from γ_2 back to γ_1 at time T.

Denote the Lieb–Liniger eigenstates at γ_1 by lowercase Greek letters $|\{\lambda_j\}\rangle$ and their eigenvalues by E_λ, and the eigenstates corresponding to γ_2 by uppercase Greek letters $|\{\Lambda_j\}\rangle$ and their eigenvalues by E_Λ. Taking as initial state one eigenstate $|\{\lambda_j^{(l)}\}\rangle$ at γ_1,[3] and setting $l = 0$ for concreteness, evolution with $\hat{H}_1$ leads to

$$|\Psi(t_1)\rangle \equiv \mathrm{e}^{-i\hat{H}_1 t_1}|\{\lambda_j^{(0)}\}\rangle = \mathrm{e}^{-iE_\lambda^{(0)}t_1}|\{\lambda_j^{(0)}\}\rangle \tag{6.15}$$

for step (I), where we denote the state of the system at time t by $|\Psi(t)\rangle$. At $t = t_1$, the system's Hamiltonian changes to $\hat{H}_2$, which corresponds to an instantaneous quench $\gamma_1 \to \gamma_2$. Expressing $|\Psi(t_1)\rangle$ in this basis leads to

$$|\Psi(t_1)\rangle = \mathrm{e}^{-iE_\lambda^{(0)}t_1}\sum_n \langle\{\Lambda_j^{(n)}\}|\{\lambda_j^{(0)}\}\rangle|\{\Lambda_j^{(n)}\}\rangle \equiv \mathrm{e}^{-iE_\lambda^{(0)}t_1}\sum_n C_{(\mathrm{II})}^{(n)}|\{\Lambda_j^{(n)}\}\rangle \tag{6.16}$$

for step (II). The time evolution for step (III) is now simply given by

$$|\Psi(t_2)\rangle = \mathrm{e}^{-iE_\lambda^{(0)}t_1}\sum_n C_{(\mathrm{II})}^{(n)}\mathrm{e}^{-iE_\Lambda^{(n)}(T-t_1)}|\{\Lambda_j^{(n)}\}\rangle \tag{6.17}$$

[2] We will deal with the representation of the initial state in the new basis later on, for now we just develop the general theory.

[3] The index j in the set stands for the individual Bethe rapidities, of which there are as many as there are particles N, cf. Chapter 2. For consistency, we denote the l–th basis set as $|\{\lambda_j^{(l)}\}\rangle$.

Step (IV) consists of quenching back to Hamiltonian $\hat{H}_1$:

$$\begin{aligned}|\Psi(T)\rangle &= \mathrm{e}^{-iE_\lambda^{(0)}t_1}\sum_{n,m} C_{(\mathrm{II})}^{(n)}\mathrm{e}^{-iE_\Lambda^{(n)}(T-t_1)}\langle\{\lambda_j^{(m)}\}|\{\Lambda_j^{(n)}\}\rangle\ |\{\lambda_j^{(m)}\}\rangle \\ &\equiv \mathrm{e}^{-iE_\lambda^{(0)}t_1}\sum_{n,m} C_{(\mathrm{II})}^{(n)}C_{(\mathrm{I})}^{(m)}\mathrm{e}^{-iE_\Lambda^{(n)}(T-t_1)}|\{\lambda_j^{(m)}\}\rangle. \end{aligned} \tag{6.18}$$

This represents the first column of $\hat{U}(T,0)$ in the basis of Lieb–Liniger eigenstates at interaction strength γ_1, i.e.

$$\langle\{\lambda_j^{(0)}\}|\hat{U}(T,0)|\{\lambda_j^{(m)}\}\rangle \equiv U^{(0,m)}(T,0). \tag{6.19}$$

Doing this for every basis state $|\{\lambda_j^{(n)}\}\rangle$ leads to the full $U^{(n,m)}(T,0)$.

6.2.2 Computing the Floquet modes and energies — Exact diagonalization

Having explicitly written down $\hat{U}(T,0)$ in the basis of Lieb–Liniger eigenstates, the Floquet modes can be obtained by solving the eigenvalue equation (6.5), which amounts to diagonalizing $U^{(n,m)} \equiv U$ (6.19). The term 'diagonalizing a matrix' refers to the procedure of finding a transformation matrix P such that $P^{-1}UP = E$, where $E = \mathrm{diag}(\kappa_0, \kappa_1, \kappa_2, \dots)$. The diagonal elements of E are the eigenvalues of U, and the columns of P are the corresponding eigenstates in the chosen basis.[4] Furthermore, because matrix multiplication is associative, the n-th power of U is given by $U^n = (PEP^{-1})^n = PE^nP^{-1}$, where $E^n = \mathrm{diag}(\kappa_0^{\mathrm{n}}, \kappa_1^{\mathrm{n}}, \kappa_2^{\mathrm{n}}, \dots)$. The eigenvalues κ_l of U are related to the Floquet quasi-energies ϵ_l via $\kappa_l = \mathrm{e}^{-i\epsilon_l T}$. Defining

$$\epsilon_l = -\frac{1}{T}\arg(\kappa_l^{-1})\ , \tag{6.20}$$

the quasi-energies fall inside the first Brioullin zone.

Since U is unitary, we first transform it into an associated Hermitian matrix A and then diagonalize it.[5] This is done via a (generalized) Cayley transform. The Cayley transform T

[4] In our numerical implementation, we make use of the Eigen library, which diagonalizes complex matrices by means of a Schur decomposition (implemented via QR-reduction).

[5] Numerical implementations for hermitian matrices are faster and more exact.

of a unitary operator U is defined as [398]

$$A = i(\mathrm{Id} + \mathrm{U})(\mathrm{Id} - \mathrm{U})^{-1} \,, \tag{6.21}$$

where Id is the identity operator and A is Hermitian. This transform has the handy property that the eigenstates of both U and A are the same, and the eigenvalues are related by a simple relation: If κ is an eigenvalue of A with eigenvector $|x\rangle$, then

$$U(\kappa) = \frac{\kappa - i}{\kappa + i} \tag{6.22}$$

is an eigenvalue of U for the *same* eigenvector $|x\rangle$.

For the quench scenario in previous chapters, we approximated the infinite-dimensional basis of Lieb–Liniger eigenstates by a finite subset of these exact eigenstates. Here, we have to truncate the number of Lieb–Liniger eigenstates to represent U in a finite basis, which entails a truncation of the formally infinite number of Floquet states. In other words, we have to truncate an infinite number of Floquet states, each of which is in turn approximated by a finite number of Lieb–Liniger eigenstates. Additionally, due to the Floquet energies being defined in the first Brioullin zone, there is no natural ordering of Floquet states and an infinite number of quasi-energies are folded into a finite interval. This leads to numerical issues and we devote Sec. 6.4 to discuss these in more detail.

6.2.3 Calculation of correlation functions at stroboscopic times

In order to be able to apply our methodology of Chapter 3, we need to express the state of the system at time t in terms of Lieb–Liniger eigenstates. We first do this for stroboscopic times nT, where n is an integer, since the expressions simplify in this case, and then generalize the procedure to arbitrary times. Recall Eq. (6.11):

$$|\Psi(nT)\rangle = \sum_j \mathrm{e}^{-i\epsilon_j nT} \langle \Phi_j(0)|\Psi(0)\rangle \, |\Phi_j(0)\rangle \,.$$

The expectation value of an arbitrary operator $\hat{O}$ in the state $|\Psi(nT)\rangle$ is then given by

$$\langle\hat{O}\rangle_{nT} \equiv \langle\Psi(nT)|\hat{O}|\Psi(nT)\rangle = \sum_{l,k} C_k^* C_l \, \mathrm{e}^{i(\epsilon_k-\epsilon_l)nT} \, \langle\Phi_k(0)|\hat{O}|\Phi_l(0)\rangle, \tag{6.23}$$

where $C_l = \langle\Phi_l(0)|\Psi(0)\rangle$ is the overlap of the initial state with the Floquet mode $|\Phi_l(0)\rangle$. The diagonalization of U can be viewed as a basis change. Denote U in the basis of Floquet modes as $U^{(F)}$, and $U^{(LL)}$ in the basis of Lieb–Liniger eigenstates. Then, $U^{(F)} = P^{-1}U^{(LL)}P$ and

$$|\Phi^{(k)}(0)\rangle = \sum_l P_{kl} |\{\lambda_j^{(l)}\}\rangle \tag{6.24}$$

describes the Floquet modes in the Lieb–Liniger basis.[6] This leads to

$$C_k^* = \langle\Phi_k(0)|\Psi(0)\rangle^* = \langle\Psi(0)|\Phi_k(0)\rangle = \sum_l P_{kl} \langle\Psi(0)|\{\lambda_j^{(l)}\}\rangle \tag{6.25}$$

and

$$\langle\Phi_k(0)|\hat{O}|\Phi_l(0)\rangle = \sum_{m,n} P^{-1}_{mk} P_{ln} \langle\{\lambda_j^{(m)}\}|\hat{O}|\{\lambda_j^{(n)}\}\rangle = \sum_{m,n} P^*_{km} P_{ln} \langle\{\lambda_j^{(m)}\}|\hat{O}|\{\lambda_j^{(n)}\}\rangle \,, \tag{6.26}$$

where in the last step we used the fact that P is unitary, which follows from the unitarity of U. The matrix elements and overlaps in Eq. (6.23) are time-independent, which allows us to calculate these quantities once and then propagate the individual terms in time with their corresponding quasi-energy phases before summing up.

6.2.4 Calculation of correlation functions at arbitrary times

To extend the calculation of correlation functions to arbitrary times t, we note that (6.13)

$$|\Psi(t)\rangle \equiv |\Psi(nT+\delta t)\rangle = \sum_j \mathrm{e}^{-i\epsilon_j nT} \langle\Phi_j(0)|\Psi(0)\rangle \, \mathrm{e}^{-i\epsilon_j \delta t} |\Phi_j(\delta t)\rangle \,,$$

[6] The columns of the transformation matrix are the eigenvectors of U in our original basis, as expected by construction.

with $0 < \delta t < T$. The expectation value of an arbitrary operator $\hat{O}$ in the state $|\Psi(t)\rangle$ is then given by

$$\langle \hat{O} \rangle_t \equiv \langle \Psi(t)|\hat{O}|\Psi(t)\rangle = \sum_l \sum_k C_k^* C_l \, \mathrm{e}^{i(\epsilon_k - \epsilon_l)nT} \mathrm{e}^{i(\epsilon_k - \epsilon_l)\delta t} \, \langle \Phi_k(\delta t)|\hat{O}|\Phi_l(\delta t)\rangle, \tag{6.27}$$

where $C_l = \langle \Phi_l(0)|\Psi(0)\rangle$ is again the time-independent overlap of the initial state with the Floquet mode $|\Phi_l(0)\rangle$. To find $|\Phi_k(\delta t)\rangle$, one could solve the eigenvalue equation (6.5) for fixed times δt similar to the procedure for finding $|\Phi_k(0)\rangle$. But since our protocol implies a constant Hamiltonian in time for each of the two half-periods, we instead choose to find the Floquet modes for the two time points $t = 0$ and $t = t_1$ and propagate the Floquet modes in between as explained in the following. For $0 \leq \delta t < t_1$, the system's time evolution is governed by $\hat{H}_1$, and the Floquet modes are

$$|\Phi_k(\delta t)\rangle = U(\delta t, 0)|\Phi_k(0)\rangle = U(\delta t, 0) \sum_l P_{kl} |\{\lambda_j^{(l)}\}\rangle = \sum_l P_{kl} \mathrm{e}^{-iE_\lambda^{(l)}\delta t} |\{\lambda_j^{(l)}\}\rangle \, , \tag{6.28}$$

which leads to

$$\langle \Phi_k(\delta t)|\hat{O}|\Phi_l(\delta t)\rangle = \sum_m \sum_n P_{km}^* P_{ln} \mathrm{e}^{i(E_\lambda^{(m)} - E_\lambda^{(n)})\delta t} \langle \{\lambda_j^{(m)}\}|\hat{O}|\{\lambda_j^{(n)}\}\rangle \, . \tag{6.29}$$

For $t_1 \leq \delta t < T$, the Hamiltonian governing the time evolution is $\hat{H}_2$ and we need to express $|\Phi_j(\delta t)\rangle$ in terms of $|\{\Lambda_j^{(l)}\}\rangle$. By solving the eigenvalue equation (6.5) at time $t = t_1$, i.e. diagonalizing $U(t_1 + T, t_1)$, we obtain the Floquet modes $|\Phi_j(t_1)\rangle$ and then propagate these in time. The procedure is identical to that for the first period, with P_{kl}, $|\{\lambda_j(m)\}\rangle$ and $E_\lambda^{(m)}$ replaced by their counterparts for the second period. The overlaps and Floquet energies, on the other hand, are time-independent and need only be evaluated once.[7]

The instantaneous energy $E(t) \equiv \langle \hat{H} \rangle_t$ in the state $|\Psi(t)\rangle$ is given by

$$E(t) \equiv \langle \Psi(t)|\hat{H}|\Psi(t)\rangle = \sum_l \sum_k C_k^* C_l \, \mathrm{e}^{i(\epsilon_k - \epsilon_l)nT} \mathrm{e}^{i(\epsilon_k - \epsilon_l)\delta t} \, \langle \Phi_k(\delta t)|\hat{H}|\Phi_l(\delta t)\rangle, \tag{6.30}$$

[7] We still evaluate the quasi-energies and compare them to those obtained for the previous half-period to ensure consistency.

where the matrix elements for $\delta t < t_1$ are

$$\begin{aligned}\langle\Phi_k(\delta t)|\hat{H}|\Phi_l(\delta t)\rangle &= \sum_m \sum_n P^*_{km} P_{ln} \mathrm{e}^{i(E^{(m)}_\lambda - E^{(n)}_\lambda)\delta t} \langle\{\lambda^{(m)}_j\}|\hat{H}|\{\lambda^{(n)}_j\}\rangle \\ &= \sum_m \sum_n P^*_{km} P_{ln} \mathrm{e}^{i(E^{(m)}_\lambda - E^{(n)}_\lambda)\delta t} E^{(n)}_\lambda \delta_{mn} \\ &= \sum_n P^*_{kn} P_{ln} E^{(n)}_\lambda \ . \end{aligned} \tag{6.31}$$

For $t_1 \leq \delta t < T$, we replace P_{kl}, $|\{\lambda_j(m)\}\rangle$ and $E^{(m)}_\lambda$ by their corresponding expressions at γ_2.

6.2.5 Floquet diagonal ensemble

Assuming that the energy phases randomize after some time, i.e. the coherences in the Floquet basis are scrambled at sone time, the system is expected to relax to the Floquet diagonal ensemble with density matrix $\hat{\rho}_{\mathrm{DE}}(\delta t) = \sum_j \rho_j |\Phi_j(\delta t)\rangle\langle\Phi_j(\delta t)|$, which leads to expectation values of observables

$$\langle\hat{O}(\delta t)\rangle_{\mathrm{DE}} = \mathrm{Tr}\{\hat{\rho}_{\mathrm{DE}}(\delta t)\hat{O}\} = \sum_j |C_j|^2 \langle\Phi_j(\delta t)|\hat{O}|\Phi_j(\delta t)\rangle \ . \tag{6.32}$$

This expression is formally the same as for the energy eigenstates in Chapters 3, 4 and the discussion and results from there carry over to here, except for one important difference. The expectation values of operators in the Floquet diagonal ensemble is time-periodic with T due to the periodicity of the Floquet modes [161]. In the following we will drop the term "Floquet" when referring to the Floquet diagonal ensemble. Diagonal-ensemble expectation values for the undriven system are of course calculated in the corresponding Lieb–Liniger basis instead of the Floquet modes.

6.3 Results

In this section, we present results for the periodically driven Lieb–Liniger system. We set $t_1 = T/2$ throughout and focus on a time-averaged post-quench interaction strength of $\overline{\gamma} = 10$. This puts the system in a superposition of several eigenstates since the added energy

due to the initial quench is larger than the energy gap in our finite system, as discussed in Chapter 4. It is also sufficiently far away from the strongly interacting Tonks–Girardeau regime, where the system maps to free fermions.

We analyze the influence of the driving for various parameters, varying both the amplitude and the period, and present results for two and three particles. Our calculations can be extended to more particles as in previous chapters, where we calculated the overlaps with the initial state for $N = 4$ and $N = 5$ particles and therefore have all the ingredients. However, a careful analysis of numerical convergence has to be performed first, as will become clear in the following.

To investigate the effect of the driving on observables, we first focus on the fidelity and quasi-energy spectrum. We then present results on the second-order coherence, before turning our attention to the energy of the system.

6.3.1 Fidelity and quasi-energy spectrum

We introduced the fidelity $F(t) = |\langle\Psi(t = 0)|\Psi(t)\rangle|^2$ of the initial state with the time-evolved state in Chapter 4, and the interpretation carries over to the Floquet case. In particular, the fidelity F_{DE} in the diagonal ensemble is the inverse participation ratio and roughly characterizes the spread of the initial state in the Floquet basis. We note that F_{DE} is constant over one period T.

In Fig. 6.2(a) we plot the fidelity $F(t)$ for $N = 2$ particles, amplitude $\Delta = 0.02$ and $\overline{\gamma} = 10$ for a wide range of periods T. For most driving periods, the fidelity stays close to the initial value of $F(t = 0) = 1$. We observe a change of temporal pattern at $T \approx 0.1$, $T \approx 0.29$, $T \approx 0.48$, $T \approx 0.67$, $T \approx 0.87$, and $T \approx 0.91$. These marked lines also appear for larger amplitudes of $\Delta = 0.2$ [Fig. 6.2(c)] and $\Delta = 2$ [Fig. 6.2(e)], and they do so at the same values of the period T. The entire pattern is very similar for all three amplitudes, with notable changes happening for $\Delta = 2$ at several periods T, where the fidelity decays to very small values.

Fig. 6.2(b) shows the fidelity F_{DE} in the diagonal ensemble for $\Delta = 0.02$. For almost all driving periods T, $F_{\mathrm{DE}} \approx 0.83$, which is equal to the diagonal ensemble fidelity of the undriven system, indicated by the black arrow on the right. At periods $T \approx 0.216$ and

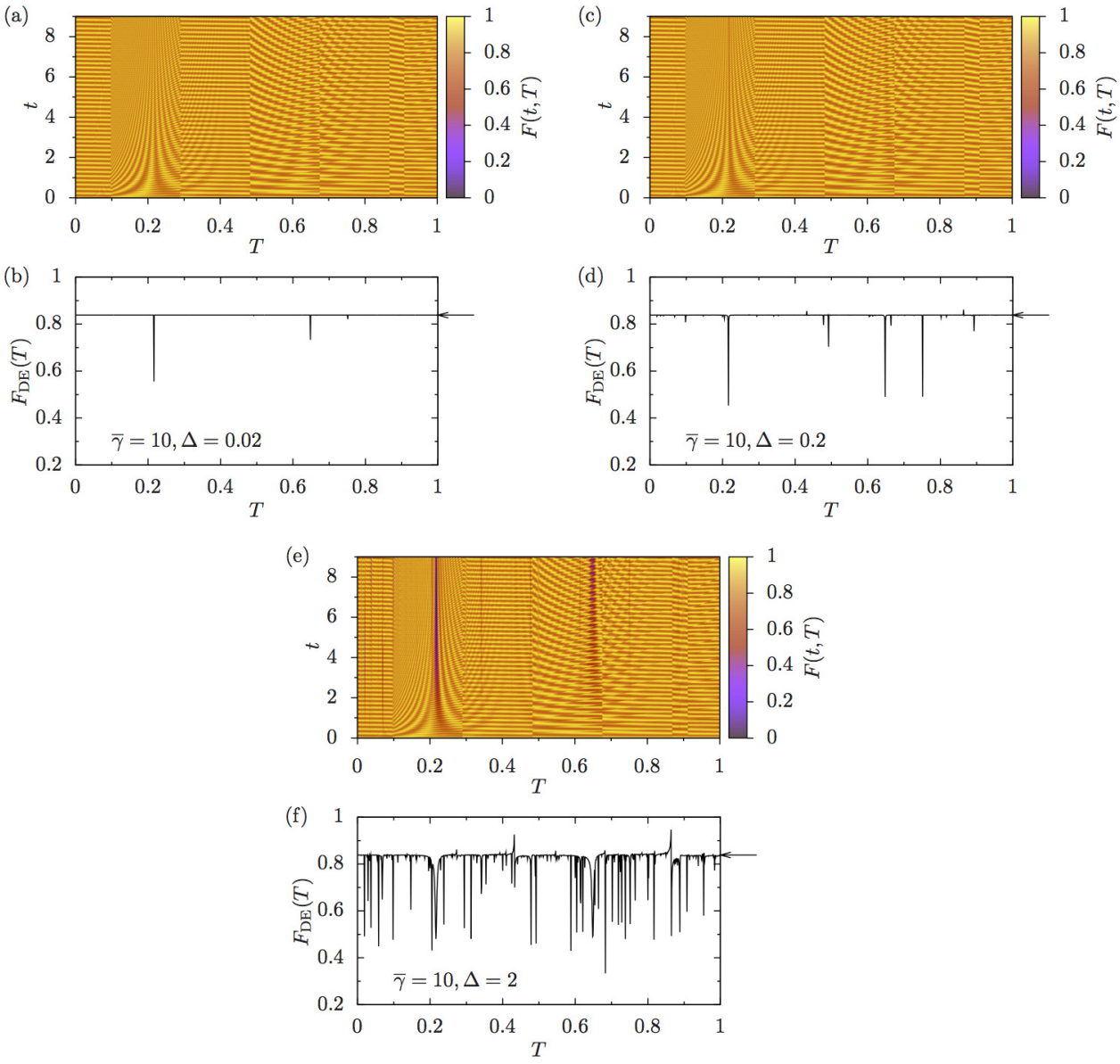

FIGURE 6.2: Fidelity F in the diagonal ensemble [(b),(d),(f)] and nonequilibrium evolution [(a),(c),(e)] for $N = 2$ particles and $\overline{\gamma} = 10$ and a wide range of periods. (a),(b): amplitude of $\Delta = 0.02$. (c),(d): amplitude of $\Delta = 0.2$. (e),(g): amplitude of $\Delta = 2$.

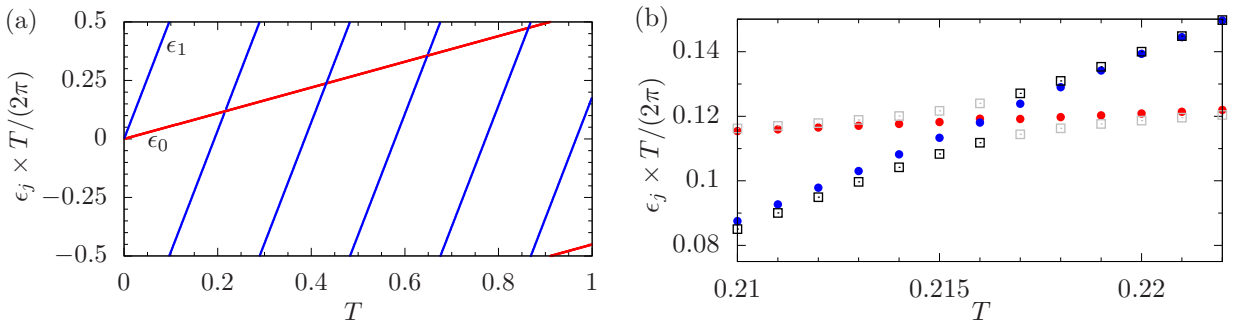

FIGURE 6.3: (a) First two quasi-energies, normalized to driving period, for $\Delta = 0.2$ and a wide range of driving periods. Right: avoided crossing at driving period corresponding to first resonance of the time-averaged system. Circles (red and blue) for $\Delta = 0.2$, squares (black and grey) for $\Delta = 2$.

$T \approx 0.648$, we observe clear dips in F_{DE}, with the first one being more pronounced. These dips also show up for $\Delta = 0.2$ in Fig. 6.2(d), and they start to widen slightly. Additionally, several more peaks show up. For $\Delta = 2$, Fig. 6.2(f), the previously sharp dips are widened considerably, and many new ones are present. The narrow dips for small amplitudes Δ and the widening with increasing Δ are due to driving being resonant with the underlying time-averaged Lieb–Liniger system at $\overline{\gamma} = 10$. The first resonance for $N = 2$ and $\overline{\gamma} = 10$ corresponds to a driving period of $T = 0.216$, which explains the marked response of F_{DE} at this position.

In Fig. 6.3(a), we plot the first two quasi-energies (multiplied by $T/(2\pi)$ to account for the changing width of the first Brioullin zone with T) with driving period T for $\Delta = 0.2$.[8] We identify the change of temporal pattern in Figs. 6.2(a),(c),(d) as the values where the quasi-energies wrap around the first Brioullin zone. The first crossing of the quasi-energies at $T = 0.216$ marks the first resonance of the undriven system at $\overline{\gamma} = 10$. Fig. 6.3(b) reveals that this is actually an avoided crossing. For larger amplitudes, the avoided crossing widens and the dip in the fidelity does so, too. Additionally, higher photon resonances become available (either corresponding to higher one-photon resonances in the Lieb–Liniger spectrum at $\overline{\gamma} = 10$ or to multiple photon resonances) and this is indeed what we observe in Fig. 6.2(f). Small avoided crossings can be problematic numerically, because truncated finite-basis size calculations might not be converged sufficiently [103, 399, 400]. Due to the Brioullin zone structure, there will be many of these, and we discuss this issue in more detail

[8] We will explain the ordering of Floquet energies in Sec. 6.4. Let us remark for now that at $T = 0$, the first two quasi-energies connect to the first two energies of the undriven system.

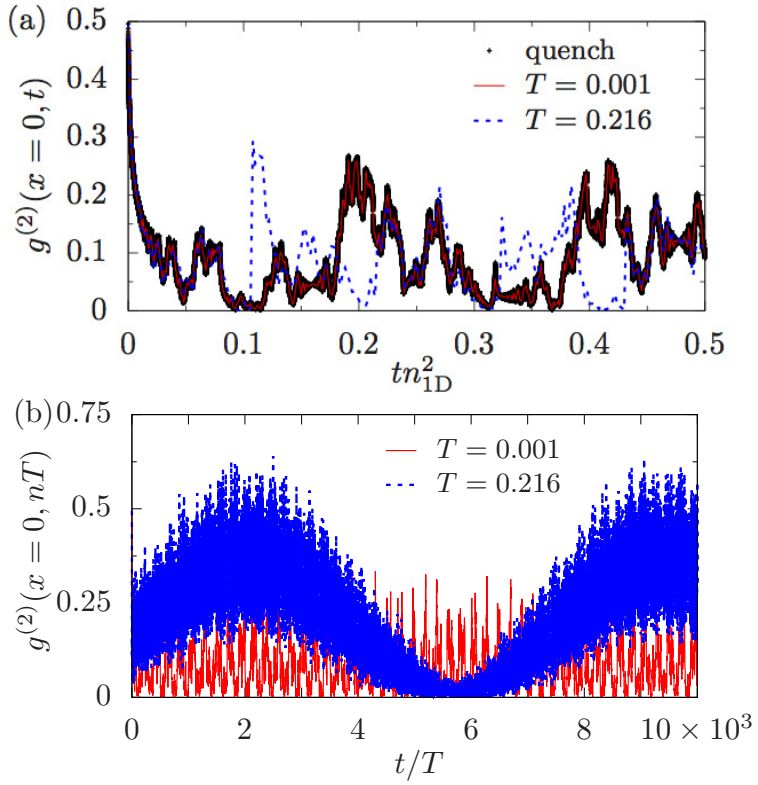

FIGURE 6.4: Local second-order coherence following a quench from $\gamma = 0$ to $\overline{\gamma} = 10$ and for the same (post-quench) state with additional periodic driving with amplitude $\Delta = 0.02$ and two different periods. (a) Time evolution for times $t \leq 0.5 n_{1D}$, which corresponds to 500 driving cycles for $T = 0.001$ (red line), compared to $4 + \epsilon$ for $T = 0.216$ (blue dashed line). (b) Stroboscopic evolution of $g^{(2)}(0, nT)$ with number of cycles $n \equiv t/T$.

in Sec. 6.4

We expect to see different behavior for the driven system when the driving becomes resonant with energy transitions of the time-averaged system. We therefore include the period corresponding to the first resonance in our calculations in the following. For $\overline{\gamma} = 10$ and $N = 3$ ($N = 2$) particles, the energy difference of the ground and first excited state corresponds to $T_{10} = 0.33$ ($T_{10} = 0.216$). Additionally, we will investigate both smaller and larger periods, as well as a higher-order one-photon resonance of $T_{32} = 0.13$ for $N = 3$.

6.3.2 Second-order coherence

In Fig. 6.4(a) we compare the time evolution of the local second-order coherence $g^{(2)}(0, t)$ of the undriven system at $\overline{\gamma} = 10$ (black diamonds) to that of the driven system with amplitude

$\Delta = 0.02$ and two different periods for $N = 2$ particles. For a small period[9] of $T = 0.001$ (red solid line), the local second order coherence follows that of the time-averaged system. For a much larger period of $T = 0.216$ (blue dotted line), $g^{(2)}(0,t)$ agrees with the time-averaged system up to $t = T/2 = 0.108$, when the first driving quench is performed. At this point, the two correlation functions start to differ up to $t = T = 0.216$, when the second quench is performed. After this, $g^{(2)}(0,t)$ quickly starts to agree with the time-averaged system. The same behavior can be observed at $t = 3T/2$, where the correlation functions start to differ again, and at $t = 2T$, where they quickly start to agree again. To see if this behavior persists, we turn our attention to longer times in Fig. 6.4(b). There, we plot the local second order coherence $g^{(2)}(0,nT)$ for the same driving parameters, i.e. periods $T = 0.001$ and $T = 0.216$ and amplitude $\Delta = 0.02$, but here for stroboscopic times $t = nT$ for many driving cycles up to $t/T = 10^4$. For $T = 0.001$ (red solid line), the system fluctuates in time in agreement with the undriven post-quench system (not shown in plot). For $T = 0.216$, on the other hand, we observe a superimposed mono-chromatic oscillation with very small frequency, corresponding to long time scales, and large amplitude. The frequency of this oscillation is given by the quasi-energy difference of the avoided crossing, cf. Fig. 6.3(b). On top of this oscillation, $g^{(2)}(0,t)$ fluctuates strongly with the same order of magnitude as for $T = 0.001$.

Time-averaged second-order coherence

The dynamical evolution of $g^{(2)}(0,t)$ in the last section showed markedly different behavior for different parameters. In this section, we analyze the diagonal ensemble values (cf. Sec. 6.2.5) of the local and non-local second-order coherence. All results in the following are for $N = 3$ particles and $\overline{\gamma} = 10$.

In Fig. 6.5, we plot the diagonal-ensemble values $g^{(2)}_{\mathrm{DE}}(x = 0, \delta t)$, $0 \leq \delta t < T$, of the local second-order coherence within one period for $N = 3$ particles. As discussed in Sec. 6.2.5, observables in the diagonal ensemble are time-periodic with period T. However, the shape within a single period is not specified by this and the system does not necessarily follow the shape of the driving. For the undriven system, $g^{(2)}_{\mathrm{DE}}(x = 0) = 0.12$ is constant and indicated by the horizontal grey line. For driving parameters of $\Delta = 0.02$ and $\Delta = 0.2$, and periods

[9] Small compared to the time-scale of significant change in $g^{(2)}(0,t)$ of the undriven system.

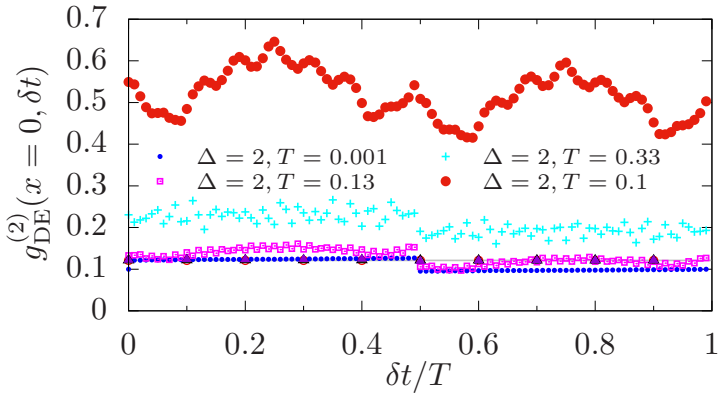

FIGURE 6.5: Local second order coherence $g^{(2)}_{\mathrm{DE}}(x=0,\delta t)$ in the diagonal ensemble for $\overline{\gamma}=10$ and $N=3$ particles. Parameters that lead to a visible deviation from the constant undriven $g^{(2)}_{\mathrm{DE}}(x=0,\overline{\gamma})$ (grey horizontal line) are labelled in the plot. The four unlabelled cases correspond to $\Delta=0.02$ and $\Delta=0.2$, and periods of $T=0.001$ and $T=0.1$ and agree closely with the undriven case.

of $T=0.001$ and $T=0.1$, $g^{(2)}_{\mathrm{DE}}(x=0,\delta t)$ agrees closely with the undriven system. [The points lie on top of each other in Fig. 6.5 and are not labelled to keep the plot legible.] For $\Delta=2$ and $T=0.001$ (blue circles), $g^{(2)}_{\mathrm{DE}}(x=0,\delta t)$ agrees closely with the undriven case up to $\delta t=T/2$, but is slightly smaller for the second half-period. The shape resembles the square-wave form of the driving. This is not the case for $T=0.13$ and $\Delta=2$ (pink squares), where $g^{(2)}_{\mathrm{DE}}(x=0,\delta t)$ is slightly increased for $\delta t<T/2$ and slightly decreased for $\delta\geq T/2$, but with oscillations on top of the square-wave shape. The same behavior can be observed for parameters of $\Delta=2$ and $T=0.33$ (cyan crosses), but now the oscillation on top of the square-wave has a much higher frequency and the value of $g^{(2)}_{\mathrm{DE}}(x=0,\delta t)$ is nearly twice as large as for the undriven system. For $\Delta=2$ and $T=0.1$ (large red circles), $g^{(2)}_{\mathrm{DE}}(x=0,\delta t)$ is largely increased compared to all other cases, with large oscillations comprised of two dominant frequencies.

We now turn our attention to the full spatial second-order coherence. Because the micromotion (i.e. the influence of the time evolution within one period) influences the diagonal ensemble values, in the following we average the second-order coherence over one period T of the drive, $\left\langle g^{(2)}_{\mathrm{DE}}(x)\right\rangle_T = T^{-1}\int_0^T g^{(2)}_{\mathrm{DE}}(x,t)\mathrm{d}t$. In Fig. 6.6 we plot $\left\langle g^{(2)}_{\mathrm{DE}}(x)\right\rangle_T$ for the same parameters as in Fig. 6.5. As for the local value, we observe very good agreement of the undriven system (grey line) with the driven system for parameters $\Delta=0.02$ and $\Delta=0.2$, and $T=0.001$ and $T=0.1$. This also applies to parameters of $\Delta=2$ and $T=0.13$ (pink

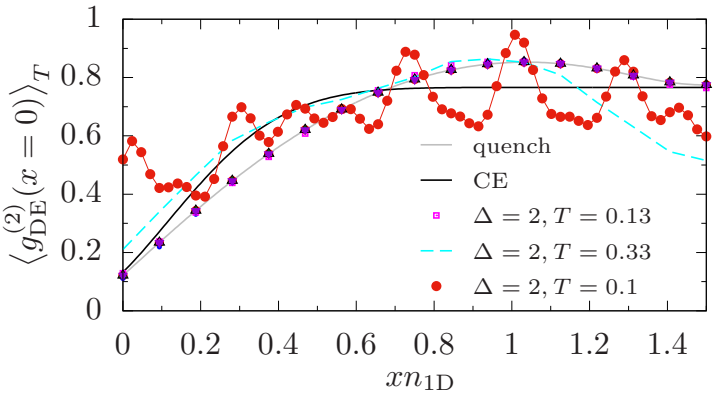

FIGURE 6.6: Second order coherence $\langle g^{(2)}_{\mathrm{DE}}(x)\rangle_T$ in the diagonal ensemble, averaged over one driving period for $N = 3$ particles. For comparison, we also plot $g^{(2)}_{\mathrm{DE}}(x)$ following a quench from $\gamma = 0$ to $\overline{\gamma} = 10$ without subsequent driving (grey line) and $g^{(2)}_{\mathrm{CE}}(x)$ in the canonical ensemble (black line) with energy set by the initial state. We only label $\langle g^{(2)}_{\mathrm{DE}}(x)\rangle_T$ for parameters that lead to visible deviations from the undriven system.

squares). For $\Delta = 2$ and $T = 0.33$ (dashed cyan line), $\langle g^{(2)}_{\mathrm{DE}}(x)\rangle_T$ is increased for $x \leq 1n^{-1}_{1\mathrm{D}}$ and correspondingly decreased for larger values of x. For $\Delta = 2$ and $T = 0.1$, $\langle g^{(2)}_{\mathrm{DE}}(x)\rangle_T$ is increased over the undriven system up to $x \approx 0.5n^{-1}_{1\mathrm{D}}$ and oscillates markedly around it at larger separations.

Neither of the parameters we inspected here leads to $\langle g^{(2)}_{\mathrm{DE}}(x)\rangle_T$ agreeing closely with the thermal $g^{(2)}_{\mathrm{CE}}(x)$ of the undriven post-quench system (black line)[10], nor with the constant infinite temperature case. At the first resonance of the undriven system, corresponding to $T = 0.33$, the shape of $\langle g^{(2)}_{\mathrm{DE}}(x)\rangle_T$ is smooth, and for $x \lesssim 0.7n_{1\mathrm{D}}$ closer to the $g^{(2)}_{\mathrm{CE}}(x)$ than to the corresponding undriven values. In future work it would be interesting to define some measure for the deviation of $\langle g^{(2)}_{\mathrm{DE}}(x)\rangle_T$ from the thermal value and the undriven correlation function, and calculate this quantity for a wide range of driving periods T. This could potentially detect the crossover where the driven system markedly differs from the undriven system and therefore identify the regime where a high-frequency approximation breaks down.

[10] As in Chapters 3, 4, we calculate the canonical ensemble value $g^{(2)}_{\mathrm{CE}}(x)$ by matching the energy with the post-quench energy of the undriven system at $\gamma = 10$.

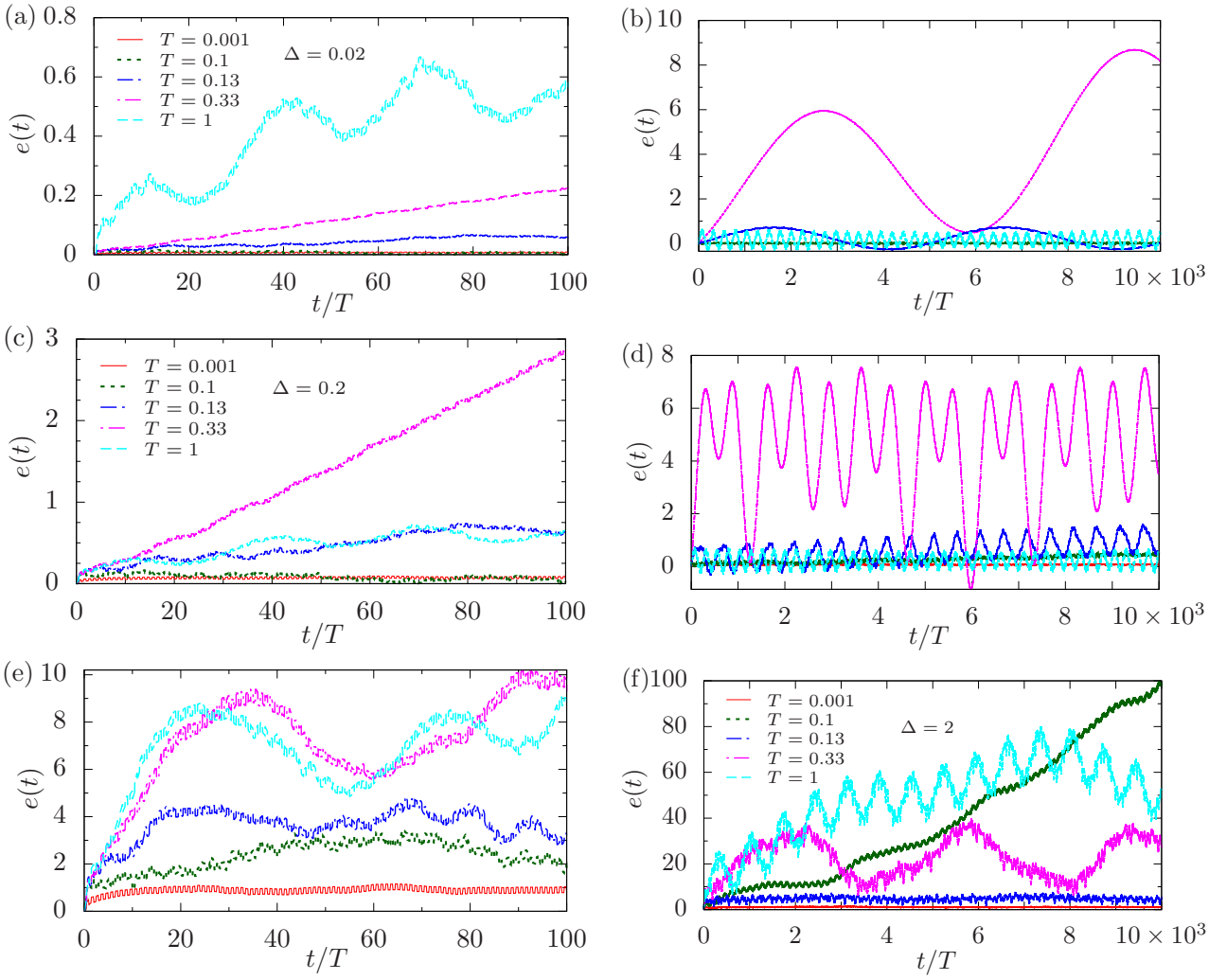

FIGURE 6.7: Absorbed energy per particle $e(t)$ for several representative parameters of the driving around $\overline{\gamma} = 10$ and for $N = 3$ particles.

6.3.3 Energy absorption

Let us define the instantaneous absorbed energy per particle

$$e(t) = \frac{\langle \hat{H} \rangle_t - \langle \hat{H} \rangle_{t=0^+}}{N n_{1\mathrm{D}}^2} , \tag{6.33}$$

where $\langle \hat{H} \rangle_{t=0^+}$ is the post-quench energy just after the quench. For the undriven system $\langle \hat{H}_{\overline{\gamma}} \rangle_{t=0^+} = n_{1\mathrm{D}}^{-2} \overline{\gamma}(N-1)$, see Sec. 3.5.

In Fig. 6.7, we plot the absorbed energy per particle $e(t)$ for $N = 3$ particles and three different amplitudes. The left panel shows the evolution up to $t/T = 100$, while the right panel shows the long-time evolution up to $t/T = 10000$.

For a small amplitude of $T = 0.001$ (red solid line), $e(t)$ stays close to its initial value for all times. For larger amplitude, the energy gain is slightly larger. For $T = 0.1$ (green dotted line), the same behavior can be observed for $\Delta = 0.02$ and 0.2, but for $\Delta = 2$ the absorbed energy keeps increasing for all shown times. For $T = 0.13$ (blue dot-dashed line), $e(t)$ oscillates regularly with small amplitude and with frequency increasing for increasing amplitude. There is no considerable energy absorption at any time. At the period corresponding to the first resonance of the time-averaged system, $T = 0.33$ (pink dot-dashed line), the early-time behavior of $e(t)$ seems to be compatible with linear increase. However, for longer times, we observe regular oscillations for all Δ. For $\Delta = 0.2$ the regular oscillations are comprised of two frequencies. While this is also true for $\Delta = 2$, the frequencies of the two components are increased. The second frequency component with smaller amplitude corresponds to the energy difference of the third and second level of the time-averaged system. For $T = 1$ (cyan dashed line), $e(t)$ increases quickly on early time scales, but settles to fluctuate around a small average value for $\Delta = 0.02$ and $\Delta = 0.2$. For $\Delta = 2$, $e(t)$ also oscillates regularly, but on top of that increases considerably up to times $t/T \simeq 8000$.

Overall, we observe regular oscillations for all amplitudes and $T = 0.33$ and $T = 1$. For $T = 0.001$, the system hardly absorbs any energy and simply follows the shape of the driving. For $T = 0.1$, there seems to be threshold behavior, since we did not observe energy absorption for $\Delta = 0.02$ and $\Delta = 0.2$, but a large increase for $\Delta = 2$ at late times. To see if the system keeps absorbing energy or if $e(t)$ oscillates on longer time scales, we now turn our attention to the diagonal ensemble values of $e(t)$.

Diagonal Ensemble values

According to Eq. (6.31), the matrix elements of the energy are independent of the micromotion within a period, and therefore the diagonal-ensemble value of the absorbed energy e_{DE} always synchronizes with the driving. In Fig. 6.8 we plot the absorbed energy in the diagonal ensemble e_{DE} for the same parameters as in Fig. 6.7. For all parameters, the values of $e_{\mathrm{DE}}(\delta t)$ are very close to each other for both halves of the driving period and $e_{\mathrm{DE}}(\delta t)$ for the second half is slightly increased. In Fig. 6.8(a), we plot $e_{\mathrm{DE}}(\delta t)$ for $\Delta = 0.02$. We see that for $T = 0.001$ (red solid line) and $T = 1$ (cyan dashed line), the system hardly gains energy in agreement with the evolution in Fig. 6.7(b). This also applies to $T = 0.13$ (green

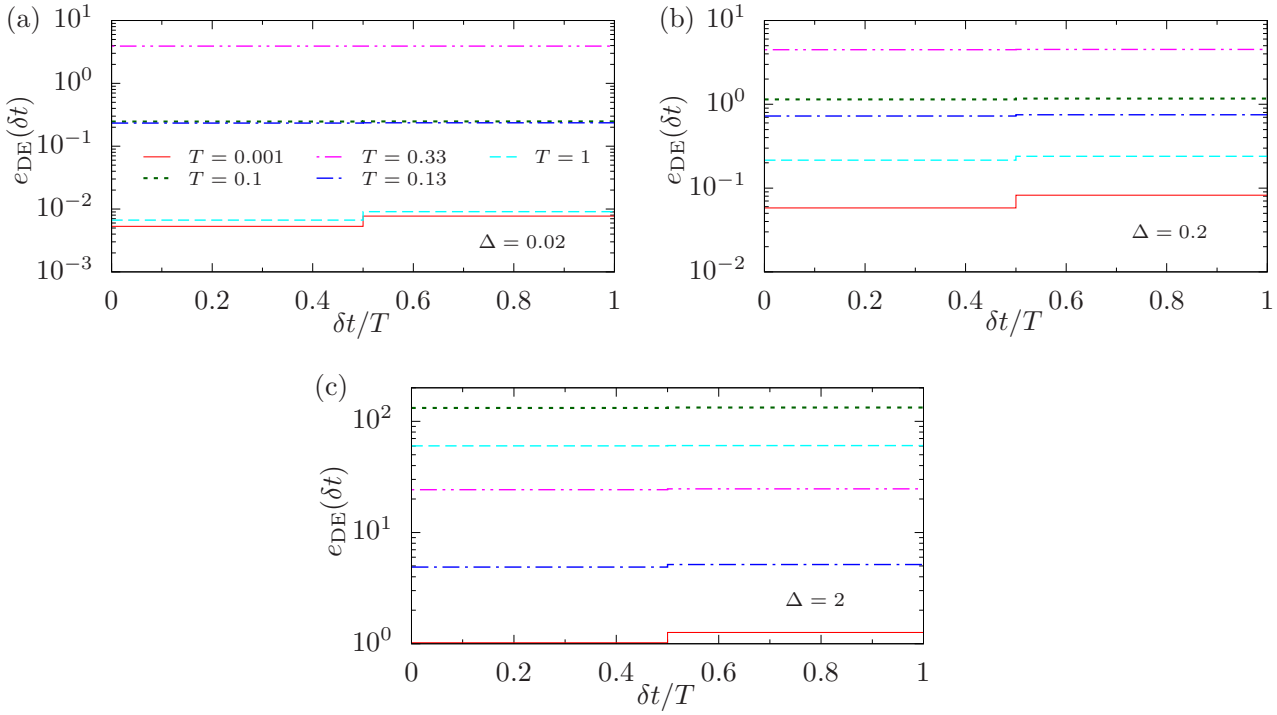

FIGURE 6.8: Absorbed energy per particle $e_{\mathrm{DE}}(\delta t)$ in the diagonal ensemble for $N = 3$ particles and $\overline{\gamma} = 10$. (a) $\Delta = 0.02$. (b) $\Delta = 0.2$. (c) $\Delta = 2$.

dotted line) and $T = 0.1$ (blue dot-dashed line). For $T = 0.33$, $e_{\mathrm{DE}}(\delta t) \approx 4$, much larger than for all other periods.

For $\Delta = 0.2$, Fig. 6.8(b), $e_{\mathrm{DE}}(\delta t)$ for $T = 0.001$ (red solid line) and $T = 1$ (cyan dashed line) are an order of magnitude larger compared to $\Delta = 0.02$. This increase can also be observed for $T = 0.13$ (blue dot-dashed line) and $T = 0.1$ (green dotted line). For $T = 0.33$, $e_{\mathrm{DE}} \approx 4.5$ is very close to that of $\Delta = 0.02$.

Turning to $\Delta = 2$ in Fig. 6.8(c), we observe that all values are largely increased compared to both previous amplitudes. Specifically, for $T = 1$ (cyan dashed line), $e_{\mathrm{DE}}(\delta t) \approx 60$ in marked contrast to its value for $\Delta = 0.02$ and 0.2, where $e_{\mathrm{DE}}(\delta t) < 1$. For $T = 0.1$ (green dotted line), $e_{\mathrm{DE}}(\delta t) \approx 130$, also very much increased compared to the values for smaller amplitudes.

Overall, the behavior of e_{DE} is consistent with the corresponding time-evolving $e(t)$ in the previous section. We do not observe infinite energy growth for any parameters. However, for parameters corresponding to resonances, $e(t)$ shows persistent fluctuations due to the small number of contributing Floquet modes, cf. 6.3.1. In the next section, we will have a

closer look at the populations of Floquet modes.

6.4 Numerical considerations

Approximating an infinite basis by a finite subset has to be done carefully in the case of Floquet theory because the Brioullin-zone structure of the quasi-energies means that there are infinitely many points in a finite interval [103, 399, 401]. As we saw in Sec. 6.3.1, the driving leads to avoided crossings of quasi-energies, which in turn have a strong influence on observables like the second-order coherence in Sec. 6.3.2 and the energy in Sec. 6.3.3. Additionally, we have to approximate the Lieb–Liniger basis by a finite subset of exact eigenstates, so there are two levels of approximation involved in our calculations. We first deal with the representation of the two Lieb–Liniger bases at interactions strengths γ_1 and γ_2 and then investigate the consequences of truncating the Floquet basis at hand.

6.4.1 Constructing $U(T+t,t)$

Due to translational invariance of our system and the initial state having zero total momentum, we can restrict the discussion to zero-momentum eigenstates of the Lieb–Liniger systems at γ_1 and γ_2 here.[11] We utilize our algorithm described in Sec. 3.7.1 to find all overlaps of the ground state at γ_1 with states at γ_2 to given precision. This provides us with a list of states at γ_2 with given quantum numbers $\{m_j\}$. We then calculate the overlaps of the eigenstates at γ_1 with the same sets of $\{m_j\}$ with the basis at γ_2.

For $N = 3$ particles and amplitude $\Delta = 2$, this approach leads to an inclusion of 5618 eigenstates for each basis and a normalization sum-rule violation of $1 - \sum_j |C_j|^2 \leq 3 \times 10^{-5}$ for the eigenstate with the worst representation in the other basis. Generally, low-lying eigenstates are much better approximated by our algorithm. for each eigenstate in the other basis.

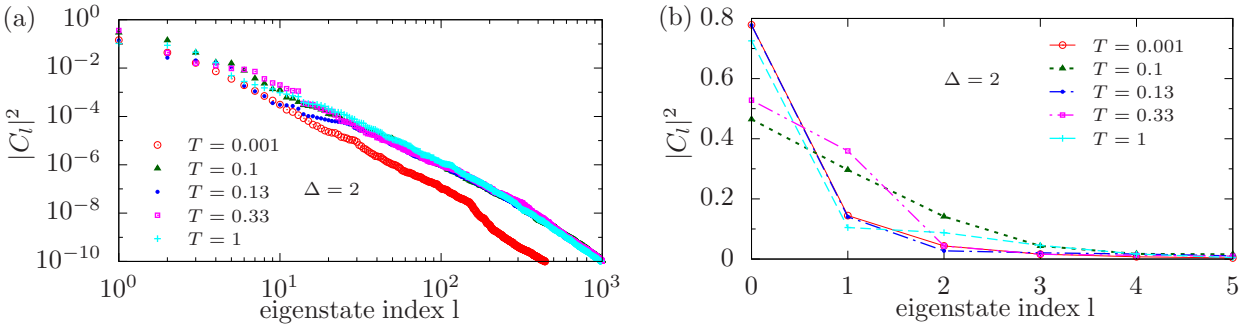

FIGURE 6.9: Populations of initial state in Floquet basis for $N = 3$ particles, $\overline{\gamma} = 10$, $\Delta = 2$ and various driving frequencies. (a) Populations for all included eigenstates in calculations with these parameters in this chapter. (b) First six populations on linear scale.

6.4.2 Overlaps of initial state with Floquet modes

According to Eq. (6.13), the overlaps of any initial state with the basis of Floquet states are time-independent and the populations are given by $|C_l|^2 = |\langle \Phi_l(0)|\Psi(0)\rangle|^2$. This allows us to identify the most dominantly contributing Floquet states and their corresponding quasi-energies.[12]

As observed in Sec. 6.3, the driven system is close to the time-averaged system for small amplitudes and for periods away from resonances. Additionally, only a few low-lying excitations of the time-averaged system were detected by the fidelity, and the corresponding resonances were very narrow. Consequently, the absorbed energy stayed small. For $\Delta = 2$, on the other hand, we saw a broadening and deepening of resonances for the fidelity in Fig. 6.2. Therefore, we focus on the numerically hardest case $\Delta = 2$ in the following. In Fig. 6.9, we plot the populations of the initial state in the Floquet basis, ordered by magnitude, for several representative driving periods T. For larger values of T the distribution is considerably wider than for small T. For $T = 0.33$ (pink squares), corresponding to the first resonance of the time-averaged system, we observe a discontinuous jump at the 14th Floquet mode. Generally, convergence of Floquet modes for finite-basis approximations is hard to establish [399]. We need to do this numerically here and a more detailed study is in order and left for future work. We illustrate the potential pitfalls of our approximation

[11] Ordering the Lieb–Liniger basis states according to their total momentum leads to $\hat{U}$ being composed of blocks, and the diagonalization of a block matrix can be performed independently for each block. The eigenvectors and eigenvalues of the full matrix are then simply given by the ones of each block.

[12] Recall that the quasi-energies are obtained from the eigenvalues of a unitary operator and are therefore distributed on the complex unit circle, defying a description in terms of the usual ordering of real numbers.

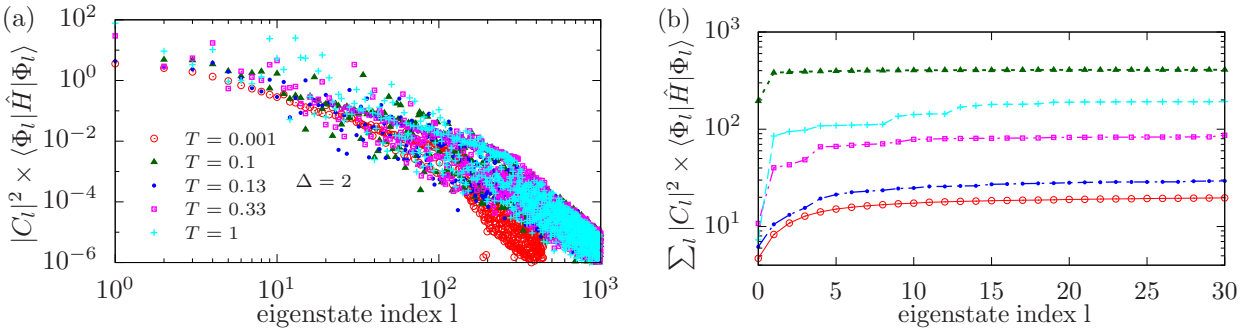

FIGURE 6.10: (a) Contributions to energy in diagonal ensemble for $N = 3$ particles, $\overline{\gamma} = 10$ and $\Delta = 2$ and various driving frequencies. (b) Summed-up contributions for the first thirty contributions.

in the next section.

6.4.3 Energy saturation

In Fig. 6.10(a) we plot the contributions $|C_l|^2 \times \langle\Phi_l(0)|\hat{H}|\Phi_l(0)\rangle$ to the energy in the diagonal ensemble at $\delta t = 0$ for $\Delta = 2$ and $N = 3$ particles. For $T = 0.001$ (red empty circles), the contributions are decaying smoothly with increasing Floquet modes for the lowest eigenstates. This can also be observed in Fig. 6.10(b), where we plot the sum of contributions to the energy over Floquet modes up to that mode. For $T = 0.1$ (green triangles), the contributions are more irregularly distributed up to $l \approx 100$. This hardly influences the convergence of E_{DE} in Fig. 6.10(b) because E_{DE} is dominated by the first two contributions. For $T = 0.13$ (blue circles), the contributions are also irregularly distributed, but the convergence of E_{DE} in Fig. 6.10(b) is relatively smooth. This is not the case for $T = 0.33$ (pink squares), where we observe small jumps in Fig. 6.10(b), corresponding to large contributions in Fig. 6.10(a). This also applies to $T = 1$, where several large contributions at values of l up to approximately 100 can be observed. For all parameters, contributions from higher eigenstates past $l \approx 300$ decrease quickly.

As an example of parameters for which we observe unexpected behavior, we plot the absorbed energy per particle, normalized to the amplitude Δ, for $T = 0.01$ in Fig. 6.11. For all considered amplitudes, $\Delta = 0.02$, 0.2 and 2, $e(t)/\Delta$ increases rapidly over the first two cycles as can be seen in Fig. 6.11(a). It then follows the driving closely. In Fig. 6.11(b), we plot $e(t)/\Delta$ for the same parameters up to $t/T = 10000$. We observe a similar behavior for

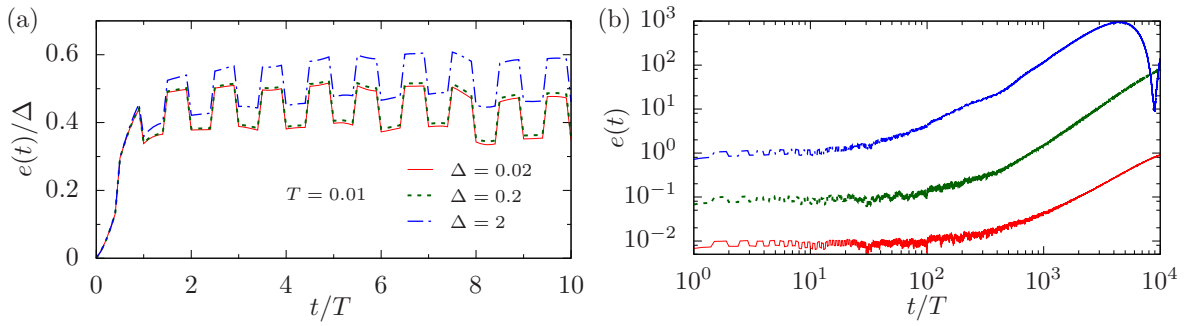

FIGURE 6.11: Absorbed energy $e(t)$ per particle for $\overline{\gamma} = 10$ and period $T = 0.01$ and $N = 3$ particles for (a) short times and (b) longer times.

all amplitudes, where $e(t)$ stays close to the value it attained after the first two cycles, but suddenly starts to increase after many cycles and goes to very large values. This increase happens slightly earlier for larger amplitudes. This behavior is in contrast to that of the absorbed energy in Fig. 6.7, where curves that settled to a constant average value over several driving amplitudes stayed at that value. A closer inspection of the quasi-energies and contributions reveals that a very small avoided crossing of the state that connects to the ground state of the undriven system with a higher excited state leads to this behavior. However, the convergence of the quasi-energies for a finite basis is not guaranteed, nor necessarily well-behaved [399, 401] and since the levels are strongly correlated a small error can lead to the appearance of avoided crossings where non should be present. We clearly need to ensure that our results are not artificially influenced by these. The fidelity in Fig. 6.2(f) also displayed resonances at unexpected positions compared to the resonances of the underlying undriven system, which we expect to be unphysical and due to the same problem of non-converged quasi-energies. It is important to discard numerically induced avoided crossings in finite-basis calculations and we need to implement this efficiently in the future. However, small avoided crossings manifest themselves at late times (and in the diagonal ensemble) and therefore they should be irrelevant for the nonequilibrium evolution of correlation functions on short time scales.

6.5 Conclusions

The truncation of Floquet states and representation with an approximate Lieb–Liniger basis leads to a considerable increase of numerical complexity compared to the quench scenario

in Chapters 3, 4, 5. We identified the influence of very small avoided crossings, due to finite-basis truncation errors, that lead to unphysical results and clearly need to improve the identification of these in the future. Nevertheless, we were able to observe the response of the system to a periodic switching of the interaction strength for two and three particles and identify fast driving regimes, corresponding to small periods, where the second-order coherence and the energy of the driven system did not appreciably differ from the time-averaged system. At resonances of the time-averaged system, the driven system absorbed energy quickly and for later times, the energy oscillated regularly around an average value. This was traced back to the populations of Floquet states, which were peaked on very few states.

For fast driving, the second-order coherence in the diagonal ensemble agreed with that of the undriven system. This did not apply to driving periods corresponding to low-lying resonances of the time-averaged system, were we observed a marked difference of the second order coherence to that of the undriven case. However, the second order coherence did not agree with the thermal value determined by the energy of the initial state, or at infinite temperature. Therefore there should be an extensive number of local conserved charges, leading to a relaxation to a generalized (periodic) Gibbs ensemble like for the undriven system.

We focussed on the second-order coherence, but other correlation functions, like the momentum distribution and the one-body entanglement entropy, are accessible as well with our methodology. Finally, let us note that our calculations can be extended to four or five particles, as in previous chapters. However, a careful analysis of numerical convergence has to be performed first.

7

Conclusions

In this thesis we studied the nonequilibrium behavior of one-dimensional bosons with binary contact interactions, which constitutes the famous Lieb–Liniger model. To this end, we developed a computational approach for small systems based on the coordinate Bethe ansatz. In contrast to higher dimensions, one dimensional systems are generally characterized by collective phenomena and strong correlations and importantly, our method is nonperturbative in nature. This enables us to study the entire regime of interactions of the strongly correlated system, in and out of equilibrium, at zero and finite temperature. The procedure to calculate correlation functions at a chosen interaction strength consists of the following steps in general:

- Solve the Bethe equations (2.61) numerically at the desired interaction strength.
- Construct the overlaps of a given initial state in terms of the basis of Bethe rapidities obtained in the previous step with the method introduced in Chapter 3.

- Calculate the matrix elements of a given operator in the basis of Bethe rapidities with the same method.

- Sum up the contributions.

The procedure is numerically exact for ground state correlation functions since for these only one set of rapidities contributes as we saw in Section 2.3.2. For dynamical quantities, however, we have to approximate an infinite basis by a finite subset of its (exact) eigenstates. Since this is a standard mathematical procedure, we can quantify the error in correlation functions in a straight-forward manner. We also have additional knowledge with respect to the contributions of the initial state in the basis, and we can control and quantify the precision of computed quantities.

In Chapter 3, we introduced the correlation functions considered throughout this thesis in terms of Bethe ansatz eigenstates and detailed the algorithmic approach employed to numerically evaluate the resulting expressions. As a first application, we obtained first-, second-, third- and fourth-order correlation functions of the ground state with repulsive interactions for up to seven particles. We compared these to known exact and approximate thermodynamic limit results where applicable and characterized the finite-size scaling. The results showed that local correlation functions at strong interaction strengths converged closely to their infinite-system counterparts. We also considered the relaxation dynamics of a system of five particles following an interaction strength quench starting from two different initial states, one the noninteracting ground state, the other a correlated ground state at strong repulsive interactions. The common final interaction strength was chosen in such a way that the post quench energy was the same for both initial conditions. We observed a strikingly similar process of relaxation for the full nonlocal second-order correlation function, where a correlation wave built up at short distances for early times, and then propagated through the system with the same velocity for both initial states. The relaxed correlation functions, however, were shown to be distinct from one another, as well as non-thermal. The contributions of the initial states in the post-quench basis seemed to be compatible with exponential decay for low energies. For conclusive statements about the emergence of a prethermalized state, however, a more detailed analysis would be necessary.

In Chapter 4, we investigated the relaxation dynamics of the initially noninteracting

ground state following a quench to various representative repulsive values of the interaction strength. For relatively small post-quench interaction strengths, the energy deposited by the quench was on the order of the finite-size induced energy gap of the system, and the dynamics of correlation functions was characterized by nearly perfect two-level dynamics. For intermediate and large interaction strengths, this was not the case and the system showed behavior consistent with the picture of dephasing many-body energy eigenstates. The relaxation time-scales of nonlocal correlation functions were characterized by those of the instantaneous fidelity of the system, while local quantities relaxed on much shorter time scales. The relaxed momentum distribution for strong post-quench interaction strengths showed an intermediate quadratic decay, in accordance with analytical calculations in the Tonks–Girardeau limit. The scaling of thermal (canonical ensemble) local correlation functions with post-quench interaction strength was found to be in agreement with grand-canonical expectations. The relaxed local second-order coherence was found to decay linearly with post-quench interaction strength, a result also obtained with the quench-action method. This did not apply for the third-order coherence, which showed a linear decay with interaction strength, in marked contrast to the quadratic decay obtained with the quench-action method. The discrepancy of the results remains an open question.

Turning to attractive interactions in Chapter 5, we calculated several ground state correlation functions around the quantum critical point for seven particles and found good agreement with the mean-field bright soliton solution, despite our relatively small system sizes. However, this did not apply to quantities that are characterized by two-body correlations. For strong attractive interactions, we obtained ground-state correlation functions for four particles and saw the characteristics of the bound state become more pronounced. The local second- and third-order coherence were found to increase linearly and quadratically with interaction strength, respectively. The studies of nonequilibrium properties was based on the same initial state and protocol as in the previous chapter. Starting from the ideal gas ground state, we quenched the interaction strength to several representative values. For relatively low post-quench interaction strengths below the critical point, the system exhibited the same two-level dynamics as the repulsively interacting system due to the finite-size induced gap of excitations. For quenches to large attractive values of the interaction strength, we observed the emergence of tightly bound two-body bound states, which led to vastly

increased values of the local second- and third-order coherence function. Since these would lead to strong particle losses in experiments, we investigated the influence of the initial state on contributions of two-body bound states and the lowest metastable scattering state of the system at strong attractive post-quench interaction strengths. We found a strong decrease of the the influence of the bound state for initial ground states of the repulsively interacting system beyond $\gamma \approx 10$. Away from the origin, the relaxation dynamics of the second-order correlation function following a quench from the noninteracting ground state was very similar to that following a quench to repulsive interactions with the same magnitude, which is characterized by propagation of correlation waves through the system. The relaxed local second- and third-order coherence seemed to converge to finite values for large attractive post-quench interaction strengths. The value of the former was shown to be consistent with a recently obtained value in the thermodynamic limit for the local second-order correlation function.

In Chapter 6, we compared the evolution of the post-quench system of previous chapters to that of a system with time-periodically varying interaction strength, prepared in the same (post-quench) initial state. This allowed us to compare the nonequilibrium dynamics of an integrable system (with constant interaction strength) to that of a non-integrable driven system. The time-averaged interaction strength of the latter was equal to the undriven post-quench system. For fast driving frequencies, the nonequilibrium evolution of correlation functions and their relaxed values agreed with the undriven system. This was not the case for frequencies corresponding to resonances of the undriven system, where we observed energy absorption and a markedly different relaxed second-order coherence. However, the energy remained bounded for all considered parameters. Our results for the Lieb–Liniger model with periodically driven interaction strength showed that the techniques developed in this thesis are promising candidates for different nonequilibrium scenarios besides interaction strength quenches as well.

References

[1] M. Rigol, V. Dunjko, and M. Olshanii, Nature **452**, 854 (2008).

[2] T. Kinoshita, T. Wenger, and D. S. Weiss, Nature **440**, 900 (2006).

[3] T. Langen, S. Erne, R. Geiger, B. Rauer, T. Schweigler, M. Kuhnert, W. Rohringer, I. E. Mazets, T. Gasenzer, and J. Schmiedmayer, Science **348**, 207 (2015).

[4] C. Chin, R. Grimm, P. Julienne, and E. Tiesinga, Rev. Mod. Phys. **82**, 1225 (2010).

[5] M. Olshanii and V. Dunjko, Phys. Rev. Lett. **91**, 090401 (2003).

[6] A. Y. Cherny and J. Brand, Phys. Rev. A **79**, 043607 (2009).

[7] M. Kormos, A. Shashi, Y.-Z. Chou, J.-S. Caux, and A. Imambekov, Phys. Rev. B **88**, 205131 (2013).

[8] J. De Nardis, B. Wouters, M. Brockmann, and J.-S. Caux, Phys. Rev. A **89**, 033601 (2014).

[9] L. Piroli, P. Calabrese, and F. H. L. Essler, Phys. Rev. Lett. **116**, 070408 (2016).

[10] L. Piroli, P. Calabrese, and F. Essler, *Quantum quenches to the attractive one-dimensional Bose gas: exact results*, preprint arXiv:1604.08141.

[11] F. Schwabl, *Statistical Mechanics* (Springer, 2006).

[12] K. Huang, *Statistical Mechanics* (Wiley, 1987), 2nd ed.

[13] J. Gemmer, M. Michel, and G. Mahler, *Quantum Thermodynamics*(Springer, 2004).

[14] T. Dauxois, Physics Today **61**, 55 (2008).

[15] E. Fermi, J. Pasta, and S. Ulam, Collected Papers of Enrico Fermi **2**, 977 (1965).

[16] G. P. Berman and F. M. Izrailev, Chaos **15**, 015104 (2005).

[17] N. J. Zabusky and M. D. Kruskal, Phys. Rev. Lett. **15**, 240 (1965).

[18] J. Dziarmaga, Adv. Phys. **59**, 1063 (2010).

[19] A. Polkovnikov, K. Sengupta, A. Silva, and M. Vengalattore, Rev. Mod. Phys. **83**, 863 (2011).

[20] L. D'Alessio, Y. Kafri, A. Polkovnikov, and M. Rigol (2015), *From Quantum Chaos and Eigenstate Thermalization to Statistical Mechanics and Thermodynamics*, preprint arXiv:1509.06411.

[21] C. Gogolin and J. Eisert, Rep. Prog. Phys. **79**, 056001 (2016).

[22] J. von Neumann, Eur. Phys. J. H **35**, 201 (2010).

[23] S. Popescu, A. J. Short, and A. Winter, Nat. Phys. **2**, 754 (2006).

[24] J. M. Deutsch, Phys. Rev. A **43**, 2046 (1991).

[25] M. Srednicki, Phys. Rev. E **50**, 888 (1994).

[26] H. Kim, T. N. Ikeda, and D. A. Huse, Phys. Rev. E **90**, 052105 (2014).

[27] P. Reimann, New J. Phys. **17**, 055025 (2015).

[28] J. Eisert, M. Friesdorf, and C. Gogolin, Nat. Phys. **11**, 124 (2015).

[29] R. Nandkishore and D. A. Huse, Annu. Rev. Condens. Matter Phys. **6**, 15 (2015).

[30] S. Goldstein, D. A. Huse, J. L. Lebowitz, and R. Tumulka, Phys. Rev. Lett. **115**, 100402 (2015).

[31] M. Rigol and M. Srednicki, Phys. Rev. Lett. **108**, 110601 (2012).

[32] N. Margolus and L. B. Levitin, Physica D **120**, 188 (1998).

[33] A. J. Short and T. C. Farrelly, New J. Phys. **14**, 013063 (2012).

[34] P. Reimann and M. Kastner, New J. Phys. **14**, 043020 (2012).

[35] S. Goldstein, T. Hara, and H. Tasaki, Phys. Rev. Lett. **111**, 140401 (2013).

[36] A. S. L. Malabarba, L. P. García-Pintos, N. Linden, T. C. Farrelly, and A. J. Short, Phys. Rev. E **90**, 012121 (2014).

[37] S. Goldstein, T. Hara, and H. Tasaki, New J. Phys. **17**, 045002 (2015).

[38] P. Calabrese and J. Cardy, Phys. Rev. Lett. **96**, 136801 (2006).

[39] T. Langen, R. Geiger, M. Kuhnert, B. Rauer, and J. Schmiedmayer, Nat. Phys. **9**, 640 (2013).

[40] M. Cramer, C. M. Dawson, J. Eisert, and T. J. Osborne, Phys. Rev. Lett. **100**, 030602 (2008).

[41] E. H. Lieb and D. W. Robinson, Commun. Math. Phys. **28**, 251 (1972).

[42] M. Kliesch, C. Gogolin, and J. Eisert, *in Many-Electron Approaches in Physics, Chemistry and Mathematics*(Springer International Publishing, 2014).

[43] M. Cheneau, P. Barmettler, D. Poletti, M. Endres, P. Schauß, T. Fukuhara, C. Gross, I. Bloch, C. Kollath, and S. Kuhr, Nature **481**, 484 (2012).

[44] M. B. Hastings and T. Koma, Commun. Math. Phys. **265**, 781 (2006).

[45] J. Eisert, M. van den Worm, S. R. Manmana, and M. Kastner, Phys. Rev. Lett. **111**, 260401 (2013).

[46] M. van den Worm, B. C. Sawyer, J. J. Bollinger, and M. Kastner, New J. Phys. **15**, 083007 (2013).

[47] Z.-X. Gong, M. Foss-Feig, S. Michalakis, and A. V. Gorshkov, Phys. Rev. Lett. **113**, 030602 (2014).

[48] M. Foss-Feig, Z.-X. Gong, C. W. Clark, and A. V. Gorshkov, Phys. Rev. Lett. **114**, 157201 (2015).

[49] A. S. Buyskikh, M. Fagotti, J. Schachenmayer, F. Essler, and A. J. Daley, Phys. Rev. A **93**, 053620 (2016).

[50] P. W. Anderson, Phys. Rev. **109**, 1492 (1958).

[51] S. S. Kondov, W. R. McGehee, W. Xu, and B. DeMarco, Phys. Rev. Lett. **114**, 083002 (2015).

[52] M. Schreiber, S. S. Hodgman, P. Bordia, H. P. Lüschen, M. H. Fischer, R. Vosk, E. Altman, U. Schneider, and I. Bloch, Science **349**, 842 (2015).

[53] J.-y. Choi, S. Hild, J. Zeiher, P. Schauß, A. Rubio-Abadal, T. Yefsah, V. Khemani, D. A. Huse, I. Bloch, and C. Gross, Science **352**, 1547 (2016).

[54] E. Altman and R. Vosk, Annu. Rev. Condens. Matter Phys. **6**, 383 (2015).

[55] B. Sutherland, *Beautiful Models*(World Scientific, Singapore, 2004).

[56] E. H. Lieb and W. Liniger, Phys. Rev. **130**, 1605 (1963).

[57] J.-S. Caux and J. Mossel, J. Stat. Mech. p. P02023 (2011).

[58] C. N. Yang, Phys. Rev. Lett. **19**, 1312 (1967).

[59] M. Jimbo, *Yang-Baxter equation in integrable systems*, vol. 10(World Scientific, 1990).

[60] E. T. Jaynes, Phys. Rev. **106**, 620 (1957).

[61] E. T. Jaynes, Phys. Rev. **108**, 171 (1957).

[62] M. Rigol, V. Dunjko, V. Yurovsky, and M. Olshanii, Phys. Rev. Lett. **98**, 050405 (2007).

[63] A. J. Daley, M. Rigol, and D. S. Weiss, New J. Phys. **16**, 095006 (2014).

[64] M. A. Cazalilla and M. Rigol, New J. Phys. **12**, 055006 (2010).

[65] T. Giamarchi, *Quantum physics in one dimension*(Oxford University Press, 2004).

[66] P. Jordan and E. Wigner, Zeitschrift für Physik **47**, 631 (1928).

[67] V. Gurarie, J. Stat. Mech. Theor. Exp. **2013**, P02014 (2013).

[68] T. Barthel and U. Schollwöck, Phys. Rev. Lett. **100**, 100601 (2008).

[69] M. Fagotti and F. H. L. Essler, Phys. Rev. B **87**, 245107 (2013).

[70] M. Collura, S. Sotiriadis, and P. Calabrese, Phys. Rev. Lett. **110**, 245301 (2013).

[71] M. Collura, S. Sotiriadis, and P. Calabrese, J. Stat. Mech. **2013**, P09025 (2013).

[72] J. Mossel and J.-S. Caux, New J. Phys. **14**, 075006 (2012).

[73] M. Kormos, M. Collura, and P. Calabrese, Phys. Rev. A **89**, 013609 (2014).

[74] T. M. Wright, M. Rigol, M. J. Davis, and K. V. Kheruntsyan, Phys. Rev. Lett. **113**, 050601 (2014).

[75] P. Calabrese, F. H. L. Essler, and M. Fagotti, J. Stat. Mech. **2012**, P07016 (2012).

[76] P. Calabrese, F. H. L. Essler, and M. Fagotti, J. Stat. Mech. **2012**, P07022 (2012).

[77] A. Iucci and M. A. Cazalilla, Phys. Rev. A **80**, 063619 (2009).

[78] M. A. Cazalilla, A. Iucci, and M.-C. Chung, Phys. Rev. E **85**, 011133 (2012).

[79] M. Kollar and M. Eckstein, Phys. Rev. A **78**, 013626 (2008).

[80] D. M. Gangardt and M. Pustilnik, Phys. Rev. A **77**, 041604 (2008).

[81] D. Sels and M. Wouters, Phys. Rev. E **92**, 022123 (2015).

[82] L. F. Santos, A. Polkovnikov, and M. Rigol, Phys. Rev. Lett. **107**, 040601 (2011).

[83] B. Wouters, J. De Nardis, M. Brockmann, D. Fioretto, M. Rigol, and J.-S. Caux, Phys. Rev. Lett. **113**, 117202 (2014).

[84] B. Pozsgay, M. Mestyán, M. A. Werner, M. Kormos, G. Zaránd, and G. Takács, Phys. Rev. Lett. **113**, 117203 (2014).

[85] E. Ilievski, M. Medenjak, and T. c. v. Prosen, Phys. Rev. Lett. **115**, 120601 (2015).

[86] E. Ilievski, J. De Nardis, B. Wouters, J.-S. Caux, F. H. L. Essler, and T. Prosen, Phys. Rev. Lett. **115**, 157201 (2015).

[87] V. Alba (2015), *Simulating the Generalized Gibbs Ensemble (GGE): a Hilbert space Monte Carlo approach*, preprint arXiv:1507.06994.

[88] M. Kollar, F. A. Wolf, and M. Eckstein, Phys. Rev. B **84**, 054304 (2011).

[89] B. Bertini, F. H. L. Essler, S. Groha, and N. J. Robinson, Phys. Rev. Lett. **115**, 180601 (2015).

[90] B. Bertini and M. Fagotti, J. Stat. Mech. Theor. Exp. **2015**, P07012 (2015).

[91] G. P. Brandino, J.-S. Caux, and R. M. Konik, Phys. Rev. X **5**, 041043 (2015).

[92] M. Buchhold, M. Heyl, and S. Diehl, Phys. Rev. A **94**, 013601 (2016).

[93] T. Langen, T. Gasenzer, and J. Schmiedmayer, J. Stat. Mech. **2016**, 064009 (2016).

[94] J. Berges, S. Borsányi, and C. Wetterich, Phys. Rev. Lett. **93**, 142002 (2004).

[95] S. Hofferberth, I. Lesanovsky, B. Fischer, T. Schumm, and J. Schmiedmayer, Nature **449**, 324 (2007).

[96] M. Gring, M. Kuhnert, T. Langen, T. Kitagawa, B. Rauer, M. Schreitl, I. Mazets, D. Adu Smith, E. Demler, and J. Schmiedmayer, Science **337**, 1318 (2012).

[97] D. A. Smith, M. Gring, T. Langen, M. Kuhnert, B. Rauer, R. Geiger, T. Kitagawa, I. Mazets, E. Demler, and J. Schmiedmayer, New J. Phys. **15**, 075011 (2013).

[98] T. Langen, M. Gring, M. Kuhnert, B. Rauer, R. Geiger, D. Smith, I. Mazets, and J. Schmiedmayer, Eur. Phys. J. ST **217**, 43 (2013).

[99] I. Bloch, J. Dalibard, and W. Zwerger, Rev. Mod. Phys. **80**, 885 (2008).

[100] J. H. Shirley, Phys. Rev. **138**, B979 (1965).

[101] H. Sambe, Phys. Rev. A **7**, 2203 (1973).

[102] M. Grifoni and P. Hänggi, Phys. Rep. **304**, 229 (1998).

[103] M. Holthaus, J. Phys. B: At. Mol. Opt. Phys **49**, 013001 (2016).

[104] C. Kittel, *Introduction to solid state physics* (Wiley, 2005).

[105] M. Aidelsburger, M. Atala, M. Lohse, J. T. Barreiro, B. Paredes, and I. Bloch, Phys. Rev. Lett. **111**, 185301 (2013).

[106] H. Miyake, G. A. Siviloglou, C. J. Kennedy, W. C. Burton, and W. Ketterle, Phys. Rev. Lett. **111**, 185302 (2013).

[107] M. Aidelsburger, M. Lohse, C. Schweizer, M. Atala, J. T. Barreiro, S. Nascimbene, N. Cooper, I. Bloch, and N. Goldman, Nat. Phys. **11**, 162 (2015).

[108] G. Jotzu, M. Messer, R. Desbuquois, M. Lebrat, T. Uehlinger, D. Greif, and T. Esslinger, Nature **515**, 237 (2014).

[109] F. Grossmann, T. Dittrich, P. Jung, and P. Hänggi, Phys. Rev. Lett. **67**, 516 (1991).

[110] A. S. Sørensen, E. Demler, and M. D. Lukin, Phys. Rev. Lett. **94**, 086803 (2005).

[111] A. Eckardt, C. Weiss, and M. Holthaus, Phys. Rev. Lett. **95**, 260404 (2005).

[112] C. Kollath, A. Iucci, I. P. McCulloch, and T. Giamarchi, Phys. Rev. A **74**, 041604 (2006).

[113] L.-K. Lim, C. M. Smith, and A. Hemmerich, Phys. Rev. Lett. **100**, 130402 (2008).

[114] E. R. F. Ramos, E. A. L. Henn, J. A. Seman, M. A. Caracanhas, K. M. F. Magalhães, K. Helmerson, V. I. Yukalov, and V. S. Bagnato, Phys. Rev. A **78**, 063412 (2008).

[115] J. Gong, L. Morales-Molina, and P. Hänggi, Phys. Rev. Lett. **103**, 133002 (2009).

[116] T. Kitagawa, E. Berg, M. Rudner, and E. Demler, Phys. Rev. B **82**, 235114 (2010).

[117] D. Poletti and C. Kollath, Phys. Rev. A **84**, 013615 (2011).

[118] J. Dalibard, F. Gerbier, G. Juzeliūnas, and P. Öhberg, Rev. Mod. Phys. **83**, 1523 (2011).

[119] L. Jiang, T. Kitagawa, J. Alicea, A. R. Akhmerov, D. Pekker, G. Refael, J. I. Cirac, E. Demler, M. D. Lukin, and P. Zoller, Phys. Rev. Lett. **106**, 220402 (2011).

[120] P. Hauke, O. Tieleman, A. Celi, C. Ölschläger, J. Simonet, J. Struck, M. Weinberg, P. Windpassinger, K. Sengstock, M. Lewenstein, et al., Phys. Rev. Lett. **109**, 145301 (2012).

[121] C. A. Parra-Murillo, J. Madroñero, and S. Wimberger, Phys. Rev. A **88**, 032119 (2013).

[122] N. Goldman and J. Dalibard, Phys. Rev. X **4**, 031027 (2014).

[123] M. Bukov, L. D'Alessio, and A. Polkovnikov, Adv. Phys. **64**, 139 (2015).

[124] A. Eckardt and E. Anisimovas, New J. Phys. **17**, 093039 (2015).

[125] W. K. Hensinger, H. Haffner, A. Browaeys, N. R. Heckenberg, K. Helmerson, C. McKenzie, G. J. Milburn, W. D. Phillips, S. L. Rolston, H. Rubinsztein-Dunlop, et al., Nature **412**, 52 (2001).

[126] D. A. Steck, W. H. Oskay, and M. G. Raizen, Science **293**, 274 (2001).

[127] N. Gemelke, E. Sarajlic, Y. Bidel, S. Hong, and S. Chu, Phys. Rev. Lett. **95**, 170404 (2005).

[128] H. Lignier, C. Sias, D. Ciampini, Y. Singh, A. Zenesini, O. Morsch, and E. Arimondo, Phys. Rev. Lett. **99**, 220403 (2007).

[129] E. Kierig, U. Schnorrberger, A. Schietinger, J. Tomkovic, and M. K. Oberthaler, Phys. Rev. Lett. **100**, 190405 (2008).

[130] A. Eckardt, M. Holthaus, H. Lignier, A. Zenesini, D. Ciampini, O. Morsch, and E. Arimondo, Phys. Rev. A **79**, 013611 (2009).

[131] A. Alberti, V. V. Ivanov, G. M. Tino, and G. Ferrari, Nat. Phys. **5**, 547 (2009).

[132] A. Zenesini, H. Lignier, D. Ciampini, O. Morsch, and E. Arimondo, Phys. Rev. Lett. **102**, 100403 (2009).

[133] S. E. Pollack, D. Dries, R. G. Hulet, K. M. F. Magalhães, E. A. L. Henn, E. R. F. Ramos, M. A. Caracanhas, and V. S. Bagnato, Phys. Rev. A **81**, 053627 (2010).

[134] E. Haller, R. Hart, M. J. Mark, J. G. Danzl, L. Reichsöllner, and H.-C. Nägerl, Phys. Rev. Lett. **104**, 200403 (2010).

[135] M. Aidelsburger, M. Atala, S. Nascimbène, S. Trotzky, Y.-A. Chen, and I. Bloch, Phys. Rev. Lett. **107**, 255301 (2011).

[136] Y.-A. Chen, S. Nascimbène, M. Aidelsburger, M. Atala, S. Trotzky, and I. Bloch, Phys. Rev. Lett. **107**, 210405 (2011).

[137] R. Ma, M. E. Tai, P. M. Preiss, W. S. Bakr, J. Simon, and M. Greiner, Phys. Rev. Lett. **107**, 095301 (2011).

[138] J. Struck, C. Ölschläger, R. Le Targat, P. Soltan-Panahi, A. Eckardt, M. Lewenstein, P. Windpassinger, and K. Sengstock, Science **333**, 996 (2011).

[139] J. Struck, C. Ölschläger, M. Weinberg, P. Hauke, J. Simonet, A. Eckardt, M. Lewenstein, K. Sengstock, and P. Windpassinger, Phys. Rev. Lett. **108**, 225304 (2012).

[140] K. Jiménez-García, L. J. LeBlanc, R. A. Williams, M. C. Beeler, A. R. Perry, and I. B. Spielman, Phys. Rev. Lett. **108**, 225303 (2012).

[141] J. Struck, M. Weinberg, C. Olschlager, P. Windpassinger, J. Simonet, K. Sengstock, R. Hoppner, P. Hauke, A. Eckardt, M. Lewenstein, et al., Nat. Phys. **9**, 738 (2013).

[142] C. V. Parker, L.-C. Ha, and C. Chin, Nat. Phys. **9**, 769 (2013).

[143] M. Atala, M. Aidelsburger, M. Lohse, J. T. Barreiro, B. Paredes, and I. Bloch, Nat. Phys. **10**, 588 (2014).

[144] K. Jiménez-García, L. J. LeBlanc, R. A. Williams, M. C. Beeler, C. Qu, M. Gong, C. Zhang, and I. B. Spielman, Phys. Rev. Lett. **114**, 125301 (2015).

[145] M. Weinberg, C. Ölschläger, C. Sträter, S. Prelle, A. Eckardt, K. Sengstock, and J. Simonet, Phys. Rev. A **92**, 043621 (2015).

[146] C. J. Kennedy, W. C. Burton, W. C. Chung, and W. Ketterle, Nat. Phys. **11**, 859 (2015).

[147] L.-C. Ha, L. W. Clark, C. V. Parker, B. M. Anderson, and C. Chin, Phys. Rev. Lett. **114**, 055301 (2015).

[148] L. D'Alessio and A. Polkovnikov, Ann. Phys. **333**, 19 (2013).

[149] H. Kim, T. N. Ikeda, and D. A. Huse, Phys. Rev. E **90**, 052105 (2014).

[150] L. D'Alessio and M. Rigol, Phys. Rev. X **4**, 041048 (2014).

[151] A. Lazarides, A. Das, and R. Moessner, Phys. Rev. E **90**, 012110 (2014).

[152] P. Ponte, Z. Papić, F. Huveneers, and D. A. Abanin, Phys. Rev. Lett. **114**, 140401 (2015).

[153] M. Bukov, S. Gopalakrishnan, M. Knap, and E. Demler, Phys. Rev. Lett. **115**, 205301 (2015).

[154] D. A. Abanin, W. De Roeck, and F. Huveneers, Phys. Rev. Lett. **115**, 256803 (2015).

[155] T. Mori, T. Kuwahara, and K. Saito, Phys. Rev. Lett. **116**, 120401 (2016).

[156] M. Bukov, M. Heyl, D. A. Huse, and A. Polkovnikov, Phys. Rev. B **93**, 155132 (2016).

[157] A. Lazarides, A. Das, and R. Moessner, Phys. Rev. Lett. **115**, 030402 (2015).

[158] T. Kuwahara, T. Mori, and K. Saito, Annals of Physics **367**, 96 (2016).

[159] D. A. Abanin, W. De Roeck, and W. W. Ho (2015), *Effective Hamiltonians, prethermalization and slow energy absorption in periodically driven many-body systems*, preprint arXiv:1510.03405.

[160] E. Canovi, M. Kollar, and M. Eckstein, Phys. Rev. E **93**, 012130 (2016).

[161] A. Russomanno, A. Silva, and G. E. Santoro, Phys. Rev. Lett. **109**, 257201 (2012).

[162] A. Lazarides, A. Das, and R. Moessner, Phys. Rev. Lett. **112**, 150401 (2014).

[163] N. Regnault and R. Nandkishore, Phys. Rev. B **93**, 104203 (2016).

[164] H. Fotso, K. Mikelsons, and J. K. Freericks, Sci. Rep. **4**, 4699 (2014).

[165] J. C. Zill, T. M. Wright, K. V. Kheruntsyan, T. Gasenzer, and M. J. Davis, New J. Phys. **18**, 045010 (2016).

[166] J. C. Zill, T. M. Wright, K. V. Kheruntsyan, T. Gasenzer, and M. J. Davis, Phys. Rev. A **91**, 023611 (2015).

[167] M. H. Anderson, J. R. Ensher, M. R. Matthews, C. E. Wieman, and E. A. Cornell, Science **269**, 198 (1995).

[168] K. B. Davis, M. O. Mewes, M. R. Andrews, N. J. van Druten, D. S. Durfee, D. M. Kurn, and W. Ketterle, Phys. Rev. Lett. **75**, 3969 (1995).

[169] C. C. Bradley, C. A. Sackett, J. J. Tollett, and R. G. Hulet, Phys. Rev. Lett. **79**, 1170 (1997).

[170] C. J. Pethick and H. Smith, *Bose-Einstein condensation in dilute gases* (Cambridge University Press, Cambridge, UK, 2002).

[171] F. Schwabl, *Quantum Mechanics* (Springer, 1999).

[172] E. Timmermans, P. Tommasini, M. Hussein, and A. Kerman, Phys. Rep. **315**, 199 (1999).

[173] T. Gasenzer, Eur. Phys. J. ST **168**, 89 (2009).

[174] T. Köhler, K. Góral, and P. S. Julienne, Rev. Mod. Phys. **78**, 1311 (2006).

[175] E. Braaten and H.-W. Hammer, Phys. Rep. **428**, 259 (2006).

[176] M. Olshanii, Phys. Rev. Lett. **81**, 938 (1998).

[177] Y. Castin, in *Coherent atomic matter waves*, edited by R. Kaiser, C. Westbrook, and F. David, *Bose-einstein condensates in atomic gases: Simple theoretical results* (Springer Berlin Heidelberg, 2001), vol. 72 of *Les Houches - Ecole d'Ete de Physique Theorique*, pp. 1–136.

[178] E. Haller, M. J. Mark, R. Hart, J. G. Danzl, L. Reichsöllner, V. Melezhik, P. Schmelcher, and H.-C. Nägerl, Phys. Rev. Lett. **104**, 153203 (2010).

[179] E. Haller, M. Gustavsson, M. J. Mark, J. G. Danzl, R. Hart, G. Pupillo, and H.-C. Nägerl, Science **325**, 1224 (2009).

[180] S. Gardiner, N. Proukakis, M. Davis, and M. Szymanska, *Finite Temperature and Non-Equilibrium Dynamics*(World Scientific, 2013).

[181] M. Rigol, Phys. Rev. Lett. **103**, 100403 (2009).

[182] R. Kanamoto, H. Saito, and M. Ueda, Phys. Rev. A **67**, 013608 (2003).

[183] R. Kanamoto, H. Saito, and M. Ueda, Phys. Rev. A **73**, 033611 (2006).

[184] D. Flassig, A. Pritzel, and N. Wintergerst, Phys. Rev. D **87**, 084007 (2013).

[185] G. Dvali, D. Flassig, C. Gomez, A. Pritzel, and N. Wintergerst, Phys. Rev. D **88**, 124041 (2013).

[186] O. E. Alon, A. I. Streltsov, and L. S. Cederbaum, Phys. Rev. A **77**, 033613 (2008).

[187] A. I. Streltsov, O. E. Alon, and L. S. Cederbaum, Phys. Rev. Lett. **100**, 130401 (2008).

[188] T. Ernst, D. W. Hallwood, J. Gulliksen, H.-D. Meyer, and J. Brand, Phys. Rev. A **84**, 023623 (2011).

[189] I. Brouzos and P. Schmelcher, Phys. Rev. A **85**, 033635 (2012).

[190] J. G. Cosme, C. Weiss, and J. Brand (2015), *Difficult-to-detect convergence problem of variational multi-mode quantum dynamics with attractive bosons*, preprint arXiv:1510.07845.

[191] U. Schollwöck, Rev. Mod. Phys. **77**, 259 (2005).

[192] U. Schollwöck, Ann. Phys. **326**, 96 (2011).

[193] R. Ors, Ann. Phys. **349**, 117 (2014).

[194] D. Muth, B. Schmidt, and M. Fleischhauer, New J. Phys. **12**, 083065 (2010).

[195] D. Muth and M. Fleischhauer, Phys. Rev. Lett. **105**, 150403 (2010).

[196] C. W. Gardiner, Springer Series in Synergetics (1985).

[197] C. Gardiner and P. Zoller, *Quantum noise: a handbook of Markovian and non-Markovian quantum stochastic methods with applications to quantum optics* (Springer-Verlag Berlin Heidelberg, 2004).

[198] A. Polkovnikov, Ann. Phys. **325**, 1790 (2010).

[199] P. Blakie, A. Bradley, M. Davis, R. Ballagh, and C. Gardiner, Adv. Phys. **57**, 363 (2008).

[200] A. Sinatra, C. Lobo, and Y. Castin, Journal of Physics B: Atomic, Molecular and Optical Physics **35**, 3599 (2002).

[201] M. Rigol, Phys. Rev. Lett. **112**, 170601 (2014).

[202] J.-S. Caux and F. H. L. Essler, Phys. Rev. Lett. **110**, 257203 (2013).

[203] J. Caux (2016), *The Quench Action*, preprint arXiv:1603.04689.

[204] J. De Nardis, B. Wouters, M. Brockmann, and J.-S. Caux, Phys. Rev. A **89**, 033601 (2014).

[205] J. De Nardis and J.-S. Caux, J. Stat. Mech. p. P12012 (2014).

[206] J. De Nardis, L. Piroli, and J.-S. Caux, J. Phys. A **48**, 43FT01 (2015).

[207] V. E. Korepin, N. M. Bogoliubov, and A. G. Izergin, *Quantum Inverse Scattering Method and Correlation Functions* (Cambridge University Press, Cambridge, UK, 1993).

[208] N. A. Slavnov, Theoret. and Math. Phys. **79**, 502 (1989).

[209] J. Mossel and J.-S. Caux, New J. Phys. **12**, 055028 (2010).

[210] V. Gritsev, T. Rostunov, and E. Demler, J. Stat. Mech. **2010**, P05012 (2010).

[211] J. Sato, R. Kanamoto, E. Kaminishi, and T. Deguchi, Phys. Rev. Lett. **108**, 110401 (2012).

[212] H. Bethe, Zeitschrift für Physik **71**, 205 (1931).

[213] J. B. McGuire, J. Math. Phys. **5**, 622 (1964).

[214] M. Girardeau, J. Math. Phys. **1**, 516 (1960).

[215] G. E. Astrakharchik, D. Blume, S. Giorgini, and B. E. Granger, Phys. Rev. Lett. **92**, 030402 (2004).

[216] G. E. Astrakharchik, J. Boronat, J. Casulleras, and S. Giorgini, Phys. Rev. Lett. **95**, 190407 (2005).

[217] M. T. Batchelor, M. Bortz, X. W. Guan, and N. Oelkers, J. Stat. Mech. **2005**, L10001 (2005).

[218] S. Chen, L. Guan, X. Yin, Y. Hao, and X.-W. Guan, Phys. Rev. A **81**, 031609 (2010).

[219] C. N. Yang and C. P. Yang, J. Math. Phys. **10**, 1115 (1969).

[220] J. Sato, R. Kanamoto, E. Kaminishi, and T. Deguchi, New Journal of Physics **18**, 075008 (2016).

[221] T. Dorlas, Commun. Math. Phys. **154**, 347 (1993).

[222] P. Calabrese and J.-S. Caux, J. Stat. Mech. Theor. Exp. **2007**, P08032 (2007).

[223] M. Takahashi, *Thermodynamics of One-Dimensional Solvable Models*(Cambridge University Press, 1999).

[224] S. Prolhac and H. Spohn, J. Math. Phys. **52**, 122106 (2011).

[225] C. A. Tracy and H. Widom, Commun. Math. Phys. **290**, 129 (2009).

[226] A. G. Sykes, P. D. Drummond, and M. J. Davis, Phys. Rev. A **76**, 063620 (2007).

[227] K. Sakmann, A. I. Streltsov, O. E. Alon, and L. S. Cederbaum, Phys. Rev. A **72**, 033613 (2005).

[228] P. Calabrese and J.-S. Caux, Phys. Rev. Lett. **98**, 150403 (2007).

[229] D. Flassig, A. Franca, and A. Pritzel, Phys. Rev. A **93**, 013627 (2016).

[230] M. Kormos, G. Mussardo, and A. Trombettoni, Phys. Rev. A **83**, 013617 (2011).

[231] E. H. Lieb, Phys. Rev. **130**, 1616 (1963).

[232] P. Kulish, S. Manakov, and L. Faddeev, Theoret. and Math. Phys. **28**, 615 (1976).

[233] M. Ishikawa and H. Takayama, J. Phys. Soc. Jpn. **49**, 1242 (1980).

[234] R. Kanamoto, L. D. Carr, and M. Ueda, Phys. Rev. A **81**, 023625 (2010).

[235] D. C. Wadkin-Snaith and D. M. Gangardt, Phys. Rev. Lett. **108**, 085301 (2012).

[236] G. E. Astrakharchik and L. P. Pitaevskii, EPL (Europhysics Letters) **102**, 30004 (2013).

[237] D. Draxler, J. Haegeman, T. J. Osborne, V. Stojevic, L. Vanderstraeten, and F. Verstraete, Phys. Rev. Lett. **111**, 020402 (2013).

[238] T. Karpiuk, T. Sowiński, M. Gajda, K. Rzkazewski, and M. Brewczyk, Phys. Rev. A **91**, 013621 (2015).

[239] A. Izergin, *Introduction to the Bethe ansatz solvable models*, lecture notes at the University of Florence, edited by F. Colomo and A. Pronko. Downloaded from http://theory.fi.infn.it/colomo/.

[240] F. D. M. Haldane, Phys. Rev. Lett. **47**, 1840 (1981).

[241] M. A. Cazalilla, J. Phys. B **37**, S1 (2004).

[242] A. Imambekov, T. L. Schmidt, and L. I. Glazman, Rev. Mod. Phys. **84**, 1253 (2012).

[243] Z. Ristivojevic, Phys. Rev. Lett. **113**, 015301 (2014).

[244] M. Pustilnik and K. A. Matveev, Phys. Rev. B **89**, 100504 (2014).

[245] A. Imambekov and L. I. Glazman, Phys. Rev. Lett. **100**, 206805 (2008).

[246] A. Imambekov and L. I. Glazman, Science **323**, 228 (2009).

[247] N. Fabbri, M. Panfil, D. Clément, L. Fallani, M. Inguscio, C. Fort, and J.-S. Caux, Phys. Rev. A **91**, 043617 (2015).

[248] F. Meinert, M. Panfil, M. J. Mark, K. Lauber, J.-S. Caux, and H.-C. Nägerl, Phys. Rev. Lett. **115**, 085301 (2015).

[249] T. D. Schultz, J. Math. Phys. **4**, 666 (1963).

[250] A. Lenard, J. Math. Phys. **5**, 930 (1964).

[251] H. G. Vaidya and C. A. Tracy, Phys. Rev. Lett. **42**, 3 (1979).

[252] M. Jimbo and T. Miwa, Phys. Rev. D **24**, 3169 (1981).

[253] D. B. Creamer, H. Thacker, and D. Wilkinson, Physica D: Nonlinear Phenomena **20**, 155 (1986).

[254] A. Y. Cherny and J. Brand, Phys. Rev. A **73**, 023612 (2006).

[255] P. J. Forrester, N. E. Frankel, and M. I. Makin, Phys. Rev. A **74**, 043614 (2006).

[256] L. Pitaevskii and S. Stringari, *Bose-Einstein Condensation* (Oxford University Press, Oxford, UK, 2003).

[257] C. Mora and Y. Castin, Phys. Rev. A **67**, 053615 (2003).

[258] J. L. Cardy, J. Phys. A Math. Gen. **17**, L385 (1984).

[259] A. Berkovich and G. Murthy, J. Phys. A Math. Gen. **24**, 1537 (1991).

[260] D. M. Gangardt and G. V. Shlyapnikov, Phys. Rev. Lett. **90**, 010401 (2003).

[261] D. M. Gangardt and G. V. Shlyapnikov, New J. Phys. **5**, 79 (2003).

[262] V. V. Cheianov, H. Smith, and M. B. Zvonarev, Phys. Rev. A **73**, 051604 (2006).

[263] G. E. Astrakharchik and S. Giorgini, Phys. Rev. A **68**, 031602 (2003).

[264] G. E. Astrakharchik and S. Giorgini, J. Phys. B **39**, S1 (2006).

[265] B. Schmidt and M. Fleischhauer, Phys. Rev. A **75**, 021601 (2007).

[266] J.-S. Caux and P. Calabrese, Phys. Rev. A **74**, 031605 (2006).

[267] J.-S. Caux, J. Math. Phys. **50**, 095214 (2009).

[268] M. Panfil and J.-S. Caux, Phys. Rev. A **89**, 033605 (2014).

[269] P. D. Drummond, P. Deuar, and K. V. Kheruntsyan, Phys. Rev. Lett. **92**, 040405 (2004).

[270] P. Deuar, A. G. Sykes, D. M. Gangardt, M. J. Davis, P. D. Drummond, and K. V. Kheruntsyan, Phys. Rev. A **79**, 043619 (2009).

[271] M. Kormos, G. Mussardo, and A. Trombettoni, Phys. Rev. A **81**, 043606 (2010).

[272] A. Lenard, J. Math. Phys. **7**, 1268 (1966).

[273] P. Vignolo and A. Minguzzi, Phys. Rev. Lett. **110**, 020403 (2013).

[274] A. G. Sykes, D. M. Gangardt, M. J. Davis, K. Viering, M. G. Raizen, and K. V. Kheruntsyan, Phys. Rev. Lett. **100**, 160406 (2008).

[275] K. V. Kheruntsyan, D. M. Gangardt, P. D. Drummond, and G. V. Shlyapnikov, Phys. Rev. Lett. **91**, 040403 (2003).

[276] T. Kinoshita, T. Wenger, and D. S. Weiss, Phys. Rev. Lett. **95**, 190406 (2005).

[277] V. Guarrera, D. Muth, R. Labouvie, A. Vogler, G. Barontini, M. Fleischhauer, and H. Ott, Phys. Rev. A **86**, 021601 (2012).

[278] A. Vogler, R. Labouvie, F. Stubenrauch, G. Barontini, V. Guarrera, and H. Ott, Phys. Rev. A **88**, 031603 (2013).

[279] D. Clément, N. Fabbri, L. Fallani, C. Fort, and M. Inguscio, Phys. Rev. Lett. **102**, 155301 (2009).

[280] B. Paredes, A. Widera, V. Murg, O. Mandel, S. Fölling, I. Cirac, G. V. Shlyapnikov, T. W. Hänsch, and I. Bloch, Nature **429**, 277 (2004).

[281] A. H. van Amerongen, J. J. P. van Es, P. Wicke, K. V. Kheruntsyan, and N. J. van Druten, Phys. Rev. Lett. **100**, 090402 (2008).

[282] J. Armijo, T. Jacqmin, K. V. Kheruntsyan, and I. Bouchoule, Phys. Rev. Lett. **105**, 230402 (2010).

[283] J. Armijo, T. Jacqmin, K. Kheruntsyan, and I. Bouchoule, Phys. Rev. A **83**, 021605 (2011).

[284] T. Jacqmin, J. Armijo, T. Berrada, K. V. Kheruntsyan, and I. Bouchoule, Phys. Rev. Lett. **106**, 230405 (2011).

[285] G. P. Berman, F. Borgonovi, F. M. Izrailev, and A. Smerzi, Phys. Rev. Lett. **92**, 030404 (2004).

[286] M. Rigol and A. Muramatsu, Phys. Rev. Lett. **93**, 230404 (2004).

[287] M. Rigol, A. Muramatsu, and M. Olshanii, Phys. Rev. A **74**, 053616 (2006).

[288] A. C. Cassidy, C. W. Clark, and M. Rigol, Phys. Rev. Lett. **106**, 140405 (2011).

[289] C. Gramsch and M. Rigol, Phys. Rev. A **86**, 053615 (2012).

[290] K. He, L. F. Santos, T. M. Wright, and M. Rigol, Phys. Rev. A **87**, 063637 (2013).

[291] T. M. Wright, M. Rigol, M. J. Davis, and K. V. Kheruntsyan, Phys. Rev. Lett. **113**, 050601 (2014).

[292] P. Deuar and P. D. Drummond, J. Phys. A **39**, 1163 (2006).

[293] S. S. Natu and E. J. Mueller, Phys. Rev. A **87**, 053607 (2013).

[294] T. Gasenzer, J. Berges, M. G. Schmidt, and M. Seco, Phys. Rev. A **72**, 063604 (2005).

[295] J. Berges and T. Gasenzer, Phys. Rev. A **76**, 033604 (2007).

[296] A. Branschädel and T. Gasenzer, J. Phys. B **41**, 135302 (2008).

[297] T. Gasenzer and J. M. Pawlowski, Phys. Lett. **B670**, 135 (2008).

[298] H. Buljan, R. Pezer, and T. Gasenzer, Phys. Rev. Lett. **100**, 080406 (2008).

[299] D. Jukić, R. Pezer, T. Gasenzer, and H. Buljan, Phys. Rev. A **78**, 053602 (2008).

[300] R. Pezer, T. Gasenzer, and H. Buljan, Phys. Rev. A **80**, 053616 (2009).

[301] D. Iyer and N. Andrei, Phys. Rev. Lett. **109**, 115304 (2012).

[302] D. Iyer, H. Guan, and N. Andrei, Phys. Rev. A **87**, 053628 (2013).

[303] G. Mussardo, Phys. Rev. Lett. **111**, 100401 (2013).

[304] L. Piroli and P. Calabrese, J. Phys. A: Math. Theor. **48**, 454002 (2015).

[305] J.-S. Caux, P. Calabrese, and N. A. Slavnov, J. Stat. Mech. **2007**, P01008 (2007).

[306] G. B. Arfken and H. J. Weber, *Mathematical Methods for Physicists* (Cambridge University Press, Cambridge, UK, 2005).

[307] M. Brockmann, J. De Nardis, B. Wouters, and J.-S. Caux, J. Phy. A **47**, 145003 (2014).

[308] M. Brockmann, J. Stat. Mech. **2014**, P05006 (2014).

[309] M. Brockmann, J. De Nardis, B. Wouters, and J.-S. Caux, J. Phys. A **47**, 345003 (2014).

[310] V. A. Yurovsky, M. Olshanii, and D. S. Weiss, Adv. At. Mol. Phys. **55**, 61 (2008).

[311] M. A. Cazalilla, R. Citro, T. Giamarchi, E. Orignac, and M. Rigol, Rev. Mod. Phys. **83**, 1405 (2011).

[312] O. Penrose and L. Onsager, Phys. Rev. **104**, 576 (1956).

[313] C. N. Yang, Rev. Mod. Phys. **34**, 694 (1962).

[314] M. Barth and W. Zwerger, Ann. Phys. **326**, 2544 (2011).

[315] S. Tan, Ann. Phys. **323**, 2952 (2008).

[316] M.-S. Wang, J.-H. Huang, C.-H. Lee, X.-G. Yin, X.-W. Guan, and M. T. Batchelor, Phys. Rev. A **87**, 043634 (2013).

[317] M. Kormos, Y.-Z. Chou, and A. Imambekov, Phys. Rev. Lett. **107**, 230405 (2011).

[318] B. L. Tolra, K. M. O'Hara, J. H. Huckans, W. D. Phillips, S. L. Rolston, and J. V. Porto, Phys. Rev. Lett. **92**, 190401 (2004).

[319] E. Haller, M. Rabie, M. J. Mark, J. G. Danzl, R. Hart, K. Lauber, G. Pupillo, and H.-C. Nägerl, Phys. Rev. Lett. **107**, 230404 (2011).

[320] A. G. Manning, W. RuGway, S. S. Hodgman, R. G. Dall, K. G. H. Baldwin, and A. G. Truscott, New J. Phys. **15**, 013042 (2013).

[321] B. Pozsgay, J. Stat. Mech. **2011**, P11017 (2011).

[322] W. Xu and M. Rigol, Phys. Rev. A **92**, 063623 (2015).

[323] V. N. Golovach, A. Minguzzi, and L. I. Glazman, Phys. Rev. A **80**, 043611 (2009).

[324] S. Sotiriadis and P. Calabrese, J. Stat. Mech. **2014**, P07024 (2014).

[325] P. Calabrese and P. L. Doussal, J. Stat. Mech. **2014**, P05004 (2014).

[326] M. Collura, M. Kormos, and P. Calabrese, J. Stat. Mech. **2014**, P01009 (2014).

[327] E. Kaminishi, T. Mori, T. N. Ikeda, and M. Ueda, Nat. Phys. **11**, 1050 (2015).

[328] P. Deuar and M. Stobinska, *Correlation waves after quantum quenches in one- to three-dimensional BECs*, preprint arXiv:1310.1301.

[329] A. Imambekov, I. E. Mazets, D. S. Petrov, V. Gritsev, S. Manz, S. Hofferberth, T. Schumm, E. Demler, and J. Schmiedmayer, Phys. Rev. A **80**, 033604 (2009).

[330] B. Davies, Physica A: Statistical Mechanics and its Applications **167**, 433 (1990).

[331] B. Davies and V. Korepin, *Higher conservation laws for the quantum non-linear Schroedinger equation*, preprint arXiv:1109.6604.

[332] D. S. Petrov, G. V. Shlyapnikov, and J. T. M. Walraven, Phys. Rev. Lett. **85**, 3745 (2000).

[333] E. H. Lieb, R. Seiringer, and J. Yngvason, Phys. Rev. Lett. **91**, 150401 (2003).

[334] R. Pezer and H. Buljan, Phys. Rev. Lett. **98**, 240403 (2007).

[335] D. Rossini, A. Silva, G. Mussardo, and G. E. Santoro, Phys. Rev. Lett. **102**, 127204 (2009).

[336] D. Rossini, S. Suzuki, G. Mussardo, G. E. Santoro, and A. Silva, Phys. Rev. B **82**, 144302 (2010).

[337] P. Calabrese, F. H. L. Essler, and M. Fagotti, Phys. Rev. Lett. **106**, 227203 (2011).

[338] G. Goldstein and N. Andrei, *Equilibration and Generalized GGE in the Lieb–Liniger gas*, preprint arXiv:1309.3471.

[339] H. Buljan, R. Pezer, and T. Gasenzer, Phys. Rev. Lett. **102**, 049903 (2009).

[340] D. Fioretto and G. Mussardo, New J. Phys. **12**, 055015 (2010).

[341] M. Kronenwett and T. Gasenzer, Appl. Phys. B **102**, 469 (2011).

[342] A. Lamacraft, Phys. Rev. A **84**, 043632 (2011).

[343] C. J. M. Mathy, M. B. Zvonarev, and E. Demler, Nat. Phys. **8**, 881 (2012).

[344] E. Kaminishi, J. Sato, and T. Deguchi, J. Phys. Soc. Jpn. **84**, 064002 (2015).

[345] M. Fagotti and F. H. L. Essler, J. Stat. Mech. **2013**, P07012 (2013).

[346] B. Pozsgay, J. Stat. Mech. **2013**, P07003 (2013).

[347] T. Bergeman, M. G. Moore, and M. Olshanii, Phys. Rev. Lett. **91**, 163201 (2003).

[348] P. P. Mazza, M. Collura, M. Kormos, and P. Calabrese, J. Stat. Mech. p. P11016 (2014).

[349] T. N. Ikeda, Y. Watanabe, and M. Ueda, Phys. Rev. E **87**, 012125 (2013).

[350] G. Biroli, C. Kollath, and A. M. Läuchli, Phys. Rev. Lett. **105**, 250401 (2010).

[351] J. Mossel and J.-S. Caux, J. Phys. A **45**, 255001 (2012).

[352] J.-S. Caux and R. M. Konik, Phys. Rev. Lett. **109**, 175301 (2012).

[353] I. Carusotto, R. Balbinot, A. Fabbri, and A. Recati, Eur. Phys. J. D **56**, 391 (2010).

[354] A. Rançon, C.-L. Hung, C. Chin, and K. Levin, Phys. Rev. A **88**, 031601 (2013).

[355] A. G. Sykes, J. P. Corson, J. P. D'Incao, A. P. Koller, C. H. Greene, A. M. Rey, K. R. A. Hazzard, and J. L. Bohn, Phys. Rev. A **89**, 021601 (2014).

[356] X. Yin and L. Radzihovsky, Phys. Rev. A **88**, 063611 (2013).

[357] C.-L. Hung, V. Gurarie, and C. Chin, Science **341**, 1213 (2013).

[358] P. Makotyn, C. E. Klauss, D. L. Goldberge, E. A. Cornell, and D. S. Jin, Nat. Phys. **10**, 116 (2014).

[359] P. Bocchieri and A. Loinger, Phys. Rev. **107**, 337 (1957).

[360] L. S. Schulman, Phys. Rev. A **18**, 2379 (1978).

[361] M. Rigol, Phys. Rev. A **80**, 053607 (2009).

[362] M. A. Nielsen and I. L. Chuang, *Quantum Computation and Quantum Information* (Cambridge University Press, Cambridge, UK, 2000).

[363] V. Zelevinsky, B. A. Brown, N. Frazier, and M. Horoi, Phys. Rep. **276**, 85 (1996).

[364] E. J. Torres-Herrera, M. Vyas, and L. F. Santos, New J. Phys. **16**, 063010 (2014).

[365] E. Braaten, in *The BCS-BEC Crossover and the Unitary Fermi Gas*, edited by W. Zwerger, *Universal relations for fermions with large scattering length* (Springer, Heidelberg, 2012), chap. 6, p. 193.

[366] N. M. Bogoliubov, C. Malyshev, R. K. Bullough, and J. Timonen, Phys. Rev. A **69**, 023619 (2004).

[367] A. Polkovnikov, Phys. Rev. Lett. **101**, 220402 (2008).

[368] G. Dvali and C. Gomez, Physics Letters B **719**, 419 (2013).

[369] G. Dvali and C. Gomez, Fortschritte der Physik **61**, 742 (2013).

[370] M. Kardar, G. Parisi, and Y.-C. Zhang, Phys. Rev. Lett. **56**, 889 (1986).

[371] M. Kardar, Nuclear Physics B **290**, 582 (1987).

[372] P. Calabrese and P. Le Doussal, Phys. Rev. Lett. **106**, 250603 (2011).

[373] Y. Lai and H. A. Haus, Phys. Rev. A **40**, 854 (1989).

[374] A. Ayet and J. Brand, *The one body density matrix of a quantum bright soliton from the coordinate Bethe ansatz*, preprint arXiv:1510.04311.

[375] Y. Hao, Y. Zhang, J. Q. Liang, and S. Chen, Phys. Rev. A **73**, 063617 (2006).

[376] F. Calogero and A. Degasperis, Phys. Rev. A **11**, 265 (1975).

[377] G. M. Kavoulakis, Phys. Rev. A **67**, 011601 (2003).

[378] R. Kanamoto, H. Saito, and M. Ueda, Phys. Rev. Lett. **94**, 090404 (2005).

[379] I. E. Mazets and G. Kurizki, EPL (Europhysics Letters) **76**, 196 (2006).

[380] L. Khaykovich, F. Schreck, G. Ferrari, T. Bourdel, J. Cubizolles, L. D. Carr, Y. Castin, and C. Salomon, Science **296**, 1290 (2002).

[381] K. E. Strecker, G. B. Partridge, A. G. Truscott, and R. G. Hulet, Nature **417**, 150 (2002).

[382] S. L. Cornish, S. T. Thompson, and C. E. Wieman, Phys. Rev. Lett. **96**, 170401 (2006).

[383] A. Marchant, T. Billam, T. Wiles, M. Yu, S. Gardiner, and S. Cornish, Nat. Commun. **4**, 1865 (2013).

[384] J. H. Nguyen, P. Dyke, D. Luo, B. A. Malomed, and R. G. Hulet, Nat. Phys. **10**, 918 (2014).

[385] P. Medley, M. A. Minar, N. C. Cizek, D. Berryrieser, and M. A. Kasevich, Phys. Rev. Lett. **112**, 060401 (2014).

[386] G. D. McDonald, C. C. N. Kuhn, K. S. Hardman, S. Bennetts, P. J. Everitt, P. A. Altin, J. E. Debs, J. D. Close, and N. P. Robins, Phys. Rev. Lett. **113**, 013002 (2014).

[387] M. D. Girardeau and G. E. Astrakharchik, Phys. Rev. A **81**, 061601(R) (2010).

[388] M. Panfil, J. De Nardis, and J.-S. Caux, Phys. Rev. Lett. **110**, 125302 (2013).

[389] L. D. Carr, C. W. Clark, and W. P. Reinhardt, Phys. Rev. A **62**, 063611 (2000).

[390] A. Montina and F. T. Arecchi, Phys. Rev. A **71**, 063615 (2005).

[391] N. Oelkers and J. Links, Phys. Rev. B **75**, 115119 (2007).

[392] L. Salasnich, Journal of Physics B: Atomic, Molecular and Optical Physics **39**, 1743 (2006).

[393] C. Herzog and Y. Castin, C. R. Acad. Sci., Ser. IV: Phys., Astrophys. **2**, 419 (2009), preprint arxiv:cond-mat/0012040.

[394] C. Chin, R. Grimm, P. Julienne, and E. Tiesinga, Rev. Mod. Phys. **82**, 1225 (2010).

[395] L. E. Reichl and W. A. Lin, Foundations of Physics **17**, 689 (1987).

[396] R. Citro, E. G. D. Torre, L. D'Alessio, A. Polkovnikov, M. Babadi, T. Oka, and E. Demler, Ann. Phys. **360**, 694 (2015).

[397] A. Chandran and S. L. Sondhi, Phys. Rev. B **93**, 174305 (2016).

[398] Y. Hardy, A. Fosner, and W.-H. Steeb, Linear Algebra Appl. **439**, 4023 (2013).

[399] D. W. Hone, R. Ketzmerick, and W. Kohn, Phys. Rev. A **56**, 4045 (1997).

[400] A. Eckardt and M. Holthaus, Phys. Rev. Lett. **101**, 245302 (2008).

[401] H. P. Breuer and M. Holthaus, Z. Phys. D **11**, 1 (1989).